A highly controllable cold Rydberg atom hollow-core fiber interface

Dissertation

zur Erlangung des Grades
„Doktor der Naturwissenschaften“
am Fachbereich Physik, Mathematik und Informatik
der Johannes Gutenberg-Universität
in Mainz

Maria Langbecker

geb. in Dresden

Mainz, den 19. März 2019

THESIS DRAFT

THESIS DRAFT

Abstract

THESIS DRAFT

THESIS DRAFT

Zusammenfassung

THESIS DRAFT

THESIS DRAFT

Gutachter der Dissertation

Erstgutachter: **Prof. Dr. Patrick Windpassinger**
Johannes Gutenberg-Universität Mainz
Fachbereich Physik, Mathematik und Informatik
Institut für Physik, QUANTUM
„Experimental Quantum Optics and Quantum Information“

Zweitgutachter: **Prof. Dr. Jochen Walz**
Johannes Gutenberg-Universität Mainz
Fachbereich Physik, Mathematik und Informatik
Institut für Physik, QUANTUM
„Laserspectroscopy, Ion Traps and Applications“

THESIS DRAFT

Erklärung zur Eigenständigkeit

THESIS DRAFT

Contents

THESIS DRAFT

THESIS DRAFT

1. Introduction

1.1. Quantum simulation and information

Quantum technologies are one of the major technological advances of the past decades and will soon become important in everyday life. At least that is what the EU is suggesting in the "European Quantum Technologies Roadmap" [1]. The four major pillars of this "Roadmap" are quantum communication, quantum computation, quantum simulation and quantum sensing and metrology. ("Europe launched in April 2016 the FET Flagship Initiative on Quantum Technologies (Quantum Flagship).")

first quantum revolution: devices which function due to quantum mechanics, such as lasers, transistors, ...

second quantum revolution: devices based on quantum technology (see roadmap discussed above)

"Quantum simulators can answer questions, for which classical computers fail, e.g. when studying strongly interacting many particle systems, like in solid-state physics. Here, we present a highly efficient and highly controllable new platform for quantum simulation: Our experiments are the first to demonstrate the feasibility of creating cold atoms in a highly excited state (so-called Rydberg atoms) inside a hollow core fiber. The confinement inside the fiber core creates a strongly coupled light-matter system, which can be used to transfer the strong long-distance interactions between Rydberg atoms to an effective light-light interaction. We believe that our results pave the way towards future use of our system for applications like quantum simulation with interacting photons or long range, non-local interactions in quantum many body systems."

quantum systems cannot be completely simulated classically (Feynman: "I therefore believe it's true that with a suitable class of quantum machines you could imitate any quantum system, including the physical world." [2]) -> quantum simulation: highly controllable quantum systems are used to simulate other quantum systems

Quantum simulation is already successfully applied using cold or ultracold atoms (e.g. magnetism, phase transitions, novel Hamiltonians, ...) [review book Lewenstein [3], [4], [5] for review on quantum simulation and [6] for Photonic quantum simulators]

A new platform is quantum simulation with photons (also relevant for quantum information as photons are ideal qbits for long-distance quantum information).

THESIS DRAFT

1.2. Photon-photon interactions

Photons in vacuum are not interacting -> coupling to medium can induce interactions

-> strongly coupled light-matter inface needed

1.3. Overview atom-light interfaces

In the following, I will focus on systems working with cold atoms. Other possibilities include for example ions, superconducting circuits, quantum dots, hot atomic vapors, molecules...

Possible systems for strongly coupled atom-light interfaces: nanofibers / surface waveguides (e.g. Rauschenbeutel), cavity systems, mode matched light (e.g. Erlangen), ...

1.4. Cold atoms inside hollow-core fibers

Hollow-core fibers can be used to trap both light field and atoms in the tight confinement of the core. Recent review on "hybrid photonic crystal fibers" (Markos2017)

For a strong light-matter coupling, typically the light beam is focussed to about the size of the atomic cloud for a good overlap. In the free-space case, this leads to a limitation of the interaction region by the Rayleigh range, which is typically on the order of hundreds of micrometer to a few millimeters. In contrast, once atoms and light field are coupled into the hollow core fiber, they can overlap tightly throughout the entire length of the fiber, which can easily be on the order of several centimeters. Thus, the light-matter interaction region inside the fiber is be vastly enhanced compared to free-space experiments. The effective light-matter interaction strength can be expressed in terms of the optical depth. In recent experiments, optical depths of more than 1000 could be achieved in hollow-core fibers filled with cold atoms [7]. Which confirms the strong light-matter interaction. Compared to typical free-space ODs of XXX.

extended quasi 1D system

Review: other experiments with atoms (possibly also molecules and hot vapors) inside hollow-core fibers

advantages of cold atoms: high controllability, i.e. for preparing system inside fiber, no limitations by e.g. transition time broadening as for room-temperature atoms

Also use of hollow-core fibers for transporting particles over long distances (comp. nanoparticles Vienna, also conveyor belt, 15 cm transport! [9]).

"Cold atoms are an ideal system for quantum simulation, computation, and sensing due to the high degree of control over their external as well as internal parameters. In the

THESIS DRAFT

most common case, these atomic properties are manipulated by coupling the atoms to a light field. Thus, for a precise control, a well-defined atom-light interface is necessary. One possibility for an efficient atom-light interface are cold atoms inside a hollow-core fiber. Here, both light and atoms can overlap tightly throughout the length of the fiber and hence the interaction region can be several orders of magnitude larger than in free space. This also increases the optical depth D_{opt}, which is a figure of merit for the effective light-matter interaction strength. Achievements with cold atoms in hollow-core fibers so far include ground-state electro-magnetically induced transparency [10–12], used for example for an all-optical switch [10] and for light storage [12], exciting and probing Rydberg atoms [13], precision spectroscopy [14], and atom interferometry [15]." [72]

"One key prerequisite for these applications is the controlled preparation of the atomic sample inside the hollow-core fiber. Different techniques have been demonstrated to load cold or ultracold atoms inside a hollow-core fiber, including the use of a single-beam red-detuned dipole trap as a guide [16, 17], a hollow beam blue-detuned dipole trap, free fall under gravity, a magnetic funnel [18], a dark funnel in combination with a red-detuned dipole trap beam [7] or combinations of the above [15, 19]. The most controllable way to transport atoms into a hollow-core fiber is to use a moving optical lattice, a so-called optical conveyor belt, first demonstrated by Okaba et al. [14]. A major advantage of this technique is that the atoms can be precisely transported and held at a specific position. This can for example enable a systematic survey of the inner part of the hollow-core fiber. Optical conveyor belts have previously been used to transport single particles [20, 21] and Bose-Einstein-condensates [22], for the study of coherence properties during the transport [23] and to transport cold atoms outside an optical nanofiber [24]. For long-distance transport in free space, Bessel beams [22] or movable lenses [25] have been used to overcome limitations of the transport potential given by the Rayleigh range. " [72]

"While transporting the atoms into the hollow-core fiber, a typical problem is heating of the atoms [7, 13–15], for example due to their acceleration or due to the funnel shape of the transport potential, which increases towards the fibertip. However, low temperatures inside the fiber are advantageous, as they result e.g. in a longer free expansion time and in less heating-induced losses of atoms. To cool the atoms during the transport, so far Raman-sideband cooling [14] or continuous cooling in the magneto-optical trap until the atoms enter the fiber [7] have been employed." [72]

"In this manuscript, we introduce a method of controlling the atomic temperature by adapting the potential depth of the optical conveyor belt according to the position of the atoms. We transport the cold atoms over a distance of several millimeters towards and into our hollow-core fiber and characterize the influence of both frequency (acceleration) and amplitude (trap depth) ramps. By optimizing these transport settings, we show that we can realize a wide range of temperatures and corresponding particle numbers, which we compare to the results of a classical transport simulation. Further, we analyze the influence of the fiber on the transport process by studying measurements for atoms transported outside and inside the hollow-core fiber. " [72]

THESIS DRAFT

1.5. Rydberg atoms for strong long-range interactions

"Rydberg nonlinear quantum optics is a recent and rapidly growing field [26]. A crucial building block is the strong induced dipole-dipole coupling between two Rydberg atoms which can easily be ten orders of magnitude larger than in conventional ground state systems [27]. This is combined with the extraordinary degree of control over the light-matter interactions obtained by electromagnetically induced transparency (EIT) [28]. As a consequence, the strong Rydberg nonlinearity yields the possibility of engineering interactions between individual photons [29–31]. Effective attractive and repulsive interactions between two photons [32–34] and a control of the interaction by microwave fields [35] have been demonstrated. Such a controllable interaction between single photons is ideal for quantum information tools like optical switches, transistors or phase gates [33, 34, 36–45]." [13]

"Furthermore, controlling the interactions between photons provides the basis for analog photonic quantum simulation [46]. For example, phase transitions in the Bose-Hubbard model [47] or relativistic physics [48] could be simulated. It also opens the possibility for investigating the field of many body polariton states [49–52], where a polariton describes a strongly coupled light-matter-system [28]. Recently significant theoretical efforts have been devoted to the understanding of the scattering and interaction potentials of Rydberg polaritons [49–53]. By spatially confining these polaritons, a strongly interacting one-dimensional system can be created. In such a system, it should for instance be possible to observe crystalline type correlations as known from Tonks-Girardeau gases [54–58] in a polariton gas [49, 51, 59, 60]. This observation would benchmark photonic quantum simulators." [13]

"Rydberg atoms inside hollow core fibers are a promising tool to create strongly interacting one-dimensional many body polariton systems. The first excitation of Rydberg states in a room temperature cesium gas inside a hollow core fiber was reported by Epple et al. [61]. In a complementary approach, cold atoms transported into a hollow core fiber [7, 14, 16, 18] offer important advantages for the initial characterization due to their high controllability. Ground state EIT measurements have already been performed in these systems [11, 12]. However, when using Rydberg EIT, one major challenge is the understanding and control of the interaction between the strongly polarizable Rydberg states and the fiber walls. Especially the influence of stray electric fields due to adsorbates on the surface has been observed in several experiments [62–68]. While first attempts have been made to reduce adsorbate fields on quartz surfaces with a specific crystalline structure [69], it was strongly debated how much Rydberg excitations inside a hollow core fiber would suffer from surface interactions. In this manuscript, we present for the first time a highly controllable hollow core fiber cold Rydberg atom interface and show how the Rydberg EIT signals inside the fiber are influenced by the fiber." [13]

unique properties of Rydberg atoms, long-range interactions stronger by more than 10 orders of magnitude than interaction between ground state atoms, Rydberg blockade mechanism

other long-range interacting systems: molecules, dipolar quantum gases, laser-induced interactions

quantum simulation with Rydberg atoms, quantum gates

THESIS DRAFT

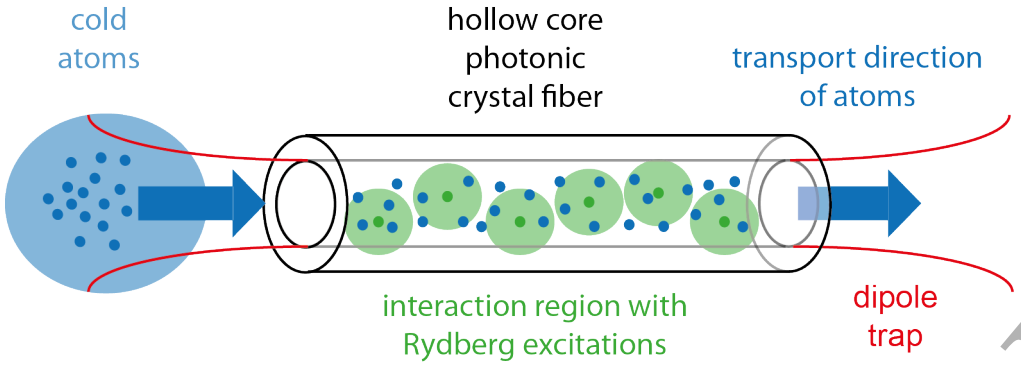

Figure 1.1.: Schematic of the experimental setup. Cold atoms are transported inside a hollow-core fiber, where they are excited into Rydberg states.

photon-photon interaction with Rydberg atoms

1.6. Hybrid Rydberg atom interfaces

Fortagh, superconducting chip, hot Rydberg atoms in hollow core fiber, Stuttgart, Sile with nanofiber, Rydberg atoms near atom chips

1.7. Structure of this thesis

Two main objectives:
1. Controlled sample preparation inside the hollow-core fiber
Challenge: controlled positioning of atoms at specific positions
Highly controlled optical transport with an optical conveyor belt
Challenge: control heating of atoms due to transport potential
Versatility in choosing particle numbers and temperature ranges by adapting the trapping potential
2. Demonstrate feasibility of exciting cold Rydberg atoms inside a hollow-core fiber
Challenge: interaction of Rydberg atoms with surfaces
Study influence of the fiber on Rydberg electromagnetically induced transparency (EIT) signals
Temporally resolved detection method to distinguish between excitation and loss

Chapter 2: Overview over experimental setup and techniques
Chapter 3: Transport results
Chapter 4: Rydberg EIT results

THESIS DRAFT

THESIS DRAFT

2. Setting the stage: Creating and probing cold atoms inside a hollow-core fiber

In the following chapter, I will give a brief overview over our experimental setup and our experimental methods for creating and probing cold atoms inside a hollow-core fiber. Our setup is based upon a setup used previously in the group of Prof. Sengstock in Hamburg [11, 16, 70], which we have transferred to the University of Mainz at the start of this thesis. Re-building this setup and building additional features has been a team effort together with Mohammad Noaman and thus a similar description of the setup will also been part of his thesis [71]. I will highlight the key aspects of my own contribution during the chapter. Parts of the methods have been mentioned in our publications [13, 72, 73] and some technical parts of the setup, especially regarding the control of the transport, have already been described in the bachelor thesis of Florian Stuhlmann [74] and the master thesis of Ronja Wirtz [75], both of which I have co-supervised during the course of my thesis.

In this chapter, I will give an overview over our experimental setup and techniques. Typically, the atoms are trapped and cooled in a magneto-optical trap (MOT) outside the fiber and then transported inside, where experiments are performed. They are either detected while still inside the fiber or once they have left the fiber [16].

2.1. Introducing our experimental setup and sequence

Here, we will learn how cold atoms are cooled and trapped in a magneto-optical trap (MOT) and what specific settings and sequences we use for our typical experiments.

Our setup consists of a two-step magneto-optical trap (2D-3D-MOT) for cooling and trapping Rubidium 87 atoms, which is a standard setup developed and used in the group of Prof. Sengstock in Hamburg and has been described in great detail for example in [cite Hamburg theses]. Figure 2.1 shows a rough draft of our setup. A more detailed sketch of the vacuum system of our specific setup can be found in the thesis of Stefan Vorrath [70]. The upper vacuum chamber contains the Rubidium dispensers and the setup for the 2D MOT. It is connected via a differential pumping stage with the main vacuum chamber,

THESIS DRAFT

where the 3D MOT is operated. Details about the lasersystems for the 2D and 3D MOT can be found in the thesis of Mohammad Noaman [71]. In the main vacuum chamber, the hollow-core fiber is mounted on a vacuum-compatible fiber stage (for details see [11]). All laser beams used in the experiment are coupled into the hollow-core fiber, also in particular the beams for a moving optical lattice which we use to transport the atoms from the MOT position towards or into the hollow-core fiber.

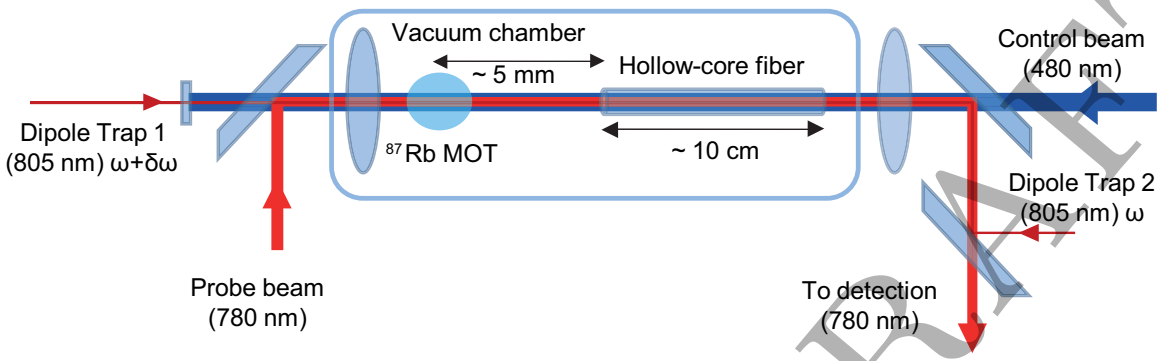

Figure 2.1.: Schematic of the experimental setup. Sketch of the vacuum system and the important beam paths, coupled through the hollow-core fiber.

In the following sections, I will mainly focus on new additions or modifications to the existing setup. During the course of this thesis, a new hollow-core fiber has been implemented (see section 2.2) and consequently new beam paths for loading and probing the atoms inside the fiber have been set up (see section 2.2.2). Further, a new dipole trap setup for the creation of an optical lattice has been implemented (see section 2.3.1). Finally, the computer control over the experiment has been optimized and adjusted to include the control over the transport of the atoms and the new pulsed detection scheme (see section 2.4 for the computer control and section 2.5 for the detection scheme).

Experimental sequence

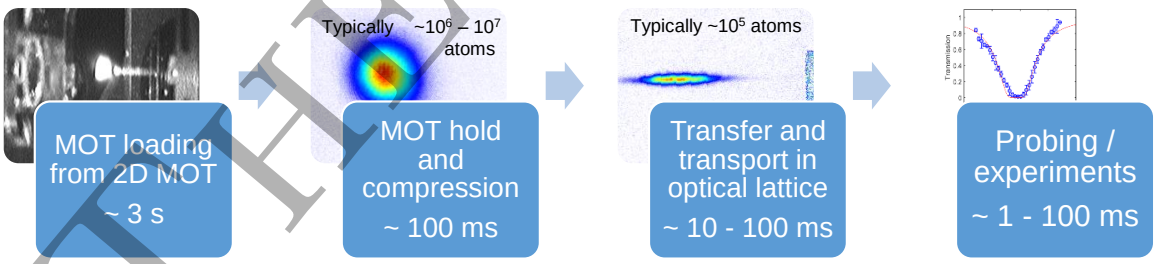

Figure 2.2.: Experimental sequence. Shown is a sketch of a typical experimental sequence for cooling and trapping, transporting, and probing the atoms.

First of all, let me give a brief overview over our experimental sequence. Figure 2.2 shows a schematic of a typical experimental sequence, which can roughly be divided into four main

THESIS DRAFT

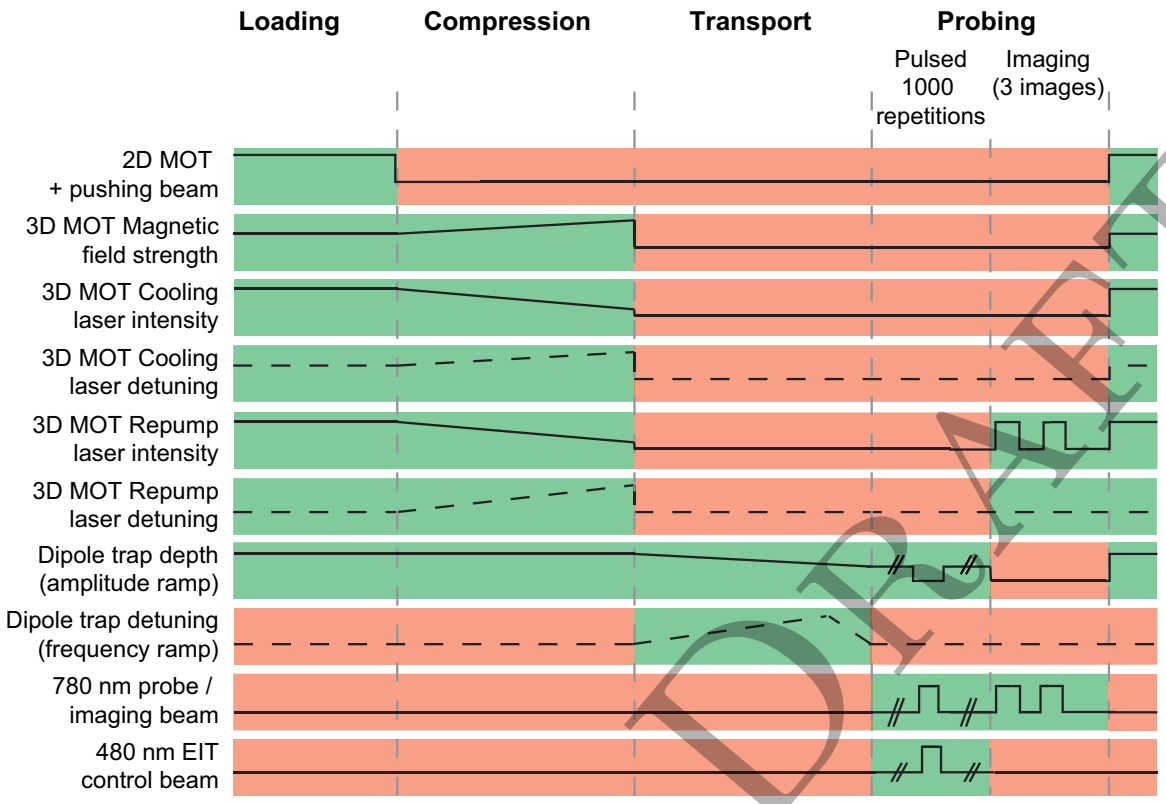

Figure 2.3.: Settings during the experimental sequence. Shown is a sketch of the settings during a typical experimental sequence for cooling and trapping, transporting, and probing the atoms.

stages. I will briefly discuss the main points of each stage in the following. Figure 2.3 gives an overview over the settings of the main experimental control parameters during the experimental sequence. Typical numbers, such as e.g. for our laser powers and detunings, for each stage of the experimental sequence are given in appendix A.1.

Loading: During the first stage, the MOT is loaded from the 2D MOT by applying the blue-detuned pushing beam. Only during this stage, 2D MOT and pushing beam are operated. The 3D MOT is loaded below the differential pumping stage and a few millimeter in front of the hollow-core fiber (see first picture of figure 2.2). Also, the MOT position is given by the magnetic field zero. Here, it is important to find a good compromise between these three different positions, which unfortunately do not coincide perfectly in our setup.

Compression: After the loading stage, the MOT is magnetically compressed during the second stage by increasing the magnetic field together with the detuning of the cooling beam (see table A.4). This stage is important for further cooling the atoms and for increasing the atomic density for a better transfer into the optical lattice during the next stage. After the compression stage, we measure typical particle numbers of $\approx 10^6 - 10^7$ atoms in the MOT with temperatures of $\approx 30\,\mu\mathrm{K}$ with maximum densities of $\approx 10^{11}\,\mathrm{atoms/cm^3}$.

Transport: After that, the atoms are transferred into the optical lattice by switching off the MOT. Note that the lattice beams are already switched on during the first two MOT

THESIS DRAFT

stages. After transferring the atoms, we start the transport process by detuning one of the lattice beams. A detailed discussion of the lattice parameters will follow in section 2.3.1. And a detailed discussion of the transport procedure will follow in section 2.3.4 and in much more detail in chapter 3. Depending on the experiment we want to do, we transport the atoms in front of or into the hollow-core fiber.

Probing: We have the possibility to probe the atoms outside the fiber with standard absorption imaging and inside the fiber with a resonant fiber-coupled probe beam. The probing procedures will be discussed in section 2.5 and further details about the individual experiments will be given in the respective chapters.

2.2. A hollow-core fiber for Rydberg excitations

Here, we will learn about different types of hollow-core fibers and their specific properties. In particular, we will learn what is important for coupling laser beams into the fundamental mode of the hollow-core fiber.

For many applications, including guiding cold atoms into hollow-core fibers, commercially available hollow-core fibers are suitable and have been used successfully (cite other fiber experiments). Such fibers have also been used previously in our experiment [11, 16, 70]. However, for our current experimental goal of exciting cold Rydberg atoms inside the hollow-core fiber, additional features are needed, which are not easily available in commercial fibers. To obtain a fiber which fulfills our requirements, we are collaborating with the fiber development group of Fetah Benabid at XLim Limoges. In section 2.2.1, I will discuss our experimental requirements and to which extend these criteria are fulfilled by our currently used fiber. In particular, I will pay attention to the guiding bandwidth and the fiber core radius. Another important point is the single-mode guiding, which I will discuss in more detail in section 2.2.2.

2.2.1. Experimental requirements

The fiber currently used in our experimental setup is a feasability study for our experimental requirements: core-size, broadband guiding, coupling into single-mode possible, ...

For exciting Rydberg atoms inside a hollow-core fiber, perhaps the most important requirement is that the fiber is able to guide all the wavelengths necessary for the excitation process. In our case, we use a two-step excitation process with 480 nm and 780 nm. Additionally, we want to use a dipole trap at around 800 nm. The challenge here is that most commercially available hollow-core fibers are not able to guide over this very broad bandwidth of more than 300 nm. To understand this challenge, let me briefly explain the guiding mechanism of hollow-core fibers. Here, I will mainly follow the book "Foundations of Photonic Crystal Fibers" (cite).

THESIS DRAFT

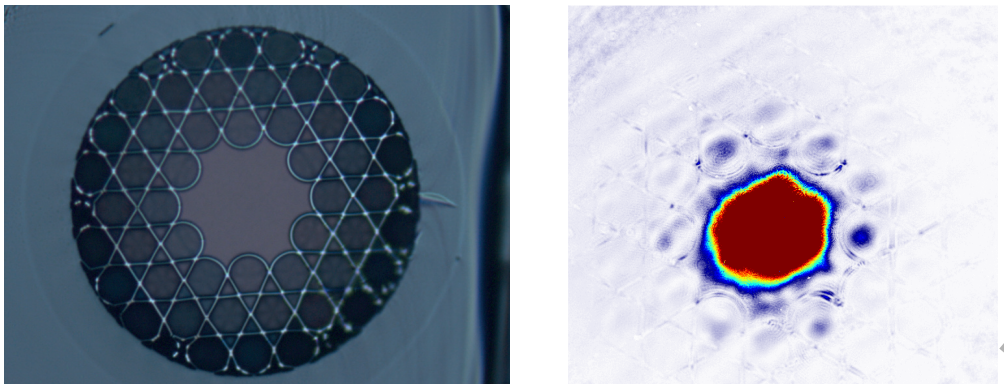

Figure 2.4.: Hollow-core photonic crystal fiber with a Kagomé cladding lattice and a hypocycloid core-contour. a) Microscope image of the fiber tip (picture with kind permission of the group of Prof. Benabid). b) Image of light guided through the fiber core. Due to oversaturation of the light guided inside the core, the light coupled into the surrounding lattice is visible.

Solid-core fibers, which are typically used for in most light guiding applications, guide light through their core due to a difference in refractive index between fiber core and cladding. For this to work, the refractive index of the core has to be higher than the one of the cladding so that total reflection can occur before light is coupled into the cladding. Hollow-core fibers, however, have a low refractive index core by design. Therefore, light guiding inside a hollow-core fiber is only possible when a guiding mechanism different from the normal step index guiding fibers (?) is used. A possibility for this are hollow-core photonic crystal fibers as discussed in the following. Photonic crystal fibers are microstructured fibers that is fibers with a crystalline structure outside the core. An example of such a photonic crystal structure is shown in figure 2.4. The most common type of hollow-core photonic crystal fibers is the photonic bandgap fiber. Bandgap fibers guide due to a bandgap which arises due to the nature of the photonic crystal structure outside the core. They typically have a very low guiding loss, but very narrow guiding bands. Typically, for hollow-core PBG fibers there exists only one guiding bandgap with a width of 20% of its center wavelength (cite book). This means, that in our case, such a bandgap at 780 nm would only be around 150 nm wide, which is not enough to cover our experimentally needed wavelengths. Although research is being done for example at NKT and for some specific cases dual-bandgap PBG fibers have been reported (e.g. Light2009, Montz2014)), creating photonic crystal bandgap fibers with two seperate guiding bands remains a highly challenging task.

Guiding for different wavelengths ranges (inhibited coupling) is a relatively new experimental achievement (cite Benabid two-color guiding paper). Kagomé fibers guide due to the inhibited coupling mechanism. The first important feature is the antiresonance which XXX. The second feature is a low overlap between core and cladding modes. Thus, these modes do not couple to each other, which means that modes from the core cannot be lost easily to the cladding and will be guided. Typically Kagomé fibers have a higher loss than photonic bandgap fibers, but several and potentially much broader guiding bands. (cite "Foundations of Photonic Crystal Fibers") Therefore, we have chosen to work with a Kagomé fiber mainly because of the broadband guiding properties. Also, for our fiber lengths of a maximum of a few centimeters, the loss is still completely negligible.

THESIS DRAFT

Typically, the core size of photonic crystal fibers is small compared to Kagomé fibers. For example, the fiber used previously in our experiment had a core size of only 8 μmXX, while the core sizes of Kagomé fibers typically range between 30 μm and 100 μm. For our goal of studying Rydberg polaritons, the core size should be comparable to typical blockade radii. These are on the order of $XX\mu m$ for Rydberg states of XXX. Our fiber has a minimal inner core diameter of about 60 μm, which corresponds to a mode field diameter of about 42 μm. This is on the large side compared to most blockade radii, but will be useful initially to reduce interactions with the fiber wall for our initial characterization measurements. Also the atom distribution inside the fiber determined by the trapping field is typically much smaller than the mode field diameter as will be discussed later.

Since we want to use the fiber-guided modes for trapping and transporting the atoms, it is important that we can couple in the fundamental mode of the fiber and that this fundamental mode is supported over the length of the fiber. Otherwise, higher mode contributions would lead to an atomic density distribution with strong contributions close to the fiber walls and not one-dimensional. However, we would like to minimize the influence of the inner fiber walls by confining the atoms in the center. Kagomé fibers are multimode fibers in principle. For this fiber, it is possible to couple into the fundamental mode. The detailed experimental steps are discussed in the following section.

One final point is the cleanliness of the fiber when inserting it into the vacuum chamber. Dirt particles stuck to the fiber wall may remain inside the fiber even inside the vacuum chamber and hinder our transport of cold atoms later on or lead to inhomogenities of the inner fiber surface. Therefore, before inserting the fiber into the main vacuum chamber, we perform the standard cleaning procedure, typically applied in our fiber preparation group (cite Benabid). For this, we place the fiber in a seperate vacuum chamber. First, we flush the cleaning chamber with nitrogen. The we re-evacuate it down to below 10^{-8} mbar and bake it out. We repeat this sequence for two times. By this procedure, we should remove most particles from inside the fiber core. (supplement of Rydberg paper, see more details in Noaman's thesis).

2.2.2. Coupling into the hollow-core fiber

As discussed above, for our applications it is of high importance to achieve very good coupling of our laser beams into the hollow core fiber, both regarding the coupling efficiency and the mode profile. In the following, I will first exemplarily explain the coupling process into the bare hollow-core fiber, before discussing which additional aspects will play an important role once the fiber is placed inside the vacuum chamber. Here, I will also give an overview over our different beam paths.

Bare hollow-core fiber

We exemplarily explain the process of coupling into the hollow-core fiber by showing mode pictures of the 480 nm beam. For coupling, it is important to match the fiber mode field

THESIS DRAFT

diameter with our beam size. We typically use a XX lens on a translation stage for fine adjustments, matching our beam sizes of approximately and the mode field diameter of about 21 μm. Also, the incoming angle is very important, for this we need two mirrors in front of the fiber. Typically the coupling is done by looking at the outcoming mode profile, once we see that we are hitting the fiber core at all.

Figure 2.6 a) shows a typical near-field mode profile, taken by placing a microscope objective close to the fiber tip and imaging onto a camera. Here, the Kagomé structure of the fiber core is visible at the edges. We manage to couple most of the light into the center of the fiber. However, when fitting a Gaussian curve to this data set (see figure 2.6), we find deviations from the Gaussian beam profile due to the shape of the fiber core.

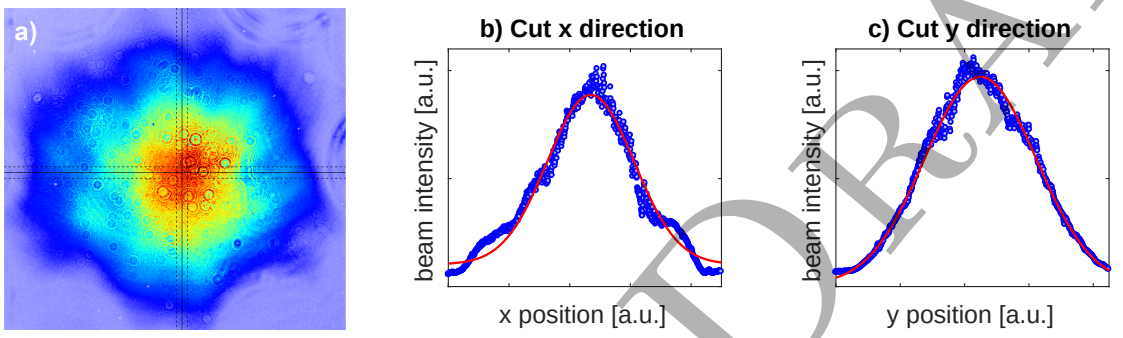

Figure 2.5.: Near field mode profile for a fiber mode coupled through in the Kagomé fiber, for 480 nm. In the near field, the Kagomé structure of the fiber core is visible. Cut along x and y direction indicated by solid lines. Dashed lines indicate the area over which the data points for the cut were averaged. b) and c) show the cuts together with a Gaussian fit to the data.

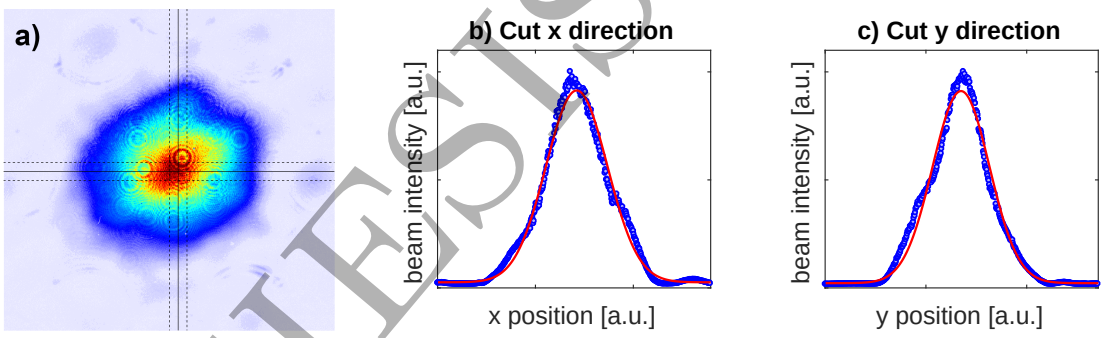

Figure 2.6.: Near field mode profile for a fiber mode coupled through in the Kagomé fiber, for 480 nm. In the near field, the Kagomé structure of the fiber core is visible. Cut along x and y direction indicated by solid lines. Dashed lines indicate the area over which the data points for the cut were averaged. b) and c) show the cuts together with a Gaussian fit to the data.

Figure 2.7 a) shows a typical far-field mode profile, which we measure at a distance of a few centimeters from the fiber tip. Here, the mode has an almost perfect Gaussian shape, which is confirmed by the Gaussian fits (see figure 2.7 b) and c).

Further, we have found out that is of utmost importance to keep the fiber piece straight as any bending of the fiber leads to coupling to higher modes and makes it impossible to guide

THESIS DRAFT

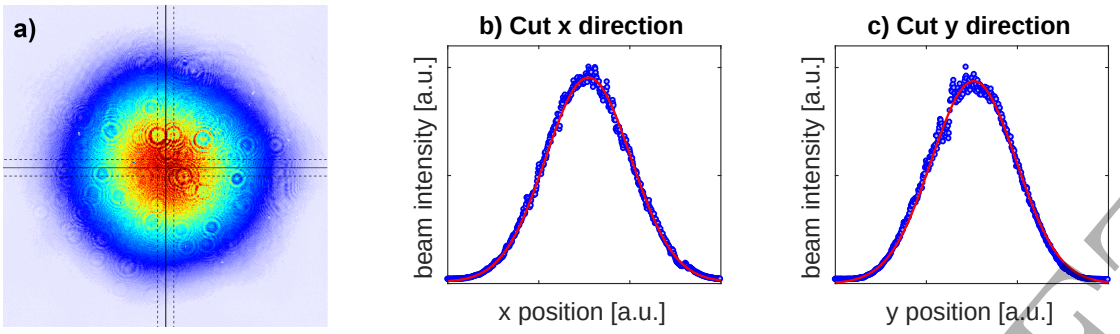

Figure 2.7.: Far field mode profile for a fiber mode coupled through in the Kagomé fiber, for 480 nm. In the far field, the light mode is the Gaussian fundamental mode of the fiber. Cut along x and y direction indicated by solid lines. Dashed lines indicate the area over which the data points for the cut were averaged. b) and c) show the cuts together with a Gaussian fit to the data.

only the fundamental mode (in stark contrast to normal single-mode fibers where bending helps to filter out higher-order modes). This seems to be typical behaviour for Kagome fibers (cite Stuttgart?).

For a 10cm long piece of fiber outside the vacuum chamber, we can achieve coupling efficiencies of close to 100 %. (See no detectable loss when coupling the beam through the fiber?) However, we only measure the total transmitted light, not particularly the light guided in the fundamental mode. For this, it is necessary to also always look at the mode profile and not only at the coupling efficiency.

For experimentally determining the mode field diameter, we measure the propagation of the beam which is coming from the fiber. Ideally, it should follow the equation for the Gaussian beam propagation (cite?):

$$w(z) = w_0 \sqrt{1 + \left(\frac{M^2 z}{z_R}\right)^2}, \tag{2.1}$$

where $w(z)$ is the waist of the Gaussian beam at position $z(t)$, with $z_R = \pi w_0^2/\lambda$ being the Rayleigh range and w_0 being the minimal beam waist at the fiber tip and M^2 being an indicator of how Gaussian the beam really is.

We measure this Gaussian beam propagation exemplarily for the 480 nm beam coupled through the bare hollow-core fiber outside the vacuum chamber, as shown in figure 2.8. From fitting equation 2.1 to the data, we obtain a minimal beam waist of about 21 μm, which fits perfectly to the expected mode field diameter. Also, we see that the M^2-value, which gives a measure for how well the beam propagation is described by a Gaussian beam, is 1, which means that the beam behaves like a perfect Gaussian beam.

Hollow-core fiber inside the vacuum chamber

Now we have gained a good understanding of the coupling into the bare hollow-core fiber and we have confirmed that the light propagating from the fiber can in good approximation

THESIS DRAFT

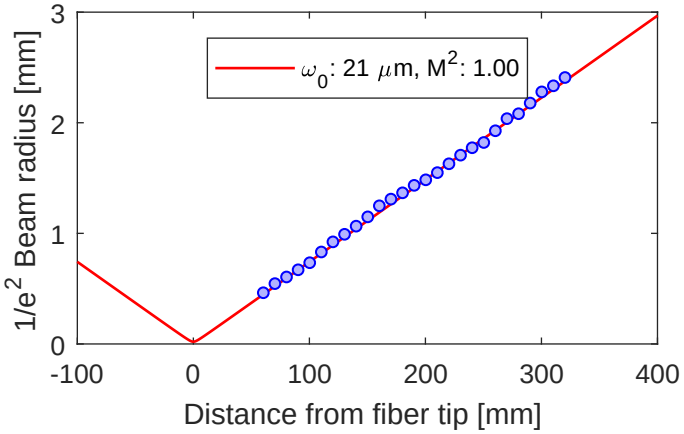

Figure 2.8.: Gaussian beam propagation of a 480 nm laser beam coupled through the HCF (bare fiber). (Data points: Experimental data, solid line: theoretical model (cf. eq. 2.1). Error bars due to measurement uncertainties are small with respect to the data points and thus not shown.)

be described by a Gaussian beam propagation. However, for all further experiments using cold atoms, our fiber has to be mounted inside the vacuum chamber. This makes both coupling and beam analysis more complicated. Therefore, I will discuss in the following which additional points have to be taken into account when coupling light into the hollow-core fiber inside the vacuum chamber.

For mounting the fiber inside the vacuum chamber, we use a Markor v-groove fiber mount discussed in detail in [11], where the fiber is lying freely horizontally on the supporting mount.

For our experiments, it is necessary to couple light of different wavelengths from both sides into the fiber. Figure 2.9 shows a sketch of the relevant laser beams and their beam paths when coupled into the hollow core fiber. We couple all relevant light beams into the hollow-core fiber (taking care of the mode matching). discuss beam paths, sizes and parameters.

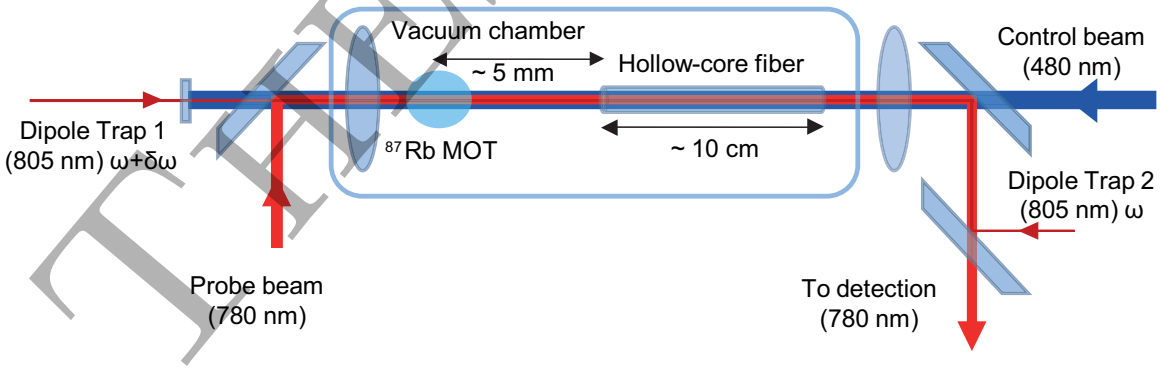

Figure 2.9.: Schematic of the experimental setup. Sketch of the vacuum system and the important beam paths, coupled through the hollow-core fiber.

On one side of the fiber (the side where later the MOT will be), we have (due to historical

THESIS DRAFT

reasons) a lens mounted inside the vacuum chamber which changes the beam propagating from the fiber. On the other side, we do not have any coupling optics inside the vacuum chamber, unlike in the previous setup described in [11]. This is due to our larger fiber core of about 60 μm in diameter compared to 8 μm in the previous setup. As the beam divergence depends inversely on the fiber core, our beam diverges much more slowly and hence, it is sufficient to use a lens outside the vacuum chamber in our case. The coupling lens on the detection side is same for all wavelengths (120 mm Achromat, Qioptiq G322-309-322) -> lens outside vacuum chamber (distance between fiber end and lens matches focal length) to collimate beam propagating from fiber.

To find waist size and position of the beam modified by the lens inside the vacuum chamber, we measure the beam propagation for the blue beam after the lens, shown in figure 2.10. By again fitting equation 2.1 to the experimental data, we can determine the beam parameters of the Gaussian beam from this measurement. From these results, we can then determine the necessary beam shaping optics for the probe and dipole trap beams coming from the MOT side. In this case, we use adjustable outcouplers to match the beam size and divergence instead of an additional lens outside the vacuum chamber. The exact lenses and collimators used for coupling are given in table 2.1.

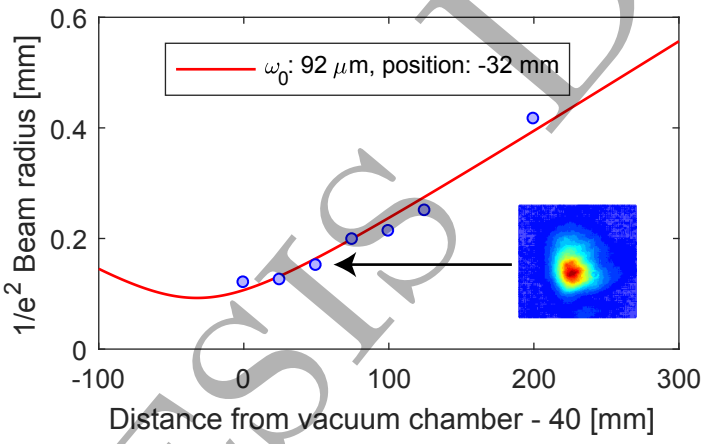

Figure 2.10.: Gaussian beam propagation of a 480 nm laser beam coupled through the HCF mounted inside the vacuum chamber and an examplary far field mode profile. (Data points: Experimental data, solid line: theoretical model (cf. eq. 2.1). Errors have not been measured for this measurement.) The inset shows a typical far field beam profile.

Wavelength	Fiber MFD	Outcoupler	Coupling lens
780 nm (1)	$\approx 5\,\mu$m (Thorlabs 780HP)	60FC-F-4-A15-02	25 mm
480 nm (2)	$\approx 4.2\,\mu$m (aeroGUIDE-5-PM-APC)	60FC-F-4-M12-33	120 mm
805 nm (1)	$\approx 5\,\mu$m (Thorlabs 780HP)	60FC-F-4-A15-02	25 mm
805 nm (2)	$\approx 5\,\mu$m (Thorlabs 780HP)	60FC-F-4-A11-02	120 mm

Table 2.1.: Beam shaping optics for coupling into the hollow-core fiber. Given are the fibers, outcouplers and coupling lenses for each wavelength and each side on the vacuum chamber, where (1) denotes the MOT side and (2) the detection side.

THESIS DRAFT

Similar measurements have been done to confirm the same guiding process for the other wavelengths used in the experiment. Once the fiber is mounted inside the vacuum chamber, we no longer have access to the near-field profile. In practice, we have observed that by adjusting the coupling until we get the best far-field profile will lead to sufficiently good coupling for performing all experiments. A typical far field profile is shown in the inset of figure 2.10. Due to the long beam paths involved, the coupling is very sensitive and slight misalignment of the mirrors will lead to a bad mode profile, a change which does not necessarily manifest itself in a loss of coupling efficiency. Therefore, in addition to optimizing the coupling efficiency, it is necessary to confirm a good far field profile of the coupled beams.

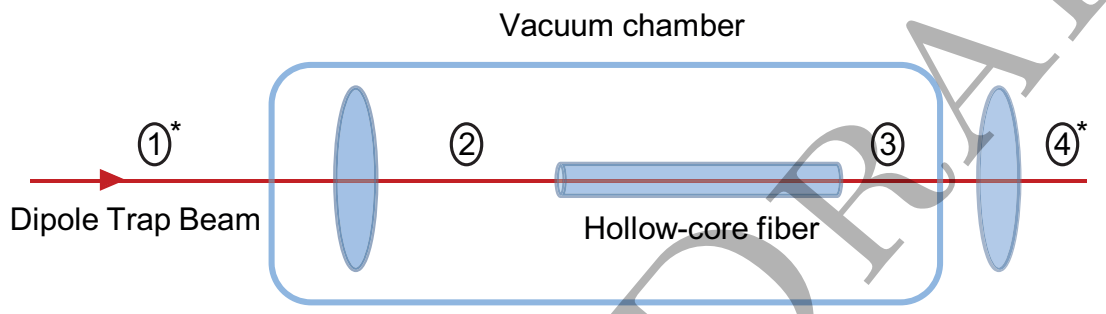

Figure 2.11.: Positions of losses when coupling into the hollow-core fiber for determining the fiber coupling efficiency into the hollow-core fiber inside the vacuum chamber, where different loss channels in the optical path have to be taken into account (for values of loss see table 2.2). Only the positions marked with * outside the vacuum chamber are experimentally accessible.

Position	1*	2	3	4*
Approximate laser power	540 mW	500 mW	465 mW	430 mW
Loss	-	$2\times \approx 4\%$	$\approx 7\%$	$2\times \approx 4\%$
Loss channel	-	vacuum window	HCF coupling	vacuum window

Table 2.2.: Determining the coupling efficiency into the hollow-core fiber inside the vacuum chamber. Exemplary laser power at different positions inside and outside the vacuum chamber (shown in figure 2.11). Positions marked with * outside the vacuum chamber are experimentally accessible and have been measured experimentally. The loss of the vacuum chamber windows has been assumed to be $\approx 4\%$ for each window surface. From these values, the laser power at position 3 and thus the coupling efficiency into the hollow-core fiber has been determined.

For the bare hollow-core fiber, we could measure coupling efficiencies close to 100%. When the fiber is mounted inside the vacuum chamber, determining the fiber coupling efficiency from the input and output light powers is not as straight forward, as different loss channels in the optical path have to be taken into account. I will estimate the coupling efficiency in the following. Table 2.2 shows examplary laser powers for the 805 nm dipole trap beam at different positions inside and outside the vacuum chamber, as depicted in figure 2.11. Only the positions outside the vacuum chamber (1 and 4) are experimentally accessible and there, the laser powers have been measured experimentally. I assume the loss of the vacuum chamber windows to be $\approx 4\%$ for each window surface as the windows have not been properly anti-reflection coated for our wavelengths, but instead only for 1064 nm which

THESIS DRAFT

has been used previously in the experiment [70]. In contrast, I assume that the lenses are properly coated and therefore do not contribute to losses. This assumption should be valid, as we have chosen the lens outside vacuum with the proper coating for all wavelengths, while the lens inside the vacuum chamber has been chosen especially for 830 nm [11] and should therefore also work for all our wavelengths, apart maybe for 480 nm. From these values, I have determined the laser power at positions 2 and 3 and thus the coupling efficiency into the hollow-core fiber, resulting in a coupling efficiency of approximately 93%. I calculate a loss due to the hollow-core fiber coupling of only about 7% and therefore find that we can achieve a hollow-core fiber coupling above 90% even inside the vacuum chamber. Note that the fiber coupling efficiency derived here gives a lower limit of the real efficiency as in principle also other loss channels can occur which have not been taken into account.

All in all, we find that we can achieve very good coupling efficiencies above 90% and good fundamental mode profiles both for the bare fiber and for the final setup of the hollow-core fiber mounted inside the vacuum chamber. We have confirmed these results for all experimentally relevant wavelengths. Therefore, in the following sections, I will now concentrate on the applications of the hollow-core-fiber-coupled laser beams, such as creating optical potentials and detecting the atoms.

2.3. A hollow-core fiber coupled optical lattice

Here, we will learn how atoms are trapped in optical dipole traps and optical lattices. In particular, we will discuss the influence of different parameters on the traps and what consequences that has in our experimental setup.

Optical potentials, such as optical lattices, are commonly used for trapping cold atoms [3]. In this section, I will first give a brief introduction to the optical dipole force and the creation of optical lattices in general (sec. 2.3.1), before discussing the specific requirements and considerations for our setup, where the lattice beams are coupled through the hollow-core fiber (sec. 2.3.2). Finally, I will discuss important points for the laser system setup (sec. 2.3.3).

2.3.1. Optical dipole traps

Resonant laser light can interact with atoms e.g. by changing the internal state of the atom, as will be discussed in section 2.5. However, even a non-resonant light field will shift the internal atomic states, which can be calculated quantum mechanically in the so-called dressed atom picture (cite Dalibard and Cohen-Tannouji). Depending on the laser frequency, the atoms will experience a force towards regions of high or low laser intensity. This force is called the optical dipole force, which can be classically interpreted as an interaction of the gradient of the electric field of the laser light with the induced dipole

THESIS DRAFT

moment of the atom. This conservative force can for example be used for trapping atoms in optical potentials. A full review and discussion of optical dipole traps can be found in e.g. [76]. In the next paragraphs, I will briefly discuss the main aspects relevant for our work, following this review [76] and cite(BlochOpticalLattices).

In the most general case, the depth of the dipole trapping potential and the scattering rate for an atom in ground state $|i\rangle$ are given by

$$\begin{aligned} U_{\mathrm{dip}}(\mathbf{r}) &= \frac{3\pi c^2}{2} \sum_j \frac{1}{\omega_{i,j}^3} \left(\frac{c_{i,j}^2 \Gamma_{i,j}}{\omega_{i,j} - \omega_L} + \frac{c_{i,j}^2 \Gamma_{i,j}}{\omega_{i,j} + \omega_L} \right) I(\mathbf{r}) \\ \Gamma_{\mathrm{sc}}(\mathbf{r}) &= \frac{3\pi c^2}{2\hbar} \sum_j \left(\frac{\omega_L}{\omega_{i,j}} \right)^3 \frac{1}{\omega_{i,j}^3} \left(\frac{c_{i,j}^2 \Gamma_{i,j}}{\omega_{i,j} - \omega_L} + \frac{c_{i,j}^2 \Gamma_{i,j}}{\omega_{i,j} + \omega_L} \right)^2 I(\mathbf{r}), \end{aligned} \tag{2.2}$$

where j denote different excited states. $\Gamma_{i,j}$ is the spontaneous decay rate of the excited state, $\omega_{i,j}$ the atomic resonance frequency between ground state and excited state, ω_L the frequency of the trapping laser and $c_{i,j}^2$ the line strength.

Depending on the trapping frequency ω_L and therefore the detuning $\Delta = \omega_L - \omega_{i,j}$, several approximations can be made to simplify equation 2.2. For detunings $\Delta \ll \omega_{i,j}$, the rotating wave approximation can be used, which neglects the counter-propagating term $\omega_{i,j} + \omega_L$ and sets $\omega_L/\omega_{i,j} \approx 1$. For detunings smaller than the fine structure splitting, the multi-level structure of the atom has to be taken into account, i.e all fine structure transition lines have to be included in the calculations. The same holds true for detunings smaller than the hyperfine structure. For detunings larger than fine and hyperfine structure, the atom can be approximated as a two-level system.

For a near-detuned dipole trap with a trapping wavelength of 805 nm, we have to include the finestructure of Rubidium (that is the D1 and D2 lines), but can neglect the hyperfine structure, and we can apply the rotating wave approximation. For linearly polarized trapping beams, the dipole potential is then given by

$$\begin{aligned} U_{\mathrm{dip}}(\mathbf{r}) &= \frac{\pi c^2}{2} \left(\frac{2\Gamma_{D2}}{\omega_{D2}^3 \Delta_{D2}} + \frac{\Gamma_{D1}}{\omega_{D1}^3 \Delta_{D1}} \right) I(\mathbf{r}) \\ \Gamma_{\mathrm{sc}}(\mathbf{r}) &= \frac{\pi c^2}{2\hbar} \left(\frac{2\Gamma_{D2}^2}{\omega_{D2}^3 \Delta_{D2}^2} + \frac{\Gamma_{D1}^2}{\omega_{D1}^3 \Delta_{D1}^2} \right) I(\mathbf{r}), \end{aligned} \tag{2.3}$$

where $\omega_{D1/D2}$ is the transition frequency from ground to excited state, $\Gamma_{D1/D2}$ is the decay rate from the excited state and $\Delta_{D1/D2}$ the detuning of the dipole trap beam from the transition frequency for the Rubidium D1 and D2 lines, respectively, and $I(\mathbf{r})$ is the position-dependent laser beam intensity.

For a red-detuned dipole trap with $\omega_L < \omega_{D1/D2}$, the atoms will be trapped in the maxima of the electric field, for example in the focus of a focussed laser beam. More complex trapping geometries can be created by using more than one dipole trap beam. The easiest and most intuitive example is a sinusoidal potential created by interfering two counterpropagating laser beams in a standing wave pattern. This one-dimensional optical lattice has the

THESIS DRAFT

following trapping potential and scattering rate:

$$\begin{aligned} U(\mathbf{r}) &= 4U_{\mathrm{dip}}(\mathbf{r})\cos^2(k_L z) = U_{\mathrm{latt}}(\mathbf{r})\cos^2(k_L z) \\ \Gamma_{\mathrm{sc,latt}}(\mathbf{r}) &= 4\Gamma_{\mathrm{sc}}(\mathbf{r}), \end{aligned} \tag{2.4}$$

with the wavevector $k_L = 2\pi/\lambda_L$. Three-dimensional lattice with different lattice geometries can also be created by interfering multiple trapping beams with specific geometries, e.g. hexagonal, triangular, Kagomé... (cite complex lattices)

To give an example of how such a trapping geometry would look like, let us assume a one-dimensional optical lattice created by two collimated Gaussian laser beams. In this case, the lattice depth $U(\mathbf{r})$ would have no dependence on the propagation direction of the laser beams z, the whole z-dependence coming from the cosine-term. Then the lattice potential in z-direction would look like depicted in figure 2.12 a), forming a periodic potential with with a periodicity given by the lattice constant $\lambda/2$. For calculating the energy levels in this potential, we use the bandstructure calculation (XX: refs). However, in our case of a very deep lattice, each lattice well can be approximated as an harmonic potential with the trapping frequency $\omega_a^2 = (2U_{\mathrm{latt}}(r=0)k_L^2)/m$.

In the radial direction, the atoms are trapped in the potential given by the Gaussian shape of the intensity distribution (assuming a collimated beam with constant waist)

$$I(\mathbf{r}) = I(r) \propto \exp\left(-\frac{2r^2}{w^2}\right) \tag{2.5}$$

in which case the radial trapping potential can be approximated as a harmonic oscillator

$$U(r) \approx \frac{1}{2} m\omega_r^2 r^2, \tag{2.6}$$

where $\omega_r = \left(4U_{\mathrm{latt}}(r=0)/(mw^2)\right)^{1/2}$ is the radial trapping frequency. The radial potential is depicted in figure 2.12 b).

For most experiments and especially for our setup, however, the lattice does not consist of two collimated beams. Therefore, the dependence of intensity and thus lattice depth on the z-position will be an important point to consider. These considerations and their implications for e.g. the choice of trapping wavelength will be discussed in the next section.

2.3.2. Design considerations

We use an optical lattice for trapping and transporting the atoms. We use a near red-detuned dipole trap to achieve sufficient trap depth at the MOT position. This has drawbacks for lifetime of the atoms in the dipole trap, esp. when using TAs with a background.

THESIS DRAFT

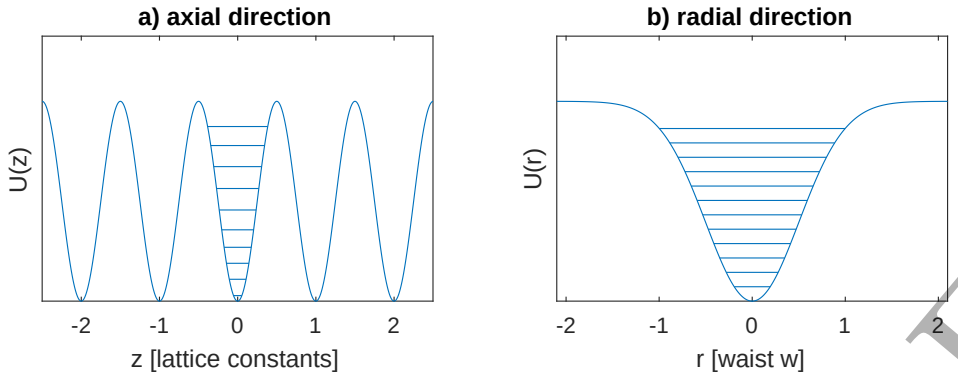

Figure 2.12.: Model optical lattice potential. Shown is the trapping potential of a one-dimensional optical lattice created by two collimated laser beams. a) In axial direction, the lattice is formed with a periodicity given by the lattice constant $\lambda/2$. b) In radial direction, the potential is given by the intensity distribution of the Gaussian laser beams with beam waist w and can be approximated as a harmonic oscillator. In both figures, an excerpt of the energy levels according to the respective trapping frequency is sketched.

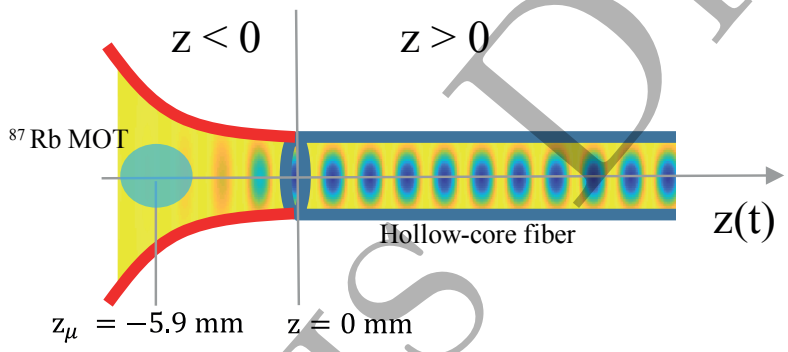

Figure 2.13.: Sketch of the optical lattice potential in our experiment (lattice constant not to scale), which increases from the MOT position to the fiber tip and stays at constant depth inside the hollow-core fiber.

Distance dependence

In our setup, where the lattice beams are coupled through the hollow-core fiber, the dependence of the trapping potential on the position is an important point. Figure 2.13 shows a sketch of the behaviour of the trap depth $U_{\text{latt}}(z, r)$ between the MOT position and the fiber tip. It is determined by the divergence of the dipole trap beams, which have their focal point at the fiber tip. Thus, for $z < 0$ the beam waist $\omega(z)$ of the dipole trap beams increases as

$$w(z) = w_0 \sqrt{1 + \left(\frac{z}{z_R}\right)^2}, \tag{2.7}$$

and thus the intensity $I(\mathbf{r})$ decreases as

$$I(\mathbf{r}) = I(z, r) = \frac{2P}{\pi w(z)^2} \exp\left(-\frac{2r^2}{w(z)^2}\right), \tag{2.8}$$

THESIS DRAFT

where P is the power in each of the dipole trap beams. Therefore, also the trap depth decreases with increasing distance from the fiber tip. This is also shown in a more quantitative manner in figure 2.14, where the increase of the beam waist and the decrease of the lattice potential is plotted as function of distance from the fiber tip.

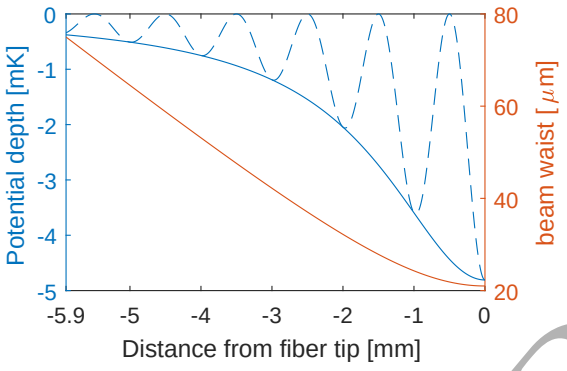

Figure 2.14.: Dependence of trap depth on beam waist. Shown are the trap depth (solid line) and the optical lattice potential (dashed line, lattice constant not to scale), which increase from the MOT position to the fiber tip (left y-axis). This is due to the divergence of the trapping laser beam (right y-axis), according to equation 2.7.

"We define the two limiting points as $U_0 = U_{\mathrm{dip}}(z = z_\mu, r = 0)$ for the potential depth at the MOT position and $U_{\mathrm{max}} = U_{\mathrm{dip}}(z = 0, r = 0)$ for the maximum potential depth at the fiber tip. For our typical experimental parameters, we find $U_{\mathrm{max}} \approx 5\,\mathrm{mK}$ and $U_0 \approx 400\,\mu\mathrm{K}$." [72]

"Inside the fiber for $z > 0$, the trap depth will stay constant at U_{max}, when neglecting the coupling efficiencies of the dipole trap beams into the fundamental mode of the hollow-core fiber. These are typically above 90% for our setup." [72] (as discussed previously in section 2.2.2)

In the following, I will discuss what implications these geometrical constraints have on our choice of trapping wavelength and powers.

Choosing the trapping wavelength

Typically, a high potential depth and low scattering rates are desirable for cold atom experiments, so that it is possible to trap as many atoms as possible with as long lifetimes in the trap as possible. As shown in the previous section, depth and scattering rate of the lattice potential depends on different parameters, given by the internal atomic structure as well as by parameters of the dipole trap beams. The most important parameters for us are the detuning and intensity of the laser beam as these parameters can be experimentally varied. Here, it is important to note the different dependencies of scattering rate and trapping potential. While the scattering rate Γ_{sc} scales as I/Δ^2, the potential depth U_{latt} scales as I/Δ. Therefore, by increasing the detuning, the scattering reduces much more strongly than the potential depth. When both detuning and laser intensity are increased in such a way as to keep the trap depth constant, the scattering rate will be reduced. Thus,

THESIS DRAFT

in principle, if enough laser power is available, high-power dipole traps at large detunings are advantageous.

To load the atoms efficiently into the optical lattice, the potential depth at the MOT position $U_0 = U_{\mathrm{latt}}(z = z_\mu, r = 0)$ needs to be sufficiently larger than the temperature of atoms in the MOT, which are typically on the order of tens of micro Kelvin. This imposes some requirements on the trapping parameters, such as trap wavelength and powers. Figure 2.15 (a) shows how much power per laser beam would be necessary to create the same trapping potential $U_0 \approx 400\,\mu$K for different trapping wavelengths for an optical lattice. The laser powers increase drastically for further detuning from the atomic transitions (compare equation 2.3). For example, for a far-detuned dipole trap at a typical trapping wavelength of 1064 nm, achieving the same trap depth would require extremely high-power trapping beams of almost 10 W per beam.[1] While such high-power lasers do exist, we have chosen to work with a nearer-detuned dipole trap to keep laser power requirements moderate.

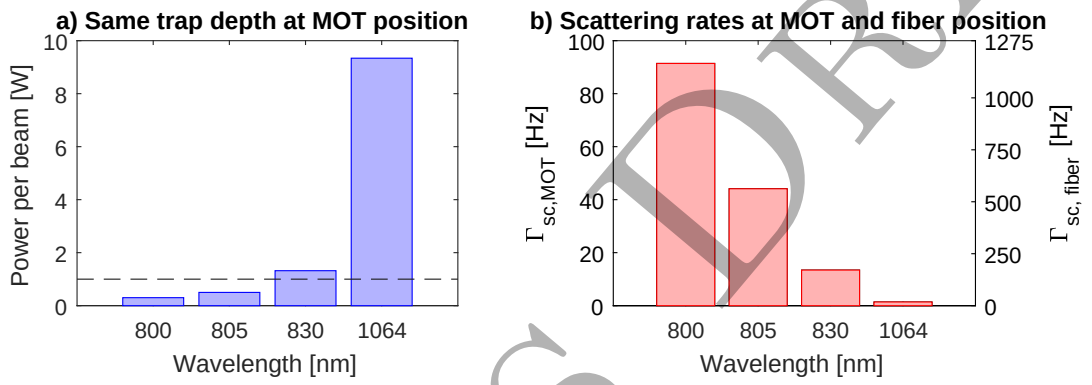

Figure 2.15.: Wavelength-dependence of dipole trap parameters. a) Depending on the dipole trap wavelength, different powers per laser beam are necessary to create the same trapping potential at the MOT position $U_0 \approx 400\,\mu$K (cf. equation 2.3). The dashed black line marks an experimentally feasible power level of 1 W. b) Here, the scattering rates corresponding to the laser powers from figure a) and the different wavelengths are plotted (cf. equation 2.3). Note that different y-scales have been used to highlight the different order of magnitude for the scattering rates at the MOT position (left y-axis) and inside the fiber (right y-axis).

Discuss 3 options for near-detuned dipole traps (too high scattering, too high power, 805 nm). "This, however, limits the lifetime of atoms in the dipole trap as will be discussed later." Differences between scattering rates at MOT position and at fiber tip. Even for 805 nm, the scattering rates at the fiber tip are still very high. In principle, here switching to far-detuned dipole trap could be useful, but has not yet been implemented in our setup.

Another possibility to increase U_0 without changing the trapping wavelength is to reduce the distance between MOT and fiber tip. Due to geometrical constraints by the beam path and the magnetic field zero, the MOT position cannot be changed by a large amount while maintaining a good MOT loading rate. It is possible to shift the MOT by applying an additional magnetic field after the loading phase, but we have not seen such a large effect

[1] Note that for these calculations the rotating wave approximation has not been applied as a trap at 1064 nm is very far detuned from the atomic transitions.

THESIS DRAFT

as e.g. Vorrath. It is in principle possible to shift the fiber closer to the MOT and we have indeed shifted the fiber by 4 mm in our setup. However, shifting the fiber too close to the MOT position has also been observed to reduce the number of atoms in the MOT by one order of magnitude, due to obstructed beam paths [70].

2.3.3. Laser system setup

Power limitations due to setup

To understand the experimental limit to the available dipole trap power, it is necessary to understand the setup of our laser system. Thus, I will briefly walk you through the most important components. discuss dipole trap laser system (TA's, power considerations). Bad mode shapes from the TAs limit the coupling efficiencies and therefore the available power.

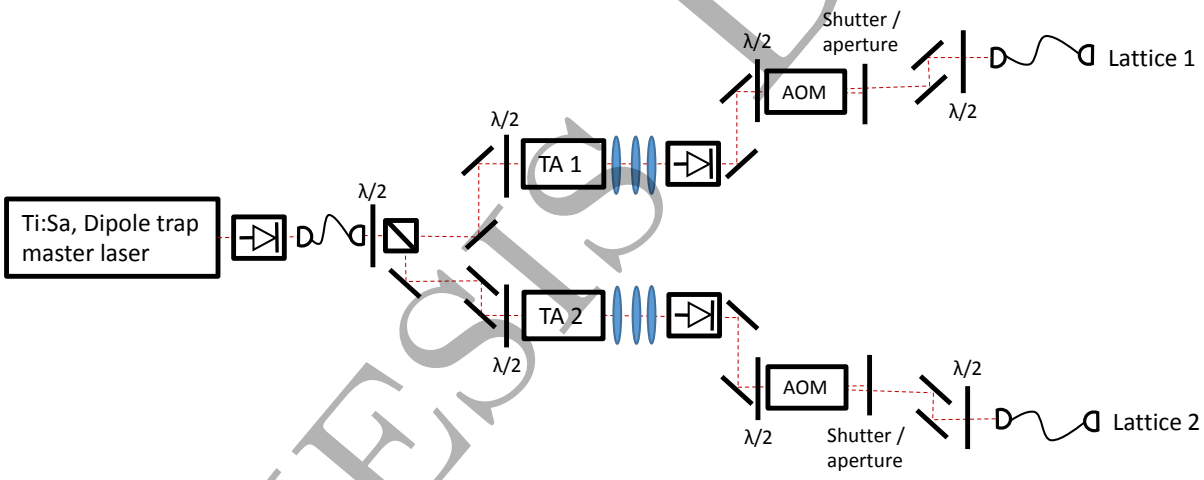

Figure 2.16.: Dipole trap lasersystem. AOMS, TAs, etc.

To achieve the power necessary for the trap depths discussed above, we use a setup consisting of two tapered amplifiers (TAs), one for each trapping beam, which are seeding by a Ti:Sa. After each amplifier, we have one AOM for controlling frequency and amplitude of the trapping light as will be discussed in detail in the transport section. The light is then guided through PM-fibers to the main setup, where it is coupled into the hollow-core fiber as discussed above. Thus in total we have a loss of XX % of power from the TA until the hollow-core fiber coupling. With a power of about 2 W right after the TAs, we can only achieve approximately 500 mW at the position of the atoms.

THESIS DRAFT

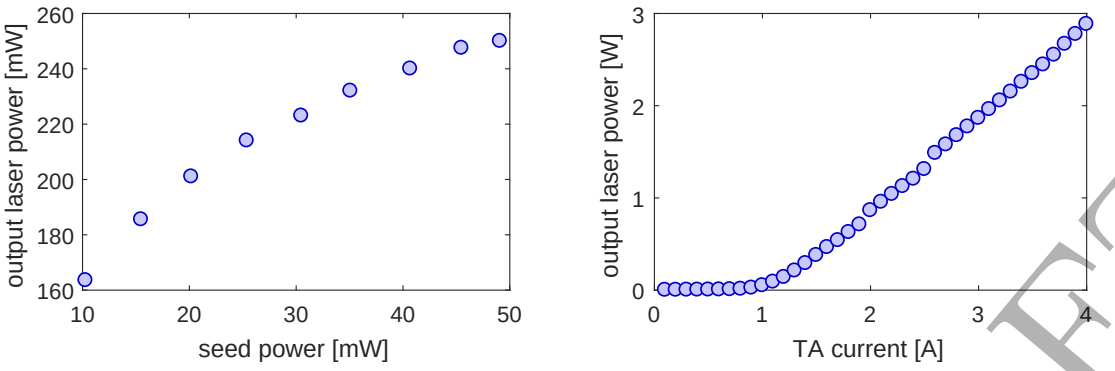

Figure 2.17.: TA output power. Plotted is the output laser power as a function of a) seed power and b) TA current.

Spectrum of the trapping wavelength

Later, the TA spectrum will become an extremely important factor for our measurements and especially the lifetime of the trapped atoms. Therefore, in addition to the peak wavelength, I will study the background of the spectrum as well as its dependence on temperature and current.

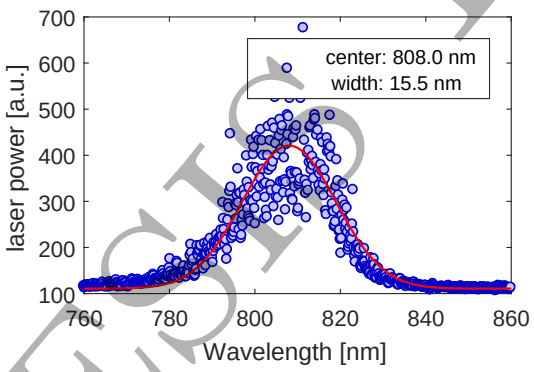

Figure 2.18.: Example spectrum of an unseeded TA. Plotted is the laser power as a function of wavelength. The solid red line shows a Gaussian fit to the data.

The tunability of the TAs is of importance as we have just established that changing the trapping wavelength might be interesting for us. As in principle the TAs work over a wide wavelength range which would be of our interest, we would like to characterize the tunability.

Also, we will see later that background light at different wavelengths has a bad influence on the lifetime in the trap. Therefore, we need to know the spectrum of the seeded TA. We have seen that we need to put bandpass filters to improve the lifetime.

We have seen that the laser output power coming from the TA has a distribution across several wavelengths. However, for most calculations made in the following, we neglect the

THESIS DRAFT

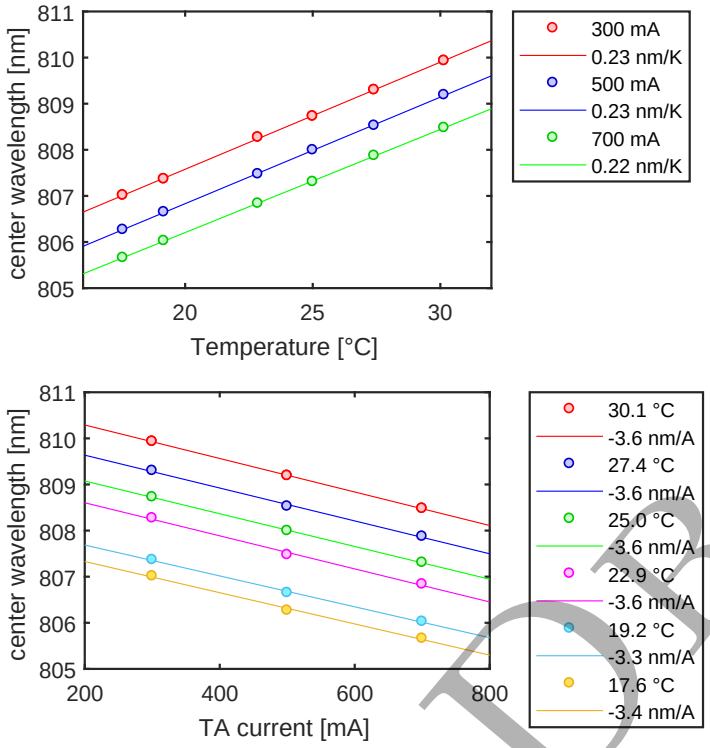

Figure 2.19.: Dependence of TA center wavelength on a) temperature and b) TA driving current.

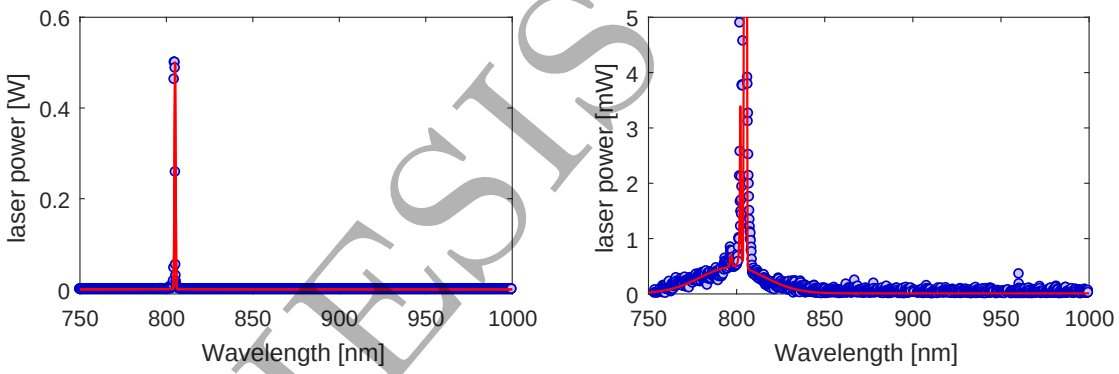

Figure 2.20.: Example spectrum of a seeded TA. Plotted is the laser power as a function of wavelength. Figure a) shows the full power range, while figure b) shows a zoom into the power region up to 1 mW, where the TA background is visible. The solid red line shows a fit to the data, where the TA background is fitted with a Gaussian, while the main peak is fitted with a Voigt profile.

background TA profile as well as the shape of the emission peak and assume that the full power of approximately 500 mW is output at the center wavelength of 805 nm. (actually, main peak is much sharper than seen here through the spectrometer)

THESIS DRAFT

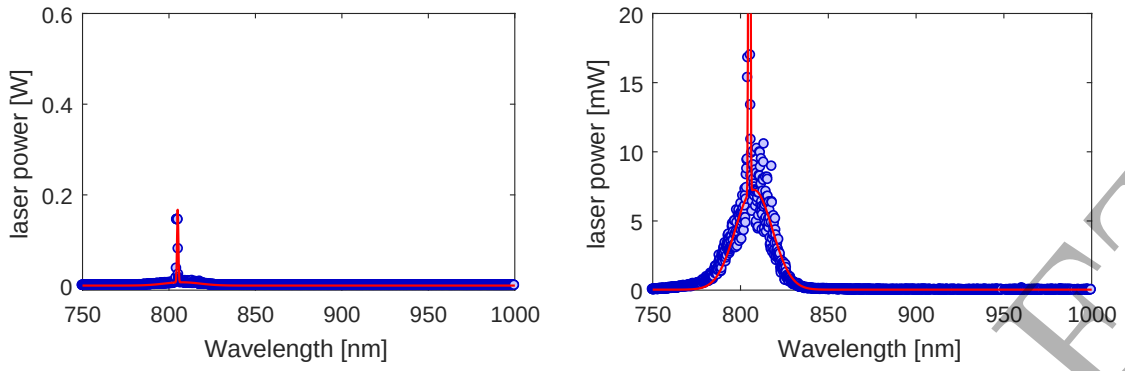

Figure 2.21.: Example spectrum of a seeded TA, without filters. Plotted is the laser power as a function of wavelength. Figure a) shows the full power range, while figure b) shows a zoom into the power region up to 1 mW, where the TA background is visible. The solid red line shows a fit to the data, where the TA background is fitted with a Gaussian, while the main peak is fitted with a Voigt profile.

2.3.4. A moving optical lattice

In the previous sections, I have discussed the formulas and our experimental requirements and considerations for a stationary optical lattice, into which the atoms are loaded. However, for our experiments we want to transport the atoms from their intial position towards or into the fiber. Perhaps the most intuitive approach would be to simply use the spatially dependent dipole force (as shown for example in figure 2.13) to pull the atoms towards the potential maximum at the fiber tip. Indeed, this approach has been successfully used in many different experiments (references XX). However, to gain higher control over transporting cold atoms, we employ a so-called optical conveyor belt, a moving optical lattice. Therefore, in this section I would like to introduce the basic working principle of such a conveyor belt. A much more detailed discussion of the individual transport parameters and their influence on the transported atoms will then be the subject of chapter 3.

The conveyor belt works by detuning the frequency of the laser beams creating the optical lattice with respect to the other one. In the easiest case of a constant frequency detuning $\Delta\nu$ between the two laser beams, a lattice moving at constant speed is created, which can be described by modifying equation 2.4 resulting in

$$U(\mathbf{r}) = U_{\text{latt}}(\mathbf{r}) \cos^2(k_L z - \pi\Delta\nu t). \tag{2.9}$$

In most cases, however, we will apply more complicated frequency detunings, which may have a time-dependent ramp shape. Equation 2.9 will then be modified to

$$U(\mathbf{r}) = U_{\text{latt}}(\mathbf{r}) \cos^2(k_L z - \pi\Delta\phi(t)) \tag{2.10}$$

where the time-dependent phase shift $\Delta\phi(t)$ depends on the time-dependent frequency difference $\Delta\nu(t)$ between the two laser beams as

$$\Delta\phi(t) = \int \Delta\nu(t) dt. \tag{2.11}$$

THESIS DRAFT

We can also choose different detuning ramps to create different acceleration and deceleration procedures.

Figure 3.1 shows examplary absorption images to illustrate the transport process of the cold atoms from the initial MOT position to the fiber tip and inside the fiber. Note that for this figure we apply the same holding time also for atoms at the MOT position. Therefore it seems like the number of atoms increases at the fiber tip. However, for a normal transport this is not true as will be discussed later. In principle, it is also possible to transport the atoms in backwards direction outside the fiber again.

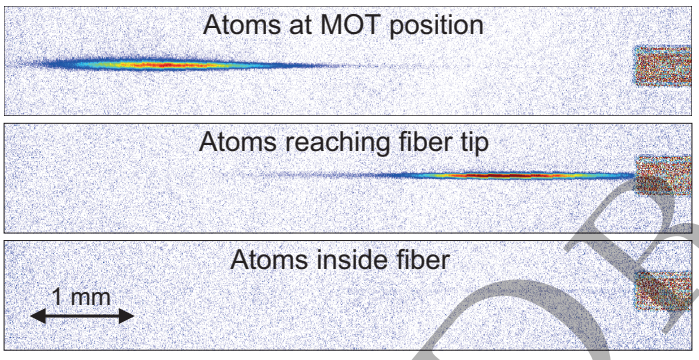

Figure 2.22.: Exemplary transport. Absorption images illustrate the transport process of the atoms from the MOT position to the fiber tip and inside the fiber.

We control the two dipole beam trap frequencies separately with two acousto-optical modulators as shown in the previous section in figure 2.16. They are driven by individual outputs of a programmable arbitrary waveform generator (FlexDDS by WieserLabs). Therefore, in principle, arbitrary frequency ramps are possible in our setup. Technical details about the FlexDDS will be discussed in the following section 2.4. In chapter 3, I will discuss the influence of time-dependent frequency detunings and their different ramp shapes.

2.4. Computer control of the experiment

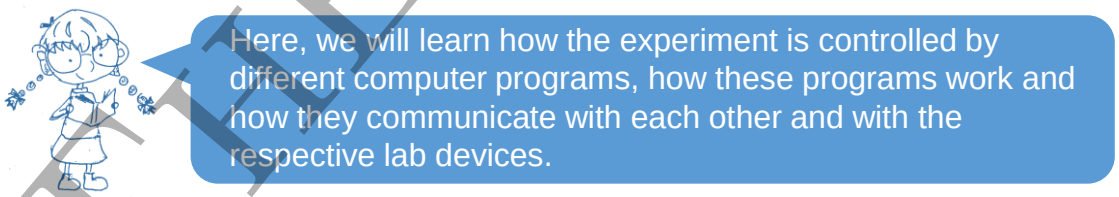

We use different control programs to control the experiment and the different machines. These need to communicate with each other. Also the calibration is often not straight forward.

Figure 2.23 shows a flow chart of the different control programs for the experiment. It shows the communication channels between different programs, between programs and lab devices and between different lab devices. Each program is depicted with the devices it controls.

THESIS DRAFT

The communication between the programs is mainly done within the labview environment by writing and reading shared variables. This leads to less loss of data, compared to sending for example the current file name between the computers, which sometimes made the camera program crash.

For details regarding the implementation and programming of the pulse generator see Noaman's thesis

Adwin program

The heart of our experimental control is the main experimental control program which controls the experimental sequence (in the center of figure 2.23) and uploads it to the Adwin system. During the course of this thesis, the communication with the other programs has been set up and in particular, the use of shared variables for the file names has been implemented.

Flex DDS program

Detailed discussions about the control of the transport can be found in the bachelor thesis of Florian Stuhlmann [74] and the master thesis of Ronja Wirtz [75], where technical details and calibration measurements can be found.

why are arbitrary $\Delta\nu$ ramps difficult (DDS-programming -> Verweis Florian's thesis)

technical details, calibration measurements, what are the difficulties?

Oscilloscope program

Based roughly on Patrick's oscilloscope program. Fast data acquisition and storage. Possibility to control the settings either via the oscilloscope manual control or via the control program. If controlling manually, the settings can be read out from the program and be used for future measurements. Read in old settings from protocol files for repeatability of experiments.

THESIS DRAFT

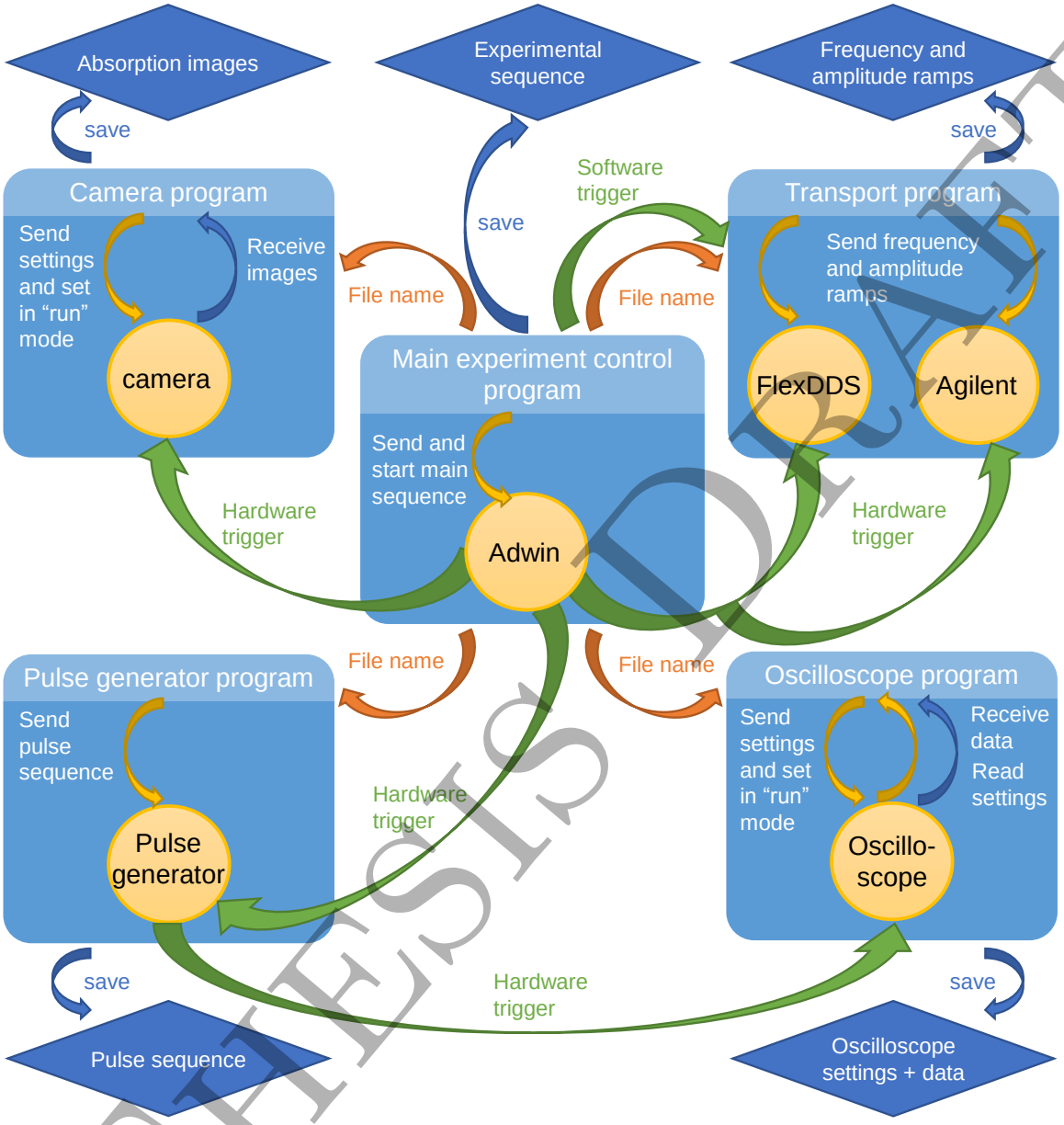

Figure 2.23.: Experiment control programs. Flow chart to visualize the communications between different control programs as well as between the control programs and the respective lab devices. Shown are the individual control programs (blue boxes) with the lab devices they control (yellow circles) and the data sets each program stores (dark blue diamonds). The communication can occur by sending file names (orange arrows), software or hardware triggers (green arrows), and sequences or settings (yellow arrows). The resulting data is received by the programs and stored in files (blue arrows).

THESIS DRAFT

2.5. Detection system

Here, we will learn how to detect the atoms outside and inside the hollow-core fiber. In particular, we will discuss what effects can influence the measured optical depth and how to get temperatures and atom numbers inside the fiber.

To detect atoms both inside and outside the fiber, we use two different detection schemes, as depicted schematically in figure 2.24. We can record either an absorption image on a CCD camera for atoms outside the fiber or a transmission spectrum on a photomultiplier tube (PMT) for probing along the fiber axis. In the following, I will discuss the specifics for both detection methods.

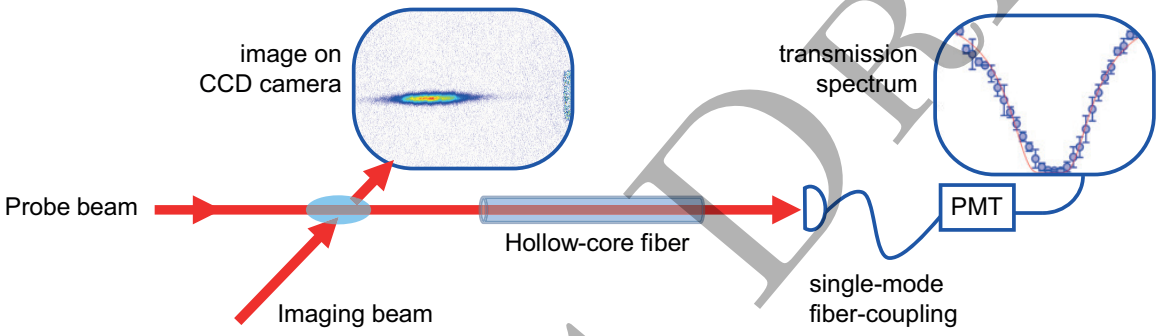

Figure 2.24.: Schematic of the detection setup. We can detect the atoms with an imaging beam perpendicular to the fiber axis or with a probe beam coupled through the hollow-core fiber into a single-mode-fiber-coupled photomultiplier tube (PMT).

Outside the fiber, we typically detect the atoms in loaded into the MOT or dipole trap using standard absorption imaging perpendicular to the fiber axis. We image resonantly on the ^{87}Rb $5S_{1/2}(F = 2) \rightarrow 5P_{3/2}(F' = 3)$ transition, with typical imaging beam powers of $130\,\mu$W, which corresponds to $\approx 2\%I_{\mathrm{sat}}$ for an imaging beam diameter of about 1 cm. In addition to the imaging beam, we shine in a repump beam resonant to the ^{87}Rb $5S_{1/2}(F = 1) \rightarrow 5P_{3/2}(F' = 2)$ transition, with a typical power of $120\,\mu$W. The shadow image of the atomic cloud is detected on a CCD camera. To normalize these absorption images, we take two additional background images, without atoms and without light, respectively, where we take care to normalize the light intensities for the two images with and without atoms.

We can then determine the atomic density distribution by fitting a Gaussian density profile $n(r) = n_0 \exp\left(-(r - r_0)^2 / \left(2\sigma_{\mathrm{at}}^2\right)\right)$ to the absorption image, where peak density n_0, atomic center of mass position r_0 and cloud radius σ_{at} are used as fit parameters. Background subtraction when imaging dipole trap while MOT is still in the picture. (Example pictures?) From this fit we determine the parameters of the atomic cloud such as atom number, size and position of the atomic cloud. Note that due to the finite time necessary for the absorption imaging (typical exposure times for the camera are $180\,\mu$s), we do not measure *in situ*, thus e.g. the cloud radius measured in the absorption images does not correspond to the

THESIS DRAFT

in situ cloud radius of the atoms in the dipole trap. This will become important in later chapters when comparing cloud radii and densities. During the detection, we switch off the dipole trap beams. We measure the temperature of the atomic cloud using a standard time-of-flight expansion method, i.e. we take several absorption images after different free evolution times to determine the expansion rate. This gives the temperature according to [70]

$$\sigma_{\mathrm{at}}(t) = \sqrt{\left(\sigma_{\mathrm{at}}(0)^2 + \frac{k_{\mathrm{B}}T}{m}t^2\right)}, \tag{2.12}$$

where T is the temperature.

We typically run the experiment for several times with the same settings to get a statistical average.

Along the fiber axis and inside the hollow-core fiber, we can probe the atoms with a resonant probe beam, which is coupled through the fiber along with the dipole trap beams. The probe beam can be detuned closely around the $5S_{1/2}(F = 2) \rightarrow 5P_{3/2}(F' = 3)$ transition, is circularly polarized and has an intensity much below the saturation intensity I_{sat}. Inside the fiber, due to the small beam waist the saturation intensity is already reached for powers as low as $\approx 20\,\mathrm{nW}$. Therefore we choose typical probe beam powers of $200\,\mathrm{pW}$, corresponding to only $\approx 1\% I_{\mathrm{sat}}$ inside the fiber. After the hollow-core fiber, the probe beam passes two bandpass filters to filter out any light from the dipole trap before it is coupled to the photomultiplier tube via a single-mode fiber. This second fiber-coupling is used as an additional selection mechanism to select the part of the probe beam that has been guided in the fundamental mode of the hollow-core fiber. Again, we record two additional background data sets (without atoms and without light) to normalize the transmission profile. When performing measurements with atoms transported inside the hollow-core fiber, we can apply a the imaging beam as a resonant push beam outside the fiber just before probing to remove any atoms outside the fiber. In the following sections, I will discuss in detail what the different challenges are when analyzing the transmission profile of the probe beam.

2.5.1. Measuring the optical depth

The transmission of a resonant light beam through an optically dense medium such as a cloud of cold atoms can be described by the Beer-Lambert law [citation]

$$T(\Delta = 0) = \frac{I_{\mathrm{out}}}{I_{\mathrm{in}}} = \exp\left(-OD\right), \tag{2.13}$$

where I_{in} and I_{out} are the light intensities before and after the atomic cloud, respectively. Here, the figure of merit for characterizing the absorption of the light beam by the atomic cloud is the optical depth OD, which is proportional to the atomic density. For very dense atomic clouds and thus high optical depths, however, the on-resonance transmission is no longer sufficient to determine OD, as within the measurement precision it will be zero for all OD above a certain threshhold. Therefore, for a frequency-dependent absorption profile,

THESIS DRAFT

the detuning Δ of the probe beam from the transition line has to be taken into account when determining the transmission

$$T(\Delta) = \exp\left(-\frac{OD}{1+4\,(\Delta/\Gamma)^2}\right), \tag{2.14}$$

where Γ again is the natural linewidth of the excited state.

A typical absorption profile is shown in figure 2.25 a), where the transmission of the probe beam is plotted as function of the probe beam detunings, together with a fit according to equation 2.14. The optical depth determined with this fit is about 17. The absorption profile shows typical features of high optical depth, the medium is opaque for about 5 MHz on each side of the resonance.

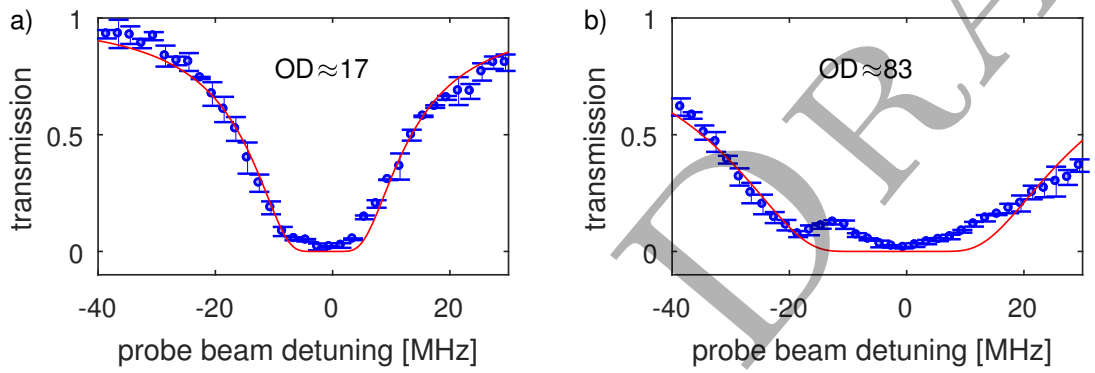

Figure 2.25.: Typical absorption profiles and corresponding optical depth fits for atoms transported in front of the fiber for two different atomic densities. In a), a typical signal for a medium atomic density is shown, in b) a typical signal for very high atomic density. (Data points: experimental data, solid red lines: optical depth fit according to equation 2.14. Error bars represent statistical errors.)

However, in our setup, where both probe beam radius and atomic beam waist are of comparable size and where we apply mode-filtering of the probe beam by coupling it into both the hollow-core fiber and the single-mode fiber in front of the PMT, obtaining the optical depth from the transmission profile is not always as straight forward as discussed above. We observe strongly distorted line shapes for high atomic densities, as depicted for example in figure 2.25 b). Typical features of these distorted line shapes are a strong asymmetry between positive and negative detuning as well as a "bump" appearing at about -15 MHz detuning. This distortion of the absorption profile can be attributed to a micro lensing effect of the atomic cloud. Thus, the optical depth values from fitting the data according to equation 2.14 cannot be trusted (even though the order of magnitude appears to be correct) and for a better result a fit including the micro lensing effect has to be used. Detailed calculations and discussions of the micro lensing effect can be found in [73] and [71] and will not be the main point of this thesis. Here, I will only give a short explanation of the effect and briefly discuss the results which are important for further investigations within this thesis.

In short, the microlensing effect can be explained as follows: the inhomogeneous density distribution of the atomic cloud leads to a frequency-dependent refractive index, which acts

THESIS DRAFT

as a lens and focusses or defocusses the probe beam according to its detuning. This modified intensity profile changes the coupling into both the hollow-core fiber and the single-mode fiber in front of the PMT. As a result, the detected line shapes look distorted. The micro lensing effect is strongest for high atomic density. An example is shown in figure 2.26, where the absorption curves for three different atomic densities are plotted together with a fit of the data with the micro lensing model. For high atomic densities (represented by small atomic cloud width σ_r), the line shape is most strongly distorted. The effect reduces for reducing atomic density. This behaviour is illustrated in figure 2.28, where the optical depth obtained from a fit according the micro lensing model and the optical depth obtained from a fit according to equation 2.14 are both plotted as function of the atomic density (represented again by the atomic cloud width σ_r). Thus, in the following, I will discuss the analysis procedure for the case of low enough atomic densities, where equation 2.14 can be used to obtain the optical depth.

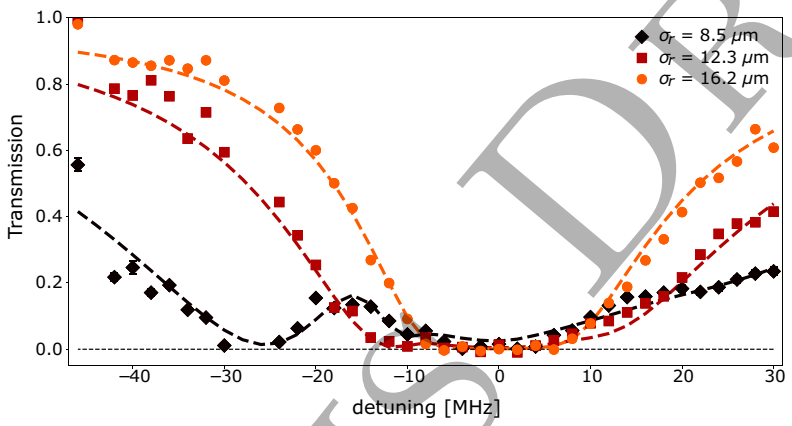

Figure 2.26.: Absorption profiles and micro lensing model for atoms transported in front of the fiber for three different atomic peak densities (increasing density for decreasing cloud width σ_r). (Data points: experimental data, dashed lines: result of the micro lensing model. Error bars represent statistical errors.) Figure adapted from our publication [73].

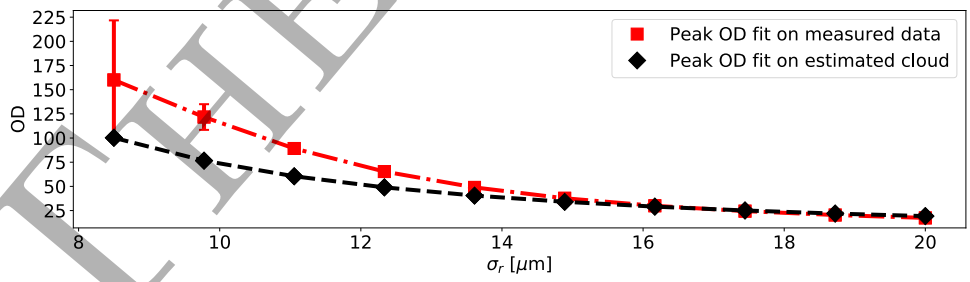

Figure 2.27.: OD correction due to the micro lensing model. Figure adapted from our publication [73].

Once the OD is known, the atomic density can be calculated by $OD = \int n(z)\sigma_{\pm}S_{23}\,dz$. However, in our case due to the geometrical factors discussed above, we need to include a correction factor to take into account the overlap between the probe beam intensity

THESIS DRAFT

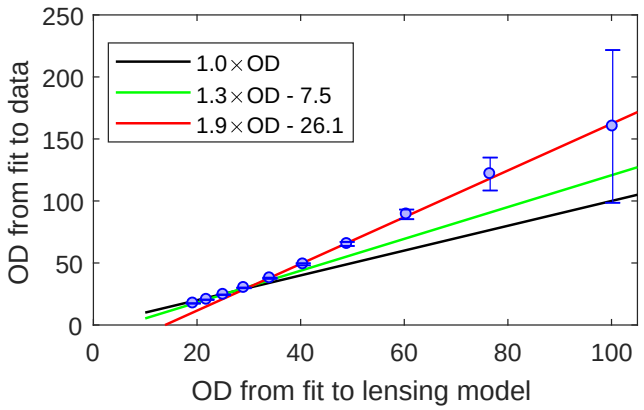

Figure 2.28.: Conversion factor between the optical depth obtained from a fit according to equation 2.14 and the optical depth obtained from a fit according the micro lensing modell. (Data points: OD fit results from our publication [73], error bars represent fitting errors. Solid lines: Different conversions between OD lensing and OD Lorentz (black/green/red: one-to-one conversion for reference / fit to the low OD data points / fit to the high OD data points).)

distribution $\propto 2/\left(\pi\omega(z)^2\right)\exp\left(-2r^2/\omega_0^2\right)$ and the atomic cloud distribution (similar to e.g. [18]). Note that in the following an atomic density distribution of $n(r) = n_0 \exp\left(-r^2/r_{\mathrm{at}}^2\right)$ is assumed, where $r_{\mathrm{at}}^2 = 2\sigma_r^2$, to keep the notation consistent with e.g. reference [18]. This correction factor is calculated by the overlap integral

$$OD = \frac{2\sigma_{\pm}S_{23}}{\pi w(z)^2}\iint n(r,z)\exp\left(-\frac{2r^2}{w(z)^2}\right)2\pi r\,dr dz, \tag{2.15}$$

where $\sigma_{\pm}$ is the resonant cross section and S_{23} the hyperfine transition strength [77]. In the z-direction, we integrate over the length of the atomic cloud. Here, we assume that the probe beam intensity does not vary in the axial direction over the length of the atomic cloud. This is true inside the fiber, in principle not true outside the fiber. (Include additional term outside the fiber over extension over atomic cloud?) However, microlensing effect is stronger than this, so this cannot be properly used anyway. In the r-direction, we integrate to infinity outside the fiber and to the core radius R_{c} inside the fiber, assuming hard boundary conditions.

Outside the fiber, this leads to the following correction factor

$$OD_{\mathrm{outside}} = \frac{N_{\mathrm{at}}\sigma_{\pm}S_{23}}{\pi w\left(\langle z\rangle\right)^2}\frac{2w\left(\langle z\rangle\right)^2}{2r_{\mathrm{at}}^2 + w\left(\langle z\rangle\right)^2}, \tag{2.16}$$

and inside the fiber, where the integral is limited to the fiber core radius R_{c}, to the following correction factor.

$$\begin{aligned} OD_{\mathrm{fiber}} &= \frac{2\sigma_{\pm}S_{23}}{\pi w(z)^2}\int_0^{L_{\mathrm{at}}} 2\pi \int_0^{R_{\mathrm{c}}} n(r,z)\exp\left(-\frac{2r^2}{w(z)^2}\right) r\,dr dz \\ &= \frac{N_{\mathrm{at}}\sigma_{\pm}S_{23}}{\pi w_0^2}\frac{2w_0^2}{2r_{\mathrm{at}}^2 + w_0^2}\left(1 - \exp\left(-\frac{R_{\mathrm{c}}^2}{r_{\mathrm{at}}^2}\right)\exp\left(-\frac{2R_{\mathrm{c}}^2}{w_0^2}\right)\right). \end{aligned} \tag{2.17}$$

THESIS DRAFT

The addional factor compared to the outside the fiber result does not make a huge impact for XXX. However, in our case we see a large impact when repeating the measurement process multiple times as will be discussed in the following section. Difference large - small core fibers?

To give an intuitive understanding of how the correction factor influences our measurements, figure 2.29 shows an examplary measurement of the experimentally obtained optical depth as a function of distance from the fiber tip. Here, measurements with relatively low atomic densities habe been chosen to avoid effects due to lensing. The impact of the correction factor introduced in equations 2.16 (outside) and 2.17 (inside the fiber) is clearly visible. As the atoms approach the fiber tip, the optical depth increases and then stays constant for positions inside the fiber. In general, the experimental data is in good agreement with the theoretical fit. Only the optical depth at the MOT position deviates from the fit, which we attribute to a mismatch of overlap between atoms and probe beam immediately after loading the atoms into the dipole trap. (Assumptions: constant atom number, constant η = constant cloud radius relative to beam radius or constant cloud radius r_0, therefore mostly the factor $1/w^2$ is incorporated in this most simple model. Inside fiber additional correction term (1-exp...) is incorporated.)

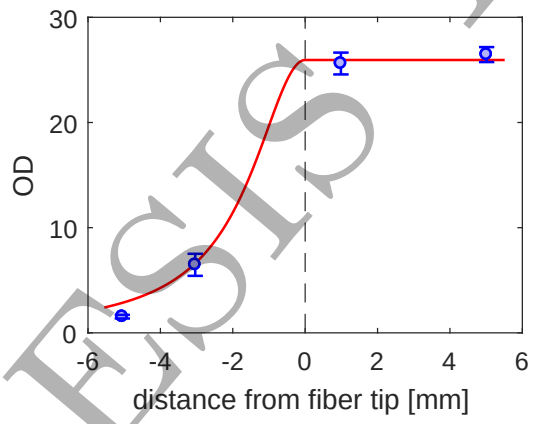

Figure 2.29.: Optical depth as function of distance from the fiber tip. (Data points: experimental data with averaging over 20 repetitions, solid red line: optical depth fit according to equations 2.16 (outside) and 2.17 (inside the fiber). Error bars represent statistical errors.) Figure adapted from the supplemental material of our publication [13].

Since here atom number and η or cloud radius are treated as independent variables, for this fit it is not possible to determine both separately. For a precise determination of the atom number, we need reliable numbers for the atomic cloud radius, which are difficult to obtain via absorption imaging as discussed above. Therefore, the release-recapture measurements are necessary. (Or estimating cloud radius via trapping potential as $r_0^2 = w_0^2(k_\mathrm{B}T)/2U_\mathrm{dip}$, when temperature is known)

THESIS DRAFT

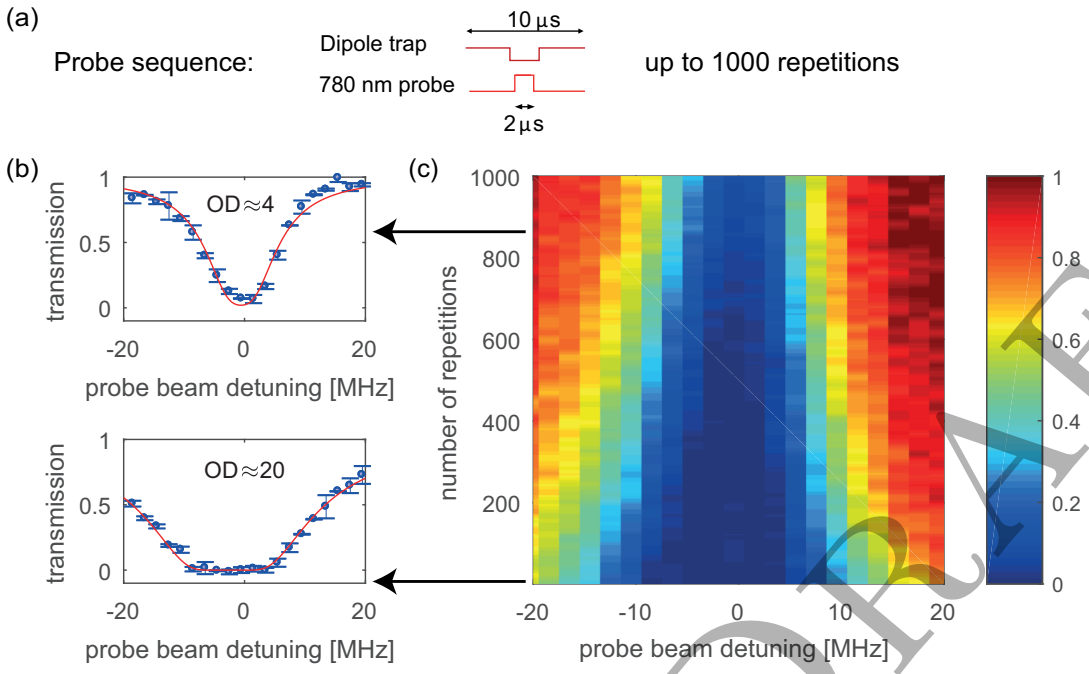

Figure 2.30.: a) Schematic of the **pulsed probing scheme**. During the probe pulses, the dipole trap is switched off. The probing sequence is repeated up to a 1000 times. b) Absorption profiles at the beginning of the probing sequence (lower figure) and after 900 repetitions of the probing sequence (upper figure) for atoms inside the fiber. (Data points: experimental data with averaging over 20 repetitions, solid red lines: optical depth fit according to equation 2.14. Error bars represent statistical errors.) The absorption profiles in b) represent cuts through the time-resolved absorption profile shown in c), where the transmission is plotted against the detuning of the probe beam and the number of repetitions of the probe sequence (Moving average over 20 neighboring repetitions).

2.5.2. Time-resolved detection scheme

To avoid influences by the dipole trap, such as an AC Stark shift, during probing, we use a pulsed probing scheme, where the dipole trap is switched off during the probe pulses. This probing sequence is depicted schematically in figure 2.30 a). We typically use a probe pulse of $2\,\mu$s. The duty cycle for the dipole trap is $\approx 80\%$ and one complete probing sequence takes $10\,\mu$s. This probing sequence is typically repeated for a 1000 times. This repetition allows us to get information about the time-evolution of the atomic cloud. Typically, we show this information in a time-resolved 3D-plot, as for example in figure 2.30 c). Here, the transmission is plotted against detuning of the probe beam and the number of repetitions of the probe sequence. It is clearly observable that the overall transmission reduces for increasing number of repetitions.

From this time-resolved detection scheme, we can also calculate the temperature of the atomic cloud using a release-recapture fit, similar to e.g. [18]. For this, we assume that during the dipole trap off time $t_{\mathrm{off}} = 2\,\mu$s the atomic cloud expands to $r_{\mathrm{at}}^2 = r_0^2 + v_{\mathrm{at}}^2 t_{\mathrm{off}}^2$, where r_0 is the initial cloud size as discussed above and $v_{\mathrm{at}}^2 = 2(k_B T)/m$ is the mean velocity of the cloud. Further assumptions are a constant temperature of the cloud and a constant

THESIS DRAFT

atomic distribution with reducing peak density. Both assumptions are valid in our opinion because dipole trap potential is kept constant during the release-recapture process. We assume that atoms which hit the fiber wall during this expansion time ($r_{\mathrm{at}} \geq R_{\mathrm{c}}$) are lost for the probing process. This loss process occurs in the same way for each release-recapture cycle. Thus with increasing number N of release-recapture cycles the optical depth reduces to

$$OD_{\mathrm{fiber}}(N) = \frac{N_{\mathrm{at}}\sigma_{\pm}S_{23}}{\pi w_0^2}\left(\frac{2w_0^2}{2r_{\mathrm{at}}^2 + w_0^2}\left(1 - \exp\left(-\frac{R_{\mathrm{c}}^2}{r_{\mathrm{at}}^2}\right)\exp\left(-\frac{2R_{\mathrm{c}}^2}{w_0^2}\right)\right)\right)^N \tag{2.18}$$

inside the fiber.

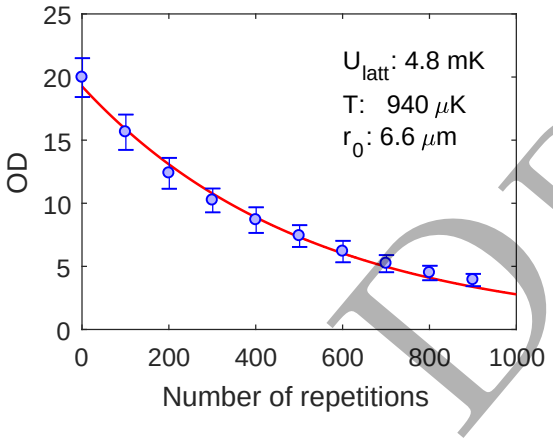

Figure 2.31.: Release-recapture measurement for atoms inside the fiber (Data points: experimental data with averaging over 20 repetitions, solid red line: release-recapture fit according to equation 2.18. Error bars represent statistical errors.).

Figure 2.31 shows a typical release-recapture fit to the same data as for figure 2.31 for atoms transported inside the fiber. Here, the optical depth is plotted as a function of the number of repetitions. As in figure 2.31, we see that the optical depth drops from around 20 to around 4. The release-recapture fit according to equation 2.18 for a given potential depth $U_{\mathrm{latt}} = 4.8\,\mathrm{mK}$. From the fit, we determine the temperature of the atoms to be around $940\,\mu\mathrm{K}$, which corresponds to a radius of the atomic cloud of about $r_0 \approx 6.6\,\mu\mathrm{m}$.

Outside the fiber, we need different boundary conditions for when we consider the expanding atoms as lost. Fit is very sensitive to these boundary conditions!!! One condition could be to define a beam radius R, which is calculated by the Gaussian beam expansion of the probe the that is limited inside the fiber by the fiber wall R_c. However, due to the lensing it is difficult to define boundary conditions for the beam propagation because we know that interaction with the atomic cloud changes the beam propagation.

$$OD_{\mathrm{outside}}(N) = \frac{N_{\mathrm{at}}\sigma_{\pm}S_{23}}{\pi w\left(\langle z\rangle\right)^2}\left(\frac{2w\left(\langle z\rangle\right)^2}{2r_{at}^2 + w\left(\langle z\rangle\right)^2}\right)^N \tag{2.19}$$

For fitting the curves, we only use the temperature T as a free parameter, which influences the atomic width as discussed above in the following form $r_{\mathrm{at}}^2 = AT + BTt_{\mathrm{off}}^2$, where $A = w_0^2 k_{\mathrm{B}}/U_{\mathrm{dip}}$ and $B = 2k_B/m$.

THESIS DRAFT

Assumptions: constant temperature, constant atom distribution (only reducing peak density) -> because dipole trap potential is kept constant. Assume, if atoms are heated by switching on and off, they will be lost anyway.

Influence of probe beam on atomic density evolution (tests for probe on / off, different probe powers, different pulse lengths).

THESIS DRAFT

THESIS DRAFT

3. Highly controlled optical transport of cold atoms into a hollow-core fiber

In this chapter, I will present the results of the first main focus of my thesis, namely optimizing the highly controlled transport of the atoms into the hollow-core fiber using an optical conveyor belt. The main results of this chapter have been published in [72]. Some parts of the setup and some early results have already been described in the bachelor thesis of Florian Stuhlmann [74]. Some preliminary measurements have also been performed together with Mohammad Noaman. All experiments and most of the data analysis discussed in this chapter were performed together with Ronja Wirtz during the course of her master thesis, in which some of the main results are also discussed [75]. Both student theses were co-supervised by me during the course of my own thesis. For the discussion here, I have added the comparison with the truncated harmonic oscillator theory and a more detailed analysis of the data, especially of the measurements inside the fiber. The results of the classical transport theory have been obtained in the context of a collaboration with the group of Prof. Dr. Speck, where the simulations have been performed by Fabian Knoch.

One of the central challenges in our experimental setup is the controlled preparation of our atomic sample inside the hollow-core fiber. As a way of controlling the atomic transport, we employ an optical conveyor belt as already briefly discussed in section 2.3.4. This technique allows us to precisely position the atoms at any position inside or outside the fiber. In section 3.1, I will present the high degree of control we have over the atomic position, velocity and acceleration.

Furthermore, in addition to these spatio-temporal parameters, we would like to be able to control the number and temperature of the transported atoms for a fully controlled sample preparation. In particular, we would like to optimize our transport to obtain high atom numbers and low temperatures. In section 3.2, I will first study how different frequency ramps, i.e. velocity ramps of the moving lattice, affect the number of transported atoms and which effects need to be taken into account when choosing frequency ramps for our specific setup. Next, in section 3.3, I will discuss how the potential depth affects the temperature of the atoms and how we can control the potential depth during the transport procedure with so-called amplitude ramps. Finally, I will characterize the influence of combined frequency and amplitude ramps on the transport process and compare our experimental results with two different theoretical approaches. Here, I will highlight the versatility of our setup in choosing particle numbers and temperature ranges by adapting the trapping potential. I will start this discussion with measurements outside the hollow-core fiber in section 3.4, before concluding with results obtained inside the hollow-core fiber in section 3.5.

THESIS DRAFT

3.1. Transport with an optical conveyor belt

Here, we will learn how to control position, velocity and acceleration of cold atoms transported using an optical conveyor belt. We will also learn which observables are best suited for characterizing the transport process.

In this section, I would like to present the case study of an exemplary transport process. While doing so, I will highlight that we already have achieved excellent control over the spatio-temporal degrees of freedom of our system, such as position, velocity and acceleration of the atoms. This initial characterization is of particular importance as for later measurements inside the fiber we will no longer have access to the atomic position. Therefore, we must be certain that our experimental results match with the theoretical prediction. Further, I will point out which additional degrees of freedom, such as number and temperature of the atoms, are affected by the transport process. Studying these effects in detail will be the subject of the following sections.

Figure 3.1 illustrates our exemplary transport process. The absorption images in figure 3.1 a) are taken at different times within the transport procedure. They show that for increasing transport time the atoms are moved from their initial position towards the tip of the hollow-core fiber over a distance of 4.4 mm. The transport process is controlled by the frequency detuning ramp applied to one of the lattice laser beams, as discussed in section 2.3.4. In this example, we use a linear frequency ramp as shown in figure 3.1 b). Initially, while loading the atoms into the optical lattice at their initial position, the relative frequency detuning $\Delta\nu$ between the two dipole trap beams is set to zero. We then start to accelerate the atoms in the moving optical lattice by increasing $\Delta\nu$, typically to a maximum value of a few hundred kilohertz. In this example, we increase the detuning linearly within 100 ms to a maximum frequency detuning of 200 kHz. Before probing, we decelerate the atoms by ramping the frequency detuning again down to zero, which stops the lattice. Typically, this deceleration is done much faster than the acceleration, in this example within 10 ms.

In the ideal case, the transport velocity of the atoms corresponds to the velocity of the moving lattice with wavelength λ, which depends on the frequency detuning ramp $\Delta\nu(t)$ as

$$v(t) = \frac{\lambda}{2}\Delta\nu(t). \tag{3.1}$$

Thus, the shape of atomic and lattice velocity will always follow the shape of the frequency ramp. In this case, we therefore expect a linearly increasing velocity. By integrating or differentiating equation 3.1, we can then theoretically determine the position and acceleration of the transported atoms as

$$z(t) = \int v(t)dt \qquad \text{and} \qquad a(t) = \frac{dv(t)}{dt}. \tag{3.2}$$

THESIS DRAFT

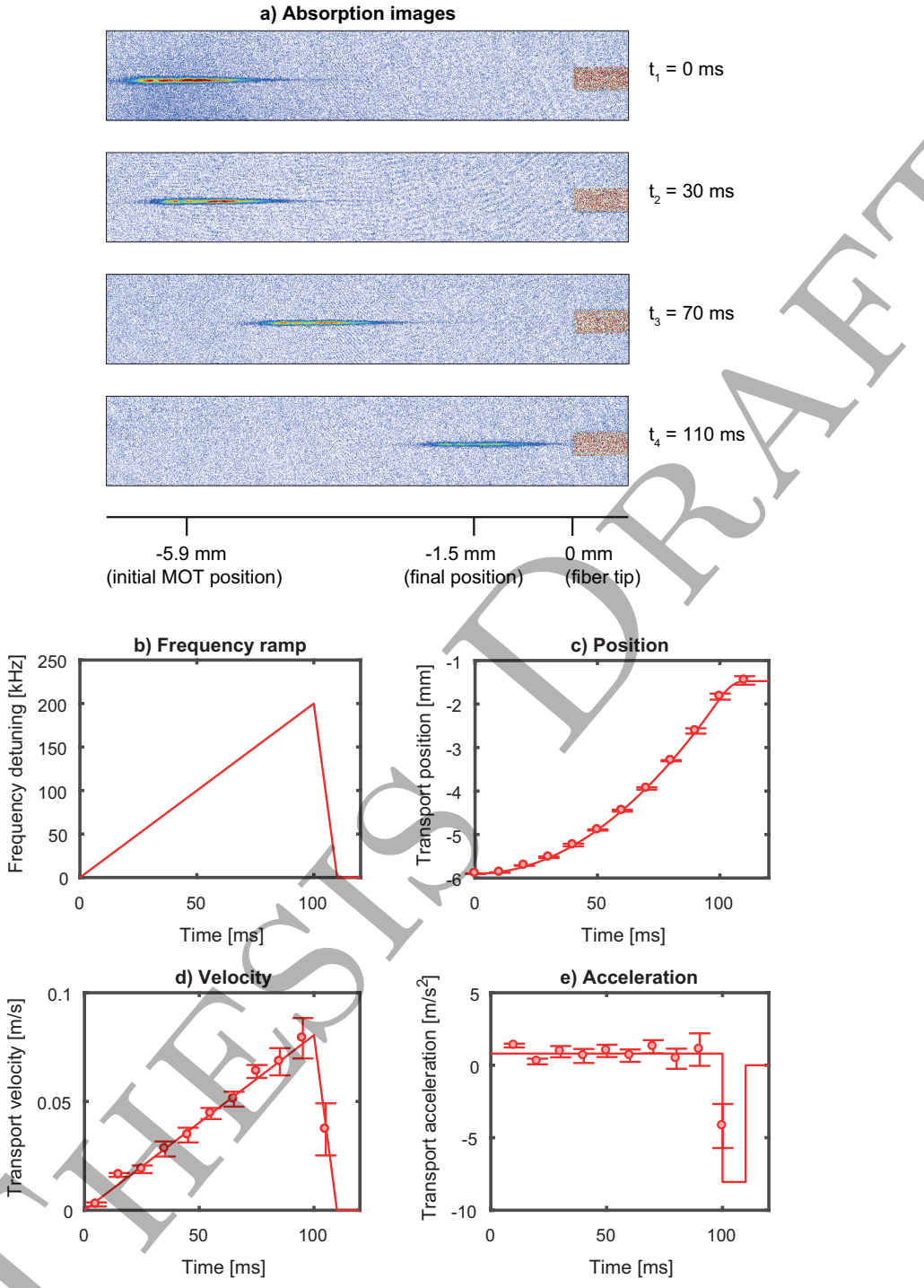

Figure 3.1.: Exemplary transport process. Figure a) shows absorption images from an exemplary transport, corresponding to the frequency ramp shown in figure b). Figures c) to e) show the center of mass position, velocity and acceleration of the transported atoms as a function of the applied ramp time. (Data points: experimental data, solid lines: theoretical model, error bars represent statistical errors.) Figure adapted from our publication [72].

THESIS DRAFT

For our example of a linearly increasing frequency detuning $\Delta\nu(t) = \frac{\Delta\nu_{\max}}{\Delta t}t$, the final position of the atoms and the maximum acceleration during the ramp are given by

$$z(\Delta t) = z_0 + \frac{\lambda\Delta\nu_{\max}\Delta t}{4} \qquad \text{and} \qquad a_{\max} = \frac{\lambda}{2}\frac{\Delta\nu_{\max}}{\Delta t} \tag{3.3}$$

respectively, where z_0 is the initial atomic position, $\Delta\nu_{\max}$ the maximum applied frequency detuning and Δt the duration of the ramp. For the linear ramp, the atoms are accelerated with constant acceleration proportional to the slope of the frequency ramp throughout the transport process. Another interesting aspect of equation 3.3 is that only the product of maximum detuning and ramp time is responsible to reach the same final position. This means, that for a fixed final position, a short ramp time can be compensated for by a high detuning or vice versa. However, as their ratio determines the acceleration, a shorter ramp time comes at the cost of high accelerations, the effects of which will be discussed later.

To verify our control over the transport process, we experimentally determine the center of mass position of the atomic cloud from the absorption images such as in figure 3.1 a), then differentiate the position as function of time to determine velocity and acceleration. Figures 3.1 c) - e) show both experimental results and theoretical calculations for position, velocity and acceleration. Note that the full frequency ramp, that is both acceleration and deceleration ramp, need to be taken into account when comparing with the experimental data. We find that experimental results and theoretical calculations agree very well with each other within the error bars. Additionally, we have also confirmed this behaviour for differently shaped frequency ramps with different final detunings (see [75] for another example). Therefore, we can conclude that by choosing an appropriate frequency ramp, we can precisely control the atomic position, velocity and acceleration.

To further characterize the transport process, we study additional properties of the transported atoms, such as atom number and temperature. From the absorption images in figure 3.1 a), where the atom density is represented by color-coding, it is already visually clear that the number of atoms decreases during the transport process. To more systematically study this loss of atoms, I have extracted the atom number at different times, again for the example of a 200 kHz linear transport ramp, as shown in figure 3.2 a), this time without considering the deceleration process. Figures 3.2 c) and d) show the normalized number of atoms during the transport process as function of the ramp time and the center of mass position of the atomic cloud, respectively. We can clearly see that during the transport the number of atoms drops to about 40% of the initial atom number. The atom loss appears approximately linear in time, which corresponds to the behaviour of the frequency detuning ramp. This would indicate that the atoms are lost at a constant rate. A reason for this could be the constant acceleration during the transport.
To study position-dependent loss effects, the atom number is also plotted as function of position. We would expect most position-dependent effects such as lifetime or heating caused by dipole trap to depend on the position-dependent trap depth as shown in figure 3.2 b). However, here no clear correlation between number of atoms and potential depth is visible. All in all, we find that it is very difficult to disentangle these different loss mechanisms which may occur during the transport process. Therefore, in the following I will only concentrate on the atom number after the transport ramp, i.e. the number of atoms which have reached the final position, as this is also what is of most experimental relevance.

THESIS DRAFT

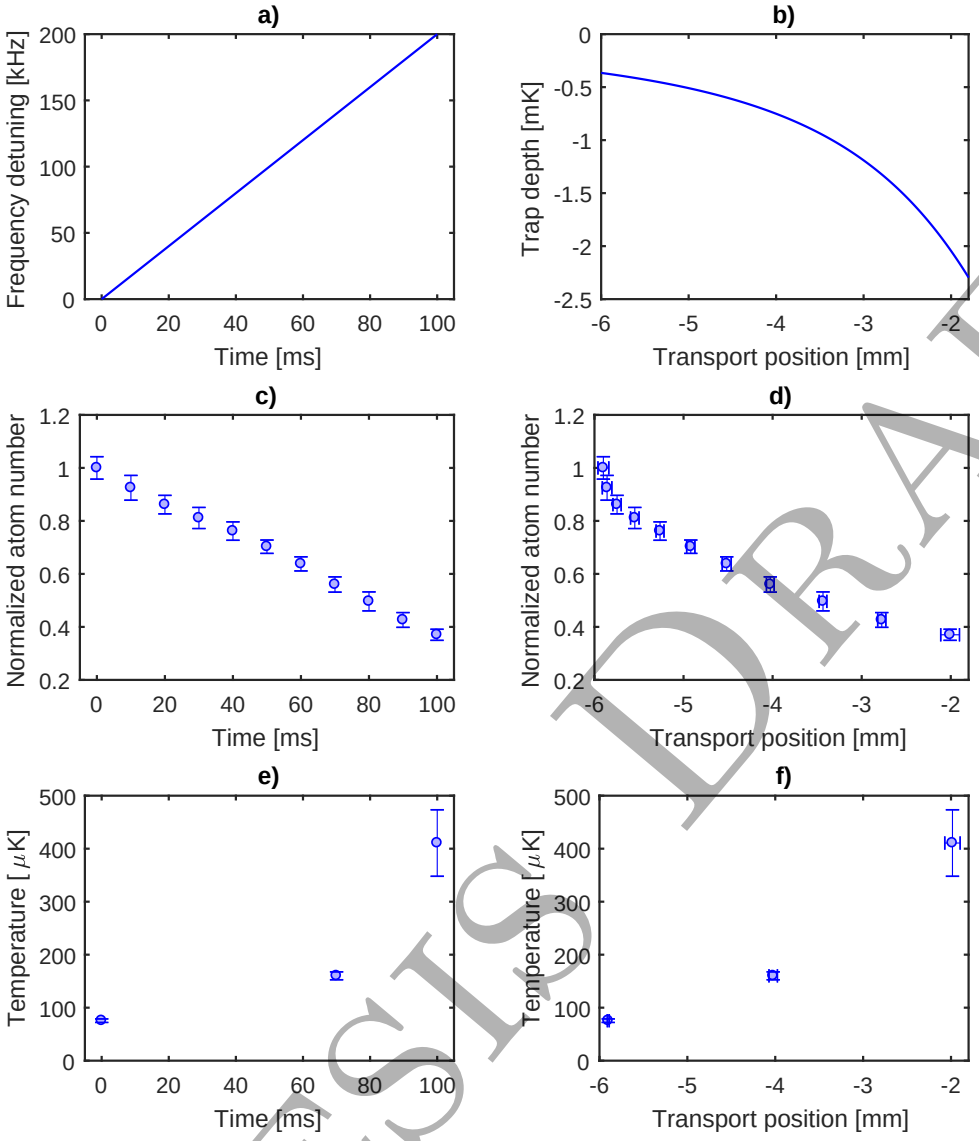

Figure 3.2.: Atom number and temperature during the transport process. Shown are the normalized number of atoms (middle row) and the atomic temperature (lower row) during the transport process as a function of the transport time (left column) and as a function of the center of mass position of the atomic cloud (right column) for a 200 kHz linear transport ramp without deceleration ramp, as shown in figure a). The trap depth as function of position is shown in figure b). (Error bars represent statistical errors and errors from the fitting procedure.)

Next, I would like to present how the transport affects the atomic temperature. Figures 3.2 e) and f) show the atomic temperature during the transport process as function of the ramp time and the center of mass position of the atomic cloud, respectively. Here, we note that the temperature drastically increases from about 75 μK to more than 400 μK as the atoms are transported towards the fiber tip. In this case, the temperature increase has no clear dependence on the timings of the frequency ramp, but rather scales approximately as

THESIS DRAFT

the position-dependent trapping potential depth. We find that this behaviour occurs for all frequency ramps (see [74] for more examples) and therefore conclude that the temperature increase is directly related to the increasing trapping potential close to the fiber tip, while the choice of the frequency ramp plays a minor role. In the following, I will introduce a method to determine the atomic temperature as a function of the trapping potential.

In conclusion, we have verified that by using an optical conveyor belt to transport our cold atoms we have very good control over the spatial degrees of freedom, such as atomic position, velocity and acceleration. As figures of merit concerning the quality of our transport, we have identified the number and temperature of the transported atoms. Note that a high quality transport for us means to achieve high final atom numbers and low final temperatures. Further, we have seen that while the number of atoms seems to depend both on frequency ramp and trapping potential, the final temperature seems to be mainly dominated by the depth of the trapping potential. In the following sections, I will first study final atom numbers as function of the applied frequency ramp (in section 3.2) and final temperatures as function of the trapping potential (section 3.3), before combining both frequency ramps and changing trapping potential to study the resulting atom numbers as well as temperatures (section 3.4).

3.2. Effect of frequency ramps on the transport efficiency

Here, we will learn how the applied frequency ramps influence the number of transported atoms. We will pay special attention to effects which occur for either slow ramps at low or fast ramps at high maximum frequency detuning.

As just discussed, the number of transported atoms is one of the figures of merit for characterizing our transport process. In this section, I will study the impact of different parameters of the frequency ramp such as ramp time, final maximum detuning and ramp shape on the number of transported atoms. For these measurements, the atoms are transported to a final position about 1.8 mm in front of the fiber tip. This will allow us to characterize our transport process without having to take into account additional influences by the hollow-core fiber. The transport into the hollow-core fiber will later be discussed in detail in section 3.5.

Instead of the absolute number of transported atoms, which may fluctuate depending on the daily experimental settings, we typically characterize our transport process by the transport efficiency, which is a measure of how many atoms of the initial cloud have successfully been transported to the final position. We calculate this transport efficiency by measuring the number of transported atoms at the final position and divide it by the initial number of atoms in the optical lattice at the MOT position. As will be discussed in detail in section 3.2.2, here it is important to only take into account the number of atoms which have really reached their final destination, discarding those which might have been lost during the transport process.

THESIS DRAFT

As an overview over the different challenges connected with achieving a high transport efficiency, I would exemplarily like to present the transport efficiency for three different frequency ramps, shown in figure 3.3 a). In addition to the 200 kHz linear frequency ramp discussed before, we use an 1000 kHz linear frequency ramp and a 1000 kHz constant frequency ramp. We choose ramp time and maximum final detuning such that all ramp reach approximately the same final position.[1] With the 1000 kHz linear frequency ramp, we can investigate the effect of ramp time and maximum detuning for the same ramp shape. To decrease the ramp time even further at the same maximum detuning, we employ a constant frequency ramp. Here, the detuning is ramped up to the maximum value of 1000 kHz within 1 ms, then kept constant for the remaining transport time. Therefore, the atoms experience a constant transport velocity and no further acceleration. For this ramp, we can reach ramp times as short as 10 ms including the deceleration ramp, which we keep at 1 ms for all ramps.

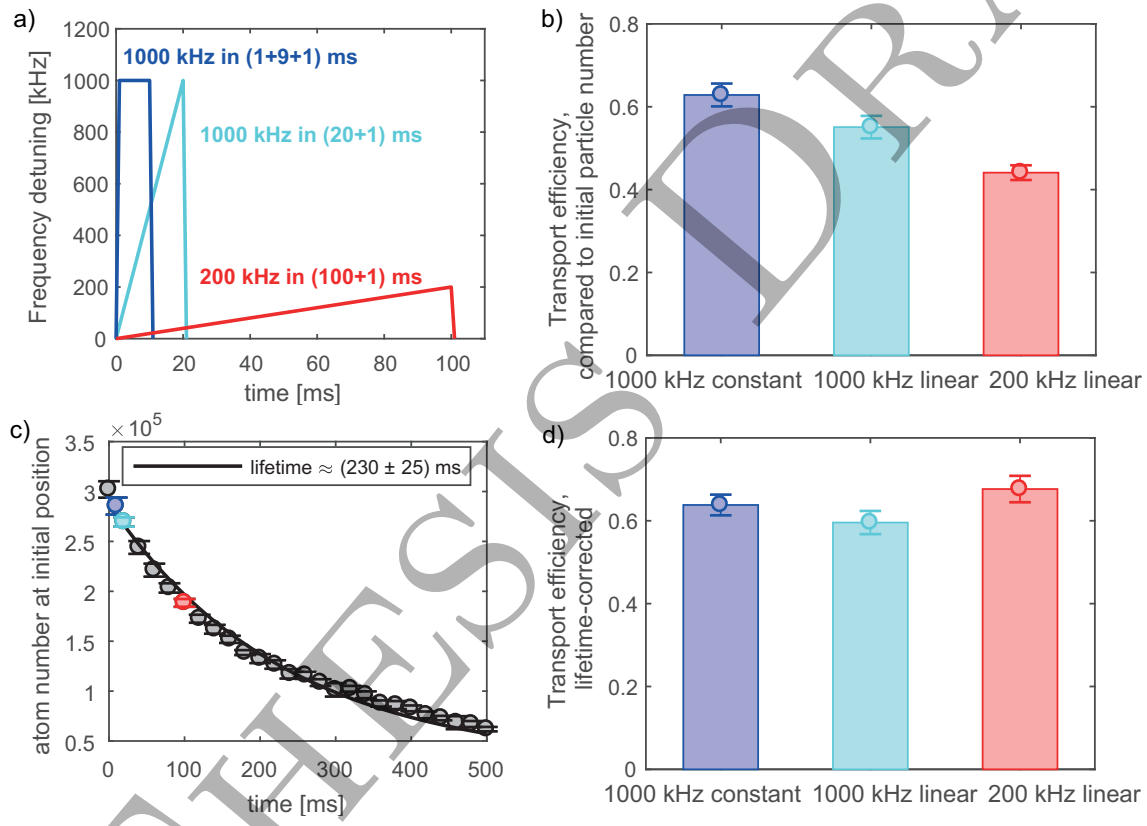

Figure 3.3.: Effect of frequency ramps on transport efficiency. a) Frequency detuning as function of time for different frequency ramps. b) Transport efficiency compared to initial particle number. c) Lifetime measurement: Number of atoms at initial position as function of holding time (markers: experimental data, solid line: exponential fit). The timings for the ramps used for the transport measurements are marked in their respective colour. d) Transport efficiency corrected for atom loss due to the finite lifetime in the dipole trap. (Error bars represent statistical errors.) Figure adapted from our publication [72].

[1] As we are experimentally limited to varying the timing of the frequency ramps in steps of 1 ms, the final position of the three ramps might slightly vary. However, this variation is small compared to typical experimental error bars.

THESIS DRAFT

Figure 3.3 b) shows the transport efficiencies for these three different frequency ramps. As is clearly visible, the transport efficiency decreases from above 60% for the 1000 kHz constant frequency ramp to about 55% for the 1000 kHz linear frequency ramp and to just above 40% for the 200 kHz linear frequency ramp. As there are clear differences in transport efficiency both for the two linear ramps as well as for the two ramps with 1000 kHz maximum detuning, we can deduce that neither the maximum final detuning nor the ramp shape can be the most important factor. Instead, the main difference between these three ramps seems to be the ramp time. While a short ramp time leads to a higher transport efficiency, a longer ramp time decreases the transport efficiency.

This can be understood as also the number of atoms at the initial position is limited by the lifetime in the dipole trap and therefore decreases with time. Figure 3.3 c) shows experimental results for measuring the number of atoms held in the stationary lattice at the initial position as a function of the holding time. Clearly, the number of atoms drops with increasing holding time. Assuming an exponential decay of the atom number, we obtain a lifetime of approximately 230(25) ms by an exponential fit to the data.

As a zero-order approach to correct for these lifetime-induced effects, we can divide the number of transported atoms by the number of atoms at the initial position after a holding time equivalent to the transport duration. Figure 3.3 d) shows these lifetime-corrected transport efficiencies for the three different frequency ramps. The result are very interesting. One point is that even these corrected efficiencies stay clearly below 100%, which means that all of our transport is fundamentally limited. A reason for this could be a position-dependent lifetime, which our zero-order correction cannot compensate for. The other point is that all the transport efficiencies are now not only almost the same for all ramps, the 200 kHz linear frequency ramp with the previously worst result now achieves clearly the highest efficiency. This seems to indicate that if the lifetime-effect were not present, frequency ramps with low maximum detunings would lead to better transport and therefore a higher transport efficiency. Further, when comparing the two ramps with 1000 kHz maximum detuning, the constant ramp seems better suited than the linear one.

Overall, in this exemplary study of different frequency ramps, we could therefore make out two major effects influencing the transport efficiency. On the one hand, the lifetime of the atoms in the optical dipole trap turns out to be one of the major limits in our setup, limiting the maximum possible transport time. In the following section 3.2.1, I will therefore discuss which major contributions may be responsible for this lifetime limit and whether we can possibly circumvent them to increase the lifetime. On the other hand, when compensating for the lifetime, fast ramps with high detunings also seem to hit a limit regarding the transport efficiency. Therefore, I will discuss in section 3.2.2 which additional effects have to be taken into account for ramps with high detunings, paying special attention to the question whether our transport happens adiabatically. The exact shape of the frequency ramp seems to be of less influence than the other two effects mentioned above. Still, in section 3.2.3 I will briefly present our results regarding different ramp shapes, before coming to a conclusion about the influence of the frequency ramps on the number of atoms which can be successfully transported.

THESIS DRAFT

3.2.1. Limited lifetime (low detunings)

As just discussed, one of the major limitations for the transport efficiency in our setup is the lifetime of the atoms in the optical dipole trap. This especially holds true for ramps with low maximum detunings, i.e. for slow ramps, therefore effectively limiting us to short transport times and ramps with high maximum detunings when we want to achieve high transport efficiencies. In this section, I would like to introduce several different effects which can play a role for the lifetime of trapped atoms and discuss the importance of each of them for our setup. In particular, I will pay attention to whether it is possible to reduce or modify these effects in order to achieve longer lifetimes.

Another interesting aspect would be to compare lifetimes for atoms transported to different final positions and especially to compare the lifetime inside and outside the hollow-core fiber. Similar measurements have e.g. been done by Okaba et al. [14]. However, as discussed previously regarding figure 3.2, we already observe a loss of atoms during the transport process. Therefore, it is very difficult to disentangle effects from transport losses and effects due to losses at the final position, making it difficult for us to compute reliable lifetimes at different final positions. As a simplification, I will first only look at atoms at the initial position when discussing which effects can limit the lifetime. Then, for each effect, I will point out whether and how it could be affected by additional position-dependent effects, such as e.g. increasing laser intensity or influences by the hollow-core fiber.

Heating due to scattering in the dipole trap

A typical and often the most important effect limiting the lifetime of trapped atoms is the scattering of photons of the trapping laser beam. In section 2.3.2, I have discussed how our trapping wavelength was chosen as a compromise between achieving a high trap depth and a low scattering rate. Here, the scattering rate describes how often a scattering process between a trapped atom and a photon from one of the lattice laser beams occurs.

For the case of a single-frequency optical lattice at 805 nm, as discussed before the scattering rate is approximately 40 Hz. Assuming that each scattering event leads to the loss of the atom participating in the scattering process, this would lead to a lifetime of about 25 ms, which is a factor of ten lower than observed experimentally. However, the assumption of an atom being lost after a single scattering event holds only true for very shallow traps or for example for a Bose Einstein condensate where each atoms needs to be in the ground state.

In our case, where we are working with a thermal cloud of cold atoms and have a very deep trap, one scattering event does not necessarily lead to the loss of the atom from the trap. Instead, due to the scattering event, the mean temperature of the atom will increase by the recoil temperature $T_{\mathrm{rec}} = \hbar^2 k^2/m$, which describes the energy gained by the emission or absorption of a single photon. Therefore, the heating rate of the atoms is a more meaningful quantity for us. It can be calculated from the mean scattering rate as follows ([76])

$$\dot{T}(\mathbf{r}) = \frac{2/3}{1+\kappa} T_{\mathrm{rec}} \overline{\Gamma}_{\mathrm{sc}}(\mathbf{r}), \tag{3.4}$$

THESIS DRAFT

where the factor κ depends on the trap geometry and is $\kappa = 1$ for the case of a 3D harmonic trapping potential, as which we can approximate each individual lattice well. The mean scattering rate in the case of a red-detuned dipole trap with trap depth much larger than the temperature of the trapped atoms can be approximated as the scattering rate given in equation 2.3. Then for our trap parameters the heating rate is given by

$$\dot{T}_{\max}(\mathbf{r}) = \frac{2/3}{1+\kappa} T_{\mathrm{rec}} \frac{\pi c^2}{2\hbar} \left(\frac{2\Gamma_{D2}^2}{\omega_{D2}^3 \Delta_{D2}^2} + \frac{\Gamma_{D1}^2}{\omega_{D1}^3 \Delta_{D1}^2} \right) I(\mathbf{r}). \tag{3.5}$$

For temperatures approaching the trap depth, the mean scattering rate is reduced as most atoms experience an effectively weaker trap. However, to give an estimate for the order of magnitude of the heating processes, in the following I will approximate the mean scattering rate by the scattering rate. Since this is always equal or larger than the temperature-corrected mean scattering rate, this approximation will give an upper limit on the heating processes due to scattering.

Again assuming a single-frequency optical lattice at 805 nm, the heating rate can be calculated as $8\,\mu$K/s. That means that for atoms at an initial temperature of about $100\,\mu$K it would take approximately 40 s to leave our $350\,\mu$K deep trap. This value, however, is about two orders of magnitude higher than observed experimentally. A possible reason for this discrepancy is that our trapping light is not strictly single-frequency, but contains a background of other frequencies due to the broad emission spectrum of the tapered amplifiers, as discussed in detail in section 2.3.3. Therefore, in principle, the heating rates of the whole contributing frequency spectrum have to be taken into account for determining the lifetime of the atoms in the trap. In the following, I will give an estimation of how the background frequencies change the heating rate, both by considering the full spectrum and the main contributing frequencies individually.

Figure 3.4 a) shows a model spectrum, modelled after the measurements discussed in section 2.3.3. Here, we have 500 mW of laser power at our main trapping wavelength of 805 nm, two further peaks at 797 nm and 802 nm and a broad spectral background, as given by the fit to the experimental data from figure 2.20. The inset shows a zoom into the low power region to reveal the two additional minor peaks. From this power distribution as a function of wavelengths, it is then possible to calculate the heating rate for each wavelength respectively. The total heating rate, integrated over all wavelengths, can then be obtained by a trapezoidal numerical integration of the heating rate as function of wavelength, while disregarding points actually on resonance to avoid divergence of the integral.

Figure 3.4 b) shows the corresponding heating rate for each wavelength (left y-axis) as well as the integrated heating rate (right y-axis). For the sake of clarity, the left y-axis has been limited to maximum values of $25\,\mu$K/s, while actually the heating rate diverges close to the Rubidium D1- and D2-transitions. Consequently, also the integrated heating rate has the strongest contribution from wavelengths very close to these resonances, whereas the contribution from the main trapping wavelength is barely visible. From this calculation, the integrated heating rate can be estimated to approximately $8400\,\mu$K/s, which for the same conditions as above means that a trapped atom will leave the trap in about 30 ms. This number is now again much lower than the experimentally observed value, indicating

THESIS DRAFT

that our estimation has overestimated the integrated heating rate. One reason for this was discussed above when the mean scattering rate was replaced by the scattering rate in equation 3.5. Further, the result can depends on the exact parameters of the numerical integration. For example, the smaller the stepsize, the more points closer to the actual resonance position will contribute to the integral, increasing the integrated heating rate. For the measurements above, the stepsize has been chosen as 0.01 nm. However, this is again just an approximation to estimate the order of magnitude of the different heating processes. Even though we might not fully trust the absolute numbers, from the results we can clearly identify the main contributions of the heating rate. Therefore, for most following discussions, I will compare the heating rates for our main trapping wavelength 805 nm with the one at 795 nm, which is one of the two main contributions.

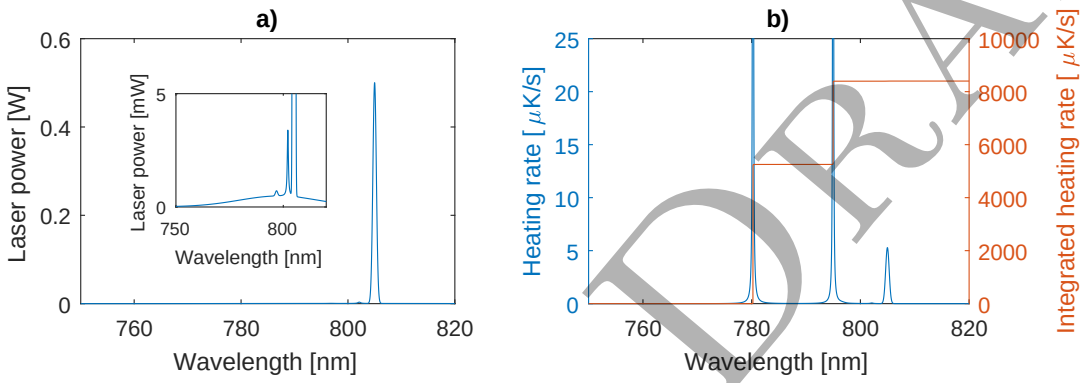

Figure 3.4.: Laser power dependent heating. a) shows a model spectrum, modelled after the measurements discussed in section 2.3.3. b) shows the corresponding heating rate for each wavelength (left y-axis) as well as the heating rate integrated up over all wavelength (right y-axis). Note that the left y-axis has been limited to values of 25 μK/s for the sake of clarity. Around the D1- and D2-transition, the heating rate diverges to much higher values.

The spectrum used for the calculations above was for a laser beam into which highpass filters suppressing light below 800 nm had already been inserted, as discussed in section 2.3.3. Applying the same procedure for the spectrum without filter (compare figure 2.21) gives an integrated heating rate of approximately 84 000 μK/s, which corresponds to a lifetime of about 3 ms for the same simulation settings as discussed above. This is a factor 10 less compared to the calculations above for the highpass filter. When comparing our experimentally determined lifetimes for measurements with and without the highpass filter (with cutoff at 800 nm), we similarly notice a lifetime increase from 50 ms to 500 ms for optimal experimental conditions. Even though the precise numbers do not match the theoretical calculation, possibly due to overestimating the integrated heating rate, the factor of 10 is the same as for the theoretical expectation. Therefore, we see that including the background spectrum or its most prominent contributions to the heating rate indeed has a large influence on the lifetime in the lattice and can at least qualitatively explain experimental observations.

Next, I would like to analyse the influence of the heating rate on the mean atomic temperature. Figure 3.5 a) shows experimental results for measuring the temperature of the trapped atoms as a function of the holding time in the optical lattice at the initial position. Here, we note that the temperature doesn't change with the holding time within

THESIS DRAFT

the experimental error bars. Figure 3.5 b) shows the theoretically expected temperature development for the same parameters, where the experimental value of about 82 μK is used as the starting temperature. On the left y-axis, the temperature increase is plotted for the case of a strictly single-wavelength trap at 805 nm. For a holding time of 200 ms, the temperature barely increases by one μK. However, if the heating rate at 795 nm is used (right y-axis), the temperature increases to more than 250 μK in the same time. Comparing the experimental observations with these predictions, at the first glance they seem to match the lower heating rate of a 805 nm single-frequency trap.

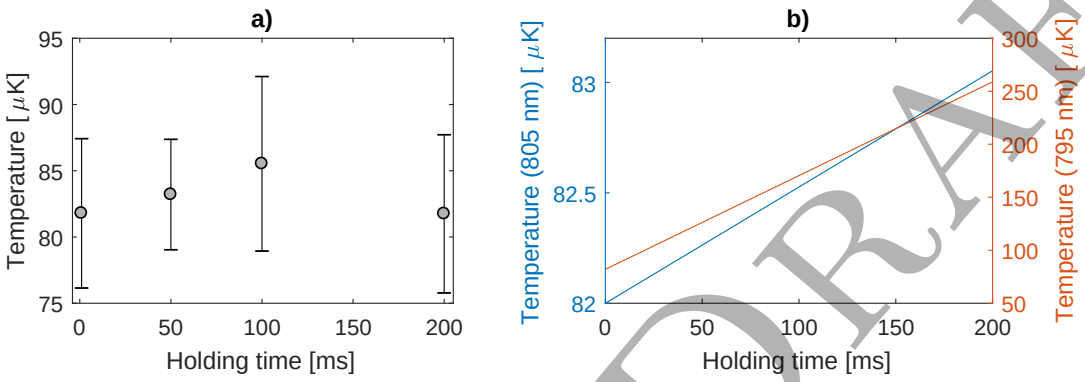

Figure 3.5.: Temperature increase due to heating rates for 805 and 795 nm. Plotted is the temperature as function of holding time in the dipole trap where the increase in temperature is due to the heating rate (cf. equation 3.5). The laser powers of 500 mW for 805 nm and $\approx$ 500 μW for 795 nm are taken from the experimental spectrum. b) Plotted is the temperature as function of holding time in the dipole trap measured experimentally. (Error bars indicate errors from the fitting procedure.)

However, while the experimentally determined atomic temperature stays constant, at the same time we measure a clear loss of atoms, as shown previously in the lifetime measurements (recall e.g. figure 3.3 c). Therefore, another reason for the constant temperature could be a constant re-equilibration of the atomic sample, as the hottest atoms with temperatures above about 350 μK are lost from the trap. In section 3.3.2, we will discuss in detail how the temperature of the atoms influences the distribution in the trap. In brief, when the mean temperature increases, also the number of atoms with higher temperatures and especially with temperatures above the trapping potential increases. When losing these hot atoms, the rest of the sample can re-equilibrate to the same mean temperature as previously. Thus, the heating process could be illustrated in the loss of the heated atoms, while the mean atomic temperature stays the same. This observation would be more in account with the high heating rate obtained by the background spectrum at 795 nm. A full calculation of this effect, however, is beyond the scope of the estimations presented here.

Finally, I would like to discuss how the heating due to scattering from the dipole trap depends on the position of the atoms. In our setup, as discussed in detail in section 2.3.2, one important point is the position-dependence of our trapping parameters. Therefore, also the heating rate strongly depends on the position of the atoms relative to the fiber tip.

Figure 3.6 shows the increasing scattering rates and heating rates for decreasing distance from the fiber tip for 805 nm and 795 nm. The laser powers of 500 mW for 805 nm and $\approx$

THESIS DRAFT

500 μW for 795 nm are taken from the experimental spectrum. As the trapping wavelength of 795 nm is much closer to the atomic resonance, both scattering rates and heating rates are almost two orders of magnitude larger than for a trapping wavelength of 805 nm, even though the laser power is four orders of magnitude smaller. All rates increase by about a factor of 10 from the initial MOT position to the fiber tip as the laser intensity increases. For the heating rates, maximum values at the fiber tip of 65 μK/s and 11 000 μK/s are reached considering the trapping wavelength of 805 nm and 795 nm, respectively.

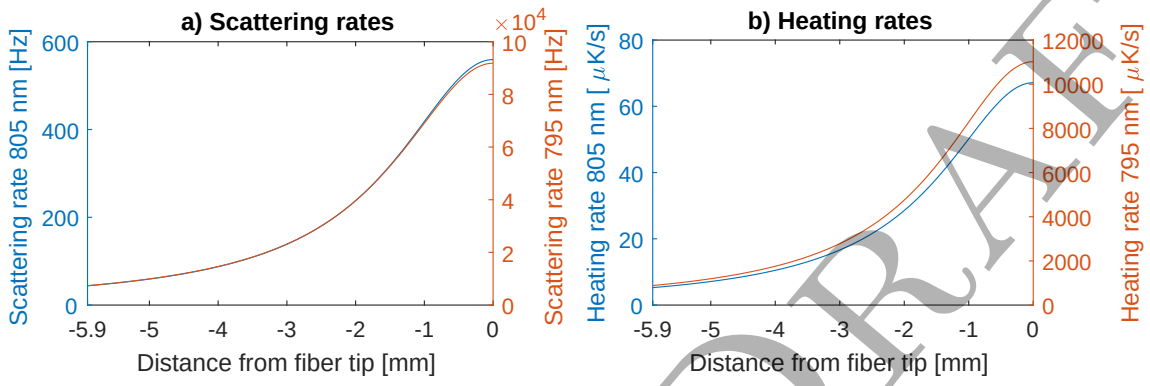

Figure 3.6.: Scattering and heating rates for 805 and 795 nm as function of position. a) Here, the scattering rates corresponding to two different wavelengths are plotted as function of distance from the fiber tip (cf. equation 2.3). The laser powers of 500 mW for 805 nm and $\approx$ 500 μW for 795 nm are taken from the experimental spectrum. b) Here, the heating rates (cf. equation 3.5) are plotted for the same parameters as in a).

Again, we can use the heating rate to estimate the lifetime of the atoms in the trap as discussed above for the initial position. Here, we have to take into account that the trap depth at the fiber tip is given by $U_{\mathrm{max}} \approx 4.7\,\mathrm{mK}$ and that the atomic temperature will also have increased to approximately 1 mK. The reason and magnitude of this temperature increase will be discussed in detail in the following section 3.3.2. Using these values, we find that at the fiber tip it would take the atoms $\approx$ 57 s to leave the trap for the 805 nm heating rate and $\approx$ 330 ms for the 795 nm heating rate. These values are approximately the same as the values at the initial position calculated and discussed previously. We find that the increased heating rate is couterbalanced by the also increased trapping potential. Considering this effect only, we would therefore not expect higher loss rates or shorter lifetimes closer towards the hollow-core fiber.

In this section, I have discussed how the scattering of photons of the trapping beams and the subsequent heating effects can contribute to the lifetime of atoms in an optical trap. In particular, I have shown how the background spectrum can influence this lifetime. Here, we find that an involved calculation is necessary to fully include the whole spectrum. However, already simplified estimations taking into account only the major contributions show that both scattering and heating rate are strongly modified. Qualitatively, we find good agreement with experimental measurements. A quantitative analysis is difficult, but likely a major contribution to the limited lifetime. Further, we find that this effect does not predict a position-dependent lifetime. In the following sections, I will further discuss different possible contributions to the limited lifetime of the atoms.

THESIS DRAFT

Heating due to collisions with background gas

Another reason for a limited lifetime of atoms in an optical or magnetical trap can be collisions with atoms or molecules from a background gas. These collisions will occur more frequently, the higher the background pressure. In the following, I would like to discuss how the lifetime can be influenced by the background pressure and give an estimate of the background pressure limit for our experimental parameters. For this discussion, I will mainly follow the approach from reference [78], which I have also used as my source for experimental values relating pressure and lifetime.

According to reference [78], the loss rate Γ of trapped atoms depends on the background pressure as

$$\Gamma = \Gamma_0 + b \times P, \tag{3.6}$$

where Γ_0 is a constant pressure-independent loss rate, P is the background pressure and b is the coefficient, which determines how much the background pressure influences the loss rate. Then, the lifetime τ is given by Γ^{-1}. For atoms trapped in a 1 K deep MOT, the value of the coefficient b has been experimentally determined as $\approx 5 \times 10^7\,\mathrm{Torr}^{-1}\mathrm{s}^{-1}$ [78]. For the following discussion, I need to modify this coefficient b according to our trapping parameters. As b depends on the trap depth U as $b \propto U^{-1/6}$ [78], this leads to $b \approx 1.55 \times 10^8\,\mathrm{Torr}^{-1}\mathrm{s}^{-1}$ for a 1 mK deep trap, which is the order of magnitude of our lattice depth. Note that in the following, I will refer to the pressure levels in mbar rather than in Torr as this is the unit used more commonly in our lab environment.

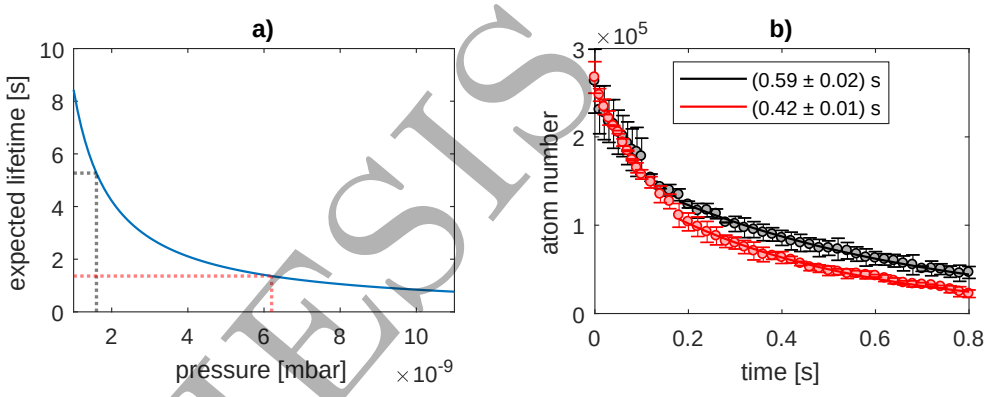

Figure 3.7.: Pressure-dependent lifetime. a) The blue solid line shows the theoretical expectation of how the lifetime should depend on the background pressure corresponding to equation 3.6 for our experimental parameters. The dotted lines mark the two pressure levels at which we have measured the lifetimes experimentally. Figure b) shows the experimentally determined atom number as function of the holding time, measured at the two different pressure levels, as well as an exponential fit to the data. The legend gives the lifetime determined from this exponential fit. (Markers: experimental data, solid line: exponential fit, error bars represent statistical errors.)

Figure 3.7 a) shows the theoretically expected lifetime of the trapped atoms as a function of the background pressure corresponding to equation 3.6 for our experimental parameters as discussed above. We see that by increasing the background pressure, the lifetime rapidly decays. For example, when increasing the background pressure from 1×10^{-9} mbar to

THESIS DRAFT

11×10^{-9} mbar, the lifetime is expected to drop from about 8 s to less than 1 s. This range of the background pressure represents possible values for our experimental setup. In the following, let me compare the theoretically expected and experimentally measured lifetimes at two different pressure levels.

The two different pressure levels are indicated by dotted lines in figure 3.7 a). They correspond to typical pressure levels before and after running the Ti:Sub pump connected to the main experimental chamber. After running the pump, the pressure measured at our pressure gauge drops from about 6.2×10^{-9} mbar to about 1.6×10^{-9} mbar by half an order of magnitude. Note that as the pressure gauge is located outside the main vacuum chamber next to the pumps, the pressure inside the chamber might possible be slightly higher. However, a drop of half an order of magnitude is expected to correspond to similar results inside the main experimental chamber.

From the theoretical calculations, we determine a lifetime of 1.3 s for the higher pressure level and of more than 5 s for the lower pressure level. Therefore, we expect to see an increase in lifetime of about a factor of 5 after running the Ti:Sub pump. Figure 3.7 b) shows the two corresponding experimental lifetime measurements, where the colors correspond to the pressure level indicators in figure a). For both measurements, we note an initially slightly steeper slope for data points up to about 200 ms. This might be due to inelastic two-particle collisions, which depend on the atomic density and not on the background pressure [cite??]. Since the atom numbers and thus atomic densities will be highest initially, this effect would occur at the beginning of the measurement. Therefore, only to the latter data points after 200 ms have been used for the exponential fit to determine the lifetimes for each pressure level. Note that this fitting method will results in longer lifetimes as compared to the method where all data points are taken into account as was used to determine the lifetime-corrected transport efficiency for figure 3.3.

From this fitting method, we determine lifetimes of about 400 ms and about 600 ms for the high pressure and low pressure level, respectively. Further we note that although they have not been included in the fit, the first few data points reveal a steeper slope at the higher pressure level. Both observations indicate an influence of the pressure level in the same way as expected, resulting in a lower lifetime for higher pressure. However, the difference between the two measurements is much smaller than the factor 5 we are expecting from the theoretical prediction. Indeed, it lies within the experimental range when repeating this measurement within a few days, even though the statistical error between individual runs as shown above is much smaller. Further, both lifetimes are much smaller than expected from the theoretical calculations. Thus, the background pressure is very likely not the limiting effect for our lifetimes.

Therefore, we conclude that although we cannot completely neglect the influence of the background pressure, it does not seem to be the limiting point in our case. This holds especially true as all our lifetimes are much smaller than expected for our typical pressure range. Even a pressure as high as 1×10^{-8} mbar should still correspond to a lifetime of more than $\tau = 800$ ms. This may be in the same order of magnitude as our experimentally observed lifetimes, but even if we systematically underestimated our pressure levels, we don't seem to be limited by the pressure-induced lifetime.

THESIS DRAFT

Outside the hollow-core fiber, there is no position-dependence of the background pressure. Therefore, we also don't expect a position-dependent lifetime. However, the pressure-dependence of the lifetime can in principle be used for estimating the pressure level inside the hollow-core fiber, as demonstrated e.g. by Okaba et al. [14]. Here, the lifetime of their Strontium atoms is measured after they have been transported towards different positions outside or inside the fiber. They observe a decrease in lifetime from about 500 ms to about 350 ms and from these values extract pressure levels of about 1×10^{-8} mbar and 1.7×10^{-8} mbar outside and inside their hollow-core fiber, respectively [14]. In principle, also in our case the lifetime inside the fiber could be limited by this effect. We experimentally determine a lifetime of 200 ms inside compared to about 500 ms outside the hollow-core fiber for optimal conditions [13]. However, this again is much smaller than expected for a typical pressure range, especially since our fiber has been inside our vacuum chamber for years before this measurement. Thus, we expect that same as outside the fiber the lifetime inside the fiber is more strongly limited by other effects and cannot directly be used as a pressure reference.

Heating due to position-dependent amplitude or phase noise

In other long-distance transport experiments with cold atoms, it has been shown that amplitude and phase noise on the laser beams creating the optical conveyor belt can severely limit the transport efficiency [e.g. 22]. "Phase jumps of 60◦ typically induce a 50 % loss of atoms. For continuous phase jitter (see Figure 7(b)) the sensitivity is much larger." Here, a few degrees of mean phase jitter can already reduce the atom number by 50 %. For example, ... numbers ... (also, example Kuhr and Alt 2003) Since we are currently not employing phase or amplitude stabilization of the lattice laser beams, we also expect to see effects of amplitude and phase noise in our setup. These could then also be major limitations of both transport efficiency and lifetime of the trapped atoms. This especially holds true in combination with the multi-frequency trap as discussed above, where in principle the noise components could be different for the different frequencies present in the trapping light.

A full study of the effects of amplitude and phase noise on the transport effiency and the lifetime of the atoms in the optical lattice is currently still ongoing and beyond the scope of this thesis. However, let me briefly give a qualitative discussion of the expected effects from either phase or amplitude noise. As is well known, any phase noise on the lattice laser beams leads to a shaking of the optical lattice [cite Spinor?]. If this happens uncontrollably, this typically leads to a heating of the trapped atoms. This heating may then result in a loss of atoms from the trap and therefore a reduced lifetime and also a reduced transport efficiency. (compare Bonn theses e.g. Alt 2003, cite Christian's thesis for phase noise introduced in the light pass?) (cite Hamburg theses for phase lock)

Introducing amplitude noise on either of the lattice laser beams will lead to a modulation of the trap depth. This will then also lead to a heating of the atoms? Look up Amplitude modulation of optical lattice! -> can excite atoms to higher energy bands of lattice! Amplitude modulation spectroscopy [cite BFM, thesis Basti?], e.g. Pichler 2018, Technical noise / amplitude noise on lattice beam (Savard). Especially important for multi-frequency trap? thesis Christoph Becker for amplitude and phase noise lattice!

THESIS DRAFT

Mention that we use the AOMs to set the intensity. In principle, setup with photodiodes to measure and feedback the real intensity available as used for calibration, but currently no feedback loop implemented. We have seen some (especially long term) intensity drifts of up to 10 % and also short term intensity fluctuations, especially if TAs are not well-coupled.

A third effect could be parametric heating (cite Hannes), where frequencies multiple of the trapping frequency are present in the system. This is also possible for our laser beams. (same as phase noise given above?)

For the effects described above, we do expect a position-dependence. As the overall intensity of our laser beams increases towards the fiber tip, we can expect that especially amplitude noise will also be amplified accordingly. "In our experiment, the intensity of the laser beams increases towards the fiber tip, which can lead to position-dependent amplitude and phase noise as well as a position-dependent lifetime. Further investigations beyond the scope of this paper will study these different loss mechanisms in detail." [72] Heating due to position-dependent phase / amplitude noise on dipole trap may limit the lifetime.

Discussion of heating effects

In the previous sections, I have introduced three main effects which can lead to heating of atoms in an optical lattice and may therefore be responsible for the limited lifetime of the trapped atoms, namely scattering of photons of the lattice beams, collisions with background atoms and amplitude and phase noise in the lattice beams. We have seen that for our experimental parameters, collisions with the background gas is very likely not a limiting factor in our setup. However, the initial steep decay of the lifetime curve might point to density related losses as discussed in this section. This effect might be interesting to further study in the future. Further, we have seen that scattering of lattice photons is likely the most relevant heating mechanism in our case, especially due to the multi-frequency nature of our lattice and the broad background. A solution for this would be to further detune the trapping wavelength. This has not yet been implemented for the measurements presented in this thesis, but is currently being investigated.

In addition, we have seen that amplitude and especially phase noise is often a limit for transport experiments and is therefore very likely also a limit in our case. In particular, as the intensity of the lattice laser beams increases towards the fiber tip, position-dependent amplitude and phase noise can occur in our setup. This would then lead to a position-dependent lifetime. To obtain the lifetime-corrected transport efficiencies as discussed above, it would thus be necessary to divide by the correct position-dependent lifetime. Therefore, our previous correction was just a zero-order approach. This might explain why even our corrected transport efficiencies were limited by about 70%, while in other experiments transport efficiencies close to 100% could be obtained [22], Schrader?.

3.2.2. Adiabaticity of the transport (high detunings)

In the previous section, I have discussed that the limited lifetime of the atoms in the optical lattice is one of the major limits for the transport efficiency achievable in our setup. I have

THESIS DRAFT

also shown how these lifetime effects can be minimized by chosing fast ramps. However, in our setup fast ramps can only be realized by choosing high final frequency detunings. Here, we encounter different problems, which I will discuss in this section. In particular, I will discuss whether our transport can still be considered adiabatic for these fast ramps.

Firstly, we experience a loss of coupling efficiency into the fibers and thus a lower trapping power when choosing higher detunings. This effect can be compensated for as discussed in the earlier technical section.

Secondly and more importantly, for fast ramps we observe a "tail" of atoms apparently lost behind in the transport process. Two example absorption images are shown in figure 3.8. In the upper image, the atoms have been transported to their position in front of the fiber tip with the fast 1000 kHz constant ramp within 10 ms as discussed previously. In addition to the atoms which have reached the correct final position, a long tail of atoms along the whole transport path can be seen in this case. These atoms appear to have been lost during the transport process. As a contrast, the lower images shows atoms which have been transported to the position in front of the fiber tip with the slow 200 kHz linear ramp within 200 ms. Here, a similar atom tail is not visible by bare eye and indeed by further analysis turns out to be negligible.

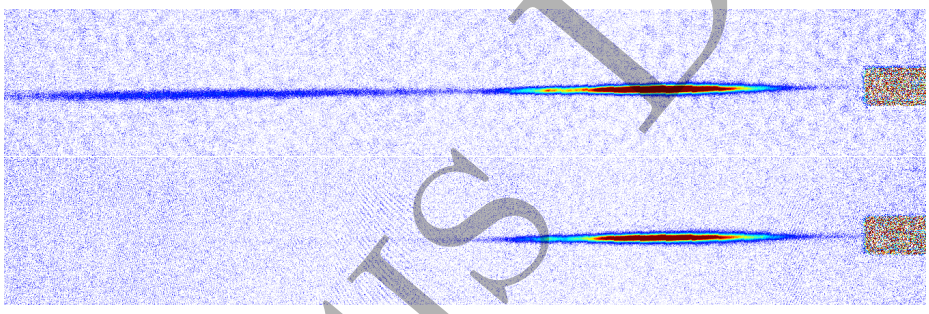

Figure 3.8.: Atom tail. Example absorption images of atoms transported to the fiber tip with a 1000 kHz constant frequency ramp (upper image) and a 200 kHz linear frequency ramp (lower image). In the upper image, a strong atomic tail is visible in addition to the atoms transported to the correct final position. Note that the colour scaling has been chosen to optimize the visibility of the tail in these figures. As a result, the particle number difference between the two ramps is not well visible here.

From these two examples, it already becomes apparent that the atomic tail is the more prominent, the higher the final transport detuning. This loss of atoms along the transport path then puts a limit on the maximum final detunings and thus the shortest possible transport times. This observation is in contrast to the previous observations regarding the lifetime-limited transport, where it seemed that the shorter the transport time, the better our efficiency. However, when also taking the atomic tail into account, these negative effects of high detunings can overtake the benefits of a shorter transport time. Figure 3.22 illustrates this behaviour. Here, the transport efficiency with and without taking the atomic tail into account is shown for three different constant frequency ramps with maximum detunings of 1000 kHz, 1250 kHz and 1500 kHz, respectively. We see that the transport efficiency with tail slightly increases for the 1250 kHz ramp, then stagnates with higher maximum detuning. However, when looking at the transport efficiencies without tail,

THESIS DRAFT

they not only stay constant, but even decrease towards higher detunings. This indicates that although more atoms are transported in total, a large part of these atoms is staying behind in the atomic tail. Additional details about the number of atoms in the atomic tail with respect to the ramp shape and maximum final detuning can be found in the master thesis of Ronja Wirtz [75]. In general, we find that a plateau of the transport efficiency is reached at a maximum detuning of about 1000 kHz and therefore do not employ ramps with much higher final detunings. Of course, we therefore have to be careful when determining our transport efficiencies and not take the tail into account. The transport efficiencies discussed in the previous sections were already calculated in the correct way.

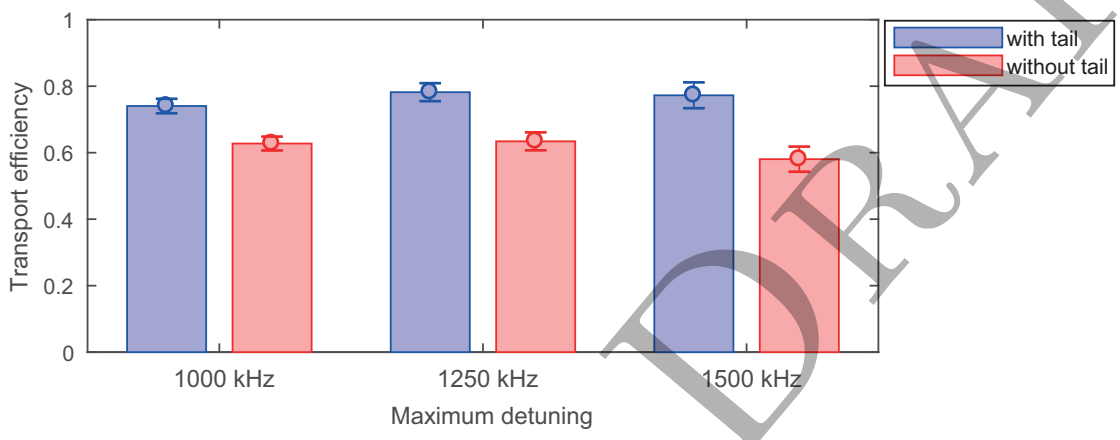

Figure 3.9.: Influence of the atomic tail for high frequency detunings. Shown are the transport efficiencies with and without taking the atomic tail into account for three different constant frequency ramps with high maximum detunings.

Further, we have seen that the number of atoms in the tails strongly depends on the overlap between MOT and initial lattice position. Very likely this is an effect of the initial temperature of the atoms, where a lower temperature leads to less loss of atoms in the tail. Preliminary measurements beyond the scope of this thesis have shown that the tail can indeed be minimized with better overlap, leading to a lower initial temperature. In this optimized case, the efficiencies for the three ramps discussed in figure 3.22 are almost the same, with or without tail. To avoid additional effects of high detunings, we therefore opt to choose the lowest possible detuning for which lifetime-effects can be reduced, which in our case is a detuning about 1000 kHz.

We have just seen that for fast ramps not all atoms are transported to the final position, but that some atoms are lost along the way, forming an atomic tail. One possible reason for the occurence of this tail is that our transport may not be adiabatic in the case of fast ramps. Therefore, in the following paragraphs I would like to discuss a criterium for the adiabaticity of the transport and whether we can consider it to be fulfilled for our different transport ramps.

First, let me very briefly revise the concept of adiabaticity, which I will employ in the following. In thermodynamics, the term adiabaticity is commonly used to describe processes where no heat is exchanged [e.g. 80]. These are typically very fast processes. In quantum

THESIS DRAFT

mechanics, however, a process is called adiabatic if the internal state of the system does not change [**?**]. This typically occurs if the process happens very slowly, in contrast to the thermodynamical use of the term adiabaticity. This second definition of slow adiabtic processes is the one which I will employ in the following discussion. More specifically, a process is considered adiabatic if it is reversible and if the shape of the occupation distribution of the energy levels does not change [**?**]. In our case, this would mean that all atoms stay in their potential well of the lattice and also stay in the same energy level, so that the occupation distribution of the energy levels does not change while the energy of this energy level itself might change. In this chapter, I will focus on the adiabaticity criterium for atoms staying inside their potential well during the transport process. A criterion for atoms staying on their energy levels will be discussed in a later chapter.

The adiabaticity criterion to be discussed now concerns the maximum allowed acceleration, for which the atoms still stay inside their potential well and are simply dragged along with the moving lattice. This is strongly connected to the observed atomic tail, as this tail might be formed by atoms which have left their potential well and are not dragged along with the lattice. In the following paragraphs, explanation and calculation of this adiabaticity criterion will closely follow reference [79].

Atoms in a lattice accelerating with maximally $a_{\max}$ experience a backdriving force due to inertia of $F_{\text{in}} = ma_{\max}$. Assuming that the atoms were initially trapped at the position of the potential minimum, they are by this moved backwards to a position z. There the lattice potential is given by $U_{\text{latt}} \cos^2(k_L z)$, thus the axially confining force is given by $F_z = U_{\text{latt}} k_L \sin(2k_L z)$. Therefore, the maximum confining force is given by $F_{z,\max} = |U_{\text{latt}}| k_L$. Equating the two forces gives an acceleration limit of [79]

$$a_{\max} = \frac{|U_{\text{latt}}| k_L}{m}, \tag{3.7}$$

for which the atoms still stay in their respective potential well.

In our case, at the initial MOT position, the initial trap depth U_0 leads to a maximally allowed acceleration of $a_{\max}(U_0) \approx 2.8 \times 10^5\,\text{m/s}^2$. At the fiber tip, the trap depth $U_{\max}$ is more than ten times deeper, therefore allowing even higher accelerations of up to $a_{\max}(U_{\max}) \approx 3.6 \times 10^6\,\text{m/s}^2$. Let us now compare these theoretically calculated accelerations with accelerations typically reached by our transport ramps. Table 3.1 shows acceleration values for some of our most frequently used frequency ramps, as discussed previously. Clearly, the acceleration values for all ramps lie well below the maximum numbers calculated above. Even the fastest ramps with 1500 kHz maximum detuning only reaches a maximum acceleration of about $600\,\text{m/s}^2$, which is almost 500 times lower than $a_{\max}(U_0)$ and 6000 times lower than $a_{\max}(U_{\max})$. This comparison would indicate that according to this adiabaticity criterion, our transport happens adiabatically.

However, the observed atomic tail as shown and discussed above clearly indicates that some atoms have left their potential well and are left behind during the transport process. To explain this, we have to consider that the derivaton of equation 3.7 has been made using several simplifying assumptions. A full calculation of the correction factors is beyond the

THESIS DRAFT

Frequency ramp	(Max.) Velocity	(Max.) Acceleration	Deceleration
1500 kHz constant	0.6 m/s	600 m/s^2	600 m/s^2
1000 kHz constant	0.4 m/s	400 m/s^2	400 m/s^2
1000 kHz linear	0.4 m/s	20 m/s^2	400 m/s^2
200 kHz linear	0.08 m/s	0.8 m/s^2	80 m/s^2

Table 3.1.: Values for velocity and acceleration for different frequency ramps, calculated according to equation XX. For the linear frequency ramps, the velocity is constant and the maximum acceleration during the transport process is given. For the constant frequency ramps, the acceleration is constant and the maximum velocity during the transport process is given.

scope of this thesis, but let me qualitatively estimate the effects of two of the most important simplifications in the following paragraphs.

The first major assumption is that all atoms occupy the ground state of the trapping potential. This assumption is not fulfilled in our case, as due to the thermal distribution also higher energy levels of the potential well will be occupied. The exact shape of this occupation distribution will be discussed in the following chapters. This occupation of the higher energy levels will reduce the potential depth experienced by the atoms and therefore reduce the maximally confining force. For example, if at the MOT position with $U_0 \approx 400\,\mu$K, the mean atomic temperature is $T = 100\,\mu$K, the mean trapping potential experienced by the atoms would be given by $|U_{\mathrm{latt}}| = U_0 - T \approx 300\,\mu$K. This is only about 3/4 of the maximum trapping potential, therefore also the maximally confining force and thus the maximally allowed acceleration would be reduced to 3/4 of the values calculated above. However, even then the maximally allowed acceleration would still be $a_{\max}(U_0 - T) \approx 2.1 \times 10^5\,\mathrm{m/s^2}$. Therefore, this effect alone cannot explain the discrepancy of a few orders of magnitude as discussed above.

The second assumption is that the atoms initially stay at the position of the potential minimum $z = 0$. However, for a thermal distribution of atoms, this is not the case. Here, the size of the cloud in radial direction is given by $r_0^2 = w^2 k_{\mathrm{B}} T/(2|U_{\mathrm{latt}}|)$ (see equation XX). In our case, at the initial MOT position with an atomic temperature of $T \approx 100\,\mu$K, a lattice depth of $|U_{\mathrm{latt}}| = U_0 \approx 400\,\mu$K and a beam waist of $w \approx 73\,\mu$m, this leads to a cloud size of $r_0 \approx 26\,\mu$m in the radial direction. In the axial direction, the site of the cloud is given by $r_a^2 = 2k_{\mathrm{B}}T/(|U_{\mathrm{latt}}|k_L^2)$ (cite?), if approximating each lattice potential well as a harmonic potential. For our typical experimental values, this gives an axial cloud radius at the MOT position of approximately 90 nm within each potential well.

This spread of the atomic cloud inside the potential wells changes the maximally allowed acceleration, as atoms located towards the outsides of the potential well need less displacement and thus less acceleration to be spilled into the next lattice well. Let me estimate this effect by considering the spread of the confining force in the radial direction. Atoms initially trapped at $z = 0$ experience the maximally confining force $F_{z,\max}$ at a position of $\sin(2k_L z) = 1 \Leftrightarrow (2k_L z) = \pi/2$. However, atoms initially located at r_a, i.e. at the outer edge of the density distribution, at the same time experience only $\sin(\pi/2 - 2k_L r_a) \approx 15\%$ of $F_{z,\max}$. Therefore, these atoms will already be lost at 15% of the maximally allowed

THESIS DRAFT

acceleration. For our experimental values this is given by $a_{\max}(r_a) \approx 4.4 \times 10^4\,\mathrm{m/s^2}$. Note that this value is still two orders of magnitude above our typical experimental accelerations given in table 3.1. However, for the simplified estimation above, I have only taken into account the spread of the atomic cloud in axial direction. For a full calculation, the spread in radial direction also needs to be included. This will further reduce the confining force experienced by the atoms located at the outer edges of the potential well and therefore the maximally allowed acceleration, likely by another order of magnitude.

A combination of these effects could bring the acceleration closer to our experimental values. However, from these estimations it is not clear whether this is the loss mechanism. However, since we see an effect of reducing the atomic temperature, a connection to the thermal distribution of the atoms in very likely.

3.2.3. Influence of different ramp shapes during transport

In the previous sections, I have discussed the influence of lifetime effects on slow ramps and the question of adiabaticity for fast ramps and how both affect the number of transported atoms. To round off this chapter about the influence of the different frequency ramps on the transport efficiency, I would now like to discuss the influence of different acceleration and deceleration ramp shapes. (linear, constant, exponential, s-ramp, ... -> compare also results from Florian), what do we expect from different ramps? (e.g. s-ramps for more adiabatic transport). In the following, I will mainly concentrate on linear and constant ramps, which we have found to be most promising.

Some of those figures in appendix, only one for discussion?

The longer the atoms spend close to the fiber tip / in deep potential, the worse the transport efficiency. Thus faster ramps and linear ramps where most of the time is spent close to the initial position. Exponential ramps could be really good! This seems to hint at an additional position-dependent loss effect!

Figure for loss of atoms during transport (x-axis: transport time or position) for different linear and constant ramps, maybe also s-ramp from Florian's thesis (possible data: 5.2.2018 + 1.2.2018 (200 kHz ramp, different shapes), s-ramp 9.1.2018, 15.8.2017 (100, 200, 400 kHz linear ramps), 4.4.2018 (1000 kHz ramp) + data from Florian (12.2016)

Frequency for s-ramp (cite Florian):

$$\nu_s(t) = \nu_0 + \frac{\nu_1 - \nu_0}{1 + \exp\left(-\frac{K_s}{\Delta t} \cdot (t - \frac{\Delta t}{2})\right)} \tag{3.8}$$

Discuss which ramps we will be using. Discuss effect of slowing down (not much seen, but atoms don't move anymore). Discuss ramp shapes. Compare to other transport experiments who see a transport of almost 100 %!.

Up to now, we have discussed the effects of chosing different frequency ramps. In the following, we will study the effect of changing the trapping potential with so called amplitude ramps.

THESIS DRAFT

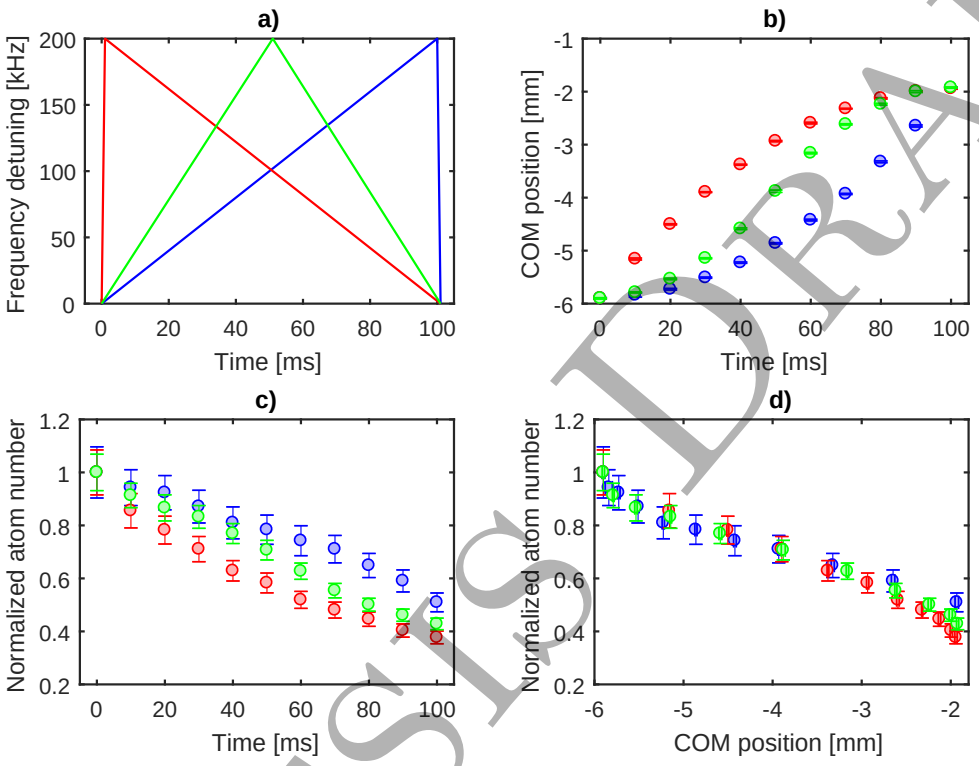

Figure 3.10.: Comparison of different linear acceleration and deceleration ramp shapes. Figure a) shows three different linear acceleration and deceleration ramps with the same maximum detuning of $200\,\mathrm{kHz}$ and the same total ramp time of $101\,\mathrm{ms}$. The center of mass position of the atomic cloud for these three different ramps is shown in figure b). Figure c) and d) show the normalized number of atoms during the transport process as a function of the transport time and the center of mass position of the atomic cloud, respectively. (Error bars represent statistical errors and errors from the fitting procedure.)

THESIS DRAFT

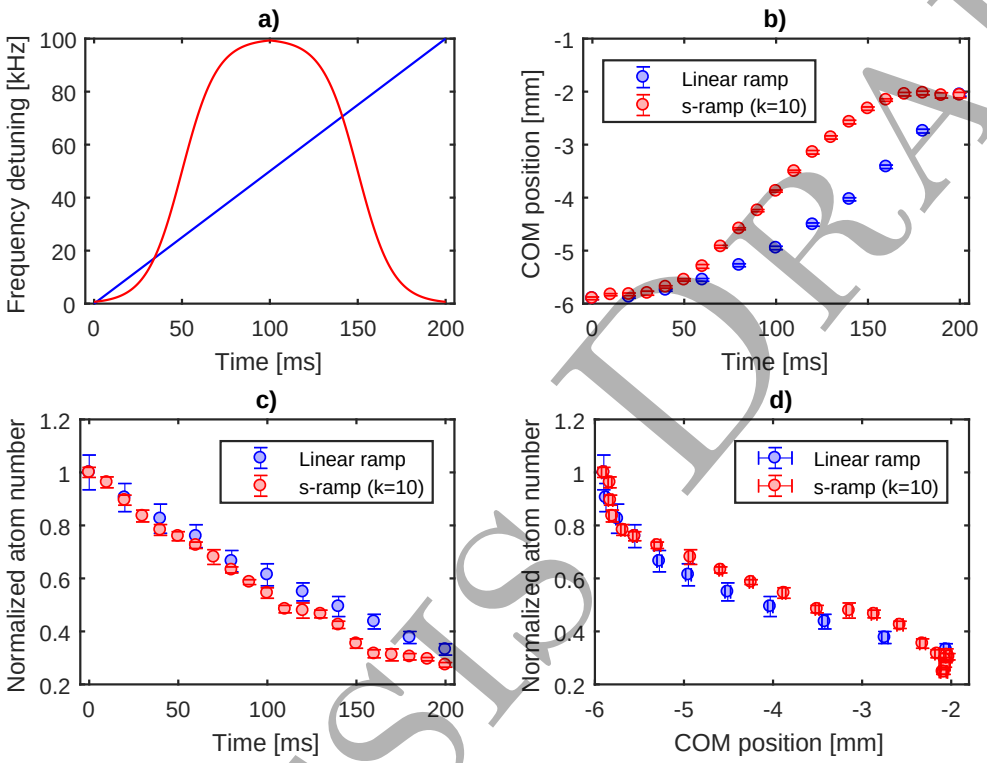

Figure 3.11.: Comparison of linear ramp and s-ramp. Figure a) shows a linear frequency ramp as well as an s-ramp (according to equation 3.8) with the same maximum detuning of $100\,\mathrm{kHz}$ and the same total ramp time of $200\,\mathrm{ms}$. The center of mass position of the atomic cloud for these two different ramps is shown in figure b). Figure c) and d) show the normalized number of atoms during the transport process as a function of the transport time and the center of mass position of the atomic cloud, respectively. (Error bars represent statistical errors and errors from the fitting procedure.)

THESIS DRAFT

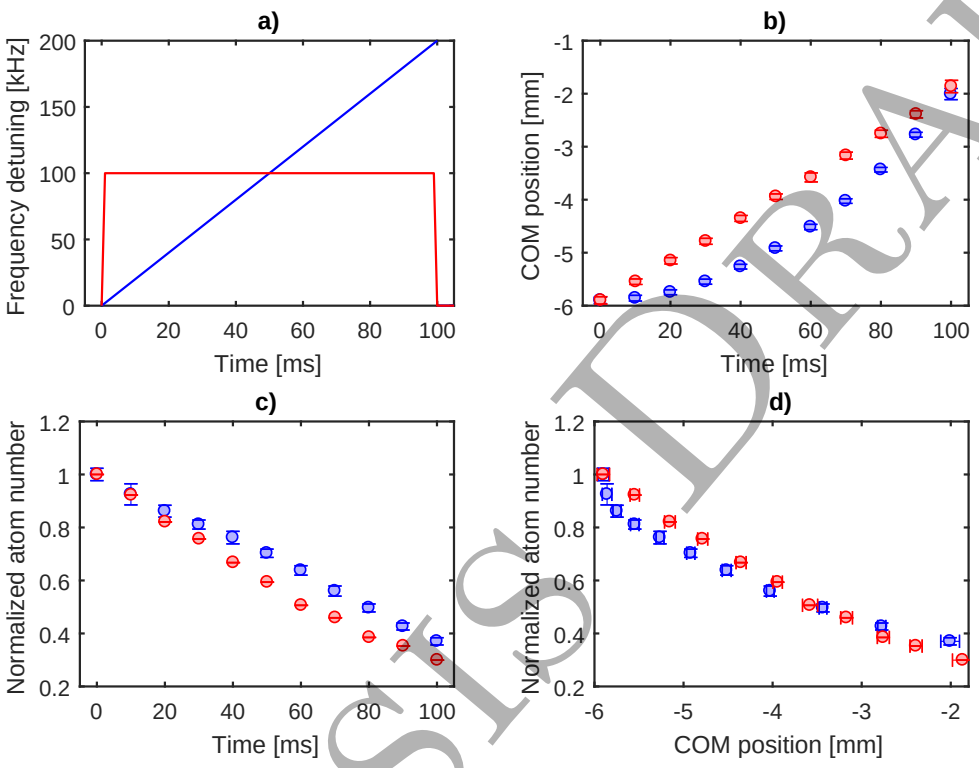

Figure 3.12.: Comparison of linear ramp and constant ramp. XX: Possibly continuously constant detuning w/o ramp up! Figure a) shows a linear frequency ramp as well as an s-ramp (according to equation 3.8) with the same maximum detuning of $100\,\mathrm{kHz}$ and the same total ramp time of $200\,\mathrm{ms}$. The center of mass position of the atomic cloud for these two different ramps is shown in figure b). Figure c) and d) show the normalized number of atoms during the transport process as a function of the transport time and the center of mass position of the atomic cloud, respectively. (Error bars represent statistical errors and errors from the fitting procedure.)

THESIS DRAFT

3.3. Effect of the trapping potential on the atomic temperature

Here, we will learn how the depth of the trapping potential influences the temperature of the trapped and transported atoms. In particular, we will discuss how to adapt the potential depth.

In the previous section, I have discussed how the parameters of the applied frequency ramp influence the number of transported atoms. In this section, I will discuss the effects of changing the trapping potential. Already during the discussion of figure 3.2 we have seen that the final temperature of the transported atoms depends strongly on the trap depth, as both increase towards the fiber tip for all frequency ramps. Therefore, in order to control the final atomic temperature, we have to adapt the potential depth. In the following section, I will first briefly introduce how we can adapt our trapping potential according to the position of the atoms different called amplitude ramps (section 3.3.1). Then, I will explain how the temperature of the transported atoms is influenced by the trapping potential and what to take into account when calculating the atomic temperature for lowering the trap depth (section 3.3.2).

3.3.1. Adapting the potential depth

I have already discussed in earlier chapters how the depth of the lattice potential increases towards the tip of the hollow-core fiber (see for example section 2.3.2). This is due to the focussing of the trapping beams into the fiber and can be described by the Gaussian beam propagation of the lattice beams. However, for many experiments we would like this change of potential depth to happen controllably. This can for example help to reduce the final atomic temperature. Therefore, we additionally control the potential depth by changing the power P of the lattice beams using acousto-optical modulators as discussed in the setup of the lattice laser system in section 2.3.3.

"In addition to this overall change in the dipole trap powers, we further can include individual corrections for each of the two dipole trap beam powers, e.g. to compensate for fiber coupling losses at high frequency detunings or for different initial power levels of the two dipole trap beams." -> discussed in detail in Ronja's thesis (or put in setup: program part!)

For this power ramp-down of the trapping beams, which will in the following be referred to as amplitude ramps, we set two conditions. First, the potential including the amplitude ramps should be modelled after the natural potential change in such a way that the overall shape of the potential is maintained. Further, we need to adapt the potential depth according to the position of the atoms. As we have seen in detail in section 3.1, this position can be calculated given the time of transport for each frequency ramp (cf. e.g. 3.3). Therefore, the time-dependence of the amplitude ramps should match this transport time. In collaboration with Fabian Knoch, we have developed a shape for the amplitude ramps which fulfills these

THESIS DRAFT

two criteria. A full derivation of the shape starting from the trapping powers can be found in [75].

Formula how $P(t)$ changes with amplitude ramp-down (see Ronja's thesis).

Eventually, our full time-dependent potential including the amplitude ramp-down of the lattice beams then has the form

$$U_{\mathrm{latt}}(z,t) = nU_0 \left(1 + A\left(\frac{z(\gamma t)}{z_R}\right)^2\right)\left(1 + \left(\frac{z(t)}{z_R}\right)^2\right)^{-1}, \tag{3.9}$$

where

$$A = \frac{z_\mu^2 + (1-n)z_R^2}{nz_\mu^2} \tag{3.10}$$

is used as a correction factor to maintain the overall shape of the potential. We have two parameters to control the amplitude ramps, n and γ. The parameter n controls the final potential depth at the fiber tip as $U_{\mathrm{max}} = nU_0$. The parameter γ is a delay factor, which can for example be used to address atoms that are not located in the center of the cloud.

Figure 3.13 illustrates the different amplitude ramps. Here, the resulting potential depth is shown in figure a), while the applied laser power ramp-down is shown in figure b). When the laser power is kept constant and no amplitude ramp is applied (solid lines), the potential changes according to the natural Gaussian beam propagation as discussed earlier. This corresponds to a maximum $n \approx 12.5$ and $\gamma = 1$, where the maximum value of n is given by U_{max}/U_0. We can also keep the trap depth constant for the duration of the entire frequency ramp and thus for all distances from the fiber tip (dashed line). This corresponds to the case of $n = 1$ and $\gamma = 1$. Note that in order to achieve a constant potential depth, we have to reduce the trapping laser power in an amplitude ramp according to equation XX, as shown in figure b). When choosing $n > 1$, higher final trap depths will be reached and accordingly the laser power will be reduced less.

When choosing a γ parameter $\neq 1$, the amplitude ramp will happen with delay with regards to the atomic COM position $z(t)$. The idea of using a delayed ramp is to adress atoms which are not located at the COM position of the atomic cloud. Let me explain this using figure 3.13 b) for the example of a $n = 1$ amplitude ramp. Atoms at the COM position of the atomic cloud will at all times experience the correct trapping potential given by the correct reduced trapping laser power, as indicated by the dashed line. For example, at $z(t) \approx -4.5\,\mathrm{mm}$, they experience a reduced laser power of about 60%, which leads to the correct constant trapping potential. However, for atoms which lag for example about 1 mm behind the COM position of the atomic cloud, this is no longer the case. When they have reached the same position $z(\gamma t) \approx -4.5\,\mathrm{mm}$, the laser power will already have been reduced to less than 40% according to atoms located at the COM position $z(t) \approx -3.5\,\mathrm{mm}$. Therefore, the atoms lagging behind will experience a too low trapping potential. To avoid this, the delay factor γ can be chosen accordingly so that the atoms lagging behind will experience the correct trapping potential at their position $z(\gamma t)$, as indicated by the dotted line. The potential depth resulting from this examplary amplitude ramp with $n = 1$ and $\gamma = 0.7$ is shown in figure 3.13 a) (dotted line). Note that in this figure the atoms at the

THESIS DRAFT

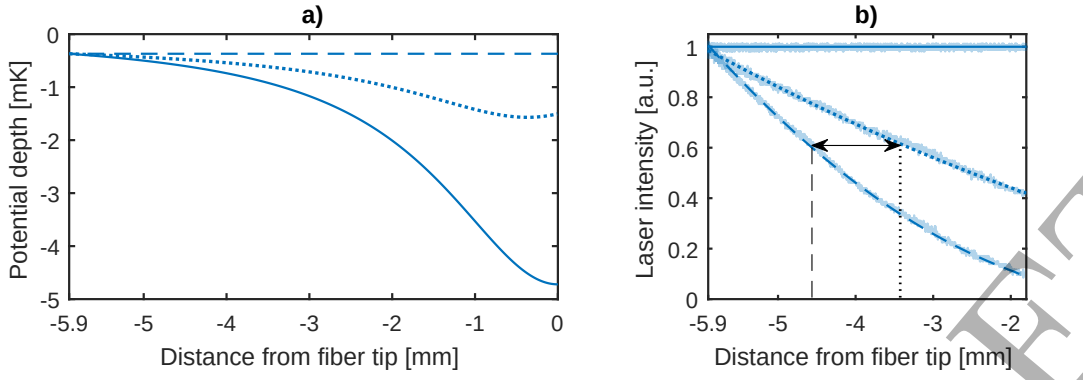

Figure 3.13.: Adapting potential depth and laser intensity. a) Potential depth (cf. equation 3.9) as function of distance from fiber tip for the case without laser intensity ramp down (solid line) and for the case of laser intensity ramp down with $n = 1, \gamma = 1$ (dashed line) and $n = 1, \gamma = 0.7$ (dotted line). b) Laser intensity as function of distance from fiber tip for the case without laser intensity ramp down (solid line) and for the case of laser intensity ramp down with$n = 1, \gamma = 1$ (cf. equation XX, dashed line) and $n = 1, \gamma = 0.7$ (dotted line). The light-blue background indicates the corresponding experimental data. (Figure partially adapted from our publication [72].)

COM position are used a a reference for the conversion $z(t)$ between transport time and position. Therefore, in this conversion the γ amplitude ramp might look slightly distorted. However, in the reference frame for the atoms lagging behind, the delayed potential will maintain its shape as per our condition. Also, the final trap depth of $U_{\max} = 1 \times U_0$ will be be reached once $z(\gamma t) = 0$ as the last atoms enter the fiber.

In the remaining part of this chapter, I will focus on n amplitude ramps, where $\gamma = 1$ is kept constant. A full discussion of examplatory results for γ ramps can be found in the master thesis of Ronja Wirtz [75]. Briefly speaking, we find that for measurements outside the fiber we obtain qualitatively similar results for both types of amplitude ramps, as the results mainly depend on the trapping potential at the final atomic position. However, we expect that for atoms transported inside the fiber, the difference between the two types of amplitude ramps might become more prominent. Although they both lead to the same final trap depth, here the exact form of the potential change might influence the loading efficiency inside the fiber. While during the course of this thesis conclusive measurements with γ amplitude ramps inside the fiber have not yet been performed, this will be an interesting direction of future studies and I will come back to amplitude ramps changing both n and γ in the outlook of this chapter.

As a final note, I would like to consider whether the potential has to be adapted in a different way depending on whether we want to keep the trap depth U_{latt} or the scattering rate Γ_{latt} constant. Recalling equation XX, the main difference between these two quantities lies in their different dependence on the trapping laser detuning Δ. In principle, we change Δ during the transport ramp as the laser frequency increases by $\Delta\nu(t)$. However, this change of $\approx 1\,\text{MHz}$ is small compared to the initial detuning of $\Delta > 10nm$. Therefore, we consider Δ not to change significantly during the transport process. Then, the scaling of both trap depth and scattering rate is only given by the light intensity I and consequently the laser

THESIS DRAFT

power P. Therefore, when adapting the laser power with an amplitude ramp as discussed above, both trap depth and scattering rate should scale in the same way.

Now that I have shown in which way we can manipulate and control the depth of our lattice potential, I will in the following discuss how these amplitude ramps influence the temperature of the transported atoms.

3.3.2. Temperature of atoms trapped in an harmonic oscillator potential

In the following section, I will discuss how the temperature of atoms trapped in an harmonic oscillator potential can be described and influences the occupation of the energy levels. In particular, I will discuss what happens to the temperature of the atoms when they have been transported towards or into the fiber for the case with or without an amplitude ramp as described above.

In section 2.3.1, we have seen that the trapping potential of an optical lattice in the radial direction can be approximated as an harmonic oscillator. In our case of the laser intensity and thus the trap depth varying with distance z, equation 2.6 is modified to

$$U(\mathbf{r}) = U(z,r) \approx \frac{1}{2}m\omega_r^2(z)r^2 = \frac{1}{2}m\omega_r^2(z)\left(x^2+y^2\right), \tag{3.11}$$

where $\omega_r(z) = \left(4U_{\mathrm{latt}}(z)/(mw(z)^2)\right)^{1/2}$ is the radial trapping frequency. In our case, $\omega_r(z)$ has a two-fold dependence on the axial position z, as it depends on both the trap depth $U_{\mathrm{latt}}(z)$ and on the beam waist $w(z)$. Therefore, even if keeping the trap depth constant, the trapping frequency will increase for atoms transported closer to the fiber tip, as the beam waist of the dipole trap beams decreases.

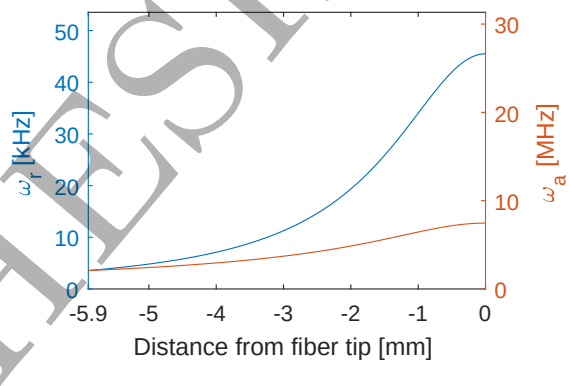

Figure 3.14.: Trapping frequencies as function of distance from the fiber tip. Shown are the trapping frequencies in radial (left y-axis) and axial direction (right y-axis). Note that the scaling of the y-axes has been chosen in identical proportion to the initial trapping frequency at the farthest distance to highlight the differences in increase of the trapping frequencies.

Figure 3.14 shows ω_r as function of the distance from the fiber tip. As it depends both on the trap depth $U_{\mathrm{latt}}(z)$ and on the beam waist $w(z)$, it increases much more strongly than ω_a.

THESIS DRAFT

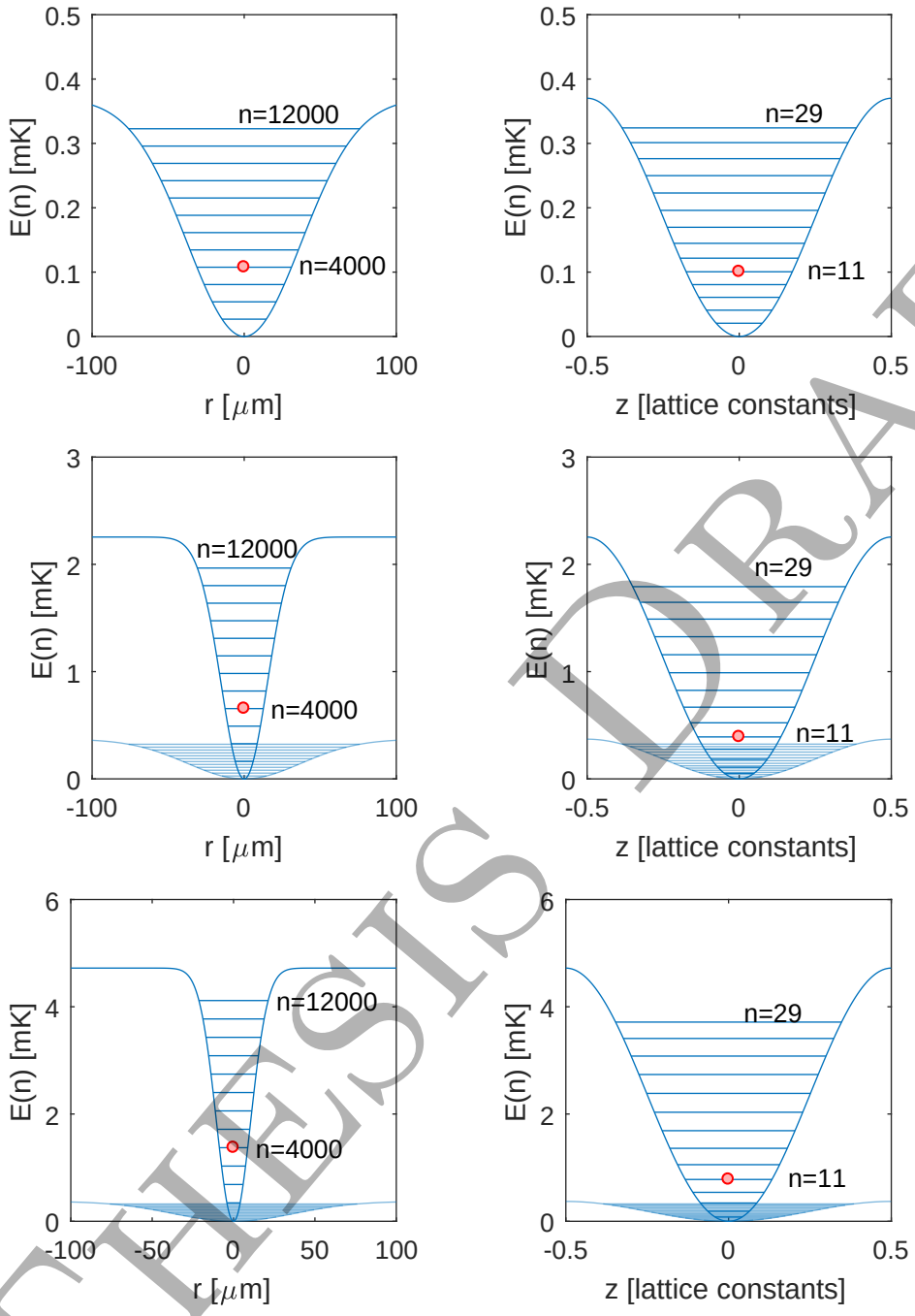

Figure 3.15.: Harmonic oscillator potential and energy levels. Shown is the trapping potential in the radial direction and the energy levels if approximating this potential as a harmonic oscillator. b) bandstructure in axial direction? Note the different length scales in a) and b). upper row: MOT position, middle row: outside fiber tip, lower row: inside fiber (transparent potential is the initial MOT potential as a comparison).

THESIS DRAFT

The energy level structure of the one-dimensional harmonic oscillator in each direction is given by

$$E_n = \hbar\omega_r \left(n_i + 1/2\right), \tag{3.12}$$

where the quantum number n_i corresponds to either n_x or n_y, depending on which direction we are measuring. Since both directions behave the same way, in the following I will exemplarily use the x-direction for first discussions of the radial direction. However, for precise calculations, we will later see that it becomes necessary to use the full two-dimensional oscillator model.

Figure 3.15 shows the harmonic potential in radial direction and the corresponding energy levels (left-hand side) at different positions with respect to the fiber tip. The upper row is at MOT position, the middle row at the usual position outside the fiber tip and the lower row for positions inside the fiber. In the lower two rows, the initial potential at the MOT position is plotted transparently to visualize the increase in trapping potential. As in radial direction, the trapping frequency increases more strongly due to the decreasing beam waist as discussed above, the squeezing of the potential is much more visible and the energy levels rise up further compared to the axial direction. Here, the mean atomic energy level is marked with red marker, assuming the same energy level for all positions. If this simple assumption were true, the energy of the corresponding atomic energy level in radial direction and thus the atomic temperature would rise from approximately 100 µK initially to about 650 µK just outside the fiber tip and to almost 1500 µK inside the fiber. Here, I am mainly looking at the radial direction because this is the direction we are measuring experimentally.

In the axial direction, we have the sinosoidal lattice potential as described in section XX above. Here, the energy level structure has to be calculated using a bandstructure approach. Figure 3.15 also shows the axial lattice potential and the corresponding band structure (right-hand side) for comparison. Here, the potential also increases towards the fiber tip. However, since the trapping frequency here stays the same, the change is less than in the radial direction. Thus, in axial direction, the atomic temperature would rise from approximately 100 µK initially to about 400 µK just outside the fiber tip and to almost 800 µK inside the fiber. Note that only the mean energy of each energy band is plotted in this figure. Therefore the curvature of the bands is not visible. However, for lattices as deep as this, the bands can in good approximation be approximated as harmonic oscillator levels anyway.

However, in reality the squeezing of the harmonic oscillator due to the decreasing beam waist makes the situation more complicated. To calculate the true atomic temperature at each position, we have to use the approach of the so-called truncated Boltzmann distribution. Before I come to how to calculate this truncation, let me briefly revise the important concepts of the Boltzmann distribution and its meaning in statistical physics.

The occupation probability of each energy level is given by the Boltzmann distribution [80]

$$P(E_n) = \frac{\exp\left(-E_n/k_BT\right)}{\sum_n \exp\left(-E_n/k_BT\right)} = \frac{\exp\left(-E_n/k_BT\right)}{Z}, \tag{3.13}$$

THESIS DRAFT

where Z is the partition function and T is the mean temperature of the atomic ensemble, corresponding to a mean energy of $\langle E \rangle = k_B T$. The occupation probability of the energy levels at the MOT positions for atoms with a mean temperature of $T = 100\,\mu\text{K}$ is shown in figure 3.16 a). Here, the occupation probability is plotted as function of the energy of each energy level (lower x axis) and the number of the energy level (upper x axis), respectively. It is clearly visible that the occupation probability drops the higher the energy level, as described by the exponential function in equation 3.13.

The energy density / distribution $EP(E)$ weighs the energy of each level with its occupation probability and is given by this Boltzmann distribution. The energy density for this case is shown in figure 3.16 b). It reaches its maximum for the mean atomic energy $\langle E \rangle$ and then drops for higher energy levels. We can note that unlike the occupation probability, it does not drop to almost zero even for values close to the maximum potential depth.

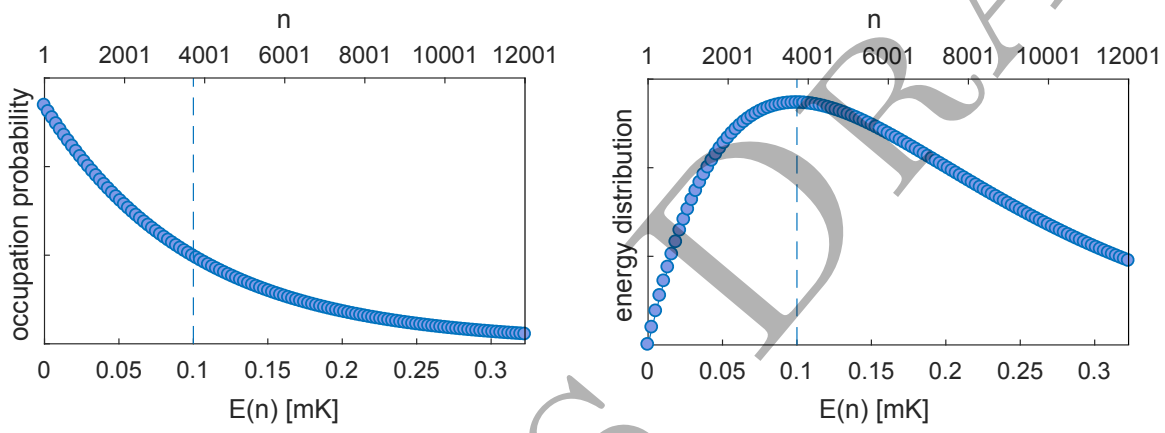

Figure 3.16.: Occupation probability and energy distribution. Both have been calculated according to Boltzmann distribution in equation 3.13 for the radial potential at the MOT position. The dashed line marks the mean atomic temperature of $T = 100\,\mu\text{K}$.

In the so-called truncated Boltzmann distribution, however, we assume that atoms with energies above the threshhold of the potential depth will no longer be trapped. Therefore, the occupation probability and thus also the energy density are truncated at the energy corresponding to the potential depth. In the following, I will show how this effects the energy and therefore the temperature of the remaining atoms, closely following reference [81]. The effect on the number of remaining atoms will be discussed later.

For the following calculation, I assume the potential depth to be U_1 and the mean atomic energy for the non-truncated atomic ensemble to be T_1. Note that for this full treatment, we now have to consider the full two-dimensional harmonic oscillator in radial direction. The detailed calculations can be found in appendix A.2. When I truncate the occupation probability at U_1, the temperature of the remaining atoms can be calculated as

$$\langle T_1 \rangle_{2D,trunc} = T_1 \frac{1 - \left(1 + \eta + \frac{1}{2}\eta^2\right) \mathrm{e}^{-\eta}}{1 - (1 + \eta)\,\mathrm{e}^{-\eta}}, \tag{3.14}$$

where $\eta = U_1 / (k_B T_1)$ is a measure of how much of the initial Boltzmann distribution will be truncated. Let me first discuss the effects of the truncated Boltzmann approach

THESIS DRAFT

at different final positions. Note that the following figure shows just one direction, 1D harmonic oscillator, for a more intuitive visualization.

After being transported to the fiber tip, the atoms will experience an increased trapping potential as has already been discussed above. It is visualized together with the corresponding energy distribution in figure 3.17 (b). Due to the increased trapping frequency of the harmonic oscillator, the same energy level will have a higher energy and corresponding higher temperature as also discussed above. If we assume the entropy to stay constant during the transport, then we expect the atoms to still occupy the same energy level. Therefore, the mean atomic temperature will also have increased (red dashed-dotted line in 3.17 (b)). However, if I now apply the truncated Boltzmann distribution, I can calculate the mean temperature of the remaining atoms as discussed above with the truncated Boltzmann formula (black dashed line in 3.17 (b)). For the case without amplitude ramp down, I calculate a value of about 510 μK. This is in good agreement with the value of 530(38) μK measured experimentally for the 1000 kHz linear ramp (blue data point in 3.17 (b)).

To reduce the final atomic temperature, we can for example keep the potential depth constant by applying an amplitude ramp-down. Figure 3.17 (c), left-hand side, shows the resulting trapping potential for a $n = 1$ amplitude ramp-down. Note that due to the smaller beam waist at the final position the shape of the potential will be compressed as compared to the initial position. Therefore, the atoms which have been transported to the fiber tip will experience a change in trapping potential profile, even though the potential depth itself is kept constant. Due to this squeezing of the potential, a large part of the Boltzmann distribution will be truncated. The mean temperature of the remaining atoms can again be calculated from equation 3.14. The value of about 110 μK is much lower than the temperature obtained for transport without amplitude ramp-down and close to the initial temperature. This theoretical prediction is in good agreement with our experimental observations, where we have measured a final temperature of about 100(7) μK for the 1000 kHz linear ramp.

Loss of atoms due to reduction of the trapping potential

The truncation of the Boltzmann distribution means that the hottest atoms will be lost. Obviously, this will not only affect the temperature of the remaining atoms as discussed above, but will also have an influence of the number of remaining atoms. Here, the intuitive picture already provides a good understanding. The larger the area of the truncated Boltzmann distribution, the larger the percentage of the lost atoms.

To calculate a number for this loss of atoms, I derive the following formula for the survival probability of the remaining atoms as

$$P_{2D,trunc}^{surv}(U_1) = 1 - (1+\eta)\,\mathrm{e}^{-\eta}. \tag{3.15}$$

A detailed calculation can again be found in the appendix A.2.

Let me discuss the amount of lost atoms for the two examples of atoms transported to the fiber tip shown in figure 3.17. When the potential depth is not adapted, only a small

THESIS DRAFT

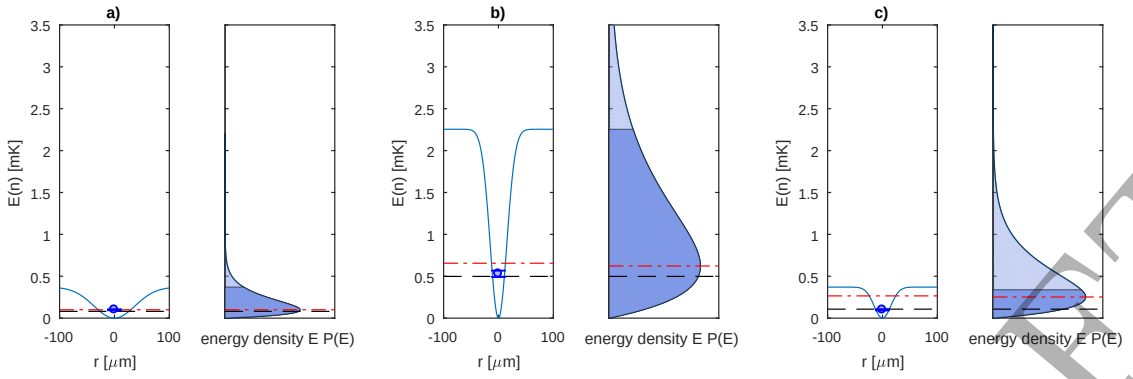

Figure 3.17.: Effect of the trapping potential on the final temperature. Shown are the trapping potential in radial direction (left-hand side) and the energy density $EP(E)$ corresponding to the theoretical mean temperature (right-hand side) for atoms a) at the intitial position, b) at the fiber tip without amplitude ramp-down and c) at the fiber tip with a $n = 1$ amplitude ramp-down. Both experimentally measured temperature (data point) as well as the theoretical mean temperature (red dashed-dotted line) and the temperature corresponding to the truncated Boltzmann distribution (black dashed line) are shown. The dark-coloured area in the energy density indicates where the Boltzmann distribution is truncated by the trapping potential. Figure adapted from our publication [72].

part of the Boltzmann distribution will be truncated (see 3.17 b), right-hand side). Here, I calculate a survival probability of almost 90%. However, when the trapping potential is adapted, a large part of the Boltzmann distribution will be squeezed out of the trap (see 3.17 c), right-hand side). In this case, about 60% of the transported atoms will be lost, only taking into account the final potential. In the following section, I will compare these numbers to experimental results and discuss the more quantitative behaviour. Qualitatively, though, it is very clear. Figure 3.18 visually illustrates the loss of hot atoms when the final trap depth is ramped down according to a $n = 1$ amplitude ramp.

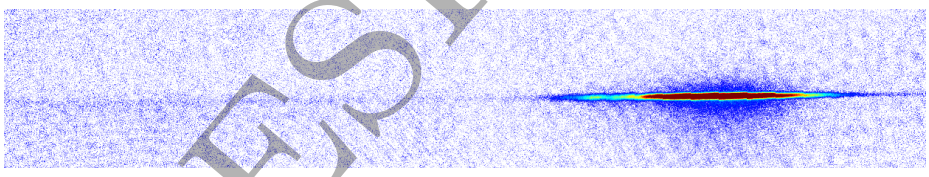

Figure 3.18.: Loss of atoms due to reduced final trap depth. Absorption image of atoms transported to the fiber tip with a 1000 kHz constant frequency ramp and $n = 1$. Atoms with a high temperature spill out of the trap and are lost, leading to the lower final temperature and lower final atom number. No tail visible as atoms lost on the way will not be trapped anymore as the trap depth is reduced too much.

One interesting point is to visualize the scaling of both survival probability and mean final temperature of the remaining atoms with regard to the final trapping potential. Due to their complex dependencies given by equations 3.14 and 3.15, we find it difficult to intuitively predict the scaling of $\langle T_1 \rangle_{2D,trunc}$ and $P^{surv}_{2D,trunc}(U_1)$ with different final trap depths. In figure 3.19, both survival probability and mean final temperature are plotted as a function of the final trap depth U_1 for atoms with a final position outside the fiber tip (a) and for atoms transported inside the hollow-core fiber (b). Note that for the two different positions the maximum attainable final trap depth in different due to the different laser intensities. The

THESIS DRAFT

scaling of the two parameters, however, is the same. While the temperature scales almost linearly with the final trap depth, we can see a saturation type behaviour for the survival probability. This means that when we only slightly lower the final trap depth, we expect a minor change in trapping and thus transport efficiency, while it should notably reduce the final mean temperature. In the following section, I will compare these expectations to the experimental values.

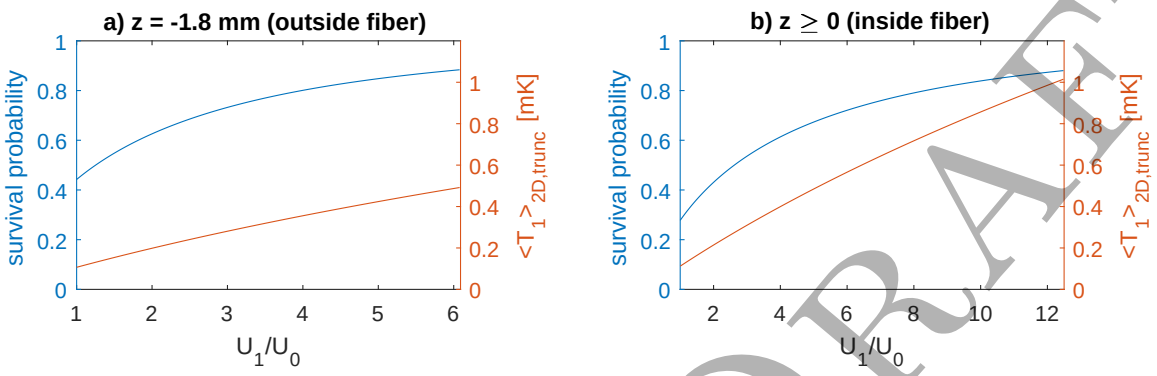

Figure 3.19.: Survival probability and mean temperature of the remaining atoms. Calculated from the truncated Boltzmann distribution according to equations 3.14 and 3.15 for atoms transported to a final position a) outside the fiber tip or b) inside the hollow-core fiber.

3.4. Combining frequency and amplitude ramps outside the fiber

Here, we will learn how the transport can be optimized regarding final atom numbers and temperatures using different frequency and amplitude ramps. We will also compare these results with a theoretical simulation.

In the previous chapters, I have discussed how our figures of merit of the transport, the transport efficiency and the temperature of the transported atoms, are influenced by the frequeny ramps and the depth of the trapping potential. I have shown that we observe an increasing transport efficiency, but also increasing temperatures for higher final dipole trap depth close to the fiber tip. In this chapter, I will use the previously introduced way of controlling the trap depth to study transport efficiency and final temperature for a combination of frequency and amplitude ramps and I will try to find optimal settings for our setup. This will all still be done for atoms outside the fiber. Further, I will compare our experimental results with two different theories - a classical transport theory and the previously introduced truncated Boltzmann theory. I will conclude this chapter by studying the behaviour of the phase-space density for different final potential depths.

THESIS DRAFT

3.4.1. Comparison with a classical transport theory

In this section, I will compare our experimental results for different amplitude ramps with the results of a classical transport theory. This theory has been developed together with Fabian Knoch from the group of Prof. Dr. Speck. This classical transport theory works by numerically solving the equations of motion in our system, using the position dependent trapping potential and the moving lattice as inputs. While being transported, atoms can be lost from this system if they due to heating acquire an energy above the trapping potential. The loss due to lifetime in the dipole trap is taken into account by multiplying the this lifetime factor after the atoms have reached their final position. The initial settings of the simulation are chosen to match with our experimentals settings (size and temperature of initial cloud). Further details regarding the initialization can be found in our publication [72].

"To model the atomic transport, we assume all Rubidium atoms to be frictionless (very low temperatures) and independent, i.e. we neglect particle-particle interactions (low atom density). Thus, the single particle dynamics is solely governed by the dipole trap potential (cf. 2.4), for which we solve Newton's equations of motion numerically by employing the implicit Adams integrator provided in the Python package SciPy [82]." [72]

"To prepare the initial state, we position 1500 particles at $x = y = 0\,\mathrm{mm}$, while z-positions are drawn from a Gaussian distribution according to the experimental parameters. In a second step, every particle's z-position is shifted such that it coincides with its closest potential energy minimum. To initialize a starting temperature, the particle velocities are drawn from a Gaussian distribution with zero mean and width $\sigma_{v_x} = \sigma_{v_y} = \sigma_{v_z} = (k_B T_{\mathrm{init}}/m)^{1/2}$. Since all particles are positioned in potential energy minima, part of their average kinetic energy is converted into potential energy. Assuming a quadratic form around the potential minima and employing the equipartition theorem, the particle ensemble's equilibrated temperature is given by $\approx 1/2\, T_{\mathrm{init}}$. After a short equilibration period of 20 ms we randomly select 1280 particles that did not escape the dipole trap, which are then used as the initial ensemble for the transport simulations. This number of particles is given by the available number of computational kernels." [72]

"To identify particles that have escaped the dipole trap, we monitor the total energy $E_i(t)$ of every particle individually. For $E_i(t) > 0$ the particle escapes the trap and is no longer considered when computing ensemble averages. The loss of particles due to lifetime is taken into account at the final transport position. Finally, to estimate uncertainties of the quantities of interest, e.g., temperature and fraction of trapped particles, we split the full ensemble into 20 subensembles and compute the standard error." [72]

In the following, I would like to study and compare the experimental and theoretical results exemplarily for the 1000 kHz linear frequency ramp and for different amplitude ramp-downs, as shown in figure 3.20 a). Here, we have chosen five different values of the final trapping potential. Note that at the position of the atoms outside the fiber tip marked by the dotted line, these final potential depths will not yet have been reached, except for the case of keeping the trap depth constant. As discussed in the previous section, we expect both

THESIS DRAFT

transport efficiency and final temperature to be highest for the highest final trap depth and decrease with decreasing trap depth.

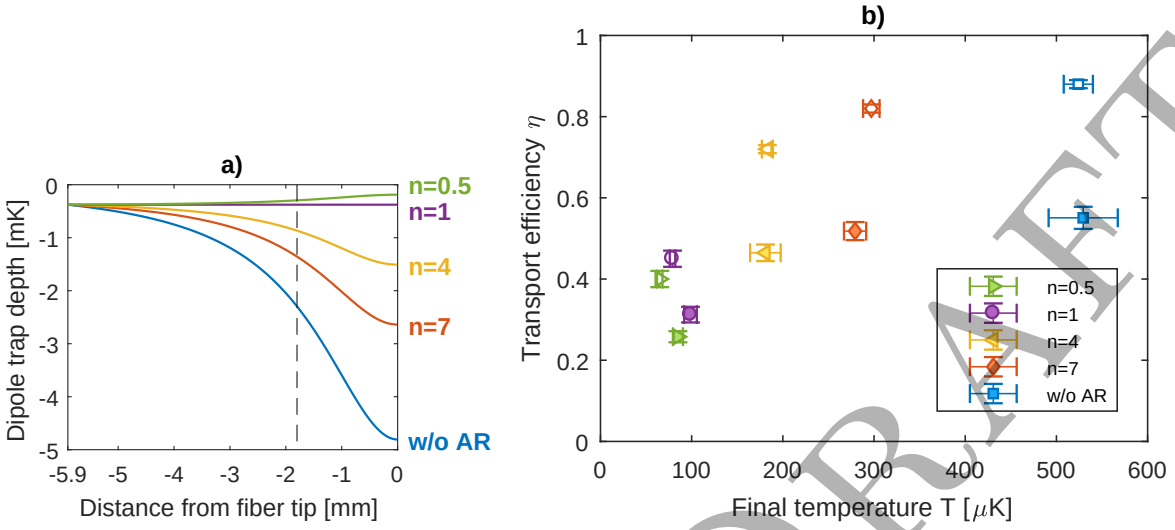

Figure 3.20.: Experimental and theoretical results outside the fiber. "a) Shown is the potential depth as a function of distance for different amplitude ramp-downs. The black dashed line marks the final atomic position for the applied frequency ramp. b) Shown are the experimental (filled markers) and theoretical (empty markers) results for transport efficiency and final temperature for atoms transported to the fiber tip for the 1000 kHz linear frequency ramp and for the different amplitude ramp-downs from figure a). (Error bars represent statistical errors and errors from the fitting procedure.)" Figure adapted from our publication [72].

Figure 3.20 b) shows both experimental and theoretical results for the transport efficiency and the final temperature. Here, the filled markers denote the experimental results and the empty markers the results from the classical transport theory. Indeed, our assumption is verified for all data points. The lower the final trap depth, the lower the transport efficiency and the lower also the final temperature.

"As discussed before, we achieve high transport efficiencies up to 55% for high final dipole trap depths, but at the same time the temperatures are much higher than the initial temperature. When lowering the final trap depth, both efficiency and final temperature decrease. For a final trap depth as low as $4U_00$, we still observe a transport efficiency of about 45%. However, the final temperature is reduced by more than a factor of 3. For very low final trap depths, the transport efficiency reduces to about 25%. Still, these ramps are a good choice if one is interested in obtaining a very low-temperature final atomic sample, with temperatures even below the initial temperature and more than 6 times lower than the temperatures without amplitude ramp." [72]

"We have confirmed that also the other two frequency ramps shown in figure 4 (a) exhibit qualitatively the same behavior as discussed above and that the qualitative overall trend for each ramp is robust with regards to day-to-day performance fluctuations of the experiment." [72] (see appendix A.3 for data.)

Constant correction factor when comparing the experimental and theoretical efficiencies,

THESIS DRAFT

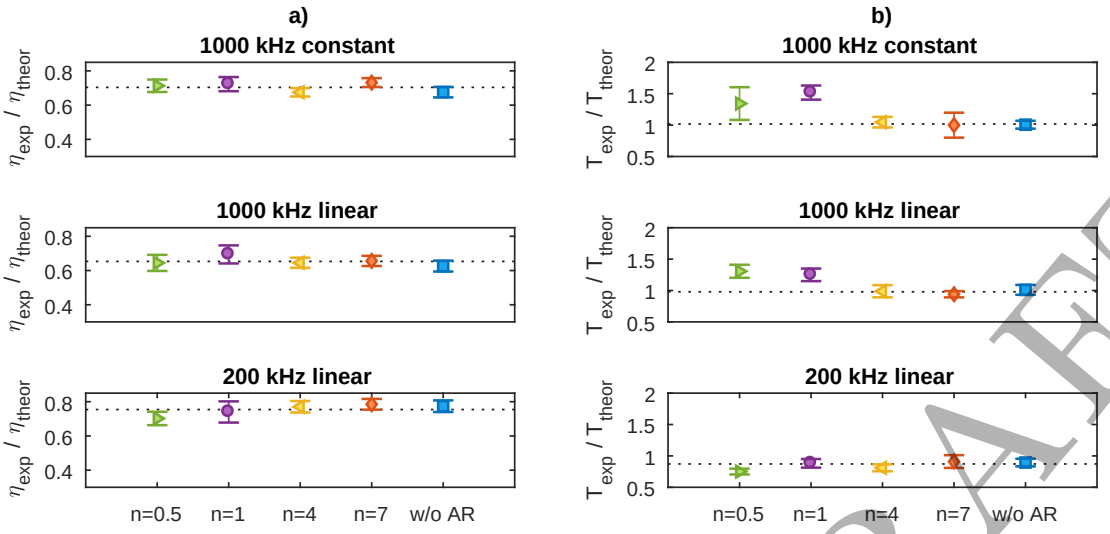

Figure 3.21.: Comparison of experimental and theoretical results outside the fiber. Shown is the ratio between experimental and theoretical values for a) transport efficiency η and b) final temperature of atoms transported to the fiber tip for two different frequency ramps and different amplitude ramp-downs. The dotted line shows the mean value of all amplitude ramps. (For temperature, only highest three amplitude ramps.) (Error bars represent statistical errors and errors from the fitting procedure.) Figure partially adapted from our publication [72].

which seems to depend on the frequency ramp (possibly position-dependent lifetime which is not being taken into account and influences slower ramp more strongly). But apart from constant factor good agreement.

"The results from the theoretical simulation (section 2.5) are plotted in figure 6 (b) (empty data points) together with the experimental results. We note a very good agreement regarding the qualitative behavior of the different ramps. When comparing the experimental and theoretical values for the temperatures, we see a very good agreement for high final dipole trap depths. However, for small dipole trap depths, we measure a higher temperature than theoretically expected. This can be due to fluctuations in laser powers as discussed above, which most strongly influence lower trap depth. When comparing the experimental and theoretical values for the transport efficiency, we find a constant correction factor of around 0.65 for the 1000 kHz linear ramp (see figure 6 (c)). In the same way, we determine a correction factor of around 0.75 for the 200 kHz linear ramp. This confirms our previous observation of the limited maximum lifetime-corrected transport efficiencies (cf. figure 4 (c)), where the efficiency for the 200 kHz linear ramp was also higher than for the 1000 kHz linear ramp. A constant correction factor further implies that the additional experimental loss mechanism does not depend on the number of transported atoms, which would be consistent with loss due to laser noise as discussed above. Overall, we find that our model gives a good understanding of the transport mechanism and predicts the results for the individual ramps well, except for correction factors for experimental imperfections." [72] (0.7 for 1000 kHz constant ramp)

For temperatures, there is a stronger difference between the two frequency ramps, especially

THESIS DRAFT

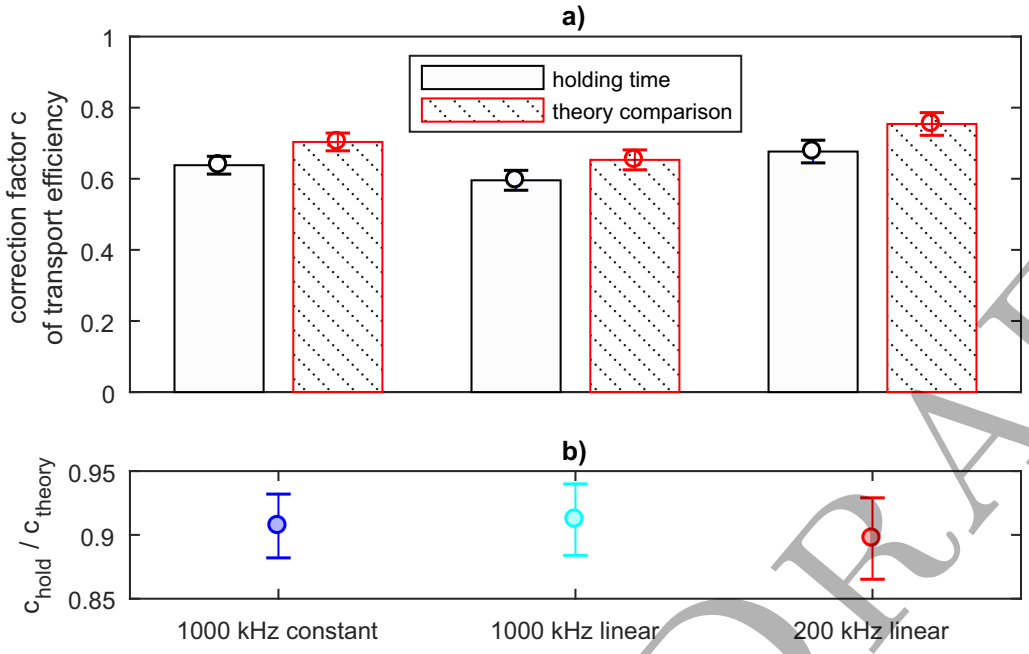

Figure 3.22.: Compare mean transport efficiency with lifetime-corrected efficiency. Shown are the transport efficiencies. Adjust legend as in atom tail eps figure.

for low final amplitude ramps. This will be investigated further in the next section. For high AR perfect agree for experiment and theory for fast ramps, for low AR disagreement (discussed in the following). For slow ramp, the AR do not make a difference, experimental data always slightly below theory: Possibly effect due to heating, loss and re-equilibration (lifetime effects), which are strongest for slow ramps.

Investigate influence of frequency ramps by keeping trap depth constant / Disentangle influence of amplitude and frequency ramps?

In order to see the effect of only the frequency ramps without taking into account the influence of the trap depth, I compare the results for different frequency ramps, while keeping the trap depth constant, that is applying a $n = 1$ amplitude ramp-down. Figure 3.23 shows the experimental and theoretical results outside the fiber. Remember: for full trap depth, we have seen no influence of the frequency ramps within our tested range within our error bars. (see figure for w/o AR) For $n = 1$, we can resolve some differences. First, the efficiencies decrease with increasing ramp duration. This behaviour is well covered by the theory and can be explained by the losses as discussed above. If we look at the ratio between experimental and theoretical values, we see exactly the same behaviour as seen above: Better efficiency for low frequency detuning. Because the lifetime-effect is compensated for. (Discuss w/o AR data for stronger agreement between different frequency ramps and different ratios.)

THESIS DRAFT

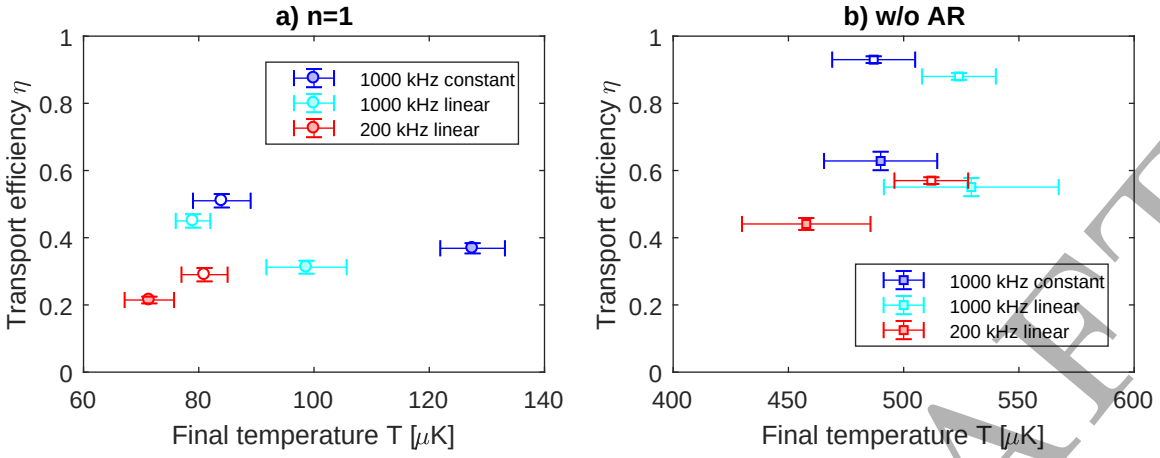

Figure 3.23.: Comparing different frequency ramps outside the fiber for $n = 1$. a) Shown are the different frequency ramps as a function of the applied ramp time. b) Shown are the experimental (filled markers) and theoretical (empty markers) results for transport efficiency and final temperature for atoms transported to the fiber tip for the different frequency ramps from figure a) and for the amplitude ramp-down with $n = 1$, that is keeping the potential depth constant. (Error bars represent statistical errors and errors from the fitting procedure.)

For $n = 1$, we see that the temperature increases for faster ramps. Interestingly, this effect is not covered by theory. This might be actually an effect from the fast ramp heating the atoms due to non-adiabatic transport. Also different temperatures might stem from slightly different final positions, but this effect is already included in the theory. For high final amplitudes, the trap depth effects dominate and we cannot see any clear distinctions between the final temperatures of the ramps.

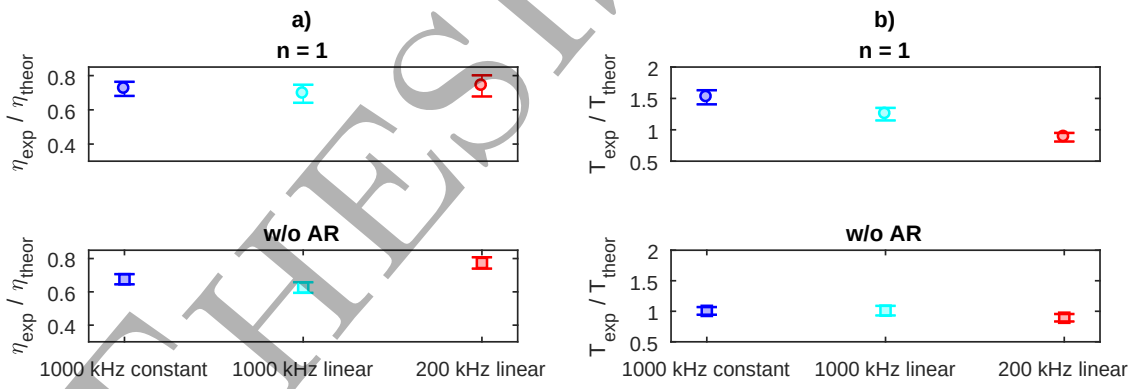

Figure 3.24.: Comparison of experimental and theoretical results for different frequency ramps outside the fiber for $n = 1$. Shown is the ratio between experimental and theoretical values for a) transport efficiency η and b) final temperature of atoms transported to the fiber tip for different amplitude frequency ramps and either applying no amplitude ramp-down (lower figures) or keeping the amplitude constant (upper figures). To the right: lifetime-corrected transport efficiencies from calculations above. (Error bars represent statistical errors and errors from the fitting procedure.)

To understand this behaviour, let me introduce a second criterion for adabatic transport.

THESIS DRAFT

Previously, we have only looked at adibaticity regarding the trapping well.

The second adiabaticity criterion concerns the maximum speed at which the trapping frequency can be changed, for which the atoms still remain in the same energy level. Here, I am following reference [81], which derives the following formula for adiabatically changing the trap frequency

$$\frac{\dot{\omega}}{\omega^2} \ll 1 \iff \Delta t \gg \frac{\Delta\omega}{\omega^2}, \tag{3.16}$$

where $\dot{\omega} = \Delta\omega/\Delta t$ is the changing rate of the trapping frequency ω. In our case, $\Delta\omega$ is usually given by the distance the atoms have been transported towards the fiber tip. Therefore, Δt tells us the allowed minimum time for a ramp that transports over this distance. Criterion for atoms staying in their same energy level. This should be fulfilled in our case as we will see later that the energy level / temperature matches quite well. Only for $n = 1$ and fast ramps discrepancy which can stem from this criterion!

	Initial and final trapping frequency	Change in trapping frequency	Minimum ramp time
w/o AR			
axial	$\omega_a = 2\,\mathrm{MHz} \to 7.5\,\mathrm{MHz}$	$\Delta\omega_a = 5.5\,\mathrm{MHz}$	$\Delta t \gg 0.3\,\mu\mathrm{s}$
radial	$\omega_r = 3.5\,\mathrm{kHz} \to 45\,\mathrm{kHz}$	$\Delta\omega_r = 41.5\,\mathrm{kHz}$	$\Delta t \gg 140\,\mu\mathrm{s}$
$n = 1$			
axial	$\omega_a = 2\,\mathrm{MHz} \to 2\,\mathrm{MHz}$	$\Delta\omega_a = 0\,\mathrm{MHz}$	$\Delta t \gg 0\,\mu\mathrm{s}$
radial	$\omega_r = 3.6\,\mathrm{kHz} \to 4.6\,\mathrm{kHz}$	$\Delta\omega_r = 1\,\mathrm{kHz}$	$\Delta t \gg 80\,\mu\mathrm{s}$

Table 3.2.: Minimum ramp times for different amplitude ramps to maintain adiabaticity criterion from equation 3.16.

3.4.2. Comparison with truncated Boltzmann theory

Compare with own theory of truncated Boltzmann distribution (discuss differences between the two theories - one incorporates the transport, the other only the final potential depth). However, Boltzmann theory provides some more intuitive understanding of the scaling/shape of efficiency and temperature with final trap depth.

Comparison subplot outside: Efficiencies are predicted slightly lower than from other theory, therefore slightly higher correction factor of about 0.7. Correction factor lower for nigher n amplitude ramps -> indication that losses during transport (which are taken into account for the other theory) play a major role. Evaporation at final point has been taken into account. Lifetime loss has been taken into account. Temperatures more or less fit. Here no effect of heating for low AR can be seen.

"Here, we note that although $T_1 \propto U_1^{1/2}$, the final temperature calculated with the truncated Boltzmann distribution $\langle T_1\rangle_{2D,trunc}$ has a more complicated dependency on the trap depth. Due to this complex dependency, we find it difficult to intuitively predict the scaling of $\langle T_1\rangle_{2D,trunc}$ and $P^{surv}_{2D,trunc}(U_1)$ with different final trap depths. Therefore, for your convenience, we have plotted both survival probability and mean final temperature as a function

THESIS DRAFT

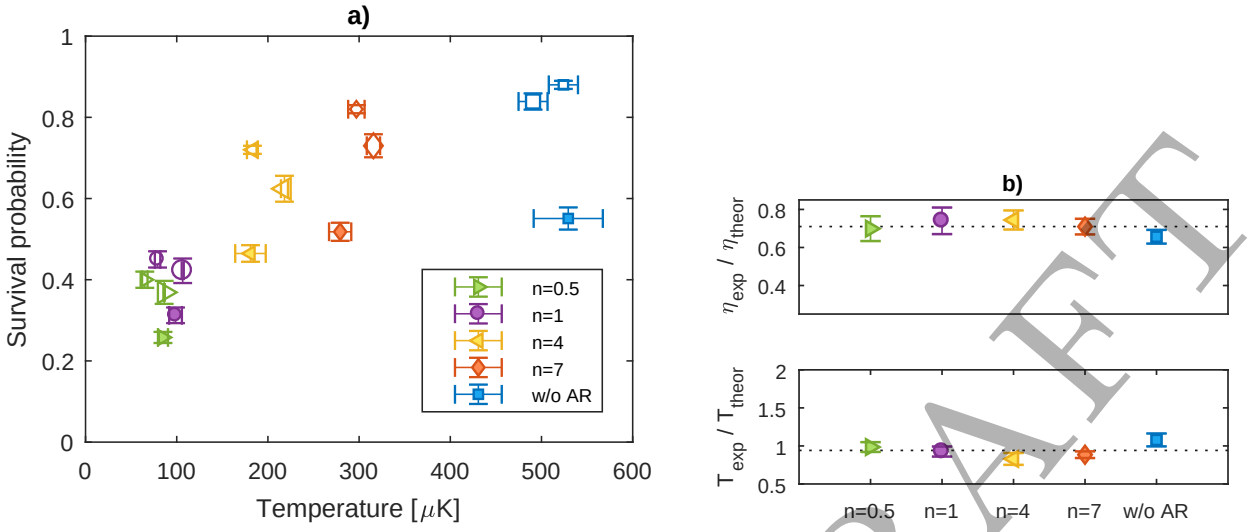

Figure 3.25.: Experimental and theoretical results from truncated Boltzmann outside the fiber. The solid line shows the survival probability as function of final temperature calculated using the truncated Boltzmann distribution according to equations 3.15 and 3.14.

of the final trap depth in the following figure. Please note that to simplify calculations, here we assume that the atoms have been transported to the focal point of the dipole trap beams directly at the fiber tip, which is a slightly different setting than explored in figure 5 in the main manuscript." [72]

3.4.3. Optimizing the phase-space density

Until now, we have mostly treated the transport efficiency and the final temperature seperately. However, in principle, we would like to optimize both in a controlled way so that we can achieve the highest number for the lowest temperature. One figure of merit for both atom number and temperature is the phase-space density [citation]

$$PSD = \frac{N_{\mathrm{at}}}{\sigma_r^2 \sigma_z 4\pi/3} \left(\hbar \sqrt{\frac{2\pi}{m_{\mathrm{Rb}} k_B T}} \right)^3 = \rho_{\mathrm{at}} \left(\hbar \sqrt{\frac{2\pi}{m_{\mathrm{Rb}} k_B T}} \right)^3, \tag{3.17}$$

where $\rho_{\mathrm{at}} = \frac{N_{\mathrm{at}}}{\sigma_r^2 \sigma_z 4\pi/3}$ is the atomic density. The phase-space density increases when either the number of atoms / the atomic density increases or the temperature decreases. Note that the dependence on temperature and atom number is not the same. Therefore, a decreasing temperature will influence the phase-space density much more strongly than an increasing atom number. This we have to keep in mind for interpreting the results later.

Figure 3.26 shows the atomic density as well as the phase-space density for each of the three frequency ramps discussed above and for all different amplitude ramps. For all frequency ramps, we observe that the atomic density decreases for lower final dipole trap depths. However, at the same time, we observe an upward trend in the phase-space density

THESIS DRAFT

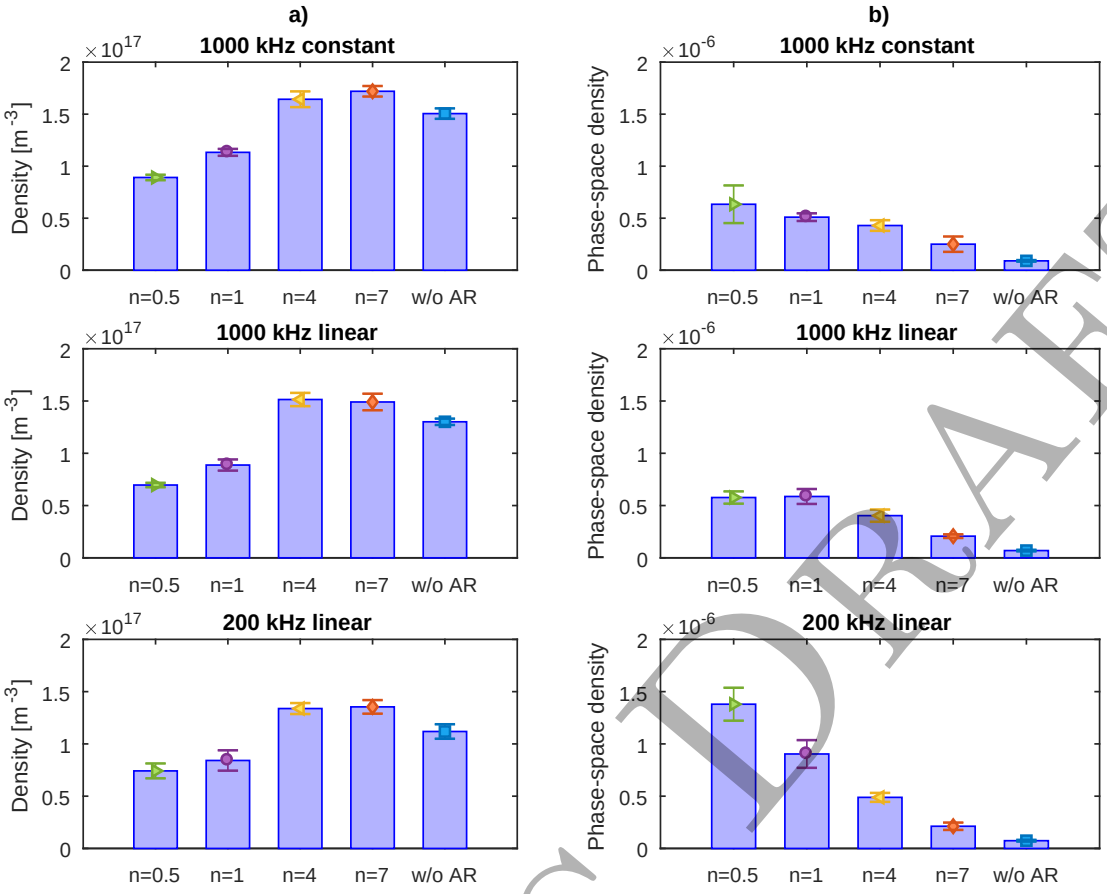

Figure 3.26.: Density and phase-space density outside the fiber. Shown are a) density and b) phase-space density of atoms transported to the fiber tip for three different frequency ramps and different amplitude ramp-downs. Note that all y-scales for a) and b) have been chosen the same, respectively, for better comparison of the results. (Error bars represent statistical errors and errors from the fitting procedure.)

towards lower final dipole trap depths. That means that even though the absolute transport efficiency decreases, this decrease is compensated by a lower temperature. -> actual phase-space density will be larger since actual cloud radius will be smaller.

plot cloud radius (estimate actual cloud radius for different amplitude ramps?). Ratio cloud radius / trap waist for different trap depths bzw. plot σ_0 calculated from atomic temperature or relation between measured x-width and σ_0.

Study x width for one ramp: Experimentally measured width + width expected from temperature of sample (a) + b) plot). Compare if relations between radii makes sense -> Then say that we can also use the experimental radius, knowing that we get a lower limit for the actual density. Approximately factor 7 between the two PSDs.

Results for the two other ramps confirm this factor and behaviour (in appendix?). However, here we find the problem that the too high temperature very strongly influences the results for low AR, since it now features in all the calculations.

THESIS DRAFT

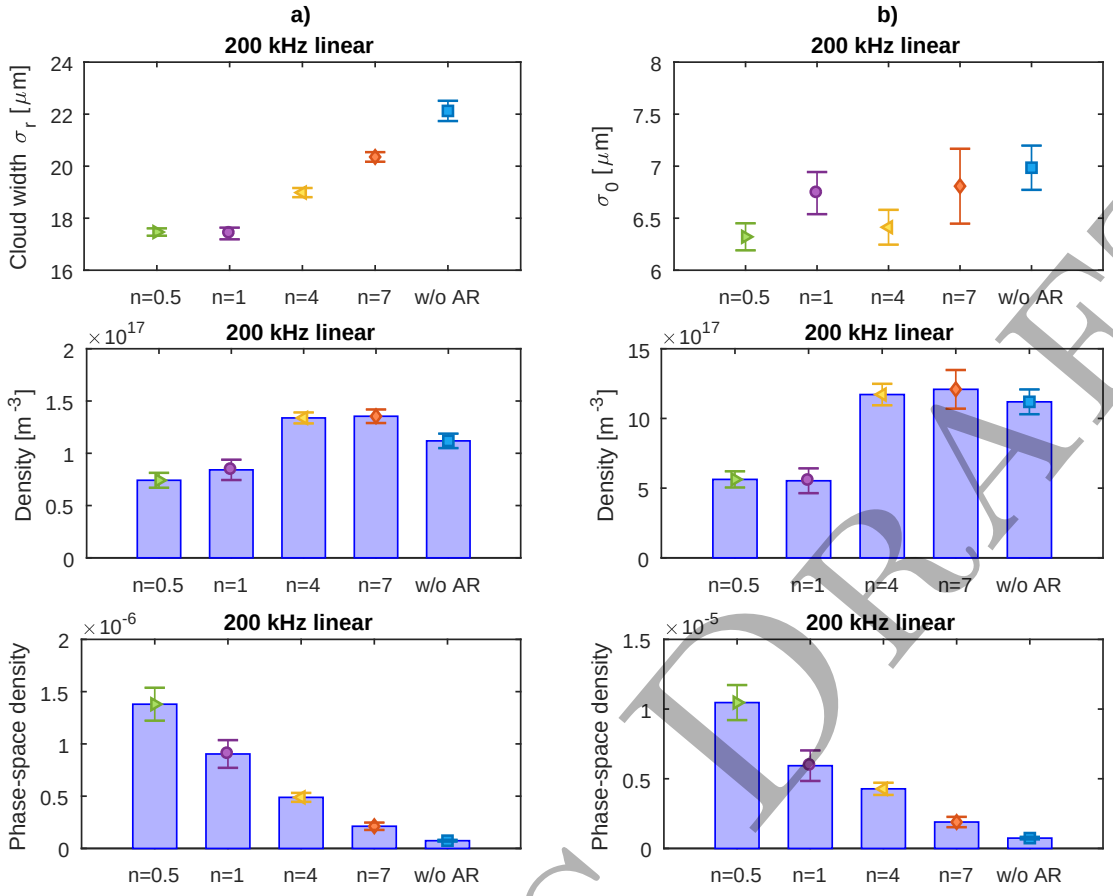

Figure 3.27.: Different approaches to calculating the phase-space density outside the fiber. Shown are cloud radius (upper row), density (middle row) and phase-space density of atoms transported to the fiber tip for the 200 kHz linear frequency ramps and different amplitude ramp-downs, calculated using two different approaches: a) using the cloud width obtained by absorption imaging and b) using the initial cloud radius σ_0 obtained by equation XX from atomic temperature and trap depth at final position. Note that here the y-scales for a) and b) have not been chosen the same for better visualization of the results. (Error bars represent statistical errors and errors from the fitting procedure.)

The y-width (r_z) is relatively constant for all frequency and amplitude ramps and lies between 550 μm and 600 μm.

3.5. Transporting cold atoms inside the fiber

Here, we will learn which additional effects play a role when transporting atoms into the hollow-core fiber. We will discuss the optimization of the transport procedure and again compare the results with theory.

THESIS DRAFT

Now that we have characterized the transport process outside the hollow-core fiber in great detail, we also want to study the transport of atoms into the fiber, as this will be of most interest for all our future experiments. Since we have seen earlier that we are somewhat limited by the maximum detunings, we use longer ramp times to achieve this. Of course this comes with the drawback of stronger influences of the lifetime.

"When transporting the atoms inside the hollow-core fiber, our figure of merit to characterize the transport is the time-dependent optical depth D_{opt}, which is proportional to the number of transported atoms, but additionally depends e.g. on the overlap between atomic cloud and probe beam (cf. earlier chapter). Due to a micro lensing effect of the atomic cloud [83, 84], we find that calculating the optical depth for high atomic densities is not straight forward. The details of this investigation are discussed elsewhere [73]. For the measurements to be discussed in the following, we have therefore transported the atoms far enough (6 mm) inside the fiber where we have observed [73] that these lensing effects play a minor role due to reduced atomic densities." [72]

To measure inside the fiber we use the release-recapture method, which has the following issues.

Briefly mention effects of blower beam (for details see Ronja's thesis [75]) and that we are measuring at low ODs for avoiding lensing effect. "To ensure that we only measure atoms transported inside the hollow-core fiber, we apply a resonant push beam outside the fiber just before probing, which is perpendicular to the fiber axis." [72]

3.5.1. Comparison with classical transport and truncated Boltzmann theory

In principle, we obtain the same effects as outside the fiber for different amplitude ramps. Comparison with theory - discuss constant correction factor - transfer efficiency of atoms into fiber.

"Figure 3.28 (a) shows the behavior of the optical depth during the pulsed probing process (cf. section data analysis) for three different final dipole trap depths for the 1000 kHz constant frequency ramp. We observe that the initial optical depth is highest for the transport without ramping down the potential and decreases for lower final trap depths. This corresponds to our expectations from studying the transport efficiencies outside the fiber. We further observe that with increasing number of probe pulses the optical depth decreases. In principle, this behavior occurs for all amplitude ramps, but is most prominent for high final trap depths, for which the atomic cloud has a higher temperature. We can determine this temperature using a release-and-recapture fit (cf. section data analysis), which is also plotted in figure 3.28 (a)." [72]

"Figure 3.28 (b) shows both the transport efficiency compared to the initial atom number and the final temperature of the atomic cloud for amplitude ramps with different final dipole trap depths for the 1000 kHz constant frequency ramp (solid data points). Here, the results inside the fiber are qualitatively very similar to the results we have obtained outside the fiber. Without amplitude ramp-down, we obtain both higher transport efficiencies and higher

THESIS DRAFT

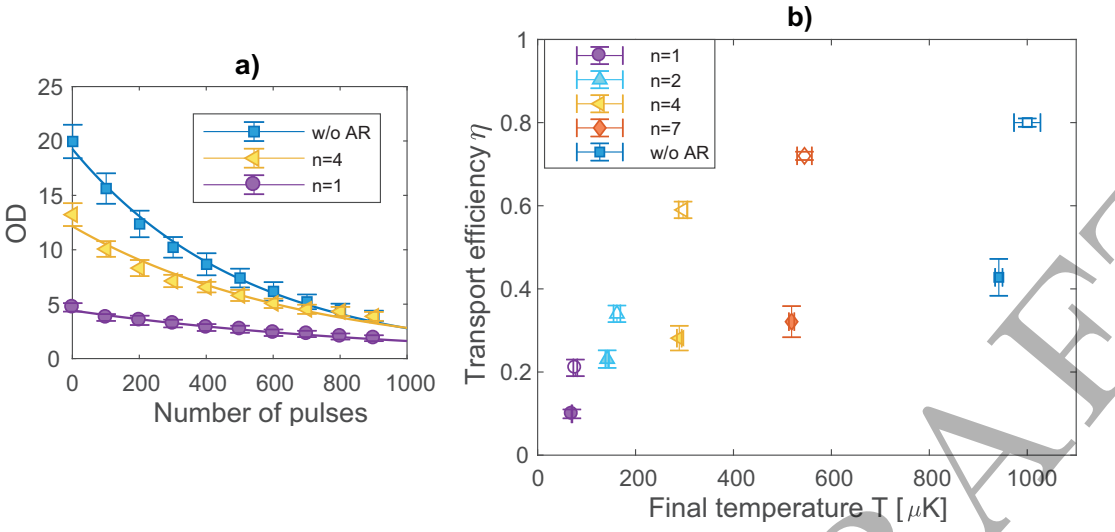

Figure 3.28.: Experimental and theoretical results inside the fiber. "a) Decay of the optical depth with number of probe pulses for different amplitude ramp-downs (data points) and corresponding release-and-recapture fits (Equation XXX, solid line). b) Experimental (filled markers) and theoretical (empty markers) results for transport efficiency and temperatures for atoms transported 6 mm inside the fiber for the 1000 kHz constant frequency ramp for different amplitude ramp-downs. (Error bars represent errors from the fitting procedure.)" Figure adapted from our publication [72].

temperatures, while when ramping down the amplitude to lower final trap depths, both transport efficiency and temperatures decrease. Also the overall shape of this decrease agrees well with the measurements outside the fiber. Our transport efficiencies range from about 40% for an atomic ensemble at about 940 μK to about 10% for a very cold atomic ensemble at about 70 μK. Thus, by adapting the trap depth, we can lower our final temperatures by more than a factor of 10, while only decreasing the transport efficiency by a factor of 4." [72]

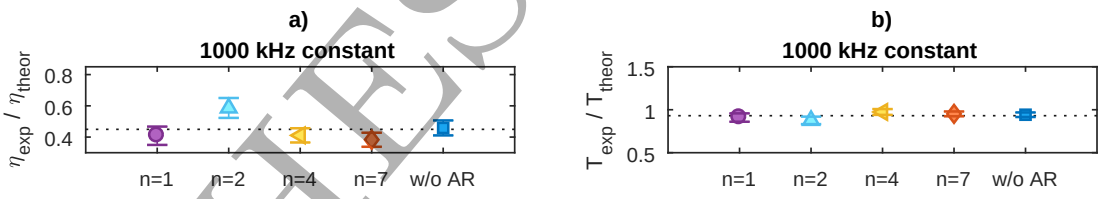

Figure 3.29.: Comparison of experimental and theoretical results inside the fiber. Shown is the ratio between experimental and theoretical values for a) transport efficiency η and b) final temperature of atoms transported inside the fiber for the 1000 kHz constant frequency ramp and different amplitude ramp-downs. The dotted line shows the mean value of all amplitude ramps. (Error bars represent statistical errors and errors from the fitting procedure.) Figure partially adapted from our publication [72].

Compare experimental and theory results.

"As for the measurements outside the fiber, we note a very good agreement between experimental results and the results from the theoretical simulation (section theory, shown

THESIS DRAFT

in figure 3.28 (b) as empty data points) regarding the qualitative behavior of the different ramps. When comparing the experimental and theoretical values for the transport efficiency, we again find a constant correction factor (see figure 3.28 (c)). With a value of about 0.45, it is lower than the correction factor measured outside the fiber. One reason for this is that the experimental limitations for the transport as observed outside the fiber have a stronger impact for longer transport distances. Another effect the theory does not consider is influences from the fiber itself other than keeping the trapping potential constant. Thus, a lower experimental transport efficiency points to an experimental limit when loading the atoms into the fiber. We expect the main reason for this to be imperfect coupling of the dipole trap beams into the fundamental mode of the hollow-core fiber as discussed in section amplitude ramps / beam coupling, as we have observed that this overlap strongly influences the transfer efficiency of atoms from outside to inside the fiber. This effect leads to a lower effective trap depth, which can also accommodate for the experimental values for the temperatures lying systematically below the theoretical values." [72]

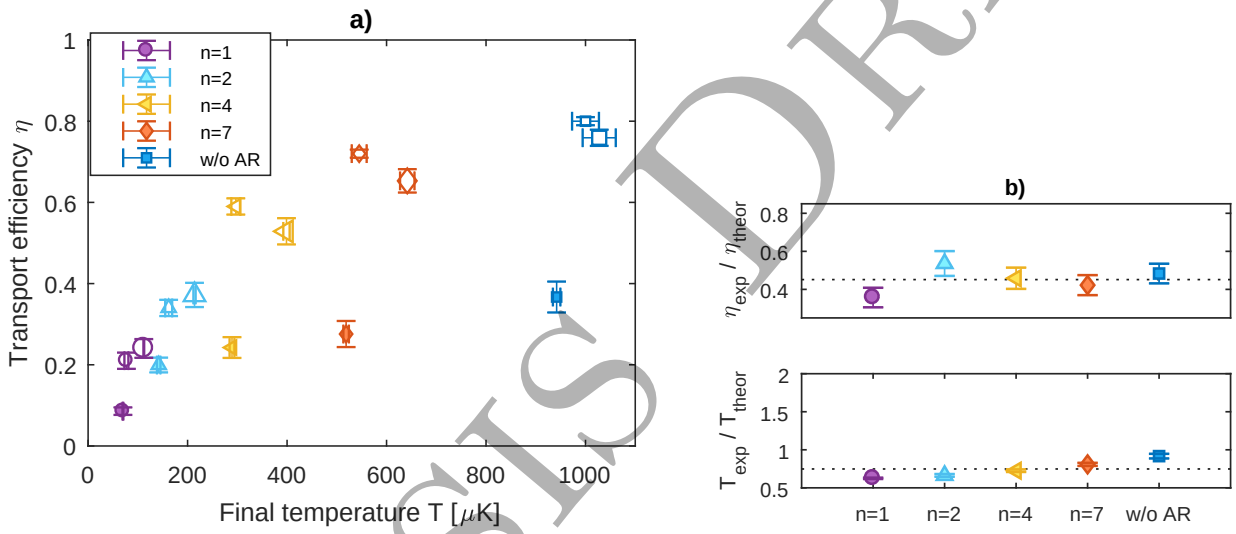

Figure 3.30.: Experimental and theoretical results from truncated Boltzmann inside the fiber. The solid line shows the survival probability as function of final temperature calculated using the truncated Boltzmann approach.

Add other theory prediction graphics, same behaviour as outside the fiber. 0.45 correction factor, same as for other theory. here, temperature of low n AR is overestimated by theory. Possibly: actually lower trap depth. Or loss of hot atoms during transport needs to be taken into account. This explains also why outside the fiber the temperature increase expected for low n AR was not seen with this theory.

3.5.2. Loading efficiency into the fiber

Loading efficiency from MOT of approximately 2.5% Table for loss / efficiencies, comparable to fiber coupling table. Discuss what is limiting each loss channel. Compare with loading efficiencies from other groups. 2.5% for lifetime corrected transport efficiencies!

THESIS DRAFT

"With our transport without amplitude ramp-down, we calculate a loading efficiency from the MOT into the hollow-core fiber of about 2.5%, which is very comparable to values reported in other groups (2.5% in [7] and 3% in [19]). We also would like to point out that this number represents a lower limit for our loading efficiency, as we measure atoms transported already 6 mm inside the fiber." [72]

Position	MOT	Lattice initial position	Lattice outside fiber	Lattice inside fiber
Atom number	3.75×10^6	2.2×10^5	1.5×10^5	8.1×10^4
Transfer efficiency	-	6%	68%	54%
Transfer efficiency from MOT	-	6%	4%	2.2%
Lifetime-corrected Atom number	3.75×10^6	2.2×10^5	1.6×10^5	9.4×10^4
Transfer efficiency	-	6%	71%	59%
Transfer efficiency from MOT	-	6%	4.3%	2.5%
Loss channel	-	overlap between MOT and lattice	transport	transport and HCF coupling

Table 3.3.: Transfer efficiencies of atoms from MOT into the hollow-core fiber. Exemplary atom numbers at different stages of the experiment. From these values, the transfer efficiency from the MOT into the hollow-core fiber has been determined.

Here: limit is MOT to dipole trap efficiency, not transport! solve with further compressed MOT - dark SPOT? - or different dipole trap, will be discussed in outlook.

Note that lattice outside to lattice inside is twice the transport distance. (efficiency per distance unit / mm?) Outside: 29/4 = 7.25, inside: 41/8 = 5.125 percent loss per mm transport distance. Or non-lifetime corrected: 32/4 = 8, inside: 46/8 = 5.75 percent loss per mm transport distance. (check with far distance as in new section)

Transporting far inside the fiber

Measurements from 12.01.2018! (1000 kHz constant ramp over 99 ms -> 4 cm transport distance, initial OD of 2.9(3) OD) (series: 3221-3311). Also step wise distance measurements in 10 ms steps (29, 39,49,99). (Blowing beam on during measurement) Lifetime correction should be same as for 200 kHz linear ramp. Thus, probably more loss due to fiber influences. (compare with initial particle number series 1652-1660) + higher heating due to much longer time in deeper potential -> do measurements with amplitude ramps! (here γ ramps might actually be useful as they transport a large number of atoms into the fiber initially, then the potential is reduced, potentially leading to less heating. -> γ ramp shape figure from Ronja?)

Positions: 6.175 10.2 14.225 34.35 mm inside the fiber

THESIS DRAFT

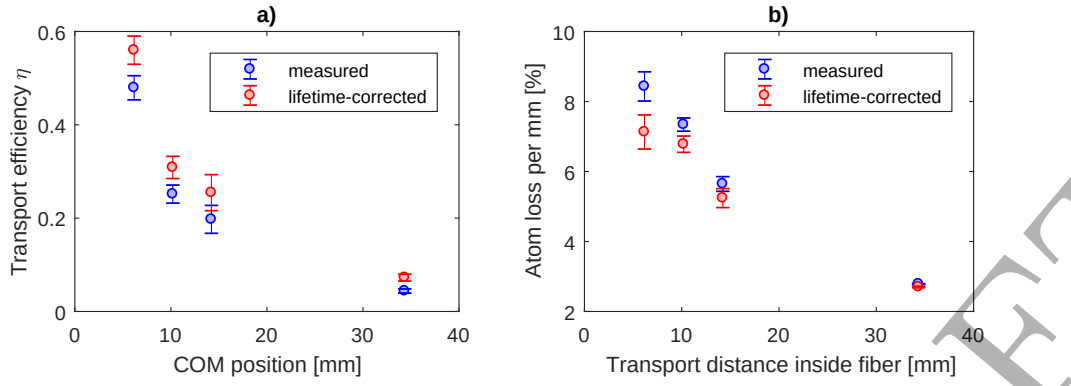

Figure 3.31.: Experimental and theoretical results from truncated Boltzmann inside the fiber. The solid line shows the survival probability as function of final temperature calculated using the truncated Boltzmann approach.

Transport efficiencies: 0.48 0.25 0.20 0.04 (lifetime-corrected: 0.56 0.31 0.25 0.07)

Calculate loss / mm for these values, e.g. lifetime-corrected first value: $44/8 = 5.5$ percent loss per mm transport distance and last value $93/36 = 2.6$ percent loss per mm transport distance; not lifetime-corrected first value: $52/8 = 6.5$ percent loss per mm transport distance and last value $96/36 = 2.7$ percent loss per mm transport distance. (in figure: only divided by distance inside fiber, full distance plot also saved)

Suggests that not fiber is responsible because loss per mm reduces. Seems to be general transport loss, maybe connected to the acceleration (non-adiabaticity) as discussed before. That would be higher for shorter distance transport ramps if time is varied as in this measurement.

Or: actually exponential loss! exp(-loss coefficient/mm) should give constant loss coefficient (kind of attenuation coefficient by transport distance, analogy to light loss when transported through a fiber)

3.5.3. Optimizing the phase-space density

Estimate phase-space density for the different amplitude ramps (use r_0 and atom number from release-recapture fit and length of cloud from typical outside measurements -> assume to stay constant). Note that the cloud radius is not directly comparable to the one shown for the outside measurements as here we really extract σ_0, i.e., we measure *in situ*. Same behaviour as outside: higher phase-space density for lower amplitude ramps. Phase-space density is absolutely higher due to smaller *in situ* radius. Similar values to the PSD calculated using the calculated radius outside the fiber. Lower transport efficiency is compensated by smaller cloud width (for low AR approximately the same temperature).

The cloud sizes obtained from the release-recapture fit are much smaller than the fiber core radius. Also similar radii for all ramps since atoms keep their energy level. Decrease for

THESIS DRAFT

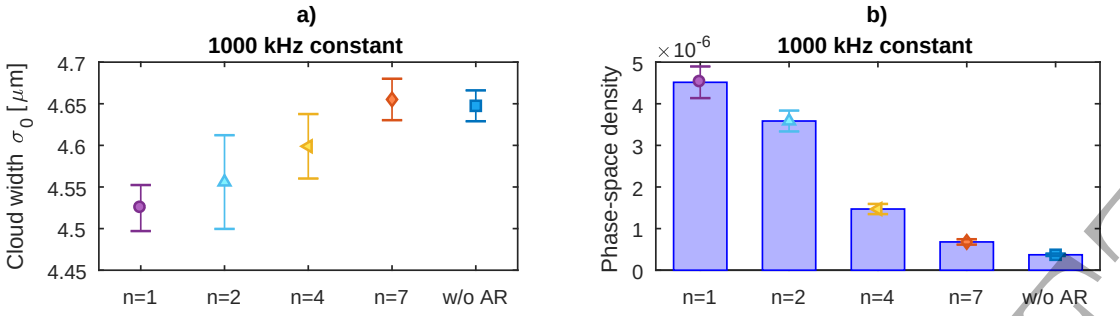

Figure 3.32.: Cloud widths and phase-space density inside the fiber. Shown are a) the cloud width and b) the phase-space density of atoms transported inside the fiber for the 1000 kHz constant frequency ramp and different amplitude ramp-downs. (Error bars represent statistical errors and errors from the fitting procedure.)

lower n amplitude ramps is due to truncated Boltzmann as discussed above which leads to an effectively lower energy state.

In Outlook?: One idea for achieving even lower radii could be to increase the trapping potential non-adiabatically (ramp up instantaneously) once the atoms are inside the fiber to produce an even smaller cloud for the colder atoms achieved by low n amplitude ramps. (if non-adiabatic, then atoms would keep their temperature and would therefore be transferred to lower energy levels, resulting in a smaller cloud size). Estimate cloud size by same temperature and normal trap depth w/o AR: e.g. for $n = 1$ to full trap depth, $\sigma_r \rightarrow \sigma_r/\sqrt{12.5} \approx \sigma_r * 0.3 \approx 1.3\,\mu$m. (That means that the atoms have a distance from the fiber wall of XX micrometers and are also within one blockade radius. For which state?)

THESIS DRAFT

3.6. Conclusion and Outlook

In the previous chapter, I have given an overview over our detailed study of transporting cold atoms with an optical conveyor belt towards and inside a hollow-core fiber. In particular, I have shown that by applying optimized frequency (acceleration) and amplitude (trap depth) ramps, we can achieve excellent control over a wide range of transport parameters, such as position, number and temperature of the transported atoms. However, we find that we have to compromise between number and temperature of atoms - we can either achieve a large number at a higher temperature or a lower number at the initial temperature or even below. Further, we have shown that we can control the sample preparation inside the hollow-core fiber in the same way. In addition, I have discussed two simple theory models for understanding our transport results, one based on the truncated Boltzmann distribution and one based on a classical transport simulation. Both models agree qualitatively well with our experimental data.

Outlook: overcome lifetime limitations by more filters or detuning dipole trap further away from resonance (attention with necessary powers). Or use shorter ramps with higher detunings: AOM double pass (problem with powers?)

Maybe by intensity and phase stabilization (intensity drifts from Ronja's measurements).

Overall transfer efficiency is mainly limited by the transfer efficiency of the MOT into the dipole trap. Therefore: increase MOT density (either by dark SPOT, stronger compression or additional crossed dipole trap) for better transfer efficiency.

Use a crossed dipole trap at the MOT position to produce smaller / shorter atomic samples. Then the fiber can be sampled / investigated in much higher spatial resolution. Estimate trapping parameters / beam sizes / powers.

Possibly, a crossed dipole trap will allow for splitting the atomic cloud and for transporting multiple small clouds into the fiber. First experimental tests are currently taken. Higher atomic density in MOT might lead to better loading efficiency of dipole trap.

In this outlook, I would also like to briefly present two side projects related to optimizing the transport procedure which I have worked on during the course of my thesis. Firstly, until now, I have shown how we have optimized the transport in a manual way. In principle, also more modern approaches such as employing machine learning would be possible. In section 3.6.1, I will briefly present our first efforts and preliminary results to do this optimization scheme using a machine learning algorithm. Secondly, I have just discussed that one limit is the transfer efficiency into the dipole trap, which could be improved by higher atomic densities. One typical way to achieve these is using a so-called dark SPOT configuration. In section 3.6.2, I will briefly present our setup and the first preliminary results for using a dark SPOT to increase the atomic density.

THESIS DRAFT

3.6.1. Transport optimization with machine learning

Very recently, machine learning has proven very successful for finding solutions to very complex and complicated problems with large parameter spaces which often are not easily solvable by either an analytic expression or systematic manual optimization. Examples include ... It works in the way that the computer tries to find optimal values by randomly sampling the parameter space and extrapolating the best results without the need to know or find out the physical model behind the data. It can also identify a parameter landscape, which shows how important each parameter is for the result or whether some parameters can effectively be neglected.

Machine learning has already been employed in the atomic physics community to optimize experimental parameters, e.g. for the production of Bose-Einstein condensates [85], where they could... using a XX-dimensional parameter space. Their "Machine-Learner Online Optimization Package" (M-LOOP), which is provided online [**?**], can also be applied in our case when feeding it the correct experimental parameters as I will discuss in the following. After finishing our manual optimization of the transport as discussed in this previous chapter, I have implemented an algorithm to test this machine learing algorithm and I have made the first preliminary measurements to showcase its functionalities. They already provide some insight into how the machine learning works and whether it provides a useful resource for our (future) optimization procedures. However, a complete optimization is beyond the scope of this thesis and may in the end not be necessary for our case, since with knowledge of the physics of the problem we may be faster than the machine learning algorithm.

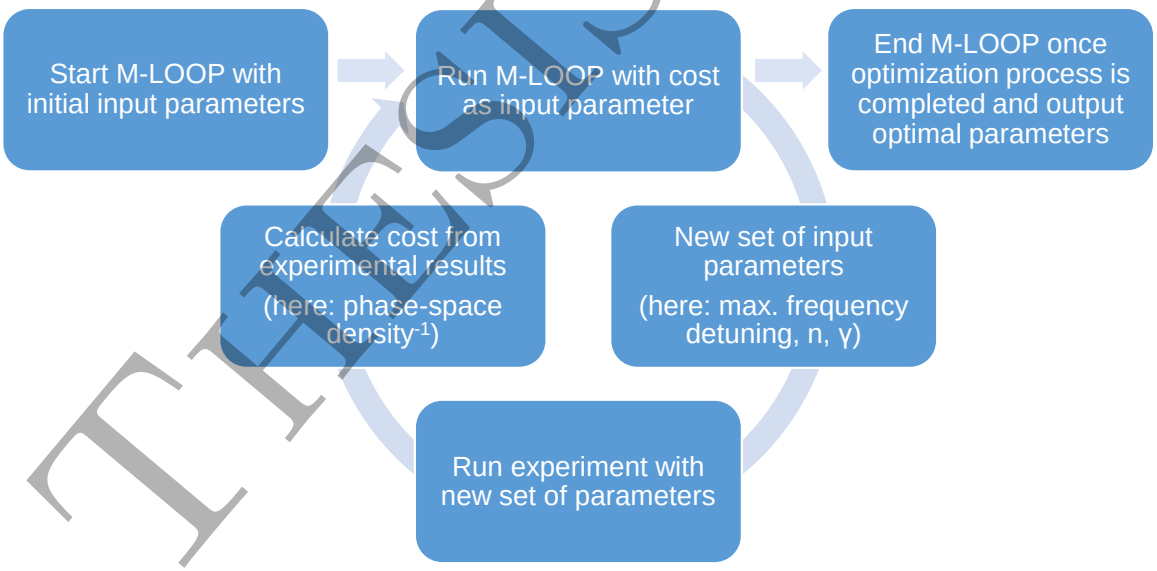

Figure 3.33.: Machine learning sequence. Shown is a typical sequence when using M-LOOP for a machine learning optimization procedure.

THESIS DRAFT

Figure 3.33 shows a flowchart of programs and processes used for our machine learning optimization. In general, all communication between M-LOOP and our experiment is done via generating text files. We initialize M-LOOP with a configuration file which determines the initial input parameters as well as the conditions for the optimization process, such as boundary conditions for the parameters. For optimizing the transport, our parameters are the maximum frequency detuning $\Delta\nu_{\mathrm{max}}$ and the two parameters for the amplitude ramp-down n and γ. In this case, we always use a constant frequency ramp and we adapt the timing of the ramp so that the atoms always reach the same final position.[2] For the first run, M-LOOP will simply create an output file with the input parameters. We then run the experiment with the set of parameters created by M-LOOP. As the result of the experiment, we finally determine phase-space density for this specific parameter set (here using the approach of estimating the phase-space density via the experimentally measured cloud radius). Since M-LOOP can only be used to find a minimum value of the optimization process, we calculate the inverse of the phase-space density and feed it back to M-LOOP as the so-called "cost" of the experiment. Here, also experimental uncertainties can be included. From this cost, M-LOOP determines the next set of input parameters, which are fed to the experiment and so forth. Once the previously determined stopping condition is reached, M-LOOP ends the optimization process and outputs the optimal parameters determined from this run.

Figure 3.34 shows the results of such a sequence for the machine learning optimization procedure of the transport process. For this specific example, we use starting conditions of $[\Delta\nu_{\mathrm{max}}, n, \gamma] = [1000\,\mathrm{kHz}, 7, 1]$, with minimum boundaries of $[100\,\mathrm{kHz}, 0.5, 0.1]$ and maximum boundaries of $[1500\,\mathrm{kHz}, 12.74, 1]$. To test the algorithm, we use a maximum number of runs as a stopping condition, rather than a specific phase-space density or optimal value to be reached. In this case, we choose 10 runs in total or 5 runs without finding better parameters, whichever occurs first. Additionally, it is possible to define a limit for how much deviation from previous values is allowed. For this example, we set a limit of 40% deviation which is allowed from the best parameters the algorithm has encountered so far. Plotted is the phase-space density as function of the number of experimental runs within one optimization sequence. Here, a high phase-space density corresponds to a low cost and is therefore the goal of the optimization procedure. We see that the results generally do not vary by a large amount. This indicates that the algorithm has mainly chosen medium parameters, with no strong outliers in either direction, neither very good nor very bad. An exception is run number 4, which clearly gives the best result in this series with a phase-space density of around 6×10^{-7} with parameters $[\Delta\nu_{\mathrm{max}}, n, \gamma] = [1219\,\mathrm{kHz}, 8.3, 0.72]$. As we have chosen the initial parameters which gave good results in our manual optimization, also the best parameters are not far from the starting values. This gives good confirmation that indeed our manual optimization was not a bad choice.

Next, I want to further analyze the influence of the individual parameters on the results. For this, I visualize the resulting phase-space density in the three-dimensional parameter space $[\Delta\nu_{\mathrm{max}}, n, \gamma]$, as shown in figure 3.35. Here, both the size of the markers and the colorcode indicate the achieved phase-space density for each run. It is apparent that both

[2] Note that in this specific procedure, we are somewhat limited with the precision of frequency detuning as we can only adapt the timing in ms steps and therefore the final position might slightly vary.

THESIS DRAFT

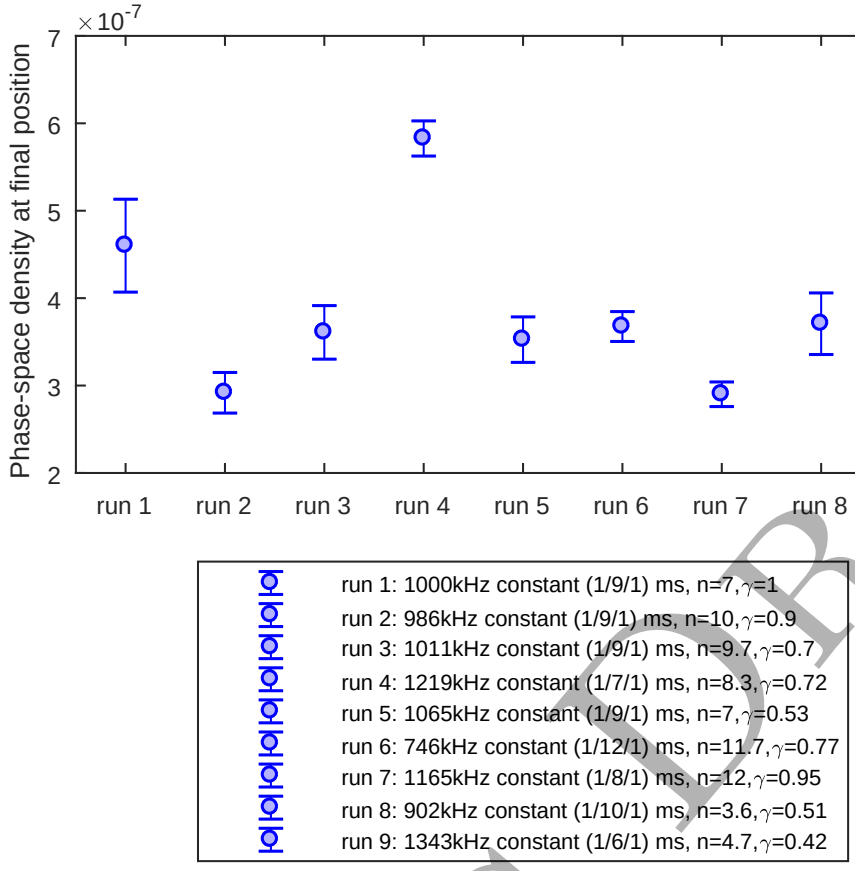

Figure 3.34.: Machine learning results. Shown are the results of a typical sequence when using M-LOOP for a machine learning optimization procedure. The parameter for optimization (here: phase-space density) is plotted against the number of experimental runs. The experimental parameters for each run are given in the legend.

results with the highest phase-space density lie close to each other. The results with the lowest phase-space densities lie at the outer regions of the parameter space, suggesting that extreme values might limit the performance of the system. From this visualization, it also becomes clear that not the whole parameter space has been sampled equally by the machine learning algorithm.

To further study the sampled parameter space for our machine learning optimization example sequence, figure 3.36 a) shows the parameter range as function of the number of the experimental runs. Here, 0 denotes the minimum and 1 the maximum value for each parameter. We can clearly see that while n and γ are varied across most of their parameter space, the spread of the maximum frequency detuning is notably less. Also, none of the values are varied closely to their minimum value, very likely due to our rather high initial choice of parameters. This is especially interesting as we have seen earlier that for low values of n, the phase-space density increases compared to higher values. The limit in sampled parameter space becomes even more clear in the three-dimensional parameter space as shown

THESIS DRAFT

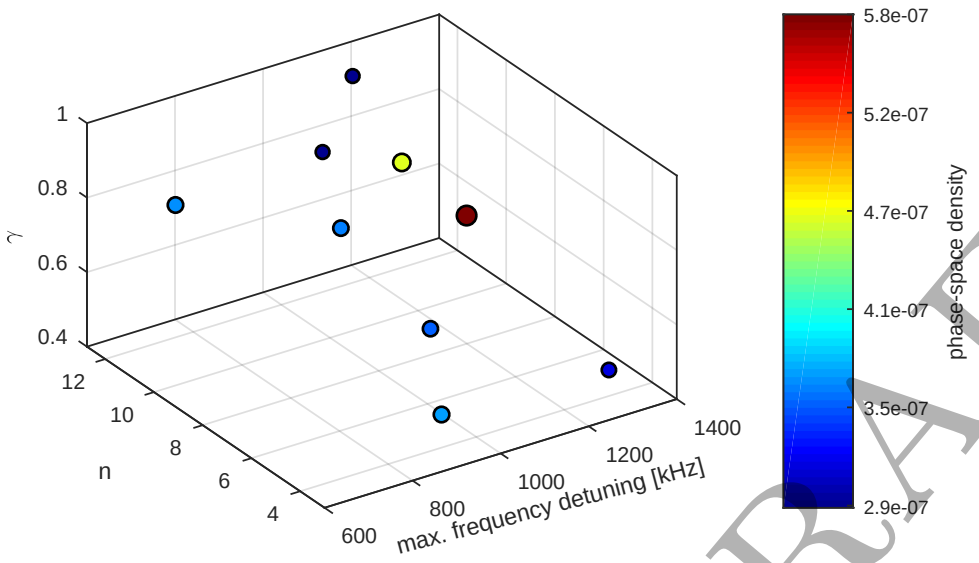

Figure 3.35.: Machine learning results in parameter space. Shown are the results in the sampled parameter space for a typical sequence when using M-LOOP for a machine learning optimization procedure. Here, our parameters are the maximum frequency detuning and the two parameters for the amplitude ramp-down n and γ. Both the size of the markers and the colorcode indicate the achieved phase-space density for each run.

in figure 3.36 b). Note that in contrast to figure 3.35, here the whole accessible parameter space is displayed, with the numbers indicating the direction of the sequence. We see that for the blue data points corresponding to the sequence discussed previously and also shown in figure a), the M-LOOP algorithm stays within a certain region of our parameter space and that most neighboring points sit in proximity to each other. This behaviour can be varied by setting how much each parameter is allowed to derivate from its previous value. For this run, this setting has been set to 40 % deviation allowed from the best parameters. Thus, at least for this small amount of experimental runs, the sampled parameter space strongly depends on our choice of initial parameters. As a test, we perform a short run with no such limitation, indicated by the red data points. Here, we see that the parameters are distributed much further away from each other. Even after only the third run, the algorithm has already traversed most of the parameter space. For sampling a large region of the parameter space within a limited amount of runs, I would therefore recommend not to limit the deviations from previous data points, since the machine learning can best show its strengths for random samples of the parameter space.

In conclusion, I have given a short insight into an alternative approach for optimizing the transport using a machine learning algorithm. Further, I have shown that even for a short sequence, the machine learning algorithm can already identify good parameters and depending on the settings cross large regions of the parameter space. If applying M-LOOP for future transport optimizations, I would recommend to use no limit on the parameters as discussed above. Also, a larger number of runs would give more insight into the sampling behaviour of the algorithm and could possibly identify optimal parameters even outside the

THESIS DRAFT

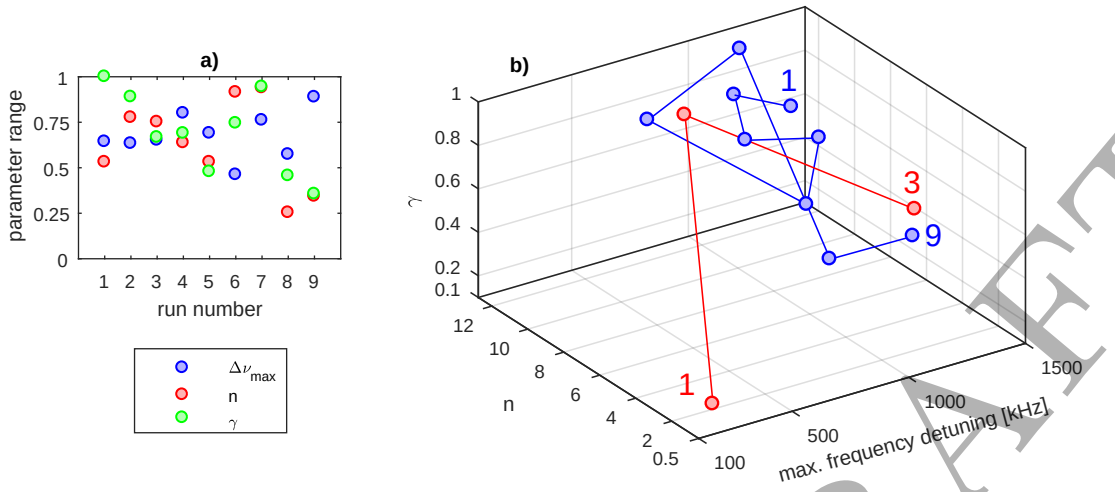

Figure 3.36.: Machine learning parameter space. Shown is the sampled parameter space for a typical sequence when using M-LOOP for a machine learning optimization procedure. Here, our parameters are the maximum frequency detuning and the two parameters for the amplitude ramp-down n and γ. Note than in contrast to the previous figure, the whole accessible parameter space is displayed. The numbers indicate the first and the ninth run of the sequence.

exact numbers sampled by the algorithm once a potential landscape has been identified. Since a large number of runs is rather time-consuming, here it would be benefitial to include a learning algorithm for previously obtained experimental results instead of conducting the whole optimization online as demonstrated in the previous section. However, at least in these first tests, the optimal results found by M-LOOP did not differ too much from the results we have found in our manual optimization. Indeed, for systems where the influence of the parameters can be understood in a physical model such as our transport model discussed earlier, the potential of machine learning is limited. Maybe it would have been good for initial guesses before we had any knowledge about the behaviour of our system. Or it could be used when including further parameters such as the ramp shape.

3.6.2. A dark SPOT to increase the atomic density

As discussed above, one of the major limiting factors for our transfer efficiency into the hollow-core fiber is our loading efficiency from the MOT into the dipole trap. Ideally, this loading efficiency can be improved by increasing the atomic density in the MOT and therefore optimizing the overlap between cold atoms in the MOT and the dipole trap. A common way to increase the atomic density is a so-called dark spontaneous-force optical trap (dark SPOT), first reported in [86]. In this section, I will briefly discuss the basic principle of a dark SPOT and present the first preliminary results of implementing it in our setup.

The working principle of a dark SPOT relies on a not-closed cooling transition, where a repump beam is needed to repump the atoms into the cooling cycle. The dark spot

THESIS DRAFT

describes a "dark" region in the center of the MOT, where no repump light is shone on the atoms. Therefore, atoms which have already been cooled enough to stay in the center of the MOT will fall into a dark state, which doesn't interact with either cooling or repump light. However, if they leave this dark region, they will again be repumped and participate in the cooling cycle. Often, an additional so-called "depump" beam is used in the center of the trap to further assist in pumping the atoms into this dark state [87, 88]. A dark SPOT is commonly used in mixture experiments working with different atomic species to avoid light-assisted collisions between the atoms ([88, 89]). It has also recently been shown that is can be used to achieve very high atomic densities of more than $10^{12}\,\mathrm{cm}^{-3}$ by eliminating reradiation forces [87].

In a previous incarnation, our experimental setup also featured a dark SPOT [70]. However, while rebuilding the MOT laser system when changing from ^{85}Rb to ^{87}Rb , the dark SPOT setup has been removed [11]. During the course of my thesis, I have set up an optics system for a dark SPOT for ^{87}Rb and I have performed first characterization measurements of this dark SPOT configuration. In these preliminary measurements I could confirm that a dark SPOT indeed increases the atomic density by at least a factor of two. Further optimizing this setup, implementing the dark SPOT into the running experiment and characterizing the improvement for loading atoms into the dipole trap remain tasks beyond the time frame of this thesis.

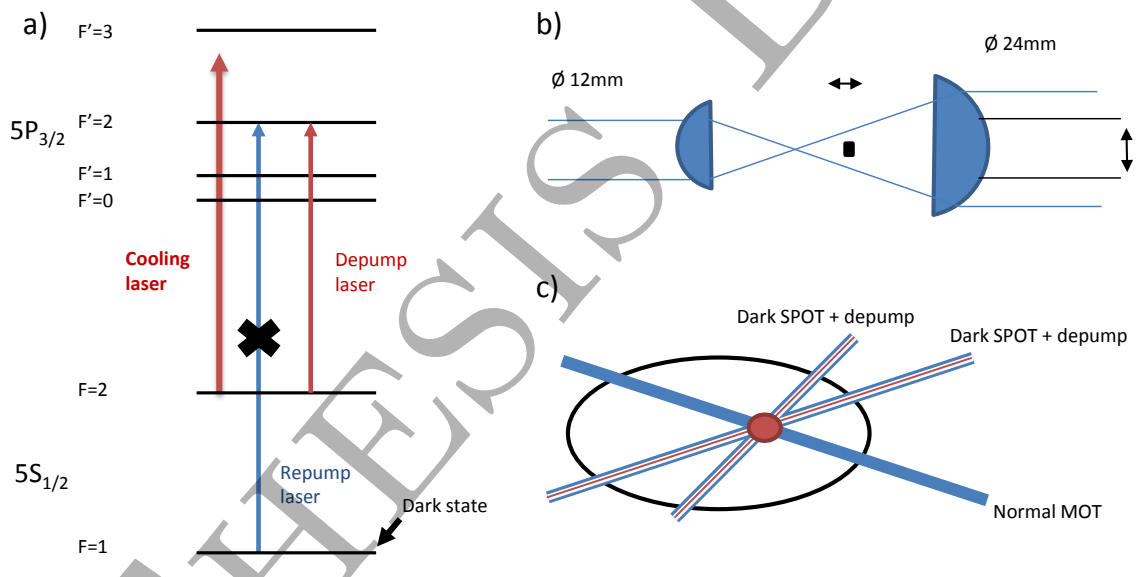

Figure 3.37.: Setup and principle of a dark SPOT. In a), the relevant atomic levels as well as laser transitions for the dark SPOT for ^{87}Rb are shown. In b), our setup for creating a dark spot in the repump beam inside a telescope is shown. In c), our laser paths for the dark SPOT repump and depump beams are shown.

The level scheme and the necessary transitions for the ^{87}Rb dark SPOT are shown in figure 3.37 a). In addition to the cooling laser, which is red-detuned from the $5S_{1/2}(F = 2) \rightarrow 5P_{3/2}(F' = 3)$, typically a repump laser resonant to the $5S_{1/2}(F = 1) \rightarrow 5P_{3/2}(F' = 2)$ transition is used. Here, the central part of the repump laser will be blocked as dicussed

THESIS DRAFT

above. In addition, we use a depump beam resonant to the $5S_{1/2}(F = 2) \rightarrow 5P_{3/2}(F' = 2)$ transition to enhance the pumping into the dark state $5S_{1/2}(F = 1)$.

The dark region in the repump beam is created by a glass plate with an opaque spot of approximatley 0.5 mm diameter in the center, which is placed inside the 2:1 telescope for magnifying the repump beam as shown in figure 3.37 b). The disk is mounted on a translation stage so that by adjusting its position inside the telescope, the size of the resulting dark spot can be determined. A typical dark spot diameter used is approximately 1 cm, which is comparable to other experiments [87, 88]. The size of the hollow repump beam is chosen to match the size of the cooling beams of the bright MOT. After preparing this dark spot repump beam, the depump beam is overlapped so that it propagates in the center of the hollow repump beam. I found this alignment to be critical for all atom numbers and densities measured in the following, as misalignment can lead to atoms being blown away from the trapping region. We choose a depump beam diameter of about 2 mm, which is a medium beam size compared to other experiments, which vary between depump beams the size of the whole dark SPOT [87] and a focussed beam in the center of the dark SPOT [88]. Finally, the hollow repump and the depump beam are overlapped with the bright MOT cooling beams on two axes as shown in figure 3.37 c), so that they are propagating in four out of the six MOT beams and form a three-dimensional dark region in the center of the MOT.

Our timing sequence of the dark SPOT works as follows: First we load the atoms in a bright 2D-3D MOT configuration as described earlier in this thesis, then hold the bright 3D MOT for about 1 s with the 2D MOT switched off. We then switch to the dark SPOT configuration by switching off the normal repump beam and instead switching on the dark SPOT repump and the depump beams. We find the optimal dark SPOT loading time to be 100 ms, which is comparable to other experiments. Finally, we compress our atoms in a dark spot CMOT configuration for 80 ms, in the same way as discussed earlier in this thesis with the addition of the dark spot repump and the depump beam. These timings have been optimized for achieving the highest atom densities, while we see that the atom number decreases for any number of additional loading or compression time.

For the power of dark SPOT repump beam, we typically chose around 4 mW. In contrast to other other experiments [70], we see no critical dependence on power level. Similarly, we chose a typical power of around 4 mW for the depump beam. Again, we see not clear evidence that the performance of the dark SPOT depends on the power level, in contrast to other experiments [88]. It seems as if we are already operating on some plateau of the dark SPOT performance with regard to the power levels. Therefore, optimizing the exact powers does not seem critical in our case.

Figure 3.38 shows a comparison between the bright MOT and the dark SPOT configuration for the experimental settings discussed above. Both absorption images and the resulting maximum atomic densities obtained from a fit to these absorption images are displayed for bright MOT and dark SPOT with and without additional depump beam. These measurements clearly indicate that the dark SPOT configuration is working as the atomic density increases from about $7.5 \times 10^{10}\,\mathrm{cm}^{-3}$ to about $1.1 \times 10^{11}\,\mathrm{cm}^{-3}$ even without the additional

THESIS DRAFT

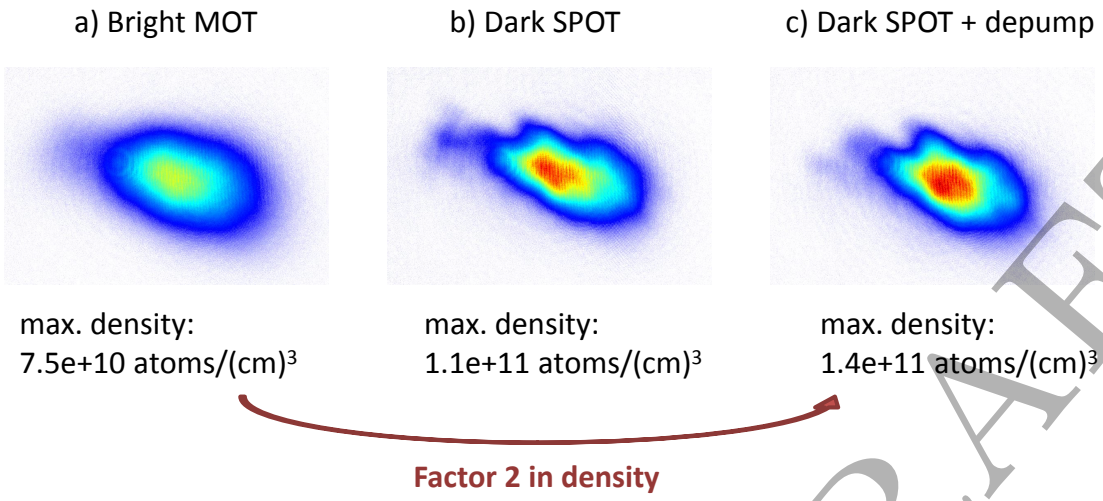

Figure 3.38.: Comparison between bright MOT and dark SPOT configuration. Shown are absorption images taken for a) the bright MOT configuration, b) the dark SPOT configuration and c) the dark SPOT configuration with an additional depump beam. Note that all images are displayed in the same colour scale. For each configuration, the maximum atomic density is obtained from a fit to the absorption images and displayed beneath the image. From a) to c), we find that the density increases by a factor of two.

depump beam. For the dark SPOT configuration with an added depump beam, the maximum atomic density even increases by a factor of two compared to the normal bright MOT configuration to a value of about $1.4 \times 10^{11}\,\mathrm{cm}^{-3}$. Typical temperatures of the atoms loaded dark SPOT configuration are about $30\,\mu\mathrm{K}$, which is comparable to temperatures in the bright MOT. Our density is comparible to previous values achieved in our experiment for the ^{85}Rb dark SPOT [70]. The best value reported so far is an increase of the atomic density by two orders of magnitude to $1.3 \times 10^{12}\,\mathrm{cm}^{-3}$ [87]. Although most other experiments report much lower typical values, these numbers nevertheless hint at an optimization potential for our setup.

One potential optimization could be the depump beam, as the presence of the depump beam has been seen to improve the performance of the dark SPOT [87]. I have therefore further investigated the influence of the depump beam by varying its frequency. Figure 3.39 shows the atom number as well as the maximum atomic density as a function of the depump laser frequency. Within the experimental error bars, the atom number shows no influence of the laser frequency. In contrast, the maximum atomic density is strongly affected by the depump frequency. Clearly, the density is highest when the depump beam is on resonance and drops to the background value of the dark SPOT without depump beam away from the resonance position. Therefore, we keep the depump laser on resonance for our measurements.

Finally, I have studied the influence of the dark spot size on atom number and atomic density, as shown in figure 3.40. For this, I have varied the dark spot size in the final

THESIS DRAFT

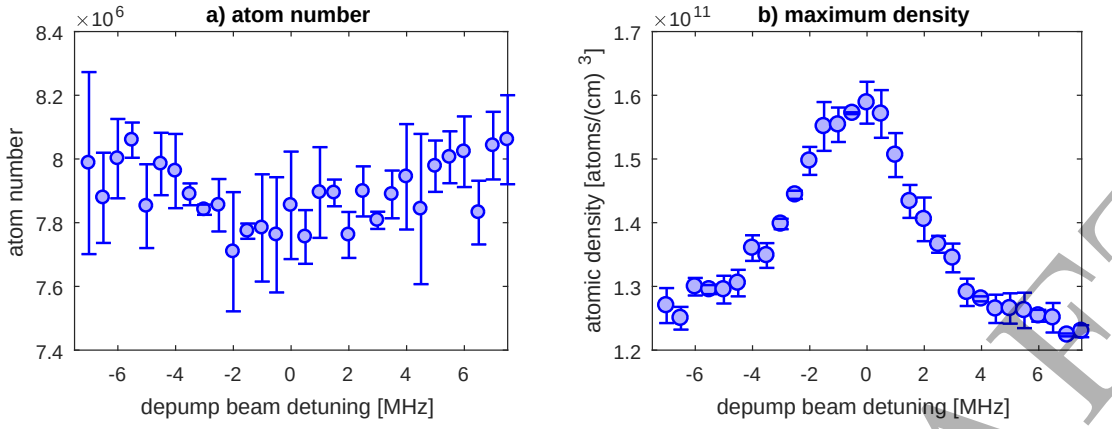

Figure 3.39.: Influence of the depump frequency. Shown is the number of atoms and the atomic density in the dark SPOT as a function of the depump beam detuning, which is varied over the resonance position.

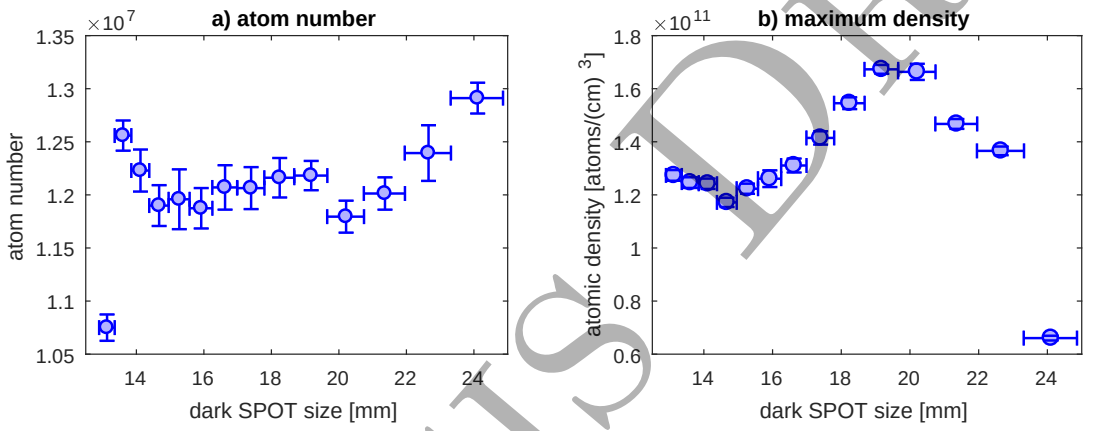

Figure 3.40.: Influence of the dark spot size. Shown are the number of atoms and the atomic density in the dark SPOT as a function of the dark spot size. This size of the final dark spot has been calculated from the position of the dark spot inside the telescope and increases from left to right. The rightmost data point belongs to a dark spot covering the full size of the repump beam.

beam by changing the position of the dark spot inside the telescope (recall figure 3.37 b)). While the atom number stays approximately constant for all dark spot sizes, a clear increase in atomic density with increasing dark spot size can be seen. Only when the dark spot covers the whole size of the repump beam (rightmost data point), the atomic density drops drastically. Note that even for this point, the number of atoms is not affected. The maximum density is reached for a dark spot size of about 20 mm in diameter in the final hollow repump beam. For smaller dark spot sizes below approximately 16 mm, the atomic density stays at a constant plateau. Since in other experiments, the highest highest atomic densities have been observed for dark spot sizes far above the size of the MOT [87, 88], I have not tested very small spot sizes for our setup, the smallest being around 10 mm used for the measurements presented earlier. Also the general behaviour of the atomic density improving for increasing dark SPOT size and then dropping again matches well

THESIS DRAFT

with experimental observations previously reported by other groups [87, 88].

Note that these previous measurements of the different dark SPOT characteristics were performed on different measurement days which leads to slight fluctuations of the absolute number of atoms and maximum density. However, the difference between the different configurations always remains the same and I am only making statements about the relative increase or decrease of the numbers with regard to the parameters.

In conclusion, after setting up a dark SPOT for ^{87}Rb, I could confirm in preliminary measurements that a dark SPOT configuration can indeed help to increase the atomic density. With the optimization of just a few parameters, I could already obtain a density increase of about a factor two compared to the bright MOT configuration. However, comparing these numbers to similar experiments, we see that there is still quite some room for improvement regarding the atomic density. The next steps for further optimizing this dark SPOT and implementing it into the running setup will be to replace the MOT compression phase by a dark molasses. For this, it is necessary to obtain better control over stray magnetic fields. Afterwards, the most interesting measurement for our experiment will be to characterize the loading of the atoms from the dark SPOT into the optical lattice. Ideally, an increased atomic density will immediately transform into a higher loading efficiency and also a higher density in the optical lattice.

THESIS DRAFT

THESIS DRAFT

4. Excitation of cold Rydberg atoms inside a hollow-core fiber

In this chapter, I will present the results of the second main focus of my thesis, namely exciting cold atoms to Rydberg states inside the hollow-core fiber. Parts of this chapter have been published in [13] and [73]. The experimental setup was built together with Mohammad Noaman and Chantal Voss, with the initial design of the setup planned by me, and most experiments were performed in a team effort together with Mohammad Noaman, who will therefore also discuss some of the results in his PhD thesis [71]. Most of the analysis and interpretation of the data, in particular regarding the interleaved two pulse measurements, has been my own work. The part about the lensing model has been based upon the calculations of Mohammad Noaman. Some parts of the setup and the results have already been described in the bachelor and master thesis of Chantal Voss [90, 91], which were co-supervised by Mohammad Noaman (master thesis) and me (bachelor thesis) during the course of our theses.
The work on cold Rydberg atoms outside an optical nanofiber has been done in the group of Prof. Síle Nic Chormaic at OIST during my research stay generously supported by a JSPS Short Term Fellowship.

This chapter contains one of the main results of my thesis. We have shown for the first time that it is possible to excite cold Rydberg atoms inside a hollow-core fiber. First, I will first give a general introduction to Rydberg atoms and how to probe and excite them with electro-magnetically induced transparency (EIT). Then I will dicuss our measurements of exciting cold Rydberg atoms inside a hollow-core fiber. To further study the influence of the fiber on the EIT signals, I will then discuss an interleaved probing scheme, which measures OD and EIT at the same time. Further effects on shifts and losses. Finally, I will give some outlook to first initial measurements on the dependence of our signal on both the Rydberg state and the position inside the hollow-core fiber. In the end, I will briefly contrast our setup with the complementary approach of exciting cold Rydberg atoms outside an optical nanofiber, which I have worked on at OIST.

THESIS DRAFT

4.1. Exciting and probing Rydberg atoms via electro-magnetically induced transparency (EIT)

Here, we will learn about the most important properties of Rydberg atoms, how to excite and probe them via electro-magnetically induced transparency and what technical steps are necessary for this.

4.1.1. Rydberg atom properties

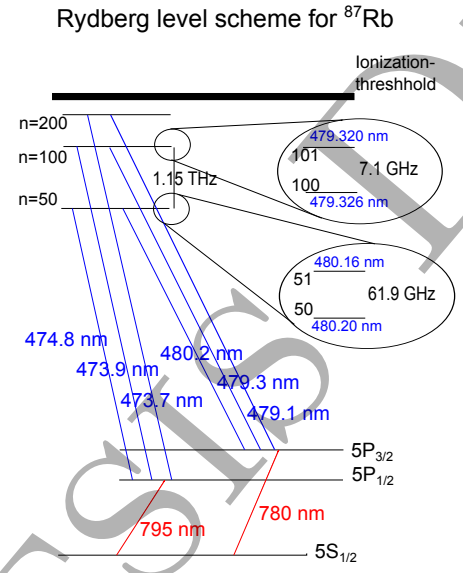

Figure 4.1.: Rydberg levels and excitation wavelengths. Sketch of the level spacing of different Rubidium energy levels up to Rydberg states of $n = 200$ (not to scale). Necessary wavelengths for a two-photon excitation are given.

Overview Rydberg atom properties, scaling with principal quantum number

energy levels and typical distances between energy levels (see figure 4.2

4.1.2. Exciting and probing via electro-magnetically induced transparency

Explain EIT in general (coherent process, interference between two beam paths leads to opening of transmission window)

THESIS DRAFT

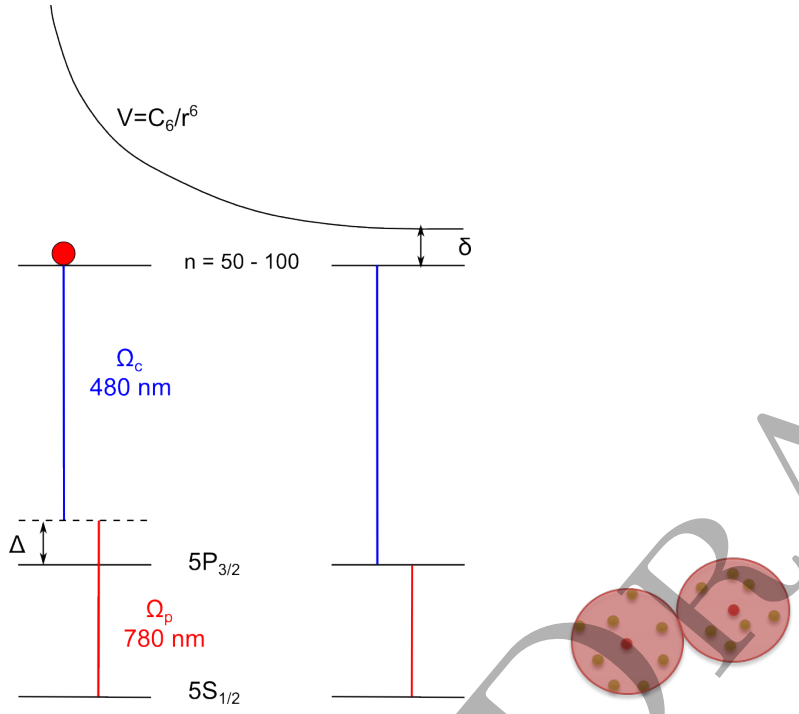

Figure 4.2.: Rydberg excitation scheme and Rydberg blockade.

"For further analysis, we fit the spectra with an EIT formula according to Ref. [43], which is valid in our limit of low probe Rabi frequency:

$$T = \exp\left[-OD\,\mathrm{Im}\left(\chi\right)\right] \tag{4.1}$$

with the susceptibility

$$\chi = i\gamma\left(\gamma - 2i\Delta + \frac{|\Omega_c|^2}{\gamma_{\mathrm{ryd}} - 2i\left(\Delta_c + \Delta\right)}\right)^{-1}, \tag{4.2}$$

where the detuning and decay rates of the probe and the control transition are denoted by Δ and γ and by Δ_c and γ_{ryd} respectively. For the Rydberg state, we are interested in the additional decay or dephasing rate $\gamma_{\mathrm{ryd},2} = \gamma_{\mathrm{ryd}} - \gamma_{29\mathrm{S}}$, where $\gamma_{29\mathrm{S}} = 2\pi/(21.7\,\mu\mathrm{s})$ is the natural linewidth [92]. Additional dephasing can for example stem from inhomogeneous electric or magnetic fields. Ω_c is the Rabi frequency of the control beam. In the absence of a control beam, i.e. in the case of $|\Omega_c| = 0$, eq. (4.1) reduces to eq. (2.14)." [13]

important parameters: e.g. Rabi frequencies (EIT vs. Autler-Townes regime), decoherence rates etc.

In principle, also for the EIT measurements, the lensing effect needs to be considered as lensing can alter the shape of our spectrum as discussed before. Figure 4.3 shows EIT measurements outside the hollow-core fiber for different detunings together with fits with and without lensing. Again, the lensing effect mainly influences the background OD signal

THESIS DRAFT

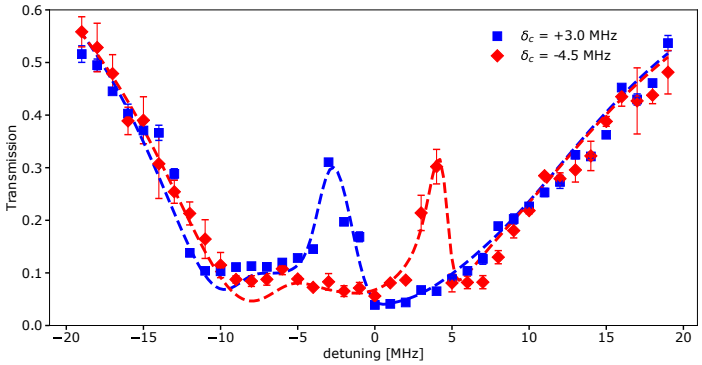

Figure 4.3.: Rydberg EIT fits with lensing. Figure adapted from our publication [73]. Include fits w/o lensing!

(maybe slope of EIT curve?). Compare fit parameters such as Rabi frequencies, decoherence rates and esp. shifts and discuss influence of lensing.

-> For large number of pulses, the OD will have decreased enough so that normal EIT can be used to estimate all the parameters and lensing fit is not necessary. (Since lensing fits are computationally much more expensive.)

4.1.3. Design considerations for the experimental setup

Briefly review our setup. Blue laser is added and overlapped by also coupling through the hollow-core fiber (one of the main requirements for choosing our fiber!). Rest of setup stays mainly as it was in earlier chapters.

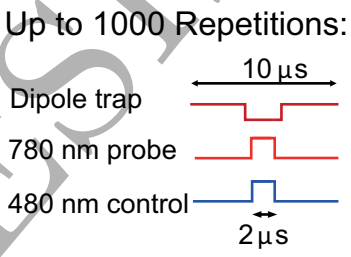

Figure 4.4.: Sketch of EIT pulsing sequence.

Figure 4.4 sketch of pulsing sequence. Blue is pulsed on at the same time as probe pulse (unless indicated differently in later measurements). Details for pulse overlap can be found in Noaman's thesis.

Consideration of hot (room-temperature vapor) vs. cold atoms (transition time broadening -> higher probe Rabi frequencies needed, higher degree of control over position and distribution of cold atomic sample -> refer to previous chapter), consideration co- vs. counterpropagating EIT (should mainly matter for room-temperature setup, discuss Doppler mismatch)

THESIS DRAFT

Toptica frequency-doubled laser system for creating the blue light. Considerations: EIT locking scheme for convenience for now. Tune the blue laser frequency only by AOM (will be a limit later on! -> cavity in outlook).

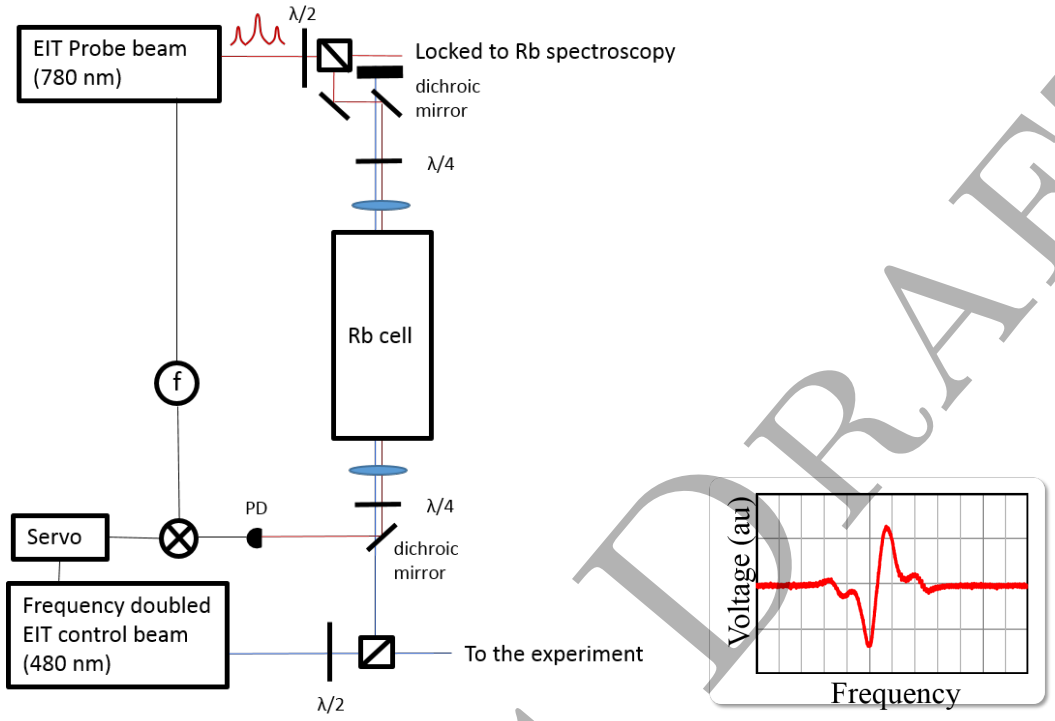

Figure 4.5.: EIT laser locking scheme. Error signal from poster DPG Hannover 2016 (analyze and plot properly!).

4.2. Exciting Rydberg atoms inside a hollow-core fiber

Here, we will learn about the challenges when exciting Rydberg atoms inside a hollow-core fiber. In particular, we will discuss the influence of electric fields inside the fiber and study the temporal behaviour of the Rydberg excitations.

We expect (and other people have seen) that Rydberg atoms close to surfaces experience large lineshifts and broadenings. Therefore, in the following, I will study Rydberg EIT signals for atoms inside and outside the fiber and compare these signals, paying special attention to lineshifts and broadenings. Later, I will in particular investigate the time-dependent behaviour of these signals, using a timeresolved measurement technique to distinguish between EIT excitation and loss.

Figure 4.6 shows EIT measurements and discussions from paper: measurements inside and outside the fiber.

THESIS DRAFT

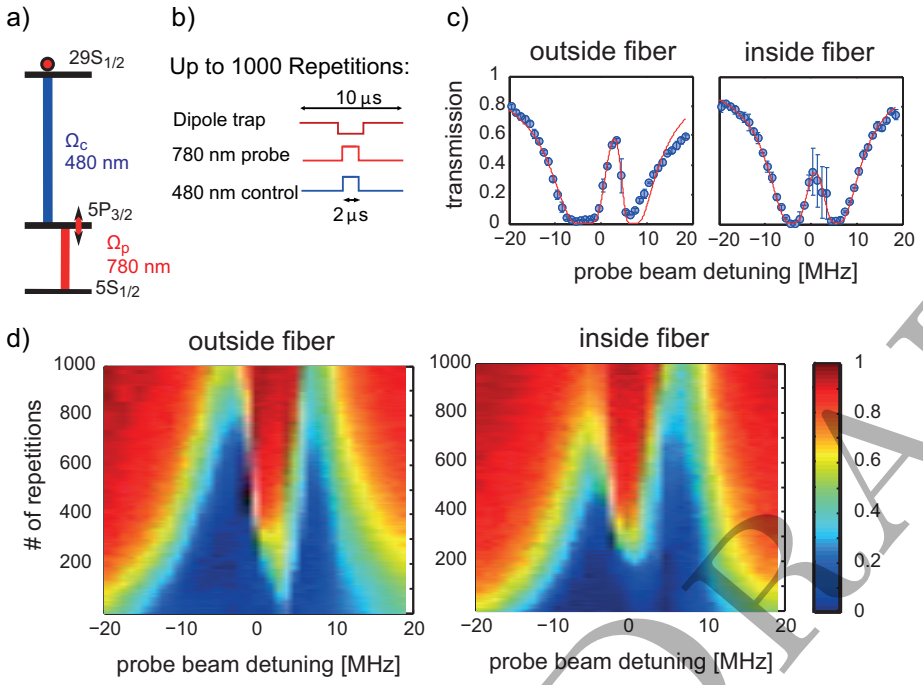

Figure 4.6.: Comparison of EIT signals inside and outside the fiber. " (a) Rydberg excitation scheme. (b) Single-pulse measurement sequence. (c) EIT signals inside and outside of the fiber (∘, averaging over 20 repetitions starting from repetition number 201, statistical error bars) and EIT fit (solid line). (d) Time resolved EIT signals inside and outside of the fiber (Moving average over 20 neighboring repetitions)." Figure adapted from our publication [13]. "Reproduced with permission from"

Two main observations:
1. Absolute shift between inside and outside and broadening / higher decoherence inside -> influence of fiber / electric fields inside the fiber (section 4.2.1)
2. Time-dependent shift of the EIT peak with number of repetitions, both inside and outside -> influence of measurement / loss processes (section 4.2.2)

4.2.1. Influences of the fiber on the EIT signal

Compare measurements inside and outside the fiber

We observe a shift of the EIT peak between inside and outside the hollow-core fiber. We can assume that for measurements inside the hollow-core fiber, we observe an electric field dependent shift (scaling according to Stark effect), shift measurement (refer to later measurement presented in outlook), very likely due to presence of adatoms on fiber wall or other inhomogeneities on fiber wall (larger shift later the higher the Rydberg state).

Also inside the fiber, we observe broadening of the EIT signal -> additional decoherence (due to inhomogeneous fields or additional decay / dephasing), very likely due to presence

THESIS DRAFT

of adatoms on fiber wall or other inhomogeneities on fiber wall (larger broadening later the higher the Rydberg state)

Already in these single-pulse measurements, we can observe a shift of the EIT peak with number of repetitions (time-resolved signal in figure d). Both inside and outside the fiber, this shift is towards lower red detunings, i.e. the blue beam detuning increases. -> will be investigated in more detail within this chapter. Maybe related to shift discussed above as the signals inside and outside may shift differently with time.

Temperature of atoms inside fiber: $\approx 500\,\mu$K from old release-recapture measurement (see paper supplement), confirmed by new release-recapture analysis (slightly lower, $\approx 470\,\mu$K without first data point to $\approx 490\,\mu$K for all data points). Note that this transport procedure was slightly different as in that we ramped down the dipole trap powers to 50% during the transport times.

Comparison with other experiments exciting Rydberg atoms close to surfaces

"Recently, the influence of stray electric fields on Rydberg atoms near silica-coated gold surfaces could be measured in the group of Robert Spreeuw in Amsterdam [Naber 2015]. It can be expected that due to the large electric dipole moment of the Rydberg atoms, also other interactions of the atoms with the fiber wall are significant - especially for high n quantum numbers. To characterize these interactions EIT spectroscopy can be used. Due to the high degree of control over the cold atoms, it will be possible to map out the influence of the fiber on the coherence and lifetime of the Rydberg excitations and analyze possible fiber - Rydberg atom interactions. As a long term goal, the deep understanding of the interaction of polarizable particles or oscillating dipoles (like Rydberg atoms) with dielectrics or other surfaces (like the fiber wall) is also very important for various (quantum) sensing applications and will lead to a thorough comprehension of e.g. near field heat transfer mechanisms." (from nanofiber proposal)

Discuss other experiments (if not done in detail before). Which amounts of shifts have they detected? Compare in particular with experiments in Stuttgart and our own hot setup.

What effects are specific for our setup? ("Patches" of cold atoms inside the fiber, no signal directly at fiber tip), estimate cloud size from old OD measurements with new analysis to estimate the distance from the fiber wall.

Compare measurements as a function of distance

Three basically different positions: Outside and inside (blue and green, respectively, as discussed before) and intermediate region (red), where we can see no clear signal. This is close to the fiber tip, so possibly stray fields there or lots of adsorbates

No / very weak EIT signal seen at fiber tip. Probably due to very inhomogeneous fields close to fiber tip. Inside fiber, signal reappears, shifted as discussed before. Reduces then with distance. (Compare with recent measurements)

THESIS DRAFT

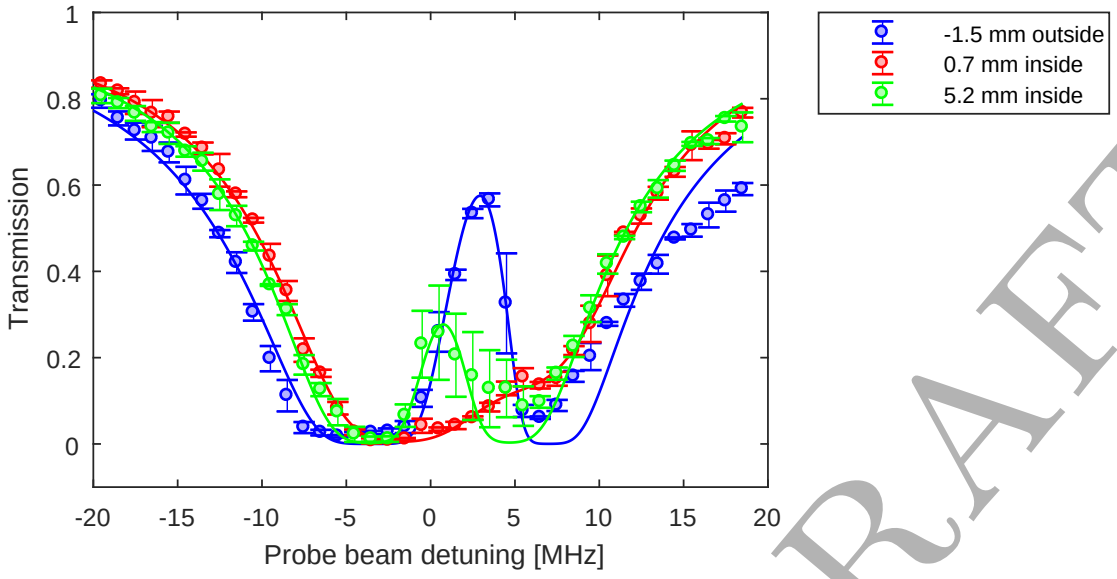

Figure 4.7.: Comparison of experimental and theoretical EIT signals at different positions. Shown is a position-resolved EIT signal inside and outside the hollow-core fiber (averaging over 20 repetitions starting from repetition number 201, statistical error bars). a) shows the experimental data and b) shows the theoretical fit to the data.

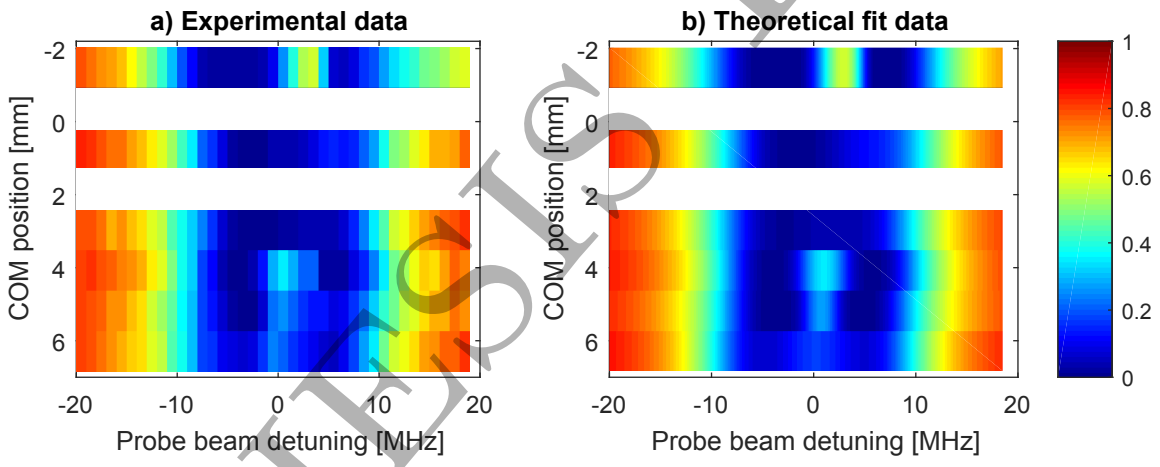

Figure 4.8.: Comparison of experimental and theoretical EIT signals at different positions. Shown is a position-resolved EIT signal inside and outside the hollow-core fiber (averaging over 20 repetitions starting from repetition number 201, statistical error bars). a) shows the experimental data and b) shows the theoretical fit to the data. For the positions marked white, no data has been taken.

Interestingly, also for the signals at the fiber tip, where initially no clear EIT peak can be seen, the loss peak develops later on in almost the same strength.

Compare experimental and fit values and find good agreement? Discuss fit parameters. Fit for higher repetition numbers to avoid lensing due to high initial ODs - however, for two high repetition numbers, loss phenomena - pulses around 200 seem to be a good compromise.

THESIS DRAFT

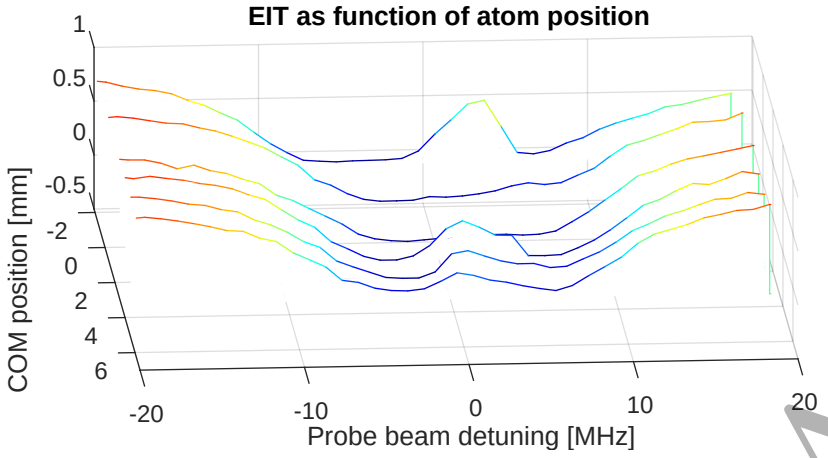

Figure 4.9.: Comparison of experimental and theoretical EIT signals at different positions. Shown is a position-resolved EIT signal inside and outside the hollow-core fiber (averaging over 20 repetitions starting from repetition number 201, statistical error bars). a) shows the experimental data and b) shows the theoretical fit to the data.

Compare with recent results, esp. regarding shift and linewidth! (Poster + talk GiRyd 2018), transport further inside the fiber due to better / faster ramps.

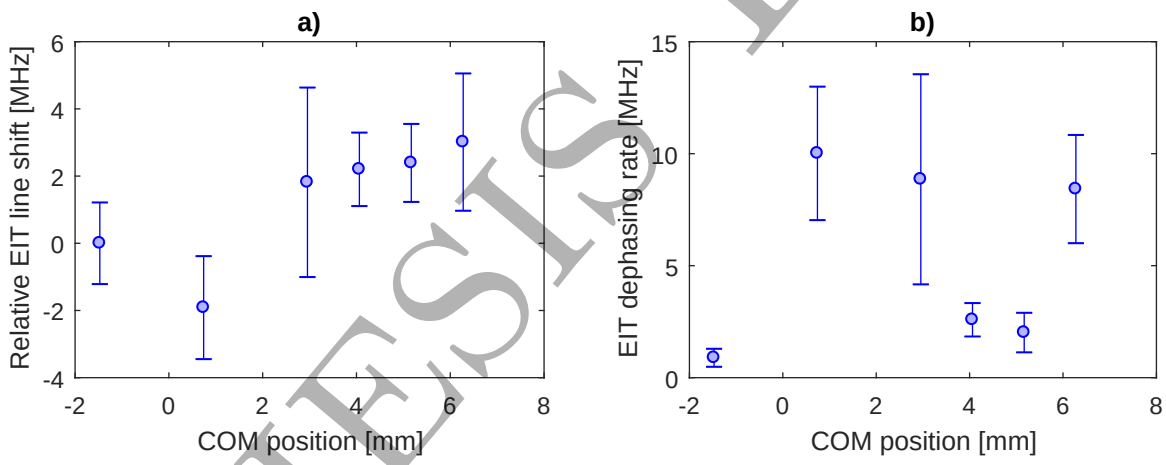

Figure 4.10.: Comparison of experimental and theoretical EIT signals at different positions. Shown is a position-resolved EIT signal inside and outside the hollow-core fiber (averaging over 20 repetitions starting from repetition number 201, statistical error bars). a) shows the experimental data and b) shows the theoretical fit to the data.

Final dephasing data point may be overestimated due to not-so-good fit. However, similar behaviour in most recent measurements.

After optimizing the transport into the fiber as discussed in detail in chapter 3, we have repeated this position-dependent measurement. In particular, we could also transport the atoms much further inside the fiber, up to a distance of 1 cm inside from the fiber tip. A full analysis and discussion of this new data is beyond the scope of this thesis and can be

THESIS DRAFT

found in [thesisNoaman]. However, I would like to highlight two interesting observations. Firstly, for these measurements, we did not observe the signal to lower as much as shown here. This might be due to a more homogeneous layer of ad-atoms inside the fiber as the measurements had a time delay of about one year. Secondly, the order of magnitude of the shifts is similar to the earlier measurements. Also, no clear distance-dependence of the shift can be observed. Also, EIT signals can be clearly observed well into the fiber. Possibly E-field for shift might be larger due to larger number of atoms (different state was used). Full analysis beyond the scope of this thesis.

THESIS DRAFT

4.2.2. Studying the time evolution of the EIT signal with an interleaved probing scheme

Now, we want to further investigate the properties of our EIT signal inside the hollow-core fiber. In particular, we want to measure OD and EIT simultaneously to see whether the EIT process has an influence on the atomic density profile, i.e. leads to a loss of atoms. For this, we employ a two-pulse measurement sequence shown in figure 4.11 a). Here, we insert a second probe pulse in the dipole trap off time. During this second pulse, we do not switch on the blue laser. Therefore, only in the first pulse, we should measure the EIT signal, while in the second pulse, we should observe the OD only signal. Figure 4.11 b) shows OD and EIT pulse for two different repetitions numbers. For early repetition numbers, we can clearly see the difference between EIT and OD pulse, with a distinct EIT peak appearing only in the EIT pulse. However, for later repetitions, we observe a peak also appearing in the OD only pulse. Since this cannot be EIT, it must result from atoms which have been lost from the probing process and there a "locally" lower OD (depending on the probe frequency). It is interesting that the position of loss peak and EIT peak do not coincide for early measurement times (both inside and outside the fiber!). Possible reasons for this are discussed in the referee reports. For later measurements, the EIT peak is shifted in the direction of the loss peak, which we interpret as the lossy part becoming the dominant mechanism. If we just plot the difference between EIT and OD pulse, it looks for later pulses as if the EIT signal vanishes. However, the opposite is true: the peak also appears in the OD pulse. We therefore distinguish between an EIT regime and a regime dominated by atom loss.

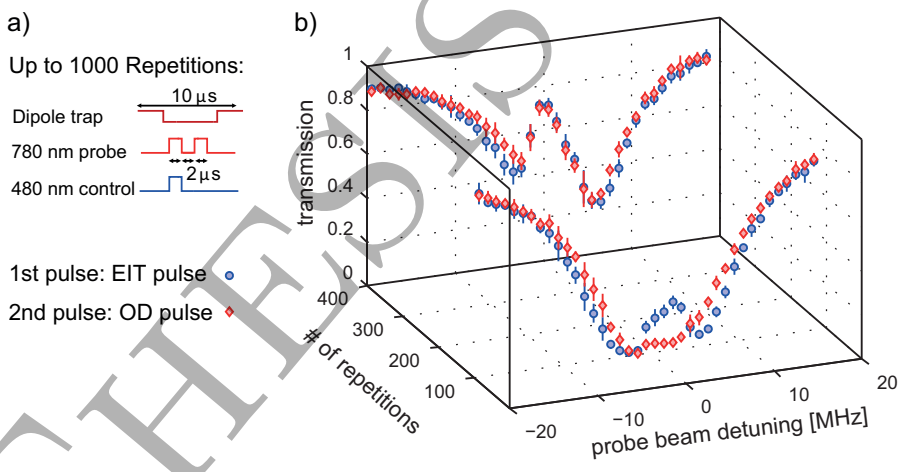

Figure 4.11.: Results from interleaved probing. a) Interleaved two-pulse measurements sequence. b) Comparison of OD (◇) and EIT (○) pulses inside the fiber for two different numbers of repetitions (averaging over 20 repetitions, statistical error bars). Figure adapted from our publication [13].

Check outside vs. inside measurements in 2-pulse-way for consistency regarding the shift between the two EIT signals! ($\approx 4\,\mathrm{MHz}$ difference between delta control outside and inside for pulses from 201, check how exactly other shift was calculated) Since outside signal shifts later to the loss peak position, this shift could also be related to the loss peak winning over

THESIS DRAFT

earlier for the measurements inside the fiber! Compare first pulses (attention with lensing!), just from EIT maximum? -> see figure 4.12!

Insert gray "cut lines" also into figure 4.12. Here, already same y-axis as in latter figure 4.14 is chosen to illustrate analysis process. Discuss shift seen here (We use ln(T) to estimate OD and to better visualize the loss peak, which is small initially).

Normal EIT fit does not make sense, as we are observing a loss (non-EIT) phenomena. Therefore, in the following, I would like to qualitatively study this effect without a quantitative fit.

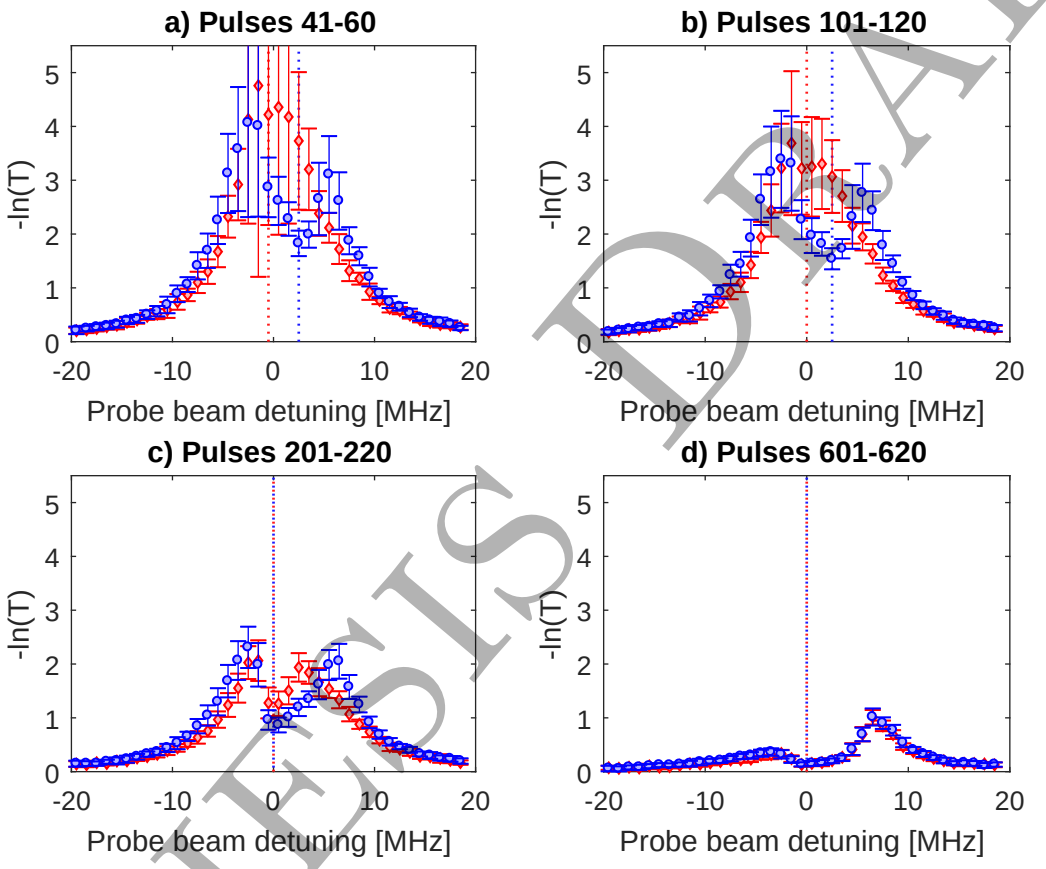

Figure 4.12.: Comparison of OD and EIT pulses as function of pulse number. Comparison of OD (◇) and EIT (○) pulses inside and outside the fiber for different number of repetitions (averaging over 20 repetitions, statistical error bars). Data from Figure 4. We use ln(T) to estimate OD and to better visualize the loss peak, which is small initially. Note that the y-scale has been confinced for figure a) for better visibility of the data points. The large error bars stem from the data points being close to zero. The dotted lines are a guide to the eye to highlight the peak position for both EIT and OD pulse for the different measurement repetition numbers.

"To visualize the temporal evolution, we subtract the two-photon EIT and the OD measurement (i.e. the two datasets in each of the two plots of Fig. 4.11 (b)) and plot this difference as a function of the repetition number in Fig. 4.13, presenting both inside and outside the

THESIS DRAFT

fiber measurements. These results confirm the previous assumption of two different time regimes. In both cases, a clear EIT signal is visible at early times, confirming a coherent excitation. Inside the fiber, this EIT peak vanishes after about 300 pulses, which indicates that now both EIT and OD pulse have become equal. Since only loss processes can also be observed in the OD pulse, they have become more dominant than the coherent EIT process for these later times. Outside of the fiber, we see a qualitatively similar behavior, but a clear EIT signal is still visible for repetition numbers up to 600. That suggests that loss processes are enhanced by the fiber and the loss-dominated regime starts earlier inside the fiber. This meets our expectations as inside the fiber atoms are lost once they hit the fiber wall, while outside the fiber they can still contribute to the signal even after expansion beyond the beam waist. Further, we notice that in this coherent EIT signal no shift with increasing number of repetitions occurs. This confirms our assumption that the previously observed time-dependent shift is due to loss processes." [13]

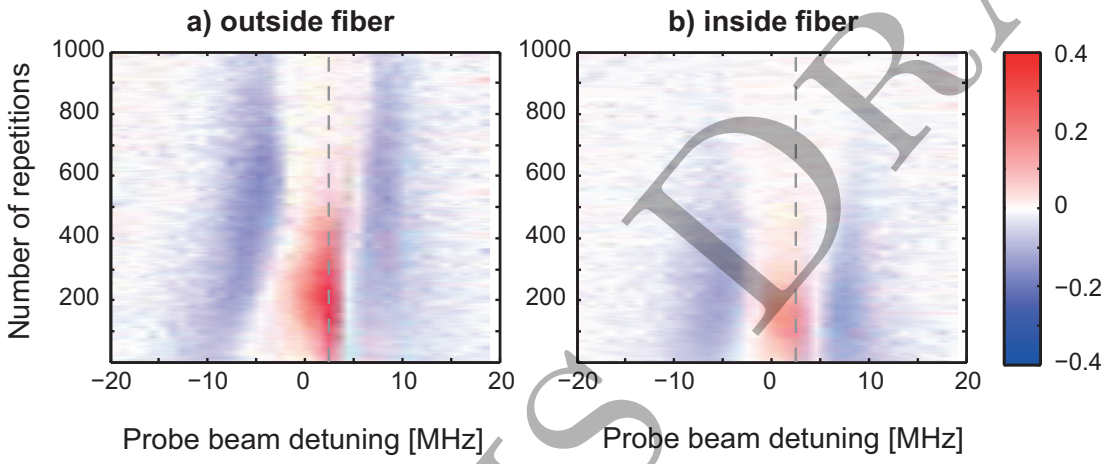

Figure 4.13.: Comparison of OD and EIT pulses as function of pulse number. Time resolved difference between EIT and OD pulses (Moving average over 20 neighboring repetitions). The dashed gray line marks the cut shown in Fig. 4.14.

Estimate time scales for the two regimes in figure 4.14 (here, pulses have been rescaled to times, of course these timings are specific for our probing scheme).

"To determine the time scales for the two different regimes, we make a vertical cut through Fig. 4.13 (c) at the position of the initial EIT peak at $\Delta = 2.5\,\mathrm{MHz}$, marked by the dashed gray line. The logarithm of the transmission for OD and EIT pulse is plotted as function of measurement time in Fig. 4.14, inside (main plot) and outside (inset) of the fiber. Inside the fiber, there exist two distinct time scales with a sharp cut at around 3 ms, i.e. 300 repetitions. The transition between the two time regimes seems to happen when the magnitudes of OD and EIT pulse become the same. Outside the fiber, this transition is less distinct, although the EIT signal also shows a different behavior before and after 3 ms. We have fitted exponential loss curves to all datasets and give the decay rates in Fig. 4.14, together with their respective errors from the fit. Only the initial loss of atoms (OD time scale 1) depends on whether the atoms are outside or inside of the fiber, with a faster loss inside the fiber. However, we cannot make a quantitative statement due to the large error

THESIS DRAFT

for this time scale. The EIT decay rates in both regimes as well as the later OD decay rate are not influenced by the fiber. Thus, while we do observe an accelerated overall loss of atoms due to Rydberg excitations inside the fiber, for time scales up to a few ms the fiber has no significant influence on the occurrence of the EIT signal itself." [13]

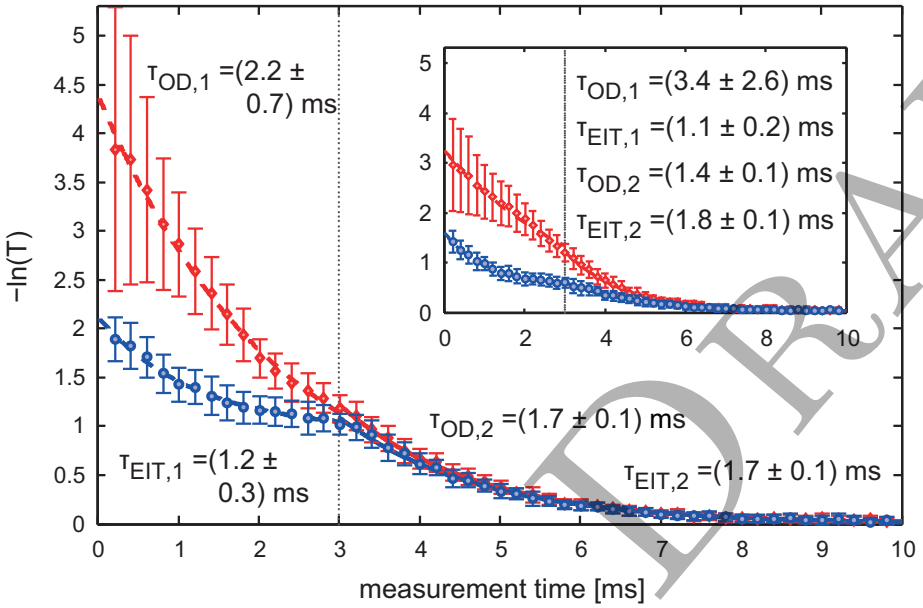

Figure 4.14.: Timeresolved results from interleaved probing. " Comparison of OD (◇) and EIT (○) signals at $\Delta = 2.5\,\mathrm{MHz}$ as function of measurement time (averaging over 20 repetitions, statistical error bars). The main figure shows the signals inside the fiber, the inset the signals outside of the fiber. The dashed (solid) lines show an exponential fit to data below (above) 300 repetitions (time scale 1 (2)). The two regimes are separated by a dotted gray line. The decay times for each regime and each dataset are given in the figure (errors from the fit)." Figure adapted from our publication [13].

Finally, to verify that our interleaved probing scheme does not rely on the order of the OD and EIT pulses, we further perform a 3-pulse measurement with a single EIT and two OD pulses. Figure 4.15 a) shows the pulsing sequence. Here, we add an OD only pulse before and after the EIT pulse. In order to keep the same pulse length and distance between pulses, the dipole trap off time is increases to approximately $10\,\mu\mathrm{s}$ and the total time of one repetition increases to approximately $19\,\mu\mathrm{s}$.

Figure 4.15 b) shows the timeresolved difference between the first and the second OD pulse. We note that within our experimental errors, the difference signal is flat, thus there is no significant difference between the two OD reference pulses. This is further confirmed when plotting the timeresolved differences between EIT pulse and the first and second OD pulse, respectively, in figures 4.15 c) and d). In both figures, we observe a loss of the distinct EIT signal after about 200 repetitions. This is again due to the loss peak developing also in the OD pulse and dominating both signals, as discussed in detail above. Afterwards a similar (loss) signal is visible in all three pulses. Thus, it does not matter for the signal whether the OD reference pulse is sent before or after the EIT pulse. Only global loss, not loss

THESIS DRAFT

within single release-recapture cycle. In general, we observe a faster decay of the OD due to the longer off time of the dipole trap during the release-recapture cycles as compared to the 2-pulse measurements shown above. As we observe no significant differences between the OD pulses, we conclude that the number of reference pulses and in particular the order of the pulses does not influence our interleaved probing scheme. Therefore, the 2-pulse measurements shown above should be sufficient.

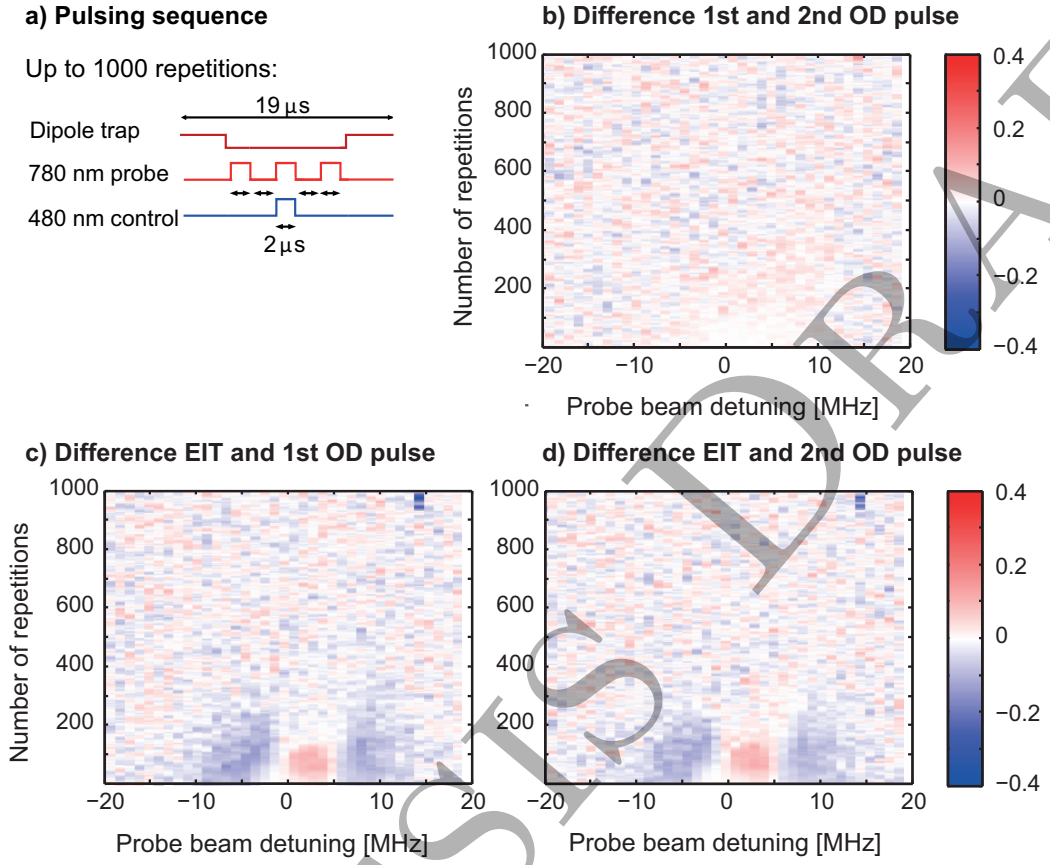

Figure 4.15.: Results from interleaved probing, 3 pulses. a) Three-pulse measurements sequence. "(b) Comparison of OD (◇) and EIT (○) pulses inside the fiber for different number of repetitions (averaging over 20 repetitions, statistical error bars). (c) Time resolved difference between EIT and OD pulses (Moving average over 20 neighboring repetitions). The dashed gray line marks the cut shown in Fig. 4.14." Inside fiber.

THESIS DRAFT

4.2.3. Effects of EIT pulses and atomic density

In the previous section, I have introduced a time-resolved two-pulse measurement technique to distinguish between the initial EIT peak and the loss peak developing later. In particular, we have seen that also the EIT peak shifts towards the position of the loss peak during the measurement time. In this section, I would like to further investigate the nature of this time-dependent shift. In particular, I would like to study whether the presence of the EIT process itself can be responsible for the shift. This I will do by studying measurements with the probe beam switched off for an initial number of pulses. Further, I will study the effect of different initial densities on the shift.

In the previous section, we have seen how during our measurement process an additional loss peak develops. To investigate whether the EIT process is responsible for creating this atom loss, we switch off the probe beam for the initial 200 measurement repetitions and compare the results with the full number of repetitions. Figure 4.16 a) shows the probing sequence for this measurement. Here, the probe beam is switched off for the first 200 measurement repetitions. Nonetheless the dipole trap is switched off and the control pulse is switched on for these 200 repetitions as usual. This is to ensure that we are not measuring any effects due to the release-recapture of the atoms in the dipole trap or for example due to LIAD when the blue control beam is switched on / or delay in switching on of blue beam. The comparison measurement is done in the usual way, where both probe and control pulse are switched on and the dipole trap is switched off for all 1000 repetitions.

Discuss before that probe pulses only have a weak influence on OD only signal (probably very early on in probe section), main influence is the release-recapture due to the dipole trap switching off and on (confirmed by same OD after pulse 201, independent of whether probe was on or off).

The results for a measurement inside the hollow-core fiber are shown in figure 4.16 b) and c) for a comparison measurement with high initial OD and in d) and e) for a comparison measurement with lower initial OD. The measurement with the first 200 probe pulses switched off is the same for all four figures. First, I would like to discuss the effects visible in figures b) and c), then afterwards discuss whether any differences can be observed for the lower OD case.

First, I would like to discuss the comparison between the first 20 EIT pulses of both measurements, as shown in figure 4.16 b). For the usual measurement, these are pulses 1 to 20, whereas in the measurement with the first 200 probe pulses switched off, the first 20 EIT pulses are pulses 201 to 220. As in previous analysises, I average over these 20 pulses. Firstly, it is clearly visible that the OD is much higher for pulses 1 to 20 than for pulses 201 to 220 (XX: numbers?). This behaviour is expected as the additional 200 release-recapture cycles will lead to a loss of atoms. Secondly, the EIT peak for the measurement with the first 200 pulses switched off is clearly much higher than the other one (XX: numbers?). Since in both cases, these are the first EIT pulses, there has not been time for any buildup of the EIT peak. Therefore, I assume that the higher peak can only be due to the lower atomic density as represented by the lower OD. (Or build-up of blue laser power?) Thirdly, we see that both EIT peaks lie at the same position at a probe beam detuning of 2.5 MHz,

THESIS DRAFT

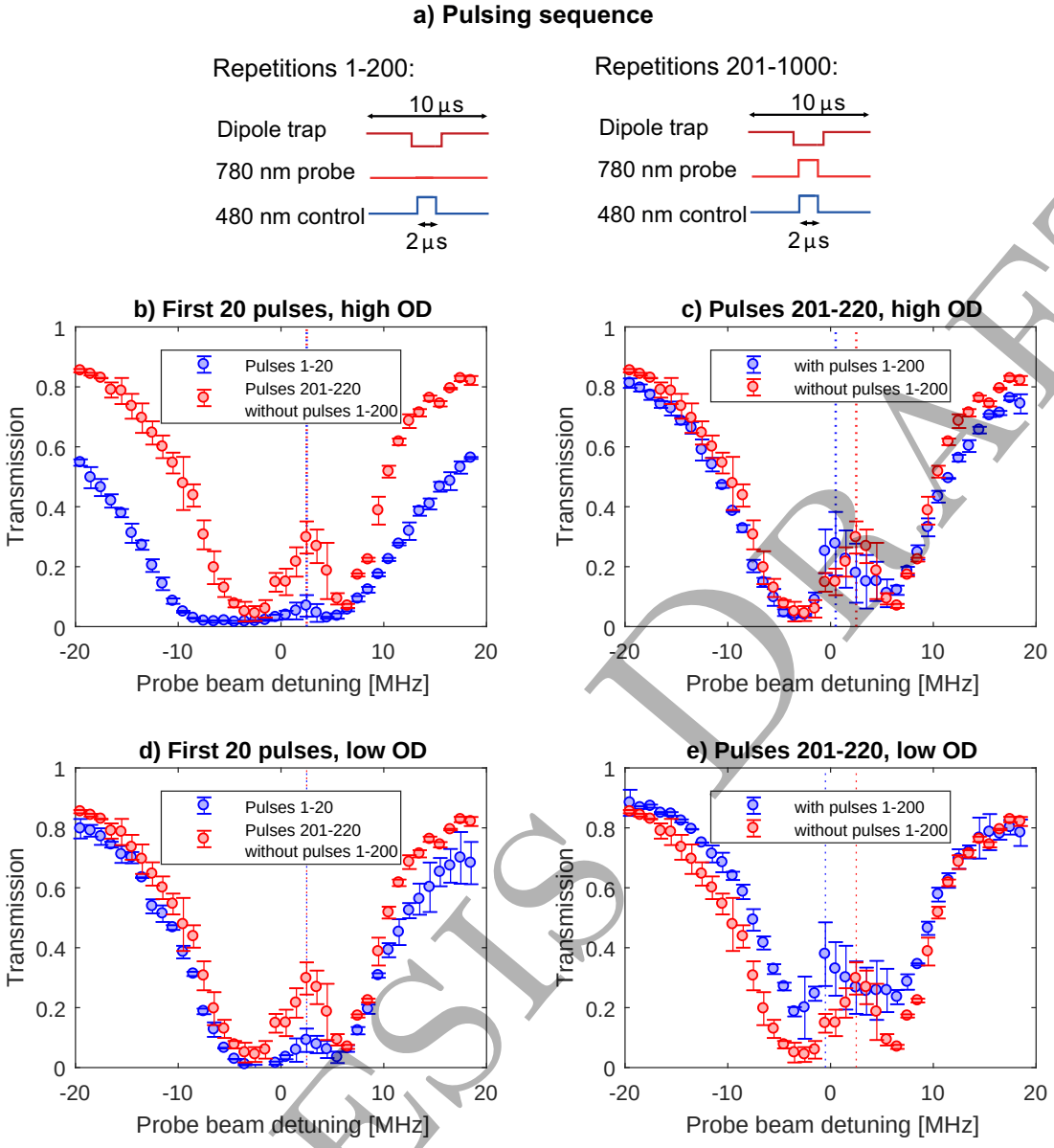

Figure 4.16.: Influence of initial pulses on EIT signals inside fiber. a) Pulsing sequence where the probe beam is switched off for the first 200 measurement repetitions. Figures b) - e) show experimental EIT signals inside the hollow-core fiber for the pulsing sequence in a) (○) as well as for a comparison measurement using the usual pulsing sequence (○). Middle and lower row show the results for two different comparison measurements with high and low initial OD, respectively (averaging over 20 repetitions, statistical error bars). Figures b) and d) show the first 20 EIT pulses, either with no dipole trap switching before or with 200 repetitions before w/o probe and control beam on. Figures c) and e) show pulses 201-220, for the first 200 pulses either switched on or off. The dotted lines are a guide to the eye to highlight the EIT peak position for the different measurements.

THESIS DRAFT

which was the typical value for the initial EIT peak inside the hollow-core fiber. Therefore, we can conclude that the loss of atoms due to the release-recapture cycles does not lead to

a shift of the EIT peak.

Next, I would like to discuss the comparison between pulses 201 to 220 of both measurements, as shown in figure 4.16 c). Both have similar EIT peak with transmission of XX % and a similar OD of XX. However, we note that the EIT peaks are shifted with respect to each other, as indicated by the guide-to-the-eye dotted lines.

Discuss measurements with probe beam initially off (especially shift of EIT peak with probing time): see figure 4.16. First pulses seem to give the same EIT shift, no matter if there has been DT on / off before. After 200 EIT pulses, the peak appears shifted (to same position as loss peak observed in OD pulse in 2 pulse measurements). Therefore -> measurement-induced shift due to loss? Comparison measurement has already crossed into loss regime, while other measurement is still in EIT regime. -> Loss regime is reached by loss due to EIT / measurement-induced.

Shift is not due to density! As initial 20 pulses always show same peak position, not depending on the initial density! Therefore: shift must be due to loss mechanisms specific to the EIT process, which build up during our measurement process and cause the shift.

See referee comments about shift due to ion formation and loss: "Assuming that negative detuning means an overall red detuning of two-photon excitation, the sign of the shift suggests that loss is enhanced for Rydberg atoms in the vicinity of stronger electric fields, which cause a downward level shift in the nS states. This would then be consistent with Rydberg atoms being preferentially excited closer to ions, free electrons, or field sources on the fiber surface when the detuning is negative. That proximity could then potentially lead to a more rapid loss, for example by collision with the field source."

Figure 4.16 d) and e) show the same pulse comparisons as discussed above for a comparison measurement with lower initial OD. Here, the initial OD of the comparison measurement is approximately the same OD as for the measurement with the first 200 pulses switched off after the first 200 release-recapture cycles. This measurement should show the density-dependent effects more clearly. When comparing the first 20 EIT pulses, again the position of the EIT peak is the same. The EIT peak of the comparison measurement is still lower, this could be due to stil slightly higher OD. (Or blue power building up???) When comparing the pulses 201 to 220 of both measurements, again we see the same shift between the two measurements as before. This shift is approximately the same as in the high OD comparison measurement. Slightly larger: due to lower OD? However, we only have a signal resolution of 1 MHz here, so maybe real shift would be in the middle (as assumed in previous discussions). Therefore, in total I can conclude that the initial density of the comparison measurement does not influence this shift. However, in the following, I will do more systematic measurements at different initial densities.

Discuss low OD measurements with shorter MOT loading time, also 2 pulse measurements, possible other reason for shift? Can time-dependent shift be seen differently? What other influences do the different densities have? Numbers from background OD fit: 3s loading, inside: initial $OD \approx 14$, 2s loading, inside: initial $OD \approx 12$; 3s loading, outside: initial $OD \approx 21$, 2s loading, inside: initial $OD \approx 15$

THESIS DRAFT

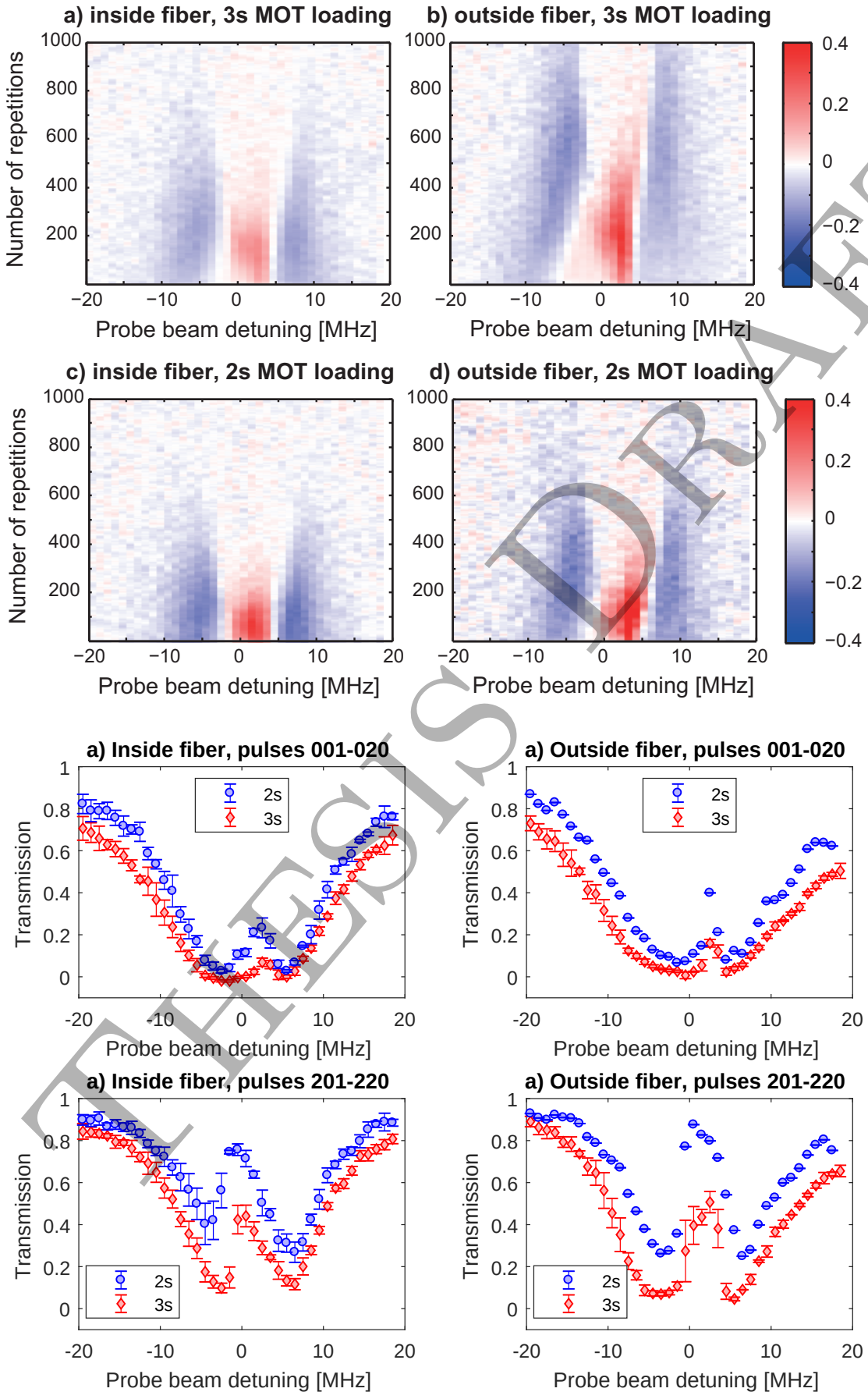

THESIS DRAFT

Figure 4.17.: Comparison of EIT signals for different MOT loading times. Shown are time-resolved difference signals between EIT and OD pulses inside and outside the hollow-core fiber for different MOT loading times (averaging over 20 repetitions starting from repetition number 201, statistical error bars). Upper row: 3s MOT loading, lower row: 2s MOT loading. Left: inside, right: outside.

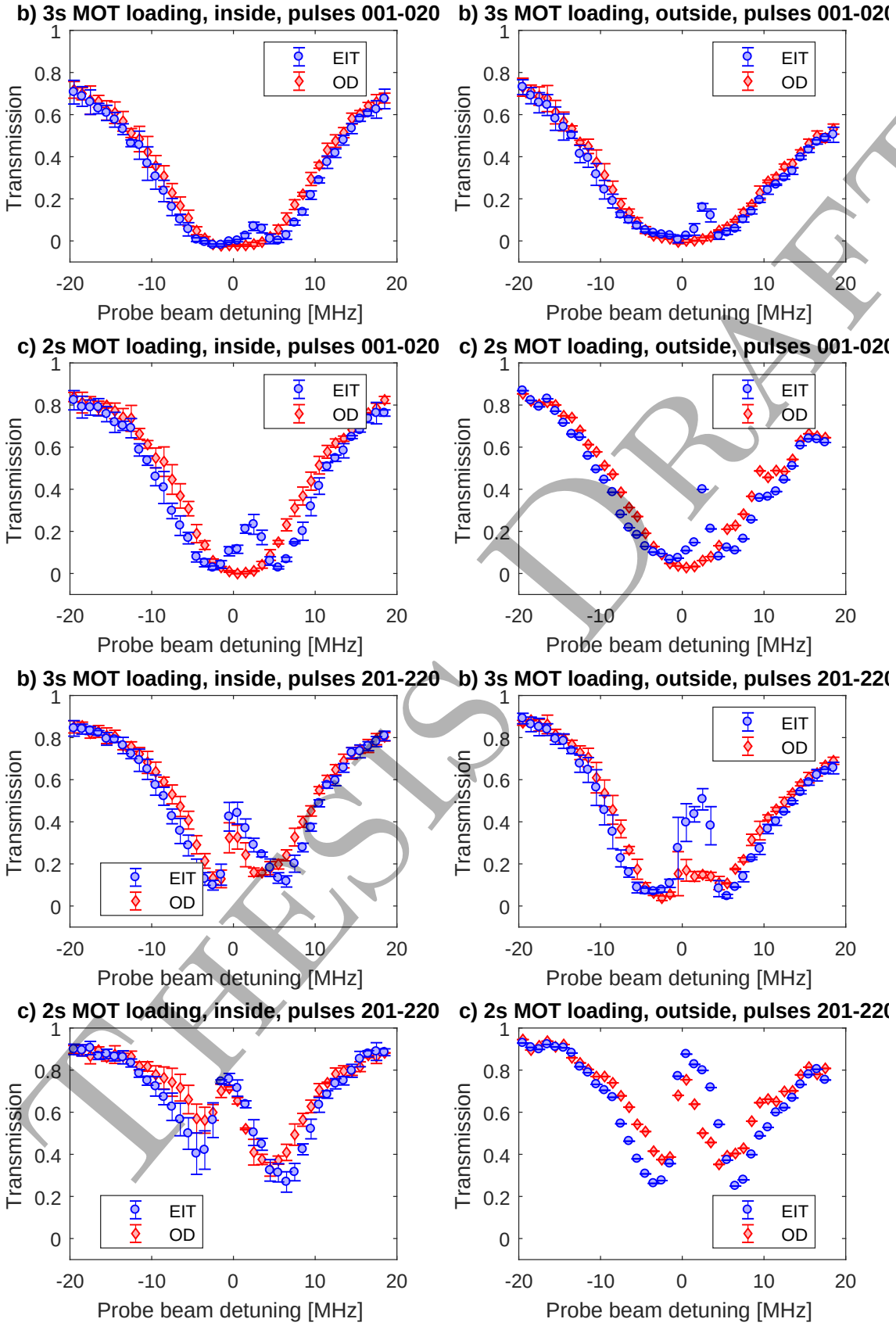

THESIS DRAFT

Figure 4.18.: Comparison of EIT signals for different MOT loading times. Shown are time-resolved difference signals between EIT and OD pulses inside and outside the hollow-core fiber for different MOT loading times (averaging over 20 repetitions starting from repetition number 201, statistical error bars). Upper row: 3s MOT loading, lower row: 2s MOT loading. Left: inside, right: outside. (Upper 4: 20 pulses from 1)

4.3. Conclusion and Outlook

In the measurements discussed previously, we have observed a shifted EIT signal between inside and outside the hollow-core fiber. This could indicate an additional electric field inside the fiber, as also reported in other experiments. Possible reasons for this are clusters of ad-atoms on the fiber wall or other inhomogeneities of the fiber surface. However, we have also observed that other time-dependent effects, such as loss of atoms due to the excitation into Rydberg states, can lead to a shift of the EIT signal. Therefore, to clearly determine whether our shift stems from electric fields inside the fiber, it is necessary to measure and compare this shift for different n-states. Then, as discussed above, the Stark effect can be used to fit to the data points.

Exciting higher Rydberg states

First preliminary measurements have been done to measure the Stark map for different states inside the hollow-core fiber. More details in Noaman's thesis. Problem: Shift for higher states leads to us not being able to detect EIT signal anymore with our current setup / locking scheme (shifted out of range).

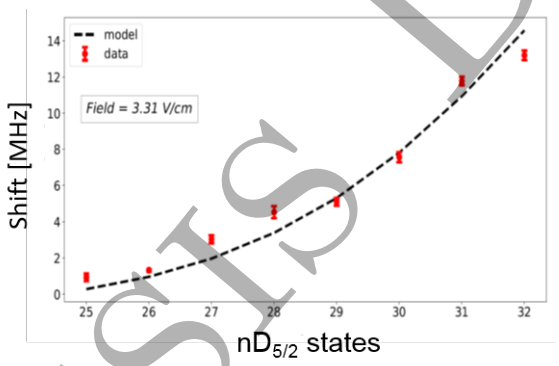

Figure 4.19.: Stark map for different states. Shown is a position-resolved EIT signal inside and outside the hollow-core fiber (averaging over 20 repetitions starting from repetition number 201, statistical error bars). a) shows the experimental data and b) shows the theoretical fit to the data.

Ideas to overcome limitations: Detune blue laser with cavity to counteract shift induced by fiber (standard procedure, cavity has been set up) -> what happes to dephasing which makes the signal smaller?

Creating a homogeneous ad-atom distribution on the fiber walls

A possible approach to reduce the number of rubidium adsorbates on the fiber walls is light-induced desorption (LIAD, cite!). Here, blue light shown onto the fiber surface can help to desorb the adsorbed atoms. This method has been used successfully especially in experiments with thermal atoms (cite Stuttgart?). Cold atoms? Surface papers! Also in a

THESIS DRAFT

setup in our group, where hollow-core fibers filled with thermal rubidium vapor are studied, LIAD has been used to desorb rubidium atoms from the fiber walls. For this, the blue laser normally used for Rydberg excitations is decoupled from the center of the fiber core, so that it propagates through the cladding of the fiber, and detuned from the atomic resonance. With this method, the OD could be increased by a factor of more than 100 during the LIAD process and even after equilibration of the system stayed a factor of 2 larger than before [91]. However, when applying the same procedure to the cold-atom setup, we observe no clear effect of the LIAD process.

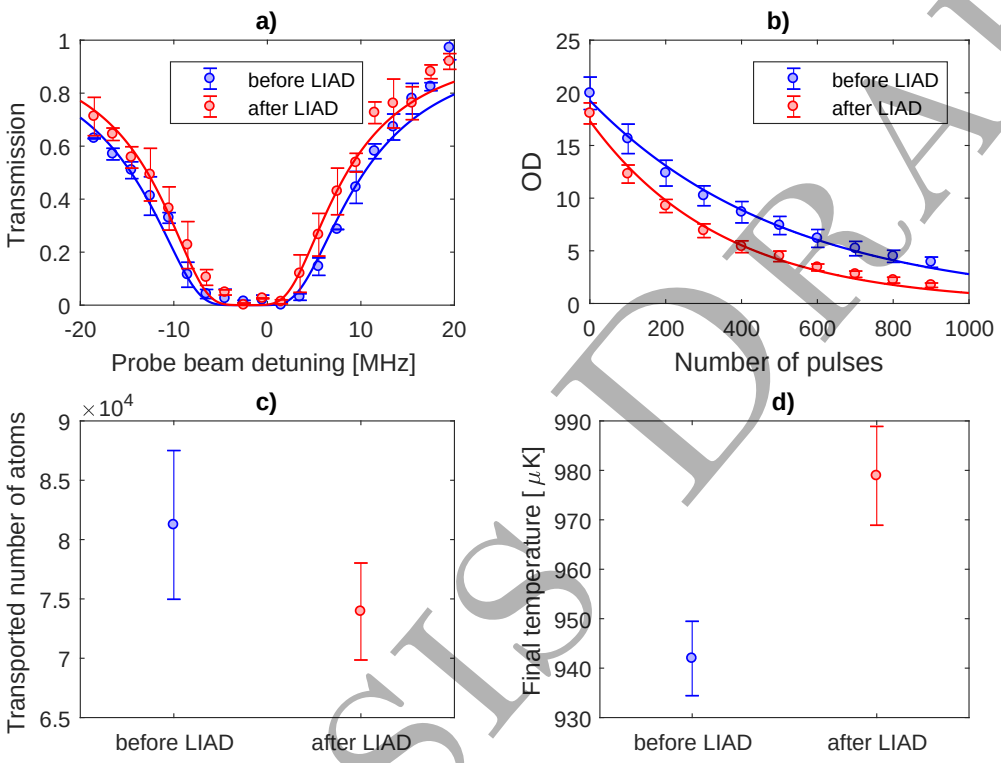

Figure 4.20.: OD measurements before and after LIAD. Comparison of two different absorption measurements before and after applying the LIAD process. For both measurements, the atoms are transported about 6 mm inside the hollow-core fiber and no amplitude ramp-down is applied. a) Transmission as function of the probe beam detuning, averaged over 20 repetitions starting from repetition number 201 (Data points: experimental data with the error bars representing statistical errors, solid line: fit according to equation XX). b) Decay of the optical depth with number of probe pulses (data points) and corresponding release-and-recapture fits (Equation XXX, solid line). c) and d) Number and temperature of the atoms transported inside the fiber at the final position obtained from the fits to the data in figure b). (Error bars in b)-d) represent errors from the fitting procedure.)

Figure 4.20 shows the results of two absorption measurements with atoms transported about 6 mm inside the hollow-core fiber without applying any amplitude ramp-down. One data set was taken before the LIAD process and the second one afterwards. Note that during the LIAD process the probe beam was still coupled through the fiber and its transmission was measured. However, in stark contrast to the results from the vapor setup, here no signs of absorption from atoms released from the fiber wall could be detected. A reason for

THESIS DRAFT

this could be that the atoms from vapor background should have much broader linewidth of absorption line and only contribute very weakly to the signal here. However, also the number of atoms is much lower than the in vapour pressure setup.

When comparing the measurements before and after LIAD, we can observe that the initial OD and therefore the number of particles transported inside the fiber is slightly smaller for the measurement after LIAD, while the decay of the OD is faster and therefore the temperature of the atoms is slightly higher. This could be an indication for thermal background atoms, which reduce the transport efficiency and heat the cold atoms due to collisions. However, the differences between the two measurements are on the same order of magnitude as the experimental error bar or as typical deviations between different measurements (note that the temperature error is just fit error and does not include statistical deviations). These are typical deviations also seen during other measurement days and therefore we cannot clearly attribute these differences to the LIAD process.

Also when detecting EIT signals before and after LIAD, no difference larger than typical experimental errors could be detected. This is also true for Stark map measurements. However, these measurements are beyond the scope of my thesis. Further information can be found in [**?**]. As a conclusion, we have not been able to detect clear effects of the LIAD process in the cold setup. Maybe a higher-order blue beam would be better to reach the fiber walls than just decoupling the beam. Also, the dipole trap could be kept on during the LIAD measurements to attract desorbed atoms. Or a pushing beam could be applied to kick them out of the fiber.

hot setup (homogeneous Rb coating, shift is negligible even for states up to n=85, there problems with magnetic fields, though), or homogeneous Rb coating or different coatings of fiber, cite Chantal's and Noaman's thesis for hot setup, maybe show picture from Chantal's thesis

A systematic survey of the inner fiber walls

Another outlook would be a more systematical survey of the inner fiber walls and the field distribution, which could be used to determine the distribution of ad-atoms. For this, a smaller atom cloud as in a crossed dipole trap sample would be useful to sample smaller portions of the fiber. For each position, a Stark map could be obtained, fully characterizing the field as function of z-value. Further discuss blockade radius vs. typical cloud radius (idea: change cloud radius by preparing cold sample with MF ramps inside fiber, then non-adiabatically ramp up dipole trap power to compress cloud even further as discussed in transport chapter). Changing the distance between atoms and fiber wall could enable to artificially create the same interaction strength for different Rydberg states. If a shift is really due to interactions with the fiber wall, then in principle the same shift should be seen for different states. If it is due to a field along the fiber axis, the shift should still change with the state. Another idea would be to couple different light modes as in Stuttgart experiment to characterize the field as function of position inside the fiber.

THESIS DRAFT

4.4. A complementary approach: Rydberg atoms outside an optical nanofiber

Here, we will study a complementary cold atom – fiber interface, namely cold atoms outside an optical nanofiber. In particular, we will discuss the first experimental results of exciting Rydberg atoms close to an optical nanofiber.

In the previous chapters, I have discussed the promises, but also the many challenges of exciting cold Rydberg atoms inside a hollow-core fiber. In this chapter, I would like to introduce a complimentary approach, namely interfaces between cold (Rydberg) atoms and optical nanofibers, where atoms are trapped in the vicinity of a very thinly tapered fiber and interact with the evanescent light field modes [e.g. Nayak2007, Vetsch2010, Nieddu2016] [e.g. 93–95]. In recent years, many different experiments have been conducted using these atom - nanofiber interfaces. Examples include a nanofiber-based optical conveyor belt already mentioned earlier in the transport chapter [Schneeweiss2012] [24], observing coherent backscattering processes of light off structured one-dimensional atomic arrays outside optical nanofibers [Reitz2014, Soerensen2016, Corzo2016] [96–98] and studying chiral effects of atoms coupled to a nanofiber, where the propagation direction of the light field depends on its polarization and therefore the absorption or emission of the atoms is also direction-dependent [Petersen2014, Lodahl2017, LeKien2017] [99–101]. Of particular interest to our setup are the realizations of electromagnetically induced transparency, used for light storage [Sayrin2015,Gouraud2015] [102, 103] or for an EIT ladder scheme, albeit not to a high n Rydberg state [Kumar2015] [104].

In addition to these experiments using ground-state atoms, the atoms outside the nanofiber can also be excited to Rydberg states by light guided in an evanescent fiber mode. In contrast to the previously discussed experiments inside the hollow-core fiber, here the Rydberg atoms will interact with the outer walls of the fiber, leading to a different symmetry of the interactions. In the following chapter, I would like to discuss the first results for this complementary Rydberg atom - fiber interface, which in future can be used to gain further understanding of interactions between Rydberg atoms and fiber surfaces. The results presented in this chapter have been obtained in the research group of Prof. Nic Chormaic at OIST, who are to the best of my knowledge the only group worldwide working on such a Rydberg atom - nanofiber interface.

4.4.1. Basic concepts of a cold Rydberg atom - nanofiber interface

Let me first introduce the basic principles of an optical nanofiber, following review [Nieddu2016] [95]. Typically, optical nanofibers (or tapered fibers) are created from commercially available single-mode fibers, which are heated and pulled using a so-called flame-brushing technique until the narrowest part of the tapered region reaches a diameter below 1 μm. Figure

THESIS DRAFT

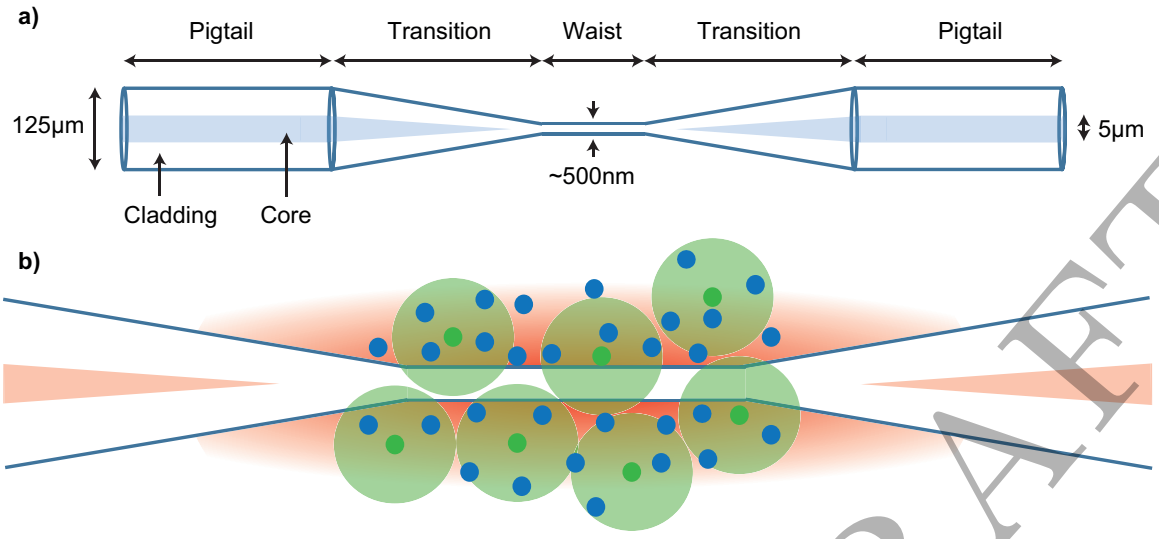

Figure 4.21.: Sketch of an optical nanofiber. a) Schematic sketch of the different components of an optical nanofiber and their respective sizes (sketch not to scale). b) Sketch of Rydberg atoms excited outside the waist of an optical nanofiber. In the narrow waist region, the light field is guided as an evanescent field outside the nanofiber.

4.21 a) shows a sketch of such an optical nanofiber after tapering. It consists of three regions. The pigtail is the remaining part of the single-mode fiber, which does not experience any forces due to the tapering process and therefore retains the typical dimensions of fiber cladding and core as indicated in the sketch. In the transition region, the fiber is tapered towards its narrow waist. The exact shape and size of this tapered region depends critically on the parameters during the creation of the nanofiber and can be tailor-made for each individual fiber. The waist of the nanofiber has a diameter of typically around 500 nm and a typical length of up to a few mm. (?? ask Krishnapriya) Due to the very small fiber diameter, here a very interesting phenomenon occurs. Light guided through the fiber is here propagating as an evanescent field, instead of inside the fiber core [Nieddu2016, more?]. As a result, high light intensities can be reached outside the nanofiber close to the fiber wall [Bures1999?]. These can then be used to interact with atoms outside the nanofiber.

As an example of such an interaction, figure 4.21 b) shows a sketch of Rydberg atoms outside the waist of an optical nanofiber. Here, cold atoms in the range of the evanescent field of the fiber can be excited to Rydberg states. Note that for reasons of clarity, only the probe beam is sketched, although both probe and control beam for the Rydberg excitation are propagating through the nanofiber. As discussed previously, the Rydberg blockade mechanism prevents more than one atom within one blockade radius to be excited. In contrast to the case of atoms inside a hollow-core fiber, here we find a different geometry of the system, as in principle atoms can be excited all around the nanofiber. Depending on the intially coupled light modes and the beam polarizations, different geometries for the evanescent fields can be obtained [Nieddu2016]. In all cases, here the Rydberg atoms will interact with the outer walls of the fiber, making the study of these interactions complementary to the

THESIS DRAFT

studies inside the hollow-core fiber as presented previously.

In principle, also in the nanofiber setup, an optical dipole trap can be used for an additional spatial confinement of the atoms. In this case, the dipole trap again consists of an evanescent field outside the waist region of the nanofiber. However, trapping in this case is more complex than for the hollow-core fiber case [LeKien2004 for two-color trapping] [105]. When only using a single-color red-detuned dipole trap, an attractive potential close to the fiber surface is created. This has the effect of confining the atoms close to the fiber, but the atoms are also attracted towards the fiber walls. Therefore, a second-color blue-detuned dipole trap has to be used to create a light shield between the atoms and the fiber surface. This two-color trapping of cold atoms outside an optical nanofiber has recently been demonstrated by e.g. [Vetsch 2010, Goban2012 and Soerensen2016] [e.g. 94, 97, 106]. Different trapping geometries are possible depending on the polarization of the light fields [LeKien2004] [105]. For example, the atoms can be trapped in two strings along two opposite sides of the nanofiber [Soerensen2016]. For atoms trapped in such a geometry, the distance between Rydberg atoms and fiber surface can be well controlled and is potentially be much smaller than in the hollow-core fiber case as the second repulsive trap prevents atom loss due to attraction. At such small distances, even the van-der-Waals interactions between ground-state atoms and the fiber wall could be detected [Nayak2007] [93]. Therefore, it should be possible to study even stronger Rydberg atom-wall-interactions.

A third difference to the experiments discussed previously is the number of atoms. While in the hollow-core experiment, tens of thousands of atoms interacts simultaneously with the fiber, here typically only tens to hundreds of atoms will be trapped near the nanofiber due to the small mode volume of the evanescent field [citations!]. Therefore, the two different fiber interfaces discussed in this thesis perfectly complement each other regarding the parameter regime of interactions which can be studied.

As a first step for creating an efficient Rydberg atom - nanofiber interface, it is again necessary to thoroughly study and understand the interactions between the Rydberg atoms and the fiber surface. As discussed previously for the hollow-core fiber case, we will be using EIT spectroscopy to map out the influence of the fiber on the coherence and lifetime of the Rydberg excitations and analyse possible nanofiber - Rydberg atom interactions. Therefore, my research stay at OIST focussed on exciting Rydberg atoms close to the nanofiber using a two-photon EIT process and on characterizing these excitations. In the following sections, I will present the experimental setup and the first results on Rydberg atom excitation near an optical nanofiber.

4.4.2. Experimental setup and sequence

In this section, I will briefly introduce the experimental setup and sequence used for the measurements discussed in the following. Since many parts of the setup are very similar to the hollow-core fiber setup described in great detail previously in this thesis, I will not give a comprehensive review, but mainly highlight the differences and specific features of this setup. More details can be found in (XX: thesis Krishnapriya, paper?).

THESIS DRAFT

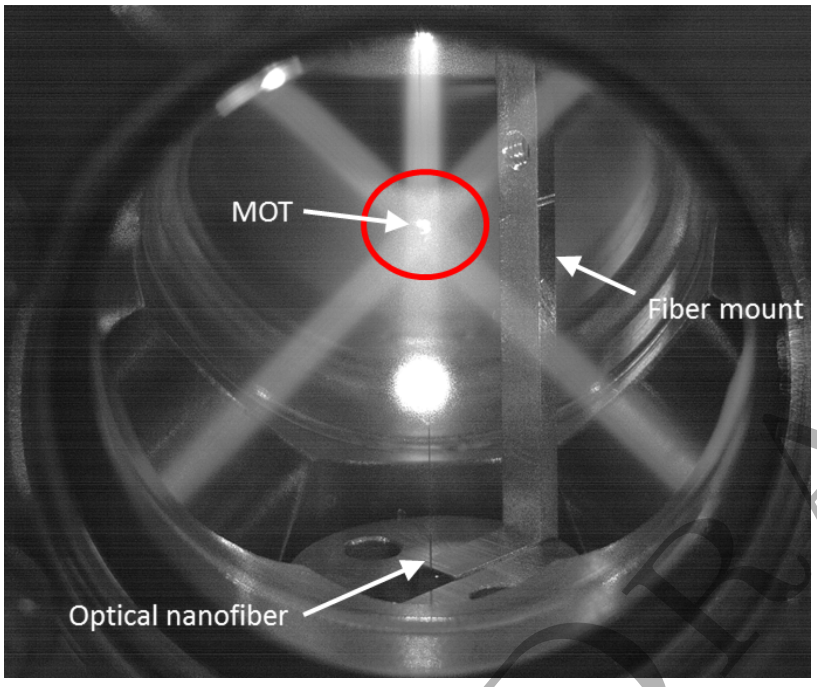

Figure 4.22.: Picture of nanofiber setup. Shown is a picture of the experimental setup. The optical nanofiber is held inside the vacuum chamber in vertical direction by a fiber mount. The MOT (highlighted in red) is overlapped with the waist of the nanofiber.

Figure 4.22 shows a picture of the experimental setup at OIST. Here, the optical nanofiber is mounted vertically inside the vacuum chamber. Its pigtails are clamped in a fiber mount inside the vacuum chamber as indicated on the picture. The fiber is also connected via a vacuum feedthrough to the outside of the vacuum chamber, where light can in principle be coupled into or out of the fiber from both fiber ends. This makes the whole coupling process much easier as compared to the hollow-core fiber setup.

The ^{87}Rb-MOT is created using a standard three beam retro-reflected configuration (?? ask Krishnapriya) and is formed surrounding the waist of the nanofiber. A good overlap of the MOT, and later the optical molasses, and the optical nanofiber is extremely important. This overlap is typically optimized in a iterative process between visually observing the position of the optical molasses relative to the tapered fiber on two cameras and measuring the fluorescence of the atomic cloud which is coupled through the nanofiber onto a single-photon detector. Another important point is the isotropic expansion of the molasses as otherwise it may leave the nanofiber region.

The setup of the laser system for the Rydberg excitation follows the same approach as the laser system described in the previous chapters. Both 780 nm probe and 480 nm control laser are stabilized to vapour cell spectroscopy signals, using the EIT locking scheme in the case of the control laser. Then AOMs are used for switching the beams on or off, controlling their intensity and their frequency detuning.

Figure 4.23 shows a sketch of a typical experimental sequence. After loading the MOT from the background pressure in the vacuum chamber (??), the atoms are additionally cooled

THESIS DRAFT

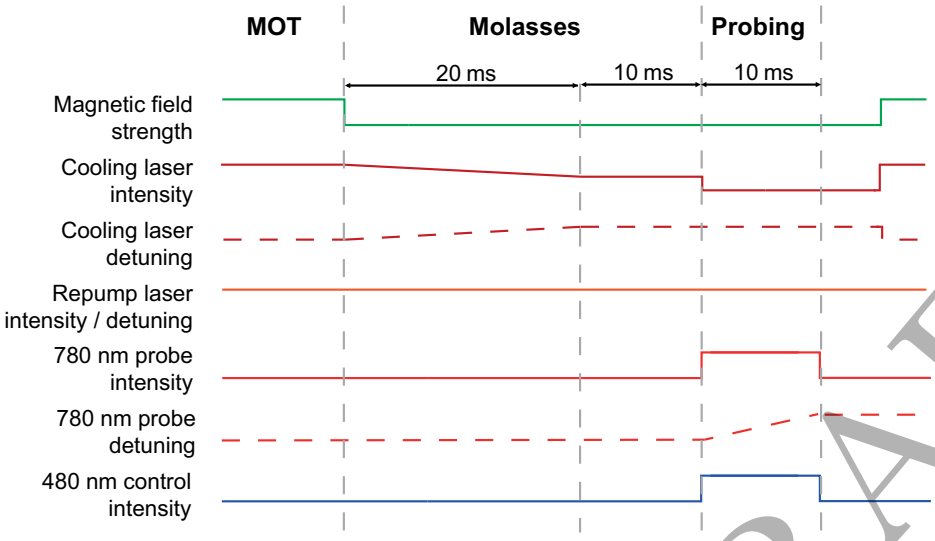

Figure 4.23.: Sketch of experimental sequence. Shown is a sketch of a typical experimental sequence (not to scale). After loading the MOT, the atoms are additionally cooled in an optical molasses phase. Then, probing is done during the time-of-flight of the molasses with a continuous probe and control beam, while scanning the detuning of the probe beam.

in an optical molasses phase. Timings and laser settings have been optimized to reach approximately 10^7 atoms at a temperature of about $150\,\mu$K in the initial MOT, which are then cooled to about $10\,\mu$K in the optical molasses. After the molasses phase, all trapping beams are switched off and the atomic cloud expands. During this time-of-flight, we probe the cloud with a continuous probe and control beam in contrast to the pulsed probing scheme discussed in earlier chapters. Also, for the following experiments, we scan the detuning of the probe beam continuously during each measurement, instead of using a step-wise scan of the probe detuning as discussed for the previous chapters.

4.4.3. First signatures of Rydberg atom formation close to the nanofiber

As discussed above, in principle we would like to guide both probe and control beam through the optical nanofiber and use their respective evanescent light fields for the Rydberg EIT process. However, as the coupling of high-power laser beams through an optical nanofiber is a non-trivial operation, intermediate steps are necessary both to test the setup and to confirm whether Rydberg excitation is at all possible in the vicinity of the optical nanofiber. In the following, I will present two of these preliminary measurements, one with both probe and control beam propagating free-space and one with the probe beam already coupled through the optical nanofiber. After presenting the results of these measurements, I will discuss the next steps and possible future directions for this experiment.

As a first proof-of-principle measurement, we want to demonstrate the feasibility of obtaining a Rydberg EIT signal in a cold atomic cloud outside an optical nanofiber. For this, we probe and excite the atoms in the optical molasses, which has been overlapped with the nanofiber, using a free-space beam configuration. The corresponding experimental setup

THESIS DRAFT

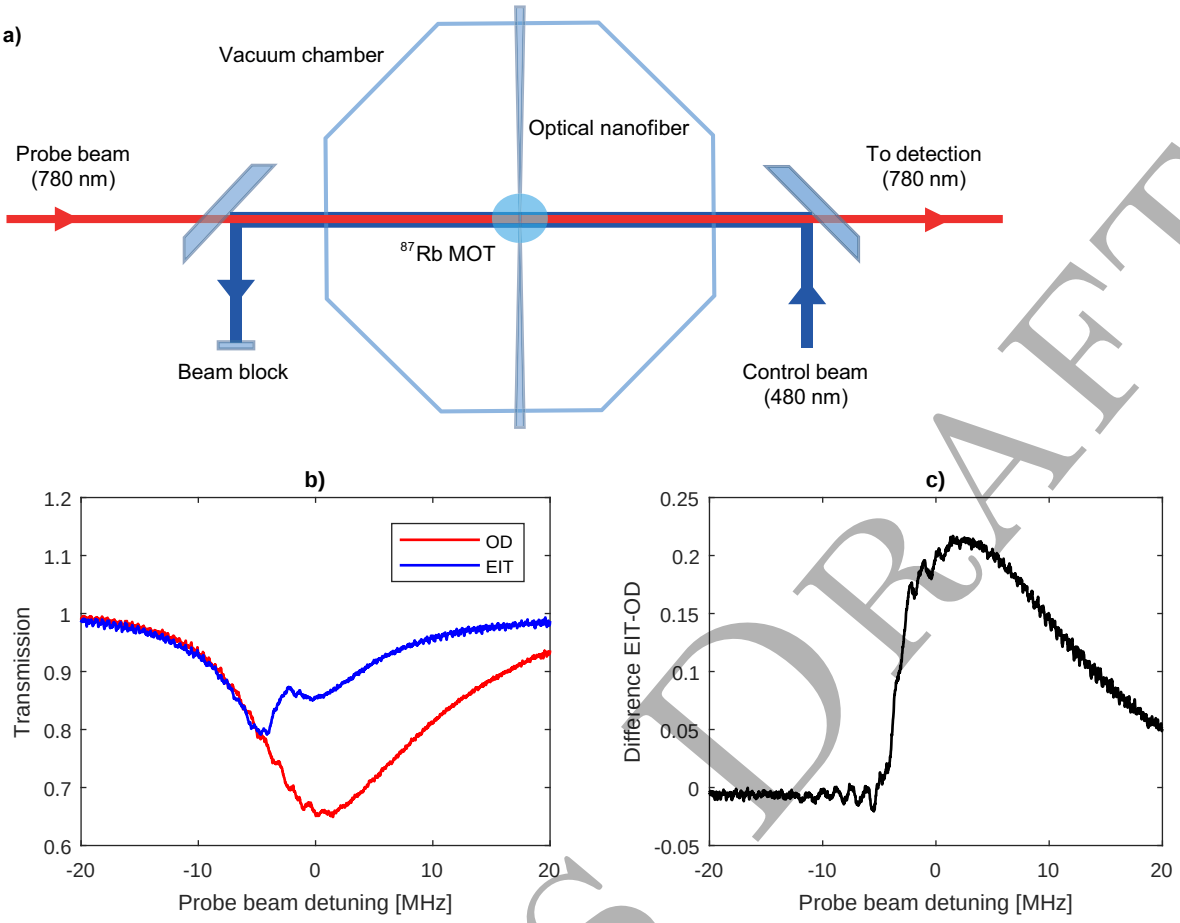

Figure 4.24.: First results of Rydberg excitation outside a nanofiber, free-space measurement. Figure a) shows the experimental setup. Here, both control and probe beam are propagating free-space in a counter-propagating configuration through the optical molasses, which is overlapped with the optical nanofiber. Figures b) and c) show the experimental results. In figure b), both OD and EIT signal are plotted as a function of the probe beam frequency. Note that for reasons of clarity, the y-axis is not plotted from 0 to 1 as in previous transmission plots. In figure c), the difference between EIT and OD signal from figure b) is plotted as a function of the frequency detuning to better visualize the occurence of the EIT peak. (Each measurement was averaged over 10 individual data sets as the data was taken. Errors have not been obtained for these preliminary measurements.)

is shown in figure 4.24 a). Here, we use a counterpropagating EIT scheme with probe and control beam coupled through the atomic cloud from opposite directions. Both beams are carefully overlapped with each other and the optical molasses. Finally, the absorption spectrum of the probe beam is measured on a photomultiplier detector.

Figure 4.24 b) shows one example signal for this type of measurement. Here, the transmission spectra of both OD and EIT signal are plotted as a function of the probe beam frequency. The OD signal taken in absence of the control beam shows a typical absorption profile. The asymmetry of the OD curve here can be due to the expansion of the atomic cloud during the probing time (Frequency sweep within 10 ms??). Lensing is unlikely for these low atomic densities, also we detect freespace (?). Maybe also due to asymmetries in

THESIS DRAFT

AOM powers / sweep. (??) In the EIT signal, a clear transmission peak is visible in the spectrum. Its occurence slightly off the maximum absorption indicates that we are slightly detuned with the control beam. Further, after the transmission peak, the signal does not return to the original transmission curve. Instead, we observe a much lower absorption of the right-hand side of the EIT peak, indicating a loss of atoms. This behaviour is highlighted in figure 4.24 c), where the difference between EIT and OD signal from figure b) is plotted as a function of the frequency detuning. Indeed, the EIT peak rises sharply on the negative detuning side, while decaying much more slowly on the positive detuning side. As the probe beam detuning is scanned continuously from the left- to the right-hand side of the graph (negative to positive detunings), we can equate the detunings with time. This means that the loss of atoms occurs temporally after scanning through the two-photon resonance, which indicates that we have indeed excited atoms to Rydberg states on the two-photon resonance, which are consequentially lost. This can for example happen by ionization or by atoms sticking to the walls of the nanofiber. A more quantitative analysis would first need a refinement of the data taking and analysis to understand and avoid the asymmetry of the OD only curve. Still, already with this qualitative analysis we could show that EIT excitation to Rydberg states is possible for atoms outside an optical nanofiber.

! New measurements from poster don't have this asymmetry and different right-hand values in absorption between OD and EIT (ask Krishnapriya). Also: mention Rydberg state ($30D_{5/2}$?)!

However, while in this measurement the optical molasses as a whole is overlapped with the optical nanofiber, not all atoms in the molasses are in the vicinity of the nanofiber. Therefore, this measurement is not yet a proof that any Rydberg atoms are really excited close to the nanofiber, as both probe and control beam traverse the whole of the optical molasses and therefore also interact with atoms far away from the nanofiber. To confirm that only atoms close to the nanofiber can be excited, in principle both probe and control beam have to be coupled through the nanofiber. Then only the atoms very close to the nanofiber can interact with the evanescent fields and thus be excited to Rydberg states. However, coupling tens or hundreds of Milliwatts of the blue control laser into a tapered fiber is a highly non-trivial endeavour and can easily result in burning or breaking of the fiber. Therefore, for the following preliminary measurements, we have only coupled the probe beam through the nanofiber, while letting the control beam propagate in free space as in the previous measurement. Since the evanescent field of the probe beam can now only interact with atoms very close to the waist of the nanofiber, this measurement is a first confirmation that there are indeed Rydberg atoms forming close to the surface of the nanofiber.

Figure 4.25 shows the experimental setup for these measurements. The probe beam is coupled into the end of the tapered fiber outside the vacuum chamber, is then propagating through the nanofiber and is finally detected outside the vacuum chamber again using a single photon counting module (SPCM). The control beam is still propagating free-space as in the previous measurement. However, to achieve a higher control beam intensity and thus Rabi frequency at the waist region of the nanofiber, the control beam is here used in a retroreflected configuration. This is necessary here, as the overlap with the probe beam is much less than in the counter-propagating configuration and also the probe intensity is

THESIS DRAFT

much higher due to the low area of the evanescent field. (XX: laser powers and intensities?? Ask Krishnapriya)

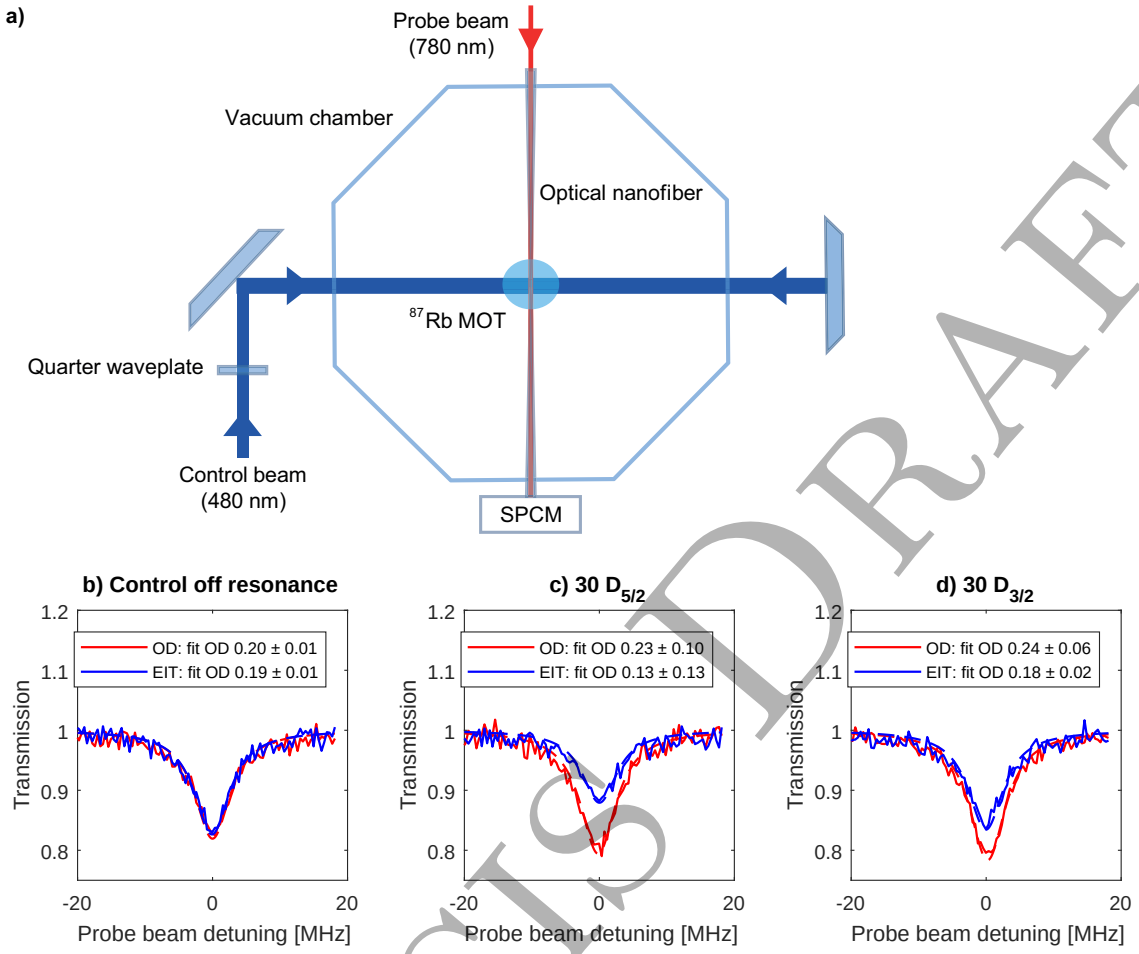

Figure 4.25.: First results of Rydberg excitation outside a nanofiber, fibercoupled probe beam. Figure a) shows the experimental setup. Here, the control beam is propagating free-space through the optical molasses, which is close to the optical nanofiber. To achieve a higher control beam intensity and thus Rabi frequency, the control beam is used in a retroreflected configuration. The probe beam is coupled through the optical nanofiber and is detected on a single-photon counting module (SPCM). Figures b) to d) show the first experimental results. OD and EIT signals are plotted as a function of the probe beam frequency for the control beam off resonance (b) as well as for the control beam stabilized to the $30D_{5/2}$ (c) and $30D_{3/2}$ (d) states (solid lines). An OD fit (cf. equation 2.14) is plotted for each data set (dashed lines) and the resulting OD values are given in the legend. Note that for reasons of clarity, the range of the y-axis is limited. (Each measurement was averaged over 100 individual data sets as the data was taken. Errors have not been obtained for these preliminary measurements.)

The first experimental results are shown in figure 4.25 b) to d). Here, again both OD and EIT signal are plotted as a function of the probe beam frequency. Additional, an OD fit to each dataset according to equation 2.14 is plotted in the figures and the resulting OD values are given in the legend. When the control laser is tuned away from the two-photon resonance (figure 4.25 b), no difference in the two absorption profiles can be seen and also the OD fit values are the same within their error bars. Note that in general the absorption is lower

THESIS DRAFT

than in previous measurements as here only the atoms within the reach of the evanescent field can contribute to the signal. From comparison to similar experiments, we assume approximately 10 atoms in the evanescent field region (??? ask Krishnapriya), however a precise calculation is involved and needs the fiber geometry and the exact overlap between atoms and light field to determine the OD correction factor analogously to equation 2.17.

When the control laser is stabilized to the transition frequency to the Rydberg states $30D_{5/2}$ in figure 4.25 c) or $30D_{3/2}$ in figure 4.25 d), a clear difference in absorption between EIT and OD measurement can be seen. In contrast to all measurements discussed previously, however, no distinct EIT peak can be seen. Instead, we observe that the overall absorption reduces. In the case of the $D_{5/2}$ state, the optical depth with the control beam on is only half of the optical depth without control beam. This reduction in optical depth is a clear indicator of a loss of atoms. As this loss only occurs when the control beam is on resonance with a Rydberg transition, this suggest that the loss of atoms is due to the formation of Rydberg atoms. This is further supported by the observation that for the $D_{3/2}$ state, which has a smaller transition matrix element and thus a lower excitation probability, the reduction in OD is less than for the $D_{5/2}$ state. However, quantitative comparisons here are difficult due to the large errors of these preliminary measurements.

A broad blurred EIT signal instead of a distinct peak would also be consistent with a broad range of possible line shifts and broadenings, resulting from different distances of the atoms from the optical nanofiber. In principle, due to the intensity distribution of the evanescent field, atoms very close to the fiber have the highest probability of being excited to Rydberg states. At the same time, they would experience the strongest shift due to the fiber surface and would also face the highest possibility of being lost when getting adsorbed onto the fiber surface. All these effects could lead to a strong loss feature and a very broad EIT signal.

In conclusion, both our preliminary measurements present good evidence that we have indeed observed the first signatures of exciting cold Rydberg atoms near an optical nanofiber. Achieving this result was the major goal of my research project at OIST. In particular, with the fibercoupled probe beam, we could show that Rydberg atoms can be excited at a subwavelength distance to the nanofiber, as this is the reach of the evanescent field.

Both types of measurements are still subject to further studies and analysis to fully understand the process of the formation of Rydberg atoms close to the nanofiber. For example, further measurements, which have been done after my time in Okinawa and confirm our preliminary results, study the dependence of the Rydberg excitation on both probe and control power. (XX: ask Krishnapriya!, cite poster or private communication) Additionally, in particular measurements with both probe and control laser coupled through the nanofiber are necessary to confirm the Rydberg excitation signal close to the optical nanofiber.

As a future direction, a two-colour dipole trap guided through the optical nanofiber can be implemented to trap the atoms close to the fiber surface and control the distance to the fiber surface by the intensity of the two light fields [LeKien2004]. Then a systematic characterization of shifts and broadenings of the EIT line due to different distances from the fiber surface will be possible. It will be highly interesting to compare these results to the

THESIS DRAFT

results obtained in the hollow-core fiber setup and to study the influences of the different fiber geometries.

THESIS DRAFT

THESIS DRAFT

5. Conclusion and Outlook

5.1. Achievements so far

Compare with goals in introduction

Highly controlled transport, good understanding of all transport parameters:

"In conclusion, we have presented a detailed study on the transport of cold atoms both inside and outside a hollow-core fiber using an optical conveyor belt. We have found that by applying optimized frequency and amplitude ramps we can control a wide range of transport efficiencies and final atomic temperatures. In particular, we can prepare final atomic ensembles at the same temperature as before the transport. Depending on the individual experimental requirements, we can find a compromise between the final number of atoms and their temperature. While for atoms with a higher mean temperature, we can achieve higher absolute transport efficiencies, colder atomic ensembles show an extended observation time before colliding with the fiber walls, which is advantageous for in-fiber experiments. We further find that our experimental results agree qualitatively well with the theoretical simulation and we have a good understanding of the correction factors between experiment and theory. Our high degree of control over the atom-fiber interface will for example allow for experiments to systematically survey the inner part of the hollow-core fiber. We also expect our results to be of importance for other conveyor belt or atoms-in-fiber experiments for reducing heating during transport." [72]

Rydberg excitation inside fiber, starting to understand shifts and broadenings, time-resolved measurements:

"In conclusion, we have demonstrated the first Rydberg excitations of cold atoms inside a hollow core fiber. We are able to produce a highly controllable sample of atoms and we find our system well suited as a hybrid cold Rydberg atom fiber interface. We have studied the influence of the fiber on the EIT signal and we observe both a broadening and shift of our signals on the order of their linewidth. Only at positions very close to the fiber tip, we see such a strong influence that we have not been able to produce a clear EIT signal, possibly due to large inhomogeneous electric fields due to adatoms as also observed in numerous other experiments [43-49]. We are currently further investigating the influences of different types of fibers on our EIT signal in a separate setup and are testing possible techniques to overcome these interaction effects, e.g. by coating of the inner fiber core or by light-induced atomic desorption (LIAD). The effects of the fiber on coherent Rydberg excitation were further quantified through a time resolved detection method. Here, we have found two different regimes of Rydberg excitations to exist: one EIT regime and one regime dominated

THESIS DRAFT

by atom loss. As within the EIT regime the fiber does not have a significant influence on the occurrence of the EIT signal, we believe that our system is an important step towards future use of hybrid systems for quantum simulation or information. One further possible future application of our system is to study the propagation of excitations and correlations in dense extended one-dimensional media [58-61]." [13]

5.2. Next steps

Overview of next steps already discussed for transport and Rydberg excitation individually (smaller, denser clouds, longer lifetimes, less shifts and influence of fiber wall) -> let's assume we get these technical limitations under control (this work has laid a solid foundation)

5.2.1. Detecting non-classical states of light

homodyne detection (non-classical states of light, g(2)-function), light storage (pulse shaping)

5.3. Suitability of our system for quantum simulation

Roadmap to creating photon-photon interactions and quantum simulation (maybe follow one theory proposal in detail)

5.3.1. Creating tunable photon-photon interactions

5.3.2. Quantum simulation with photons

Example: Angelakis proposal for simulating relativistic physics

THESIS DRAFT

A. Appendix

A.1. Typical experimental parameters

In the following table, our typical experimental parameters for the individual stages within our experimental sequence are given, which has been discussed in section 2.1.

Laser	Frequency detuning from resonance
Pushing beam	+18 MHz
2D MOT cooling	−10 MHz
2D MOT repump	on resonance
3D MOT cooling	−10 MHz (increased to −50 MHz during compression stage)
3D MOT repump	on resonance

Table A.1.: Typical laser frequencies during MOT loading and compression.

Laser	Power
Pushing beam	140 μW
2D MOT cooling	45 mW per beam
2D MOT repump	8 mW per beam
3D MOT cooling	42 mW / 22 mW / 42 mW for the three initial MOT beams (decreased to 21 mW / 11 mW / 21 mW during compression stage)
3D MOT repump	16 mW / 5 mW / 7 mW for the three initial MOT beams

Table A.2.: Typical laser powers during MOT loading and compression.

THESIS DRAFT

	Loading	Compression
Pushing beam	+18 MHz, 140 μW	off
2D MOT cooling	−10 MHz, 45 mW per beam	off
2D MOT repump	on resonance, 8 mW per beam	off
3D MOT cooling	−10 MHz, 42 mW / 22 mW / 42 mW	−50 MHz, 21 mW / 11 mW / 21 mW
3D MOT repump	on resonance, 16 mW / 5 mW / 7 mW	on resonance, 16 mW / 5 mW / 7 mW
MOT magnetic field	14 A (5.3 G/cm axial)*	38 A (14.4 G/cm axial)*

Table A.3.: Typical experimental parameters during the different stages of the experimental sequence. * Calculated by using the magnetic field gradients axial 0.38 G/Acm, radial −0.19 G/Acm [70].

	Loading	Compression	Transport	Experiments
Pushing beam	blue detuned 18 MHz, 140 μW	off	off	off
2D MOT cooling	−10 MHz, 45 mW per beam	off	off	off
2D MOT repump	on resonance, 8 mW per beam	off	off	off
3D MOT cooling	−10 MHz, 42 mW / 22 mW / 42 mW	−50 MHz, 21 mW / 11 mW / 21 mW	off	off
3D MOT repump	on resonance, 16 mW / 5 mW / 7 mW	on resonance, 16 mW / 5 mW / 7 mW	off	off
MOT magnetic field	14 A (5.3 G/cm axial)*	38 A (14.4 G/cm axial)*	off	off
dipole trap	on	on	on, power and detuning varied	off / pulsed
detection	off	off	off	on / pulsed
blue EIT	off	off	off	on / pulsed

Table A.4.: Typical experimental parameters during the different stages of the experimental sequence. * Calculated by using the magnetic field gradients axial 0.38 G/Acm, radial −0.19 G/Acm [70].

THESIS DRAFT

A.2. Truncated Boltzmann distribution

For the calculation of the truncated Boltzmann distribution, it is necessary to use the full two-dimensional oscillator model instead of the more intuitive one-dimensional oscillator model used earlier for visualization. Therefore, let me first point out the main differences to the one-dimensional case discussed earlier in the text, following reference XYZ.

For the two-dimensional harmonic oscillator, the energy levels are given by

$$E_{n,\mathrm{2D}} = \hbar\omega\,(n+1)\,, \tag{A.1}$$

where the quantum number $n = n_x + n_y$. Note that here several combinations of n_x and n_y can lead to the same n_r. Therefore, we have to take into account the degeneracy of each state. We do that by calculating the density of states $g\,(E_{n,\mathrm{2D}})$, which counts the number of states dN within an energy volume dE. In our case, the total number of states is given by $N = \pi n^2/4$. This factor $1/4$ arises, as both quantum numbers n_x and n_y have to be positive. We then calculate a density of states

$$g\,(E_{n,\mathrm{2D}}) = \frac{dN}{dE} = \frac{dN}{dn} \times \frac{dn}{dE} = \frac{\pi}{2}\frac{1}{\hbar\omega}\left(\frac{E_{n,\mathrm{2D}}}{\hbar\omega} - 1\right). \tag{A.2}$$

The occupation probability of each energy level is given by the Boltzmann distribution and also has to be weighed with the density of states:

$$P(E_{n,\mathrm{2D}}) = \frac{g\,(E_{n,\mathrm{2D}})\exp\left(-E_{n,\mathrm{2D}}/k_\mathrm{B}T\right)}{Z_{2D}}, \tag{A.3}$$

where $Z_\mathrm{2D} = \sum_n g\,(E_{n,\mathrm{2D}})\exp\left(-E_{n,\mathrm{2D}}/k_\mathrm{B}T\right)$ is the partition function and T is the mean temperature of the atomic ensemble. Note that in the two-dimensional case, the mean energy of the atomic ensemble is given by $\langle E\rangle = 2k_\mathrm{B}T$.

When using the truncated Boltzmann distribution, we assume that atoms with energies above the threshhold of the potential depth U_trunc will no longer be trapped. Therefore, the occupation probability will be truncated at the energy corresponding to this potential depth. In the following, I will derive the formulas for number and temperature of the remaining atoms, closely following reference [81]. Note that I will neglecting the zero-point energy for the following calculations, as the temperature of our system is typically much higher than $\hbar\omega$. For the same high-temperature argument, I will use an integral over the continuous energy states E_2D instead of the sum over the discrete energy levels $E_{n,\mathrm{2D}}$.

The formula of the survival probability of the atoms in the trap can be calculated by truncating the original occupation probability given in equation A.3 at the potential depth U_trunc and is given by

$$\begin{aligned} P^\mathrm{surv}_\mathrm{2D,trunc}\,(U_\mathrm{trunc}) &= \int_0^{U_\mathrm{trunc}} P\,(E_\mathrm{2D})\,dE \\ &= \frac{1}{(k_\mathrm{B}T)^2}\int_0^{U_\mathrm{trunc}} E_\mathrm{2D}\exp\left(-E_\mathrm{2D}/k_\mathrm{B}T\right)dE \\ &= 1-(1+\eta)\,\mathrm{e}^{-\eta}, \end{aligned} \tag{A.4}$$

THESIS DRAFT

where the factor $\eta = U_{\mathrm{trunc}}/(k_{\mathrm{B}}T)$ is a measure of how much of the distribution is actually truncated.

For deriving the expression for the temperature of the remaining atoms, I first calculate the truncated partition function

$$\begin{aligned} Z_{\mathrm{2D,trunc}} &= \int_0^{U_{\mathrm{trunc}}} g\left(E_{\mathrm{2D}}\right) \exp\left(-E_{\mathrm{2D}}/k_{\mathrm{B}}T\right) dE \\ &= \frac{\pi \left(k_{\mathrm{B}}T\right)^2}{2\left(\hbar\omega\right)^2} \left[1 - (1+\eta)\,\mathrm{e}^{-\eta}\right]. \end{aligned} \tag{A.5}$$

Then I can calculate the mean energy of the remaining atoms as

$$\langle E\rangle_{\mathrm{2D,trunc}} = \frac{\int_0^{U_{\mathrm{trunc}}} E_{\mathrm{2D}}\, g\left(E_{\mathrm{2D}}\right) \exp\left(-E_{\mathrm{2D}}/k_{\mathrm{B}}T\right) dE}{Z_{\mathrm{2D,trunc}}} = 2k_{\mathrm{B}}T \frac{1 - \left(1 + \eta + \frac{1}{2}\eta^2\right)\mathrm{e}^{-\eta}}{1 - (1+\eta)\,\mathrm{e}^{-\eta}}. \tag{A.6}$$

Therefore, the mean temperature of the remaining atoms is given by

$$\langle T\rangle_{\mathrm{2D,trunc}} = \frac{\langle E\rangle_{\mathrm{2D,trunc}}}{2k_{\mathrm{B}}} = T \frac{1 - \left(1 + \eta + \frac{1}{2}\eta^2\right)\mathrm{e}^{-\eta}}{1 - (1+\eta)\,\mathrm{e}^{-\eta}}. \tag{A.7}$$

A.3. Transport results for other frequency ramps

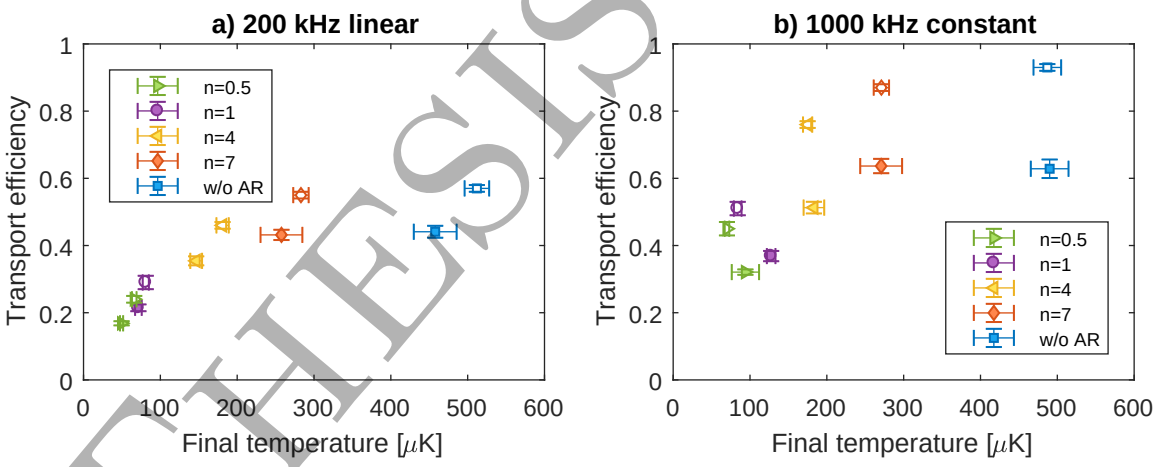

Figure A.1.: Experimental and theoretical results outside the fiber for other frequency ramps. "a) Shown is the potential depth as a function of distance for different amplitude ramp-downs. The black dashed line marks the final atomic position for the applied frequency ramp. b) Shown are the experimental (filled markers) and theoretical (empty markers) results for transport efficiency and final temperature for atoms transported to the fiber tip for the 1000 kHz linear frequency ramp and for the different amplitude ramp-downs from figure a). (Error bars represent statistical errors and errors from the fitting procedure.)"

THESIS DRAFT

List of Figures and Tables

List of Figures

THESIS DRAFT

THESIS DRAFT

THESIS DRAFT

List of Tables

THESIS DRAFT

Bibliography

[1] A. Acín, I. Bloch, H. Buhrman, T. Calarco, C. Eichler, J. Eisert, D. Esteve, N. Gisin, S. J. Glaser, F. Jeletzko, et al., "The European Quantum Technologies Roadmap," arXiv preprint arXiv:1712.03773 (2017).

[2] R. P. Feynman, "Simulating physics with computers," International Journal of Theoretical Physics **21**, 467 (1982).

[3] M. Lewenstein, A. Sanpera, and V. Ahufinger, *Ultracold Atoms in Optical Lattices: Simulating quantum many-body systems* (Oxford University Press, 2012).

[4] I. Bloch, J. Dalibard, and S. Nascimbene, "Quantum simulations with ultracold quantum gases," Nature Physics **8**, 267 (2012).

[5] I. M. Georgescu, S. Ashhab, and F. Nori, "Quantum simulation," Reviews of Modern Physics **86**, 153 (2014).

[6] A. Aspuru-Guzik and P. Walther, "Photonic quantum simulators," Nature Physics **8**, 285 (2012).

[7] F. Blatt, T. Halfmann, and T. Peters, "One-dimensional ultracold medium of extreme optical depth," Optics Letters **39**, 446 (2014).

[8] H. Ito, T. Nakata, K. Sakaki, M. Ohtsu, K. I. Lee, and W. Jhe, "Laser Spectroscopy of Atoms Guided by Evanescent Waves in Micron-Sized Hollow Optical Fibers," Physical Review Letters **76**, 4500 (1996).

[9] D. Grass, J. Fesel, S. G. Hofer, N. Kiesel, and M. Aspelmeyer, "Optical trapping and control of nanoparticles inside evacuated hollow core photonic crystal fibers," Applied Physics Letters **108**, 221103 (2016).

[10] M. Bajcsy, S. Hofferberth, V. Balic, T. Peyronel, M. Hafezi, A. S. Zibrov, V. Vuletic, and M. D. Lukin, "Efficient All-Optical Switching Using Slow Light within a Hollow Fiber," Physical Review Letters **102**, 203902 (2009).

[11] H. Duncker, "Ultrastable Laser Technologies and Atom-Light Interactions in Hollow Fibers," Ph.D. thesis, Universität Hamburg (2014).

[12] F. Blatt, L. S. Simeonov, T. Halfmann, and T. Peters, "Stationary light pulses and narrowband light storage in a laser-cooled ensemble loaded into a hollow-core fiber," Physical Review A **94**, 043833 (2016).

THESIS DRAFT

[13] M. Langbecker, M. Noaman, N. Kjærgaard, F. Benabid, and P. Windpassinger, "Rydberg excitation of cold atoms inside a hollow-core fiber," Physical Review A **96**, 041402 (2017).

[14] S. Okaba, T. Takano, F. Benabid, T. Bradley, L. Vincetti, Z. Maizelis, V. Yampol'skii, F. Nori, and H. Katori, "Lamb-Dicke spectroscopy of atoms in a hollow-core photonic crystal fibre," Nature Communications **5**, 4096 (2014).

[15] M. Xin, W. S. Leong, Z. Chen, and S.-Y. Lan, "An atom interferometer inside a hollow-core photonic crystal fiber," Science Advances **4**, e1701723 (2018).

[16] S. Vorrath, S. A. Möller, P. Windpassinger, K. Bongs, and K. Sengstock, "Efficient guiding of cold atoms through a photonic band gap fiber," New Journal of Physics **12**, 123015 (2010).

[17] C. A. Christensen, S. Will, M. Saba, G.-B. Jo, Y.-I. Shin, W. Ketterle, and D. Pritchard, "Trapping of ultracold atoms in a hollow-core photonic crystal fiber," Physical Review A **78**, 033429 (2008).

[18] M. Bajcsy, S. Hofferberth, T. Peyronel, V. Balic, Q. Liang, A. S. Zibrov, V. Vuletic, and M. D. Lukin, "Laser-cooled atoms inside a hollow-core photonic-crystal fiber," Physical Review A **83**, 063830 (2011).

[19] A. P. Hilton, C. Perrella, F. Benabid, B. M. Sparkes, A. N. Luiten, and P. S. Light, "High-efficiency cold-atom transport into a waveguide trap," Physical Review A **10**, 044034 (2018).

[20] S. Kuhr, W. Alt, D. Schrader, M. Müller, V. Gomer, and D. Meschede, "Deterministic Delivery of a Single Atom," Science **293**, 278 (2001).

[21] D. Schrader, S. Kuhr, W. Alt, M. Müller, V. Gomer, and D. Meschede, "An optical conveyor belt for single neutral atoms," Applied Physics B **73**, 819 (2001).

[22] S. Schmid, G. Thalhammer, K. Winkler, F. Lang, and J. H. Denschlag, "Long distance transport of ultracold atoms using a 1D optical lattice," New Journal of Physics **8**, 159 (2006).

[23] S. Kuhr, W. Alt, D. Schrader, I. Dotsenko, Y. Miroshnychenko, W. Rosenfeld, M. Khudaverdyan, V. Gomer, A. Rauschenbeutel, and D. Meschede, "Coherence Properties and Quantum State Transportation in an Optical Conveyor Belt," Physical Review Letters **91**, 213002 (2003).

[24] P. Schneeweiss, S. T. Dawkins, R. Mitsch, D. Reitz, E. Vetsch, and A. Rauschenbeutel, "A nanofiber-based optical conveyor belt for cold atoms," Applied Physics B **110**, 279 (2012).

[25] T. Middelmann, S. Falke, C. Lisdat, and U. Sterr, "Long-range transport of ultracold atoms in a far-detuned one-dimensional optical lattice," New Journal of Physics **14**, 073020 (2012).

THESIS DRAFT

[26] O. Firstenberg, C. S. Adams, and S. Hofferberth, "Nonlinear quantum optics mediated by Rydberg interactions," Journal of Physics B: Atomic, Molecular and Optical Physics **49**, 152003 (2016).

[27] M. Saffman, T. G. Walker, and K. Mølmer, "Quantum information with Rydberg atoms," Reviews of Modern Physics **82**, 2313 (2010).

[28] M. Fleischhauer, A. Imamoglu, and J. P. Marangos, "Electromagnetically induced transparency: Optics in coherent media," Reviews of Modern Physics **77**, 633 (2005).

[29] I. Friedler, D. Petrosyan, M. Fleischhauer, and G. Kurizki, "Long-range interactions and entanglement of slow single-photon pulses," Physical Review A **72**, 043803 (2005).

[30] A. V. Gorshkov, J. Otterbach, M. Fleischhauer, T. Pohl, and M. D. Lukin, "Photon-Photon Interactions via Rydberg Blockade," Physical Review Letters **107**, 133602 (2011).

[31] J. D. Pritchard, C. S. Adams, and K. Mølmer, "Correlated Photon Emission from Multiatom Rydberg Dark States," Physical Review Letters **108**, 043601 (2012).

[32] T. Peyronel, O. Firstenberg, Q.-Y. Liang, S. Hofferberth, A. V. Gorshkov, T. Pohl, M. D. Lukin, and V. Vuletić, "Quantum nonlinear optics with single photons enabled by strongly interacting atoms," Nature **488**, 57 (2012).

[33] O. Firstenberg, M. D. Lukin, T. Peyronel, Q.-Y. Liang, V. Vuletic, A. V. Gorshkov, S. Hofferberth, and T. Pohl, "Quantum Nonlinear Optics: Strongly Interacting Photons," Optics & Photonics News **24**, 48 (2013).

[34] Y. O. Dudin and A. Kuzmich, "Strongly interacting Rydberg excitations of a cold atomic gas," Science **336**, 887 (2012).

[35] D. Maxwell, D. J. Szwer, D. Paredes-Barato, H. Busche, J. D. Pritchard, A. Gauguet, K. J. Weatherill, M. P. A. Jones, and C. S. Adams, "Storage and Control of Optical Photons Using Rydberg Polaritons," Physical Review Letters **110**, 103001 (2013).

[36] V. Parigi, E. Bimbard, J. Stanojevic, A. J. Hilliard, F. Nogrette, R. Tualle-Brouri, A. Ourjoumtsev, and P. Grangier, "Observation and Measurement of Interaction-Induced Dispersive Optical Nonlinearities in an Ensemble of Cold Rydberg Atoms," Physical Review Letters **109**, 233602 (2012).

[37] D. Maxwell, D. J. Szwer, D. Paredes-Barato, H. Busche, J. D. Pritchard, A. Gauguet, M. P. A. Jones, and C. S. Adams, "Microwave control of the interaction between two optical photons," Physical Review A **89**, 043827 (2014).

[38] H. Gorniaczyk, C. Tresp, J. Schmidt, H. Fedder, and S. Hofferberth, "Single-Photon Transistor Mediated by Interstate Rydberg Interactions," Physical Review Letters **113**, 053601 (2014).

[39] D. Tiarks, S. Baur, K. Schneider, S. Dürr, and G. Rempe, "Single-Photon Transistor Using a Förster Resonance," Physical Review Letters **113**, 053602 (2014).

THESIS DRAFT

[40] S. Baur, D. Tiarks, G. Rempe, and S. Dürr, "Single-Photon Switch Based on Rydberg Blockade," Physical Review Letters **112**, 073901 (2014).

[41] H. Gorniaczyk, C. Tresp, P. Bienias, A. Paris-Mandoki, W. Li, I. Mirgorodskiy, H. P. Büchler, I. Lesanovsky, and S. Hofferberth, "Enhancement of Rydberg-mediated single-photon nonlinearities by electrically tuned Förster Resonances," Nature Communications **7** (2016).

[42] C. Tresp, C. Zimmer, I. Mirgorodskiy, H. Gorniaczyk, A. Paris-Mandoki, and S. Hofferberth, "Single-Photon Absorber Based on Strongly Interacting Rydberg Atoms," Physical Review Letters **117**, 223001 (2016).

[43] D. Tiarks, S. Schmidt, G. Rempe, and S. Dürr, "Optical π phase shift created with a single-photon pulse," Science Advances **2** (2016).

[44] M. Saffman, "Quantum computing with atomic qubits and Rydberg interactions: progress and challenges," Journal of Physics B: Atomic, Molecular and Optical Physics **49**, 202001 (2016).

[45] J. D. Thompson, T. L. Nicholson, Q.-Y. Liang, S. H. Cantu, A. V. Venkatramani, S. Choi, I. A. Fedorov, D. Viscor, T. Pohl, M. D. Lukin, et al., "Symmetry-protected collisions between strongly interacting photons," Nature **542**, 206 (2017).

[46] C. Noh and D. G. Angelakis, "Quantum simulations and many-body physics with light," Reports on Progress in Physics **80**, 016401 (2017).

[47] M.-X. Huo and D. G. Angelakis, "Sine-Gordon and Bose-Hubbard dynamics with photons in a hollow-core fiber," Physical Review A **85**, 023821 (2012).

[48] D. G. Angelakis, M.-X. Huo, D. Chang, L. C. Kwek, and V. Korepin, "Mimicking Interacting Relativistic Theories with Stationary Pulses of Light," Physical Review Letters **110**, 100502 (2013).

[49] J. Otterbach, M. Moos, D. Muth, and M. Fleischhauer, "Wigner Crystallization of Single Photons in Cold Rydberg Ensembles," Physical Review Letters **111**, 113001 (2013).

[50] P. Bienias, S. Choi, O. Firstenberg, M. F. Maghrebi, M. Gullans, M. D. Lukin, A. V. Gorshkov, and H. P. Büchler, "Scattering resonances and bound states for strongly interacting Rydberg polaritons," arXiv preprint arXiv:1402.7333 (2014).

[51] M. Moos, M. Höning, R. Unanyan, and M. Fleischhauer, "Many-body physics of Rydberg dark-state polaritons in the strongly interacting regime," Physical Review A **92**, 053846 (2015).

[52] M. F. Maghrebi, M. J. Gullans, P. Bienias, S. Choi, I. Martin, O. Firstenberg, M. D. Lukin, H. P. Büchler, and A. V. Gorshkov, "Coulomb bound states of strongly interacting photons," Physical Review Letters **115**, 123601 (2015).

THESIS DRAFT

[53] B. He, A. V. Sharypov, J. Sheng, C. Simon, and M. Xiao, "Two-Photon Dynamics in Coherent Rydberg Atomic Ensemble," Physical Review Letters **112**, 133606 (2014).

[54] L. Tonks, "The Complete Equation of State of One, Two and Three-Dimensional Gases of Hard Elastic Spheres," Physical Review **50**, 955 (1936).

[55] M. Girardeau, "Relationship between systems of impenetrable bosons and fermions in one dimension," Journal of Mathematical Physics **1**, 516 (1960).

[56] E. H. Lieb and W. Liniger, "Exact Analysis of an Interacting Bose Gas. I. The General Solution and the Ground State," Physical Review **130**, 1605 (1963).

[57] B. Paredes, A. Widera, V. Murg, O. Mandel, S. Fölling, I. Cirac, G. V. Shlyapnikov, T. W. Hänsch, and I. Bloch, "Tonks–Girardeau gas of ultracold atoms in an optical lattice," Nature **429**, 277 (2004).

[58] T. Kinoshita, T. Wenger, and D. S. Weiss, "Observation of a one-dimensional Tonks-Girardeau gas," Science **305**, 1125 (2004).

[59] D. E. Chang, V. Gritsev, G. Morigi, V. Vuletić, M. D. Lukin, and E. A. Demler, "Crystallization of strongly interacting photons in a nonlinear optical fibre," Nature Physics **4**, 884 (2008).

[60] A. V. Gorshkov, R. Nath, and T. Pohl, "Dissipative Many-Body Quantum Optics in Rydberg Media," Physical Review Letters **110**, 153601 (2013).

[61] G. Epple, K. S. Kleinbach, T. G. Euser, N. Y. Joly, T. Pfau, P. S. J. Russell, and R. Löw, "Rydberg atoms in hollow-core photonic crystal fibres," Nature Communications **5**, 4132 (2014).

[62] H. Kübler, J. P. Shaffer, T. Baluktsian, R. Löw, and T. Pfau, "Coherent excitation of Rydberg atoms in micrometre-sized atomic vapour cells," Nature Photonics **4**, 112 (2010).

[63] A. Tauschinsky, R. M. T. Thijssen, S. Whitlock, H. B. van Linden van den Heuvell, and R. J. C. Spreeuw, "Spatially resolved excitation of Rydberg atoms and surface effects on an atom chip," Physical Review A **81**, 063411 (2010).

[64] R. P. Abel, C. Carr, U. Krohn, and C. S. Adams, "Electrometry near a dielectric surface using Rydberg electromagnetically induced transparency," Physical Review A **84**, 023408 (2011).

[65] H. Hattermann, M. Mack, F. Karlewski, F. Jessen, D. Cano, and J. Fortágh, "Detrimental adsorbate fields in experiments with cold Rydberg gases near surfaces," Physical Review A **86**, 022511 (2012).

[66] J. D. Carter, O. Cherry, and J. D. D. Martin, "Electric-field sensing near the surface microstructure of an atom chip using cold Rydberg atoms," Physical Review A **86**, 053401 (2012).

THESIS DRAFT

[67] K. S. Chan, M. Siercke, C. Hufnagel, and R. Dumke, "Adsorbate Electric Fields on a Cryogenic Atom Chip," Physical Review Letters **112**, 026101 (2014).

[68] J. B. Naber, A. Tauschinsky, H. B. Heuvell, and R. J. C. Spreeuw, "Electromagnetically induced transparency with Rydberg atoms across the Breit-Rabi regime," arXiv:1606.08260 (2016).

[69] J. A. Sedlacek, E. Kim, S. T. Rittenhouse, P. F. Weck, H. R. Sadeghpour, and J. P. Shaffer, "Electric Field Cancellation on Quartz by Rb Adsorbate-Induced Negative Electron Affinity," Physical Review Letters **116**, 133201 (2016).

[70] S. Vorrath, "Entwicklung eines neuartigen, laserbasierten, photonischen Wellenleiters für ultrakalte Atome," Ph.D. thesis, Universität Hamburg (2008).

[71] M. Noaman, "tba," Ph.D. thesis, Johannes Gutenberg-Universität Mainz (expected 2018).

[72] M. Langbecker, R. Wirtz, F. Knoch, M. Noaman, T. Speck, and P. Windpassinger, "Highly controlled optical transport of cold atoms into a hollow-core fiber," New Journal of Physics **20**, 083038 (2018).

[73] M. Noaman, M. Langbecker, and P. Windpassinger, "Micro-lensing-induced line shapes in a single-mode cold-atom-hollow-core-fiber interface," Optics Letters **43**, 3925 (2018).

[74] F. Stuhlmann, "Programmierung und Implementierung einer flexiblen AOM-Ansteuerung," Bachelor's thesis, Johannes Gutenberg-Universität Mainz (2016).

[75] R. Wirtz, "Optischer Transport von kalten Atomen in eine Hohlkernfaser," Master's thesis, Johannes Gutenberg-Universität Mainz (2018).

[76] R. Grimm, M. Weidemüller, and Y. B. Ovchinnikov, "Optical Dipole Traps for Neutral Atoms," in *Advances In Atomic, Molecular, and Optical PhysicsAdvances*, edited by B. Bederson and H. Walther (Academic Press, 2000), vol. 42 of *Advances In Atomic, Molecular, and Optical Physics*, pp. 95 – 170.

[77] D. A. Steck, "Rubidium 87 D Line Data,", available online at http://steck.us/alkalidata (revision 2.1.4, 23 December 2010) (2010).

[78] T. Arpornthip, C. A. Sackett, and K. J. Hughes, "Vacuum-pressure measurement using a magneto-optical trap," Phys. Rev. A **85**, 033420 (2012).

[79] D. Schrader, "Ein Förderband für einzelne Atome," Diploma thesis, Friedrich-Wilhelms-Universität Bonn (2000).

[80] F. Reif, *Fundamentals of Statistical and Thermal Physics* (McGraw-Hill, New York, 1965).

[81] C. Tuchendler, A. M. Lance, A. Browaeys, Y. R. P. Sortais, and P. Grangier, "Energy distribution and cooling of a single atom in an optical tweezer," Physical Review A **78**, 033425 (2008).

THESIS DRAFT

[82] E. Jones, T. Oliphant, P. Peterson, et al., "SciPy: Open source scientific tools for Python," (2001–), [Online; accessed 07.05.2018].

[83] S. Roof, K. Kemp, M. Havey, I. M. Sokolov, and D. V. Kupriyanov, "Microscopic lensing by a dense, cold atomic sample," Optics Letters **40**, 1137 (2015).

[84] J. R. Gilbert, C. P. Roberts, and J. L. Roberts, "Near-resonant light propagation in an absorptive spatially anisotropic ultracold gas," Journal of the Optical Society of America B **35**, 718 (2018).

[85] P. B. Wigley, P. J. Everitt, A. van den Hengel, J. W. Bastian, M. A. Sooriyabandara, G. D. McDonald, K. S. Hardman, C. D. Quinlivan, P. Manju, C. C. N. Kuhn, et al., "Fast machine-learning online optimization of ultra-cold-atom experiments," Scientific Reports **6**, 25890 (2016).

[86] W. Ketterle, K. B. Davis, M. A. Joffe, A. Martin, and D. E. Pritchard, "High densities of cold atoms in a dark spontaneous-force optical trap," Physical Review Letters **70**, 2253 (1993).

[87] N. Radwell, G. Walker, and S. Franke-Arnold, "Cold-atom densities of more than 10^{12} cm^{-3} in a holographically shaped dark spontaneous-force optical trap," Physical Review A **88**, 043409 (2013).

[88] L. Wacker, N. B. Jørgensen, D. Birkmose, R. Horchani, W. Ertmer, C. Klempt, N. Winter, J. Sherson, and J. J. Arlt, "Tunable dual-species Bose-Einstein condensates of ^{39}K and ^{87}Rb," Physical Review A **92**, 053602 (2015).

[89] S. Ospelkaus-Schwarzer, "Quantum Degenerate Fermi-Bose Mixtures of ^{40}K and ^{87}Rb in 3D Optical Lattices," Ph.D. thesis, Universität Hamburg (2006).

[90] C. Voss, "EIT-Spektroskopie von Rydbergzuständen an Rubidium," Bachelor's thesis, Johannes Gutenberg-Universität Mainz (2015).

[91] C. Voss, "Rydbergspektroskopie in Hohlkernfasern," Master's thesis, Johannes Gutenberg-Universität Mainz (2017).

[92] N. Šibalić, J. D. Pritchard, C. S. Adams, and K. J. Weatherill, "ARC: An open-source library for calculating properties of alkali Rydberg atoms," arXiv preprint arXiv:1612.05529 (2016).

[93] K. P. Nayak, P. N. Melentiev, M. Morinaga, F. L. Kien, V. I. Balykin, and K. Hakuta, "Optical nanofiber as an efficient tool for manipulating and probing atomic fluorescence," Optics Express **15**, 5431 (2007).

[94] E. Vetsch, D. Reitz, G. Sagué, R. Schmidt, S. T. Dawkins, and A. Rauschenbeutel, "Optical Interface Created by Laser-Cooled Atoms Trapped in the Evanescent Field Surrounding an Optical Nanofiber," Physical Review Letters **104**, 203603 (2010).

[95] T. Nieddu, V. Gokhroo, and S. N. Chormaic, "Optical nanofibres and neutral atoms," Journal of Optics **18**, 053001 (2016).

THESIS DRAFT

[96] D. Reitz, C. Sayrin, B. Albrecht, I. Mazets, R. Mitsch, P. Schneeweiss, and A. Rauschenbeutel, "Backscattering properties of a waveguide-coupled array of atoms in the strongly nonparaxial regime," Physical Review A **89**, 031804 (2014).

[97] H. L. Sørensen, J.-B. Béguin, K. W. Kluge, I. Iakoupov, A. S. Sørensen, J. H. Müller, E. S. Polzik, and J. Appel, "Coherent Backscattering of Light Off One-Dimensional Atomic Strings," Physical Review Letters **117**, 133604 (2016).

[98] N. V. Corzo, B. Gouraud, A. Chandra, A. Goban, A. S. Sheremet, D. V. Kupriyanov, and J. Laurat, "Large Bragg Reflection from One-Dimensional Chains of Trapped Atoms Near a Nanoscale Waveguide," Physical Review Letters **117**, 133603 (2016).

[99] J. Petersen, J. Volz, and A. Rauschenbeutel, "Chiral nanophotonic waveguide interface based on spin-orbit interaction of light," Science **346**, 67 (2014).

[100] P. Lodahl, S. Mahmoodian, S. Stobbe, A. Rauschenbeutel, P. Schneeweiss, J. Volz, H. Pichler, and P. Zoller, "Chiral quantum optics," Nature **541**, 473 (2017).

[101] F. Le Kien and A. Rauschenbeutel, "Nanofiber-mediated chiral radiative coupling between two atoms," Physical Review A **95**, 023838 (2017).

[102] C. Sayrin, C. Clausen, B. Albrecht, P. Schneeweiss, and A. Rauschenbeutel, "Storage of fiber-guided light in a nanofiber-trapped ensemble of cold atoms," Optica **2**, 353 (2015).

[103] B. Gouraud, D. Maxein, A. Nicolas, O. Morin, and J. Laurat, "Demonstration of a Memory for Tightly Guided Light in an Optical Nanofiber," Physical Review Letters **114**, 180503 (2015).

[104] R. Kumar, V. Gokhroo, and S. N. Chormaic, "Multi-level cascaded electromagnetically induced transparency in cold atoms using an optical nanofibre interface," New Journal of Physics **17**, 123012 (2015).

[105] F. Le Kien, V. I. Balykin, and K. Hakuta, "Atom trap and waveguide using a two-color evanescent light field around a subwavelength-diameter optical fiber," Physical Review A **70**, 063403 (2004).

[106] A. Goban, K. S. Choi, D. J. Alton, D. Ding, C. Lacroûte, M. Pototschnig, T. Thiele, N. P. Stern, and H. J. Kimble, "Demonstration of a State-Insensitive, Compensated Nanofiber Trap," Physical Review Letters **109**, 033603 (2012).

THESIS DRAFT

Danksagung

THESIS DRAFT